Understanding Morphology and Optoelectronic Properties of Powder-Based Pressure-Processed Lead Halide Perovskites

Von der Universität Bayreuth
zur Erlangung des Grades eines
Doktors der Naturwissenschaften (Dr. rer. nat.)
genehmigte Abhandlung

von
Christina Witt

aus Bayreuth, Deutschland

1. Gutachterin: Prof. Dr. Anna Köhler
2. Gutachter: Prof. Dr. Georg Herink
3. Gutachter: Prof. Dr. Lukas Schmidt-Mende

Tag der Einreichung: 07.02.2024
Tag des Kolloquiums: 17.06.2024

Geh nicht dorthin, wo alle anderen sind.
Geh stattdessen dorthin, wo noch niemand war,
und hinterlass dort deine Spuren.

nach Jean Paul*

Table of Contents

1 Abstract

Metal halide perovskites (MHPs) constitute an emerging class of semiconductor materials that have attracted increasing attention in recent years due to their exceptional optoelectronic properties, the potential for low-cost production and a wide range of applications such as X-ray detectors, LEDs, lasers and solar cells. The lab-scale efficiencies of MHP-based solar cells are today already on par with those of commercial silicon-based solar cells, and tandem solar cells based on silicon and MHP achieve even higher efficiencies, encouraging more and more start-ups and companies to develop MHP-based solar cells.

The progress and achievements in the field of MHPs over the last 15 years are remarkable, especially since they were mostly achieved through simple trial-and-error approaches. However, the still missing profound understanding of the correlation between morphology, structural and optoelectronic properties as well as the resulting functionality and stability, now becomes important to resolve the remaining current issues for commercialization so that the potential of MHP based devices actually comes into play. The current issues are grouped into technological hurdles such as upscalable processing methods and the avoidance of toxic solvents as well as MHP material quality-related hurdles such as improved process control, performance optimization and stability. The resolution of the purely technological hurdles is addressed in this work by developing, using and investigating dry (i.e. without any solvent), powder-based pressure processing approaches for the production of MHP thick and thin films (suitable for use in X-ray detectors and solar cells), which can potentially be upscaled. At the same time, these dry powder-based processing approaches are also a valuable tool to overcome the often used trial-and-error approaches for performance optimization, but to gain a comprehensive fundamental understanding of the relationship between morphological, structural and optoelectronic properties. Such fundamental understanding can be key to resolve current MHP material quality related issues. The possibility of gaining such a fundamental understanding from the dry powder-based approaches is based on the high degree of process control because of separated material synthesis and film formation. This separation is in contrast to common solution-based processing approaches and enables targeted investigation and improvement of individual processing parameters. Thus, this work aims for the understanding of morphology and optoelectronic properties of powder-based pressure-processed lead halide perovskites for improved functionality and stability, required for commercialization.

The dry pressure processing approaches are based on mechanochemically synthesized MHP powders, which can be produced in a variety of stoichiometries. However, their synthesis mechanism (influence of particle sizes and milling parameters) as well as resulting powder morphology and optoelectronic properties are still largely not understood. Related studies were therefore carried out in Chapter 4.1 in order to optimize perovskite

powder synthesis in terms of further processing into films and resulting device functionality. Here, we found larger reactant sizes to result in prolonged perovskite synthesis and shortened subsequent crushing stage during ball milling, which goes along with lower defect density as shown by NQR and TRPL measurements.

The identification of compaction processes occurring during MHP powder pressing, and systematic investigation of the pressing parameters pressing pressure, pressing time and pressing temperature with regard to induced film properties were addressed in Chapter 4.2 by means of time-resolved pressure monitoring and modelling of pressure dependent thick film densities. Here, I identified particle rearrangement and plastic deformation (including crushing) as occuring compaction processes during room-temperature powder pressing, where the latter becomes especially important at pressures $\geq$ 50 MPa. Besides increased pressure and pressing time I observed an increased pressing temperature to significantly accelerate compaction which I attributed to a sinter process. In addition, XRD measurements indicated temperature-induced crystallographic orientation increasing with pressing temperature.

Having understood both the powder properties and powder compaction during pressing in Chapters 4.1 and 4.2, I studied the influence of MHP powder microstructure on the compaction processes during pressing and resulting morphological and optoelectronic thick film properties in Chapter 4.3. Here, I found decreased compaction dynamic for larger powder particles with stronger sintered connnections between neighbouring particles by characterization of relaxation times from time-resolved pressure relaxations. In addition, I concluded plastic deformation to contribute more to the overall compaction process when pressing powders with larger powder particle sizes. The latter was also reflected in the degree of crystallite size reduction evaluated from XRD measurements, which I found to go along with increased defect-associated excited state recombination. Moreover, we found increased plastic deformation to deteriorate the grain boundary quality, facilitating ion migration reflected in higher electrical dark conductivities.

Having elucidated the many-faceted structure-properties relationship in powder-based pressure-processed MHP thick films in Chapter 4.3, I investigated the structure-properties relationship in powder-based MHP thin films deposited via PAD method in Chapter 4.4. Here, by using insights from Chapter 4.2, I specifically induced small morphology differences relevant for optimization of high efficiency devices by pressing the films with different temperatures. An increased temperature resulted in larger grain size and increased preferred crystallographic orientation, i.e. improved film morphology. By means of temperature-dependent absorption and PL analyses between 300 K and 5 K I found the induced morphology improvements to be correlated with and increased phase transition temperature and attributed this to less strain. In addition, including also fluence-dependent PL analyses and TRPL analyses I found the morphology improvements to correlate with decreased defect density. Here, I observed that besides often-considered larger grain sizes also increased preferred crystallographic orientation results in longer charge carrier lifetimes. The identified correlation of improved film morphology with reduced strain and lower defect densities also indicated reduced energetic disorder which was shown by absorption analyses of the Urbach energy in Chapter 4.5.

In Chapter 4.5 I carried out profound Urbach energy analyses from PL and absorption spectra between 300 K and 160 K to investigate the origin of present discrepancies in Urbach energy values derived from different measurement and analyses methods. As the Urbach energy is a popular figure of merit representing the performance potential of semiconductor materials like MHPs, I aimed to reveal the origin of these discrepancies to sensitize for reliable and reasonable interpretation and comparison of extracted Urbach energy values. From profound optical analyses, I concluded that energy-range dependent exaggeration effects on extracted Urbach energy values are only relevant down to 0.02 eV below the bandgap where non-Urbach absorption states contribute. Besides that, I attributed general lower Urbach energy values as well as a lower temperature-dependence of the Urbach energy from PL compared to from absorption to a preferential sensitivity of PL for sites with lower energetic disorder, i.e. sites of higher film quality. Moreover, I discussed the lower temperature-dependence of the Urbach energy to potentially also stem from higher phonon energies in the excited state geometry probed by PL.

In Chapter 4.6 we used our newly developed dry-powder-based MHP thin film processing approach via PAD and pressing to build up solar cells with completely dry-processed MHP absorber layer - the first of their kind. Here, using insights from Chapters 4.2, 4.4 and 4.5 we succeeded in setting the film quality of our dry-processed MHP absorber layers on par with common solution processed films as proven by e.g. high compaction visible in SEM images or evaluated Urbach energies from absorption spectra. Remaining issues at the interfaces between MHP and charge transport layers, e.g. increased energetic disorder of the ETL after PAD processing limiting the overall device performance were identified. Nevertheless, because of promising approaches presented to overcome the current issues we are confident that efficient solar cells can be produced with our novel dry procesing approach in the future.

Overall, the insights gained in this thesis contribute to a profound understanding of morphology and related optoelectronic properties in powder-based pressure-processed lead halide perovskite films. This gained understanding is valuable for in general improved MHP film processing and resulting functionality of MHP based optoelectronic devices such as X-ray detectors or solar cells.

Kurzfassung

Metallhalogenperowskite (MHP) stellen eine aufstrebende Klasse von Halbleitermaterialien dar, die in den letzten Jahren aufgrund ihrer außergewöhnlichen optoelektronischen Eigenschaften, des Potenzials für eine kostengünstige Produktion und eines breiten Spektrums von Anwendungen wie Röntgendetektoren, LEDs, Laser und Solarzellen immer mehr Aufmerksamkeit auf sich gezogen haben. Die Wirkungsgrade von Solarzellen auf MHP-Basis im Labormaßstab liegen heute bereits gleichauf mit denen kommerzieller Solarzellen auf Silizium-Basis, und Tandem-Solarzellen auf der Basis von Silizium und MHP erreichen sogar noch höhere Wirkungsgrade, was immer mehr Startups und Unternehmen dazu ermutigt, Solarzellen auf MHP-Basis zu entwickeln.

Die Fortschritte und Errungenschaften auf dem Gebiet der MHP in den letzten 15 Jahren sind bemerkenswert, zumal sie zumeist durch einfache Trial-and-Error Ansätze erzielt wurden. Das immer noch fehlende tiefgreifende Verständnis des Zusammenhangs zwischen Morphologie, strukturellen und optoelektronischen Eigenschaften sowie der daraus resultierenden Funktionalität und Stabilität wird nun wichtig, um die verbleibenden aktuellen Probleme im Hinblick auf Kommerzialisierung zu beheben, damit das Potenzial von MHP-basierten Bauteilen tatsächlich zum Tragen kommen kann. Die aktuellen Probleme lassen sich in technologische Hürden wie hochskalierbare Verarbeitungsmethoden und die Vermeidung toxischer Lösungsmittel sowie in MHP materialqualitätsbezogene Hürden wie verbesserte Prozesskontrolle, Performance-Optimierung und Stabilität unterteilen. Die Lösung der rein technologischen Hürden wird in dieser Arbeit durch die Entwicklung, Anwendung und Untersuchung von trockenen (d.h. ohne Lösungsmittel), pulverbasierten Druckverarbeitungsansätzen für die Herstellung von MHP-Dick- und Dünnschichten (geeignet für den Einsatz in Röntgendetektoren und Solarzellen) angegangen, die potenziell hochskaliert werden können. Gleichzeitig sind diese pulverbasierten Ansätze auch ein wertvolles Instrument, um die häufig verwendeten Trial-and-Error Ansätze zur Performance-Optimierung zu überwinden und ein umfassendes grundlegendes Verständnis der Beziehung zwischen morphologischen, strukturellen und optoelektronischen Eigenschaften zu gewinnen. Ein solch grundlegendes Verständnis kann der Schlüssel zur Lösung der aktuellen Probleme bezüglich der MHP Materialqualität sein. Die Möglichkeit, ein solch grundlegendes Verständnis aus den trockenen pulverbasierten Ansätzen zu gewinnen, beruht auf dem hohen Grad an Prozesskontrolle aufgrund der getrennt voneinander ablaufenden Materialsynthese und Filmbildung. Diese Trennung steht im Gegensatz zu gängigen lösungsbasierten Verarbeitungsansätzen und ermöglicht die gezielte Untersuchung und Verbesserung einzelner Verarbeitungsparameter. Somit zielt diese Arbeit auf das Verständnis der Morphologie und der optoelektronischen Eigenschaften von pulverbasierten druckverarbeiteten Bleihalogenperowskiten ab, um die für die Kommerzialisierung erforderliche verbesserte Funktionalität und Stabilität zu erreichen.

Die trockenen, pulverbasierten Verarbeitungsansätze basieren auf mechanochemisch synthetisierten MHP-Pulvern, die in einer Vielzahl von Stöchiometrien hergestellt werden können. Der Synthesemechanismus (Einfluss von Partikelgrößen und Mahlparametern) sowie die daraus resultierende Pulvermorphologie und die optoelektronischen Eigenschaften sind jedoch noch weitgehend unverstanden. Daher wurden in Kapitel 4.1 entsprechende Studien durchgeführt, um die Synthese von Perowskit-Pulver im Hinblick auf die Weiterverarbeitung zu Filmen und die daraus resultierende Funktionalität der Bauteile zu optimieren. Hier haben wir festgestellt, dass größere Reaktantgrößen zu einer verlängerten Perowskit-Synthese und einer verkürzten anschließenden Zerkleinerungsphase beim Kugelmahlen führen, was mit einer geringeren Defektdichte einhergeht, wie NQR- und TRPL-Messungen zeigen.

Die Identifizierung von Verdichtungsprozessen, die während des MHP-Pulverpressens auftreten, und die systematische Untersuchung der Pressparameter Pressdruck, Presszeit und Presstemperatur im Hinblick auf die induzierten Filmeigenschaften wurden in Kapitel 4.2 mittels zeitaufgelöster Drucküberwachung und Modellierung der druckabhängigen Dickschichtdichten behandelt. Hier identifizierte ich Partikelumlagerung und plastische Deformation (einschließlich Zerkleinerung) als auftretende Verdichtungsprozesse während des Pulverpressens bei Raumtemperatur, wobei letzterer bei Drücken von ≥ 50 MPa besonders wichtig wird. Neben erhöhtem Druck und erhöhter Presszeit beobachtete ich, dass eine erhöhte Presstemperatur die Verdichtung deutlich beschleunigte, was ich auf einen Sinterprozess zurückführte. Darüber hinaus zeigten XRD-Messungen eine temperaturinduzierte kristallografische Orientierung, die mit der Presstemperatur zunahm.

Nachdem ich in den Kapiteln 4.1 und 4.2 sowohl die Pulvereigenschaften als auch die Pulververdichtung während des Pressens verstanden hatte, habe ich in Kapitel 4.3 den Einfluss der MHP-Pulvermikrostruktur auf die Verdichtungsprozesse während des Pressens und die daraus resultierenden morphologischen und optoelektronischen Dickschichteigenschaften untersucht. Hier fand ich eine verringerte Verdichtungsdynamik für größere Pulverpartikel mit stärkeren Sinterverbindungen zwischen benachbarten Partikeln durch Charakterisierung der Relaxationszeiten aus zeitaufgelösten Druckrelaxationen. Darüber hinaus kam ich zu dem Schluss, dass die plastische Deformation beim Pressen von Pulvern mit größeren Pulverteilchen mehr zum gesamten Verdichtungsprozess beiträgt. Letzteres spiegelte sich auch im Grad der Kristallitverkleinerung wider, der anhand von XRD-Messungen ermittelt wurde und mit einer erhöhten defektassoziierten Rekombination angeregter Zustände einherging. Darüber hinaus haben wir festgestellt, dass eine verstärkte plastische Deformation die Qualität der Korngrenzen verschlechtert und die Ionenwanderung erleichtert, was sich in höheren elektrischen Dunkelleitfähigkeiten widerspiegelte.

Nachdem ich in Kapitel 4.3 die vielschichtige Struktur-Eigenschafts-Beziehung in pulverbasierten druckverarbeiteten MHP-Dickschichten aufgeklärt hatte, untersuchte ich in Kapitel 4.4 die Struktur-Eigenschafts-Beziehung in pulverbasierten MHP-Dünnschichten, die mittels PAD-Methode abgeschieden wurden. Hier habe ich unter Verwendung der Erkenntnisse aus Kapitel 4.2 gezielt kleine Morphologieunterschiede induziert, die für die Optimierung hocheffizienter Bauteile relevant sind, indem ich die Schichten bei unterschiedlichen Temperaturen gepresst habe. Eine erhöhte Temperatur führte zu größeren Korngrößen und einer erhöhten bevorzugten kristallographischen Orientierung, d.h. zu

einer verbesserten Filmmorphologie. Mit Hilfe von temperaturabhängigen Absorptions- und PL-Analysen zwischen 300 K und 5 K konnte ich feststellen, dass die Verbesserungen der Morphologie mit einer erhöhten Phasenübergangstemperatur korrelieren, was ich auf geringere Spannungen zurückführte. Darüber hinaus habe ich mit Hilfe von fluenzabhängigen PL-Analysen und TRPL-Analysen festgestellt, dass die Morphologieverbesserungen mit einer geringeren Defektdichte korrelieren. Dabei stellte ich fest, dass neben der oft betrachteten größeren Korngröße auch die bevorzugte kristallographische Orientierung zu längeren Ladungsträgerlebensdauern führt. Die festgestellte Korrelation der verbesserten Filmmorphologie mit reduzierten Spannungen und geringerer Defektdichte deutete auch auf eine geringere energetische Unordnung hin, was durch Analysen der Urbach-Energie aus Absorption in Kapitel 4.5 gezeigt werden konnte.

In Kapitel 4.5 habe ich tiefgreifende Analysen der Urbach-Energie an PL- und Absorptionsspektren zwischen 300 K und 160 K durchgeführt, um den Ursprung bestehender Diskrepanzen in Urbach-Energie-Werten zu untersuchen, die anhand verschiedener Mess- und Analysemethoden bestimmt wurden. Da die Urbach-Energie eine populäre Kenngröße für das Performance-Potenzial von Halbleitermaterialien wie MHPs repräsentiert, wollte ich den Ursprung dieser Diskrepanzen aufdecken, um zuverlässige und vernünftige Interpretationen und Vergleiche extrahierter Urbach-Energie-Werte zu ermöglichen. Aus tiefgreifenden optischen Analysen schloss ich, dass energiebereichsabhängige Überhöhungseffekte auf die extrahierten Urbach-Energie-Werte nur bis zu 0,02 eV unterhalb der Bandlücke relevant sind, wo Nicht-Urbach-Absorptionszustände beitragen. Außerdem führte ich die allgemein niedrigeren Urbach-Energie-Werte sowie die geringere Temperaturabhängigkeit der Urbach-Energie aus PL im Vergleich zu aus Absorption auf eine bevorzugte Sensitivität der PL für Stellen mit geringerer energetischer Unordnung zurück, d.h. Stellen mit höherer Filmqualität. Darüber hinaus habe ich diskutiert, dass die geringere Temperaturabhängigkeit der Urbach-Energie möglicherweise auch auf höhere Phononen-Energien in der von PL untersuchten Geometrie des angeregten Zustands zurückzuführen sein kann.

In Kapitel 4.6 haben wir unsere neu entwickelte, trockene, pulverbasierte MHP-Dünnfilm-Verarbeitungsmethode mittels PAD und Pressen verwendet, um Solarzellen mit vollständig trocken prozessierter MHP-Absorberschicht aufzubauen - die ersten ihrer Art. Unter Verwendung der Erkenntnisse aus den Kapiteln 4.2, 4.4 und 4.5 ist es uns gelungen, die Schichtqualität unserer trocken prozessierten MHP-Absorberschichten auf das Niveau herkömmlicher lösungsprozessierter Schichten zu bringen, wie z.B. durch die in REM-Bildern sichtbare hohe Verdichtung oder ausgewertete Urbach-Energien aus Absorptionsspektren belegt wurde. Verbleibende Probleme an den Grenzflächen zwischen MHP und Ladungstransportschichten, wie z.B. eine erhöhte energetische Unordnung der ETL nach der PAD-Prozessierung, die die Performance des Bauteils einschränken, wurden identifiziert. Aufgrund der vorgestellten vielversprechenden Ansätze zur Überwindung der aktuellen Probleme sind wir jedoch zuversichtlich, dass in Zukunft effiziente Solarzellen mit unserem neuartigen Trockenprozessierungsansatz hergestellt werden können.

Insgesamt tragen die in dieser Arbeit gewonnenen Erkenntnisse zu einem tiefgreifenden Verständnis der Morphologie und der damit verbundenen optoelektronischen Eigenschaften von pulverbasierten, druckverarbeiteten Bleihalogenperowskit-Filmen bei. Dieses gewonnene Verständnis ist allgemein wertvoll für verbesserte MHP-Filmverarbeitung und daraus resultierende verbesserte Funktionalität von MHP-basierten optoelektronischen Bauteilen wie Röntgendetektoren oder Solarzellen.

2 Introduction

2.1 Motivation

The global warming is a major global challenge of our time, which together with the increasing demand for energy requires the development of more efficient and cost-effective renewable energies to make decarbonization globally attractive and to provide sufficient green energy everywhere at all time.[1,2]

Currently, in the solar energy sector, solar cells with silicon as the active layer are mainly used,[3,4] with efficiencies of around 26.8 % on laboratory scale,[5] and around 24.4 % for standard modules.[6] Higher efficiencies of 33.7 % on laboratory scale,[5] and around 28.6 % for commercial-sized solar cells are achieved by so-called tandem solar cells, which consist of silicon and a metal halide perovskite (MHP) as active layers.[7] Here, the MHP material constitutes a cost-effective improvement by its appropriately tuned higher bandgap energy enabling a more efficient use of light in an extended spectral range towards higher energies.[8] As a result, such tandem solar cells are today already on the verge of commercialization.[7] However, solar cells with a pure MHP thin film as active layer are also of interest, as after only 15 years of research they now already achieve efficiencies on laboratory scale of 26.1 % that are on par with silicon cells.[3,5,9] These pure MHP solar cells are attractive due to their simple and cost-effective processing,[3,10] as well as the possibility of novel implementations, e.g., in the form of flexible and lightweight devices,[10,11] requestet for especially in the context of the rising "Internet of Things" (IoT).[10,12]

Besides solar cells, MHPs are also promising for the application in other optoelectronic devices such as LEDs, lasers, photo- and X-ray detectors.[13–16] For the latter, the successful integration of thick films of the standard perovskite $MAPbI_3$ on pixelated backplanes for MHP based flat-panel X-ray detector arrays has already been demonstrated.[17,18] In addition, MHP based sensitivities comparable to those of commercially established materials such as CdTe, or even higher in the case of a-Se, have already been achieved on laboratory scale.[19,20] The development of such novel X-ray technologies with enhanced sensitivity is of great interest to improve imaging quality and reduce required radiation dose, thus enabling better and safer diagnosis and therapy of patients.

Essential for the rapid development and improvement of MHP-based devices was the conceptual recognition that the device functionality is determined by the optoelectronic film properties, which in turn depend on the structural and morphological film properties.[10,21,22] Thus, remarkable progress has been made through improved processing, the use of novel stoichiometries and, most common, the incorporation of additives or passivating agents,[23–26] where often a simple trial-and-error approach has been successful.[24–28] Such simple approach has been used since despite the rapid development of MHPs a profound understanding of the relationship between morphological, structural

and optoelectronic properties (often shortly referred to as structure-properties relationship) is still missing.[29, 30] Here, even the reliable and reasonable characterization of a popular figure of merit for the energetic disorder and the performance potential of semiconductors, the Urbach energy, has not yet been fully resolved.[31, 32] The reason for the still missing knowledge is the complexity of the structure-properties relationship,[29, 30] which is hard to access in common film fabrication methods such as evaporation or, most popular, solution-based spincoating, as material synthesis and film formation proceed simultaneously.[33] To address this issue, the number of resarch studies on optical in-situ spectroscopy, which aim to identify MHP film formation processes and understand the relationship between structural and optoelectronic properties, is currently increasing.[34–36] Nevertheless, process control remains difficult, which is necessary for a systematic investigation of the structure-properties relationship.[30, 33]

In view of these considerations, in this thesis I use an alternative attractive film fabrication approach, namely dry powder-based pressure processing of MHPs, where material synthesis and film formation occur separately from each other, enabling a high level of process control. Through this approach, I systematically investigate the morphology and optoelectronic properties of powder-based, pressure-processed lead halide perovskite films to gain a thorough understanding of the structure-properties relationship for targeted functionality improvements of MHP based devices.

In the first part of this thesis, in Chapter 2, MHPs are introduced, including film processing methods, basic optical and structural characteristics, and what is known about the relationship between these characteristics and film morphology. In addition, MHP device applications are presented and their prospects for commercialization are discussed. In Chapter 3 the thesis summary is given with details of what I investigated and found in the six paper publications contributing to the thesis aim, which is the understanding of morphology and optoelectronic properties of powder-based pressure-processed lead halide perovskites. Subsequent to an outlook, the full publications are then presented in Chapter 4.

2.2 Metal Halide Perovskites (MHPs)

The perovskite class of materials dates back to the discovery of ceramic oxides with the general molecular formula ABX_3 by the mineralogist Gustav Rose in 1839 and got its name from the designation of the calcium titanate mineral $CaTiO_3$ according to the mineralogist Lew Perowski.[37,38] Today, the perovskite class of materials summarizes all compounds with ABX_3 crystal structure, i.e. compounds with perovskite structure.[37–39] The formation of a perovskite structure requires the fulfillment of a tolerance factor

$$t = \frac{R_A + R_X}{\sqrt{2}(R_B + R_X)} \tag{2.1}$$

between 0.8 and 1.0 by the ionic radii R_A, R_B and R_X.[39] Fig. 2.1a shows the perovskite crystal lattice, which consists of $(BX_6)^{4-}$ octahedra with A cations in between.[40] The tilting of the octahedra dictates the crystal symmetry space group (crystallographic phase see Fig. 2.4c).[39]

The most common stoichiometries of metal halide perovskites (MHPs) are indicated in Fig. 2.1a.[40] The standard MHP is methylammonium lead iodide (MAPbI$_3$).[43] In addition, a variety of other stoichiometries exists,[39] with mixed cation and mixed halide anion
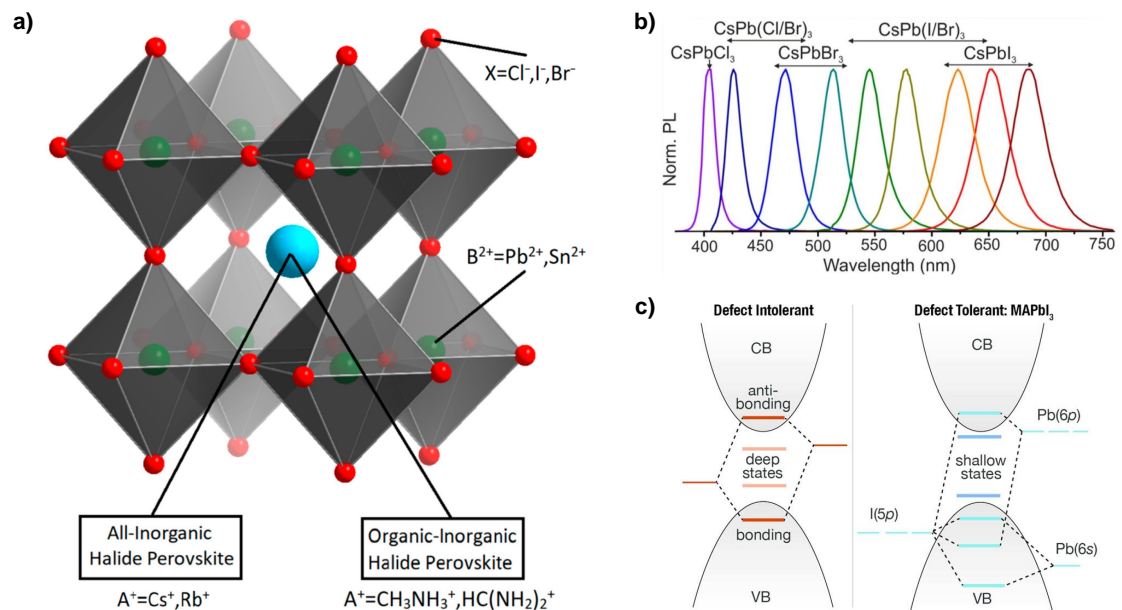

Figure 2.1: a) Sketch of the metal halide perovskite ABX_3 crystal structure with indication of common stoichiometries. Reprinted as adapted version with permission according to the CC BY 4.0 license from Dai et al.[40] Copyright 2021 by the authors. Licensee MDPI, Basel, Switzerland. b) Tuning of the PL wavelength by varying the MHP stoichiometry. Reprinted as adapted version with permission according to the CC BY 4.0 license from Zhang et al.[41] Copyright 2022 by the authors. Licensee MDPI, Basel, Switzerland. c) Electronic structure of a defect intolerant semiconductor material and MAPbI$_3$ as defect tolerant semiconductor material. Reprinted with permission from Brandt et al.[42] Copyright 2017 American Chemical Society.

MHPs being used, especially with respect to solar cell application, to tune the band gap and achieve higher efficiencies and improved stability.[44] Limited stability currently remains as major hurdle on the way to commercialization.[45] For this reason, besides these so-called 3D perovskites with ABX_3 structure, research is also done on 0D, 1D and 2D perovskites, which are characterized by higher stability. However, these low-dimensional perovskites lag behind in their optoelectronic properties and functionality, keeping research focus on 3D perovskites.[23,46]

The integration of MHPs in optoelectronic devices such as solar cells, LEDs, lasers, photo- and X-ray detectors is attractive due to MHPs beneficial optoelectronic properties like their high absorption coefficient, high defect tolerance, high charge carrier mobility and diffusion length,[13,38,47] the tunable bandgap by stoichiometry variation (e.g. Fig. 2.1b),[13,38,41,44,47] as well as low-cost processing.[13,38,45]

The exceptionally beneficial optoelectronic properties result from the electronic structure of MHPs,[13] which is essentially determined by the orbitals of the inorganic B and X anions,[13,30,44,47] resulting in some similar characteristics as known for classical inorganic semiconductors (e.g. Si or GaAs).[39,48] However, MHPs consist of a soft ionic crystal lattice,[48,49] thus differing from classical inorganic semiconductors in terms of specific structural and optoelectronic properties.[39,48,50] Basically, in contrast to classical inorganic semiconductors, where conduction band (CB) and valence band (VB) are formed by antibonding and bonding orbitals, rendering them susceptible to deep defect generation (Fig. 2.1c left),[47] the CB minimum and VB maximum in MHPs are formed only by orbital interactions with antibonding character (Fig. 2.1c right).[13,47] Consequently, in MHPs mainly so-called shallow defects are present, which are located close to or in the bands. The benign nature of such shallow defects is referred to as defect tolerance in MHPs. Deep defects, e.g. due to halide interstitials, occur only in much smaller numbers.[47] The A cation in MHPs does not contribute directly to the band structure, but still influences the resulting bandgap.[44,51] Exemplarily, this effect becomes clear when substituting the methylammonium (MA) cation in $MAPbI_3$ ($E_g \approx 1.6$ eV)[39] with the formamidinium (FA) cation to $FAPbI_3$ ($E_g \approx 1.4$ eV),[52] which shifts the bandgap energy down in an optimum range in terms of solar cell efficiency according to the Shockley-Queisser Limit.[44,52,53] Here, the larger FA cation is more prone for hydrogen bond formation with the inorganic structure than the MA cation, leading to reduced octahedral tilting, which in turn leads to an increased lead character of the conduction band states and ultimately to increased spin-orbit coupling, shifting the bandgap to lower energies.[39,54] MHPs such as $FAPbI_3$ or $MAPbI_3$ are referred to as direct bandgap semiconductors,[13,48,52] which is due to their high symmetry crystal structure.[13]

2.3 MHP Processing Methods

2.3.1 General Overview

Depending on their application, MHPs are processed as thick films (film thickness > 10 µm up to several mm, e.g. in X-ray detectors)[20,55] or thin films (film thickness $<\approx$ 5 µm, e.g. in solar cells).[56,57]

Polycrystalline thick films can be processed solution-based by e.g. doctor blading[58] or using a mist deposition method.[59,60] In addition, powder can be melted so that it recrystallizes into a polycrystalline thick film upon cooling.[61,62] Improved optoelectronic properties are achieved with thick films made of single crystals grown from solution, as these contain a lower number of bulk defects and grain boundaries (where also defects and strain are localized) compared to polycrystalline films, resulting in modified optoelectronic properties such as increased charge carrier diffusion and charge carrier lifetime.[63,64] However, thick film manufacturing from single crystals is difficult to scale up, which represents a problem in terms of commercialization.[63] Furthermore, melting of perovskite powders is limited to certain perovskite stoichiometries such as $CsPbBr_3$ because the melting temperature may not exceed the degradation temperature,[62] and process control in solution-based methods is complex.[65,66] In view of these drawbacks, (hot-)pressing of perovskite powder into thick film pellets (Fig. 2.3b), which is investigated in this work, represents an attractive alternative processing approach. In this (hot-)pressing approach, material synthesis and film formation occur separately, enabling a high degree of process control and targeted improvement of individual processing parameters.[67] In addition, the perovskite source powders are feasible in a variety of stoichiometries[68] and promising upscaling methods have already been presented (see Section 2.5.2).[18,69]

Since most MHP research is being done with regard to solar cell application, the main focus in the perovskite community is on thin film processing, for which many different approaches exist.[51,70] Most common are solution processing methods, since often only simple and cost-effective equipment is required, and crystallization of the perovskite films occurs quite fast and at relatively low temperatures.[33,65,70] The most popular method is spincoating (Fig. 2.2a), where the reactants are dissolved in solution, dropped onto a
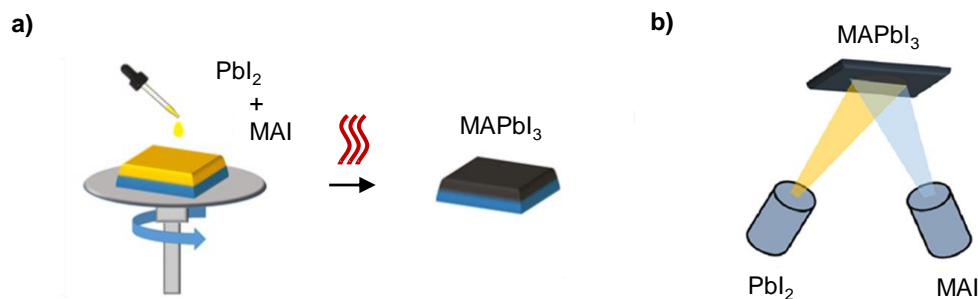

Figure 2.2: Common MHP film processing methods illustrated for $MAPbI_3$: a) Spincoating. b) Thermal vapor deposition. a), b) Reprinted as adapted version with permission from Song et al.[65] Copyright 2016 Society of Photo-Optical Instrumentation Engineers (SPIE). Permission conveyed through Copyright Clearance Center, Inc.

substrate and distributed by rotation before the solvent evaporates and the perovskite crystallization takes place.[33, 65] For complete perovskite formation, a subsequent annealing step at 100 to 150 °C is usually necessary.[65] Spincoating is well suited for laboratory scale, yet upscaling this method is difficult. For this purpose, several other solution-based approaches have been designed specifically for the manufacturing of large-scale thin films (Section 2.5.2), but corresponding solar cell efficiencies still lag behind those of spincoated films.[65, 70] In addition to solution-based film manufacturing, vapor deposition of reactants onto a substrate on which film formation and perovskite formation take place is a well-established alternative dry film manufacturing approach (Fig. 2.2b), although it is more laborious and expensive than solution-based methods.[33, 65, 70] Both, solution-based thin film processing methods and also dry thin film processing by evaporation, however, share the disadvantage of difficult process control.[65] For higher process control, thin film processing methods in which material synthesis and film formation occur separately from each other are of interest. However, to the best of my knowledge, up to now, only one such method has been demonstrated by Nejand et al. which is a wet MHP powder processing method. In this wet method of Nejand et al., a suspension of MAPbI$_3$ powder is deposited as thin film on a substrate by spray coating at 80 °C and then hot-pressed with 0.5 MPa at 120 °C.[71] In this work, I develop a new thin film processing method, where material synthesis and film formation occur seperately, which is completely dry. Specifically, in this dry method, mechanochemically synthesized MHP powder is directly deposited as thin film on a substrate by powder aerosol deposition (PAD) at room temperature following posttreatmemt by hot-pressing with 25 MPa at 120 °C (Fig. 2.3c).

2.3.2 Dry Powder-Based Pressure Processing

MHP thin films and thick films investigated in this work are not produced by common solution processing methods, where material synthesis and film formation occur simultaneously, but by dry powder-based pressure processing methods, where material synthesis and film formation occur separately. This separation makes it possible to investigate the relationship between material properties and morphological, structural and optoelectronic film properties in order to specifically optimize processing parameters and resulting film functionality. In addition to the high level of process control thus ensured, these film processing methods do not use toxic solvents and can be scaled up, which is of great relevance with regard to commercialization (Section 2.5.2).

Mechanochemical MHP Powder Synthesis

The basis for the dry powder-based pressure processing methods used in this work is MHP powder (e.g. MAPbI$_3$ or MAPbBr$_3$ powder), which is synthesized via mechanochemical synthesis (Fig. 2.3a). For the mechanochemical synthesis of e.g. MAPbI$_3$ powder, the reactants MAI and PbI$_2$ (in powder form) are weighed into a milling jar. In addition, milling balls and cyclohexane as a milling agent, which is not involved in the perovskite reaction, are put into the milling jar which is then closed and mounted in a planetary ball mill. The powders are milled by the rotation of the milling jar around its own axis, as well as by the rotation of the disc on which the milling jar is fixed in
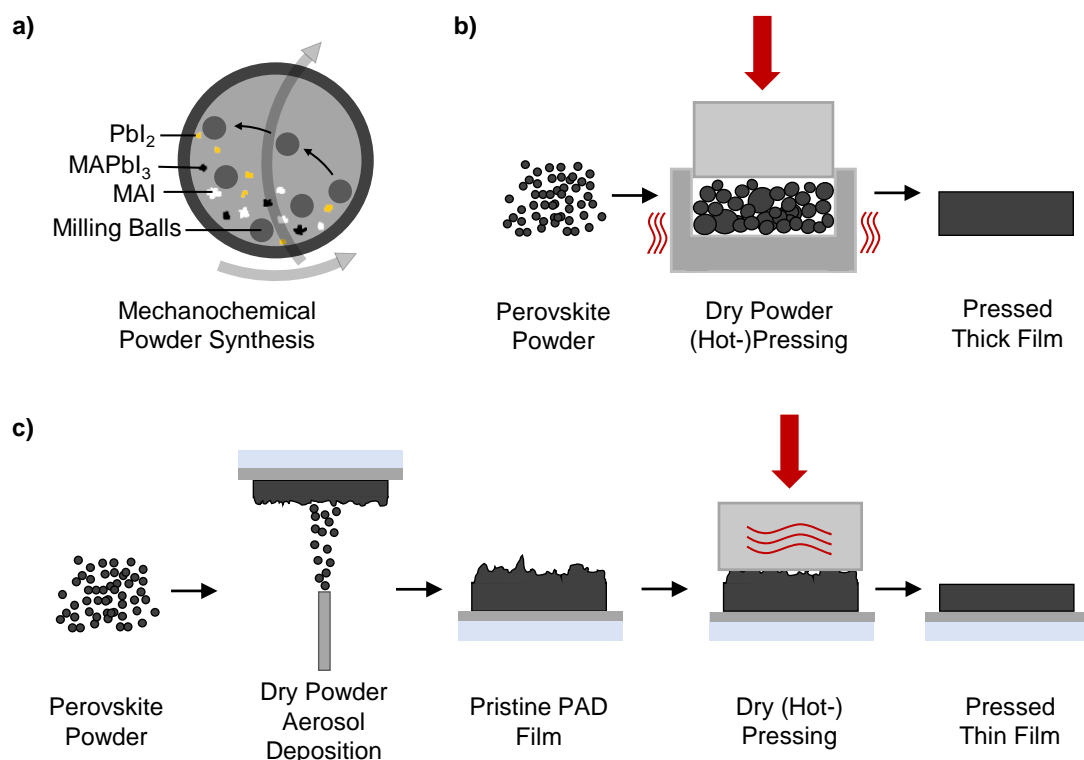
Figure 2.3: Dry powder-based MHP film processing methods applied in this thesis illustrated for MAPbI$_3$: a) Mechanochemical perovskite powder synthesis. b) Powder (hot-)pressing into thick film pellets. c) Powder aerosol deposition of perovskite powder into a thin film and subsequent (hot-)pressing. b) and c) Reprinted as adapted version with permission according to the CC BY 4.0 license from Biberger et al.[72] Copyright 2023 The Authors. Solar RRL published by Wiley-VCH GmbH.

the planetary ball mill. Through these rotations, the milling balls in the jar are smashed against the wall of the jar and onto powder located there, thus providing the energy for the reaction of the reactants to the perovskite (e.g. MAPbI$_3$).[68] After completion of the milling process (total milling time $\approx$ 30 min for MAPbI$_3$),[73–75] which may include breaks to avoid excessive heat generation ($< \approx$ 40 °C) due to friction,[76] the milling jar is opened to allow the milling agent to evaporate, thus retaining the synthesized perovskite powder.[68]

As alternatives to mechanochemical synthesis, other methods for perovskite powder synthesis exist, namely thermal annealing (dry method limited to certain stoichiometries, which do not degrade at required high temperatures) as well as solution-based sonochemical synthesis and precipitation reactions.[62] In contrast to solution-based powder synthesis methods, the morphology of powders resulting from mechanochemical synthesis is not characterized by individual crystals but by agglomerated powder particles, i.e. aggregates and larger agglomerates.[62,68] The mechanochemically synthesized MHP powders exhibit exceptional long-term stability ($>$ 2.5 years) when stored in nitrogen atmosphere,[68] and larger quantities (kg range) can be synthesized within a few hours which is useful in view of commercialization.[77] Moreover, no toxic solvents are requi-

red in the mechanochemical synthesis and without solubility limitations a wide range of perovskite stoichiometries can be realized. Here, control of the stoichiometric ratio is exceeding compared to solution-based methods.[62, 78]

Despite these advantages of the mechanochemical synthesis method, only few studies on the understanding of the mechanochemical synthesis mechanism exist.[62] So far, it is known that rapid crushing of brittle PbI_2 particles during the milling process promotes the $MAPbI_3$ perovskite synthesis as the small PbI_2 particles are squeezed into plastical-ly deformed MAI particles,[79] and that the $MAPbI_3$ perovskite synthesis proceeds faster for smaller MAI particles.[68] In addition, Palazon et al. concluded from PL spectra that continuing the milling process of the inorganic perovskite $CsPbBr_3$ after fully completed perovskite conversion for up to 10 hours leads to crushing of the powder and induction of defects.[80] However, comprehensive studies regarding the influence of particle sizes and milling parameters on resulting morphology and optoelectronic properties of mechano-chemically synthesized MHP powders are still missing.[62] In this work, related studies are therefore carried out in order to optimize perovskite powder synthesis in terms of further processing into films and resulting device functionality.

Powder Pressing to Thick Film Pellets

To make MHP powders usable for optoelectronic devices such as X-ray detectors, they can be pressed into a compact thick film pellet. Basically, two pressing concepts exist. In isostatic pressing, high pressures ($\approx$ 200 MPa) are applied isotropically via a fluid, where hot-pressing via temperature control of the fluid is still often limited to temperatures below 100 °C owing to technological and cost reasons.[81, 82] Alternatively, single action pressing is used, for example, with a hydraulic press or, as in the context of this work, with a home-built manual press setup, where pressure (up to $\approx$ 300 MPa) is applied from one direction via a press punch (Fig. 2.3b).[55, 83] Here, the press mold can be hea-ted, allowing temperatures of up to $\approx$ 150 °C to be realized.[83] For the pressing process, the MHP powder is filled into the press mold, and pressure is applied by moving the press punch into the press mold. To prevent the pressed MHP thick film pellet from sticking in the mold in the course of compaction, a low surface roughness of the press mold ($<$ 5 µm) and press punch (down to $\approx$ 0.005 µm) is required.[62, 84] Depending on stoichiometry and powder synthesis, however, MHP powders differ in morphology and texture, for example, lead-free 0D perovskite powders appear to suffer less from adhesion problems than $MAPbI_3$.[62, 85]

The first thick film pellets pressed from MHP powder to be used as active layer in an optoelectronic device were presented by Shrestha et al. in 2017. These $MAPbI_3$ thick film pellets, pressed with 300 MPa at room temperature, had a high relative density (with respect to the single crystal density) of about 90 % and showed remarkably high sensitivity under X-ray exposure of 2.5 µC/(Gycm^2) at an electric field of 0.2 V/µm.[55] Tie et al. pressed lead-free 0D perovskite powder ($MA_3Bi_2I_9$) with 200 MPa at room temperature and even achieved relative densities of 97 %,[86] which compared to the work of Shrestha et al. suggests that the MHP powder morphology and microstructure are crucial for the compaction processes during pressing and the resulting thick film pro-perties. However, to the best of my knowledge, studies on the influence of MHP powder microstructure on the compaction processes during pressing and resulting morphologi-

cal and optoelectronic thick film properties are still missing. In addition, in general, knowledge of the compaction processes occurring during MHP powder pressing does not yet exist, and the pressing parameters - pressing pressure, pressing time and pressing temperature - have not yet been systematically investigated with regard to induced film properties. Only from pressing solution-processed MAPbI$_3$ thin films it is known that higher pressing pressures and pressing times reduce film thickness,[71] and higher pressing temperatures increase resulting grain sizes.[87,88] For this reason, this work uses the home-built press-setup, which allows for time-resolved pressure monitoring, to reveal the compaction processes during powder (hot-)pressing and to in detail investigate the influence of the pressing parameters on the resulting film properties.

Pressing Thin Films Deposited via PADM

Transferring MHP powders into a MHP thin film has been limited to wet powder processing, either directly via suspension deposition or by powder dissolution with subsequent MHP recrystallization.[62] In this work, I develop a novel dry MHP powder-based thin film processing method (Fig. 2.3c).[72] In this method, mechanochemically synthesized MAPbI$_3$ powder is deposited by powder aerosol deposition (PAD) at room temperature to form a thin film, which tends to contain less strain compared to solution-processed films processed at elevated temperatures or using an annealing step, since the film formation is not followed by an uncontrolled cooling process.[73,89] For optimized film properties, the deposited films are posttreated via hot-pressing with 25 MPa and up to 120 °C, where elevated pressing temperature induces a sinter effect, allowing for significant improvements in film morphology and resulting optoelectronic properties.[67] The successful integration of these MAPbI$_3$ thin films into solar cell configuration represents the first solar cells with dry-processed MHP absorber layer. Here, the deposition of MHP layers via PAD with only about 1 µm film thickness and at the same time sufficient quality of film morphology is key to success.[72] So far, only about 20 to 35 µm thick CsPbBr$_3$ films deposited via PAD have been reported to have a suitable quality of film morphology for application in optoelectronic devices.[90] However, such a high film thickness is suitable for photodetectors but not for solar cells.[72,90]

2.4 MHP Characteristics

2.4.1 Optical Properties

For MHPs, three different photoinduced absorption processes are observed, analogous to classical inorganic semiconductors such as GaAs: Band-to-band absorption, exciton absorption and tail state absorption.[21, 32, 91–94]

Band-to-band absorption is a process in which light of a suitable wavelength (energy equal to or higher than the bandgap energy, see Fig. 2.4a blue shaded area) induces optical transitions in the band scheme, i.e. electrons are excited from the VB into the CB, whereby one hole is generated in the VB for each electron. Here electron and hole can be considered separately from each other.[91]

In MHP materials, also correlated electron-hole pairs, so-called Wannier-Mott excitons, are photoinduced, i.e. such generated electrons and holes are weakly bound to each other by Coulomb interaction while spatially extending over a larger area (multiple unit cells).[91, 95] Wannier-Mott excitons can be described analogously to the hydrogen atom (weakly bound electron around positive charge), i.e., with a Rydberg series of energy levels.[91, 95–97] Below the bandgap, the series principally appears in specific exciton absorption peaks and above the bandgap in a continuum of exciton states superimposed with band-to-band absorption.[97, 98] However, for MHPs such as $MAPbI_3$, only one exciton peak can be observed below the bandgap (Fig. 2.4a red shaded area),[93, 98] owing to broadened linewidths caused by disorder.[93] This exciton peak below the bandgap is not yet visible at room temperature, but becomes more pronounced with decreasing temperatures and is clearly visible below 150 K (Fig. 2.4b).[21, 93]

Additional absorption below the bandgap energy takes place due to so-called Urbach tail absorption states resulting from static and dynamic disorder, which is reflected in an exponential band edge (details in Section 2.4.2).[32, 91, 93, 94]

After optical excitation, electron and hole can again recombine. Recombination under emission of a photon is described as photoluminescence (PL), where also three processes are possible: Band-to-band recombination, exciton recombination and defect-related recombination.[91, 99–101] In MHPs like $MAPbI_3$, exciton recombination and defect-related recombination get only relevant at lower temperatures, i.e. below $\approx$ 150 K.[100, 102]

Band-to-band recombination describes the recombination of electrons in the CB with holes in the VB.[39, 91, 99] The corresponding recombination probability is proportional to the concentration of free electrons and holes.[103] Due to charge carrier thermalization, mainly near band edge emission occurs.[39, 99]

In the case of radiative exciton recombination (relevant if thermal energy is smaller than exciton binding energy)[39] one distinguishes between free excitons, i.e. freely moving electron-hole pairs, and bound excitons, i.e. electron-hole pairs bound to defects or impurities.[91, 100] The PL of bound excitons is red-shifted compared to the PL of free excitons due to the energy required for binding.[100, 102]

Defect-related radiative recombination describes the recombination of charge carriers at defects and impurities, where the intensity contribution of this emission to the overall PL depends on the defect density and decreases with increasing fluence (excitation density) and above a certain temperature.[101, 102]
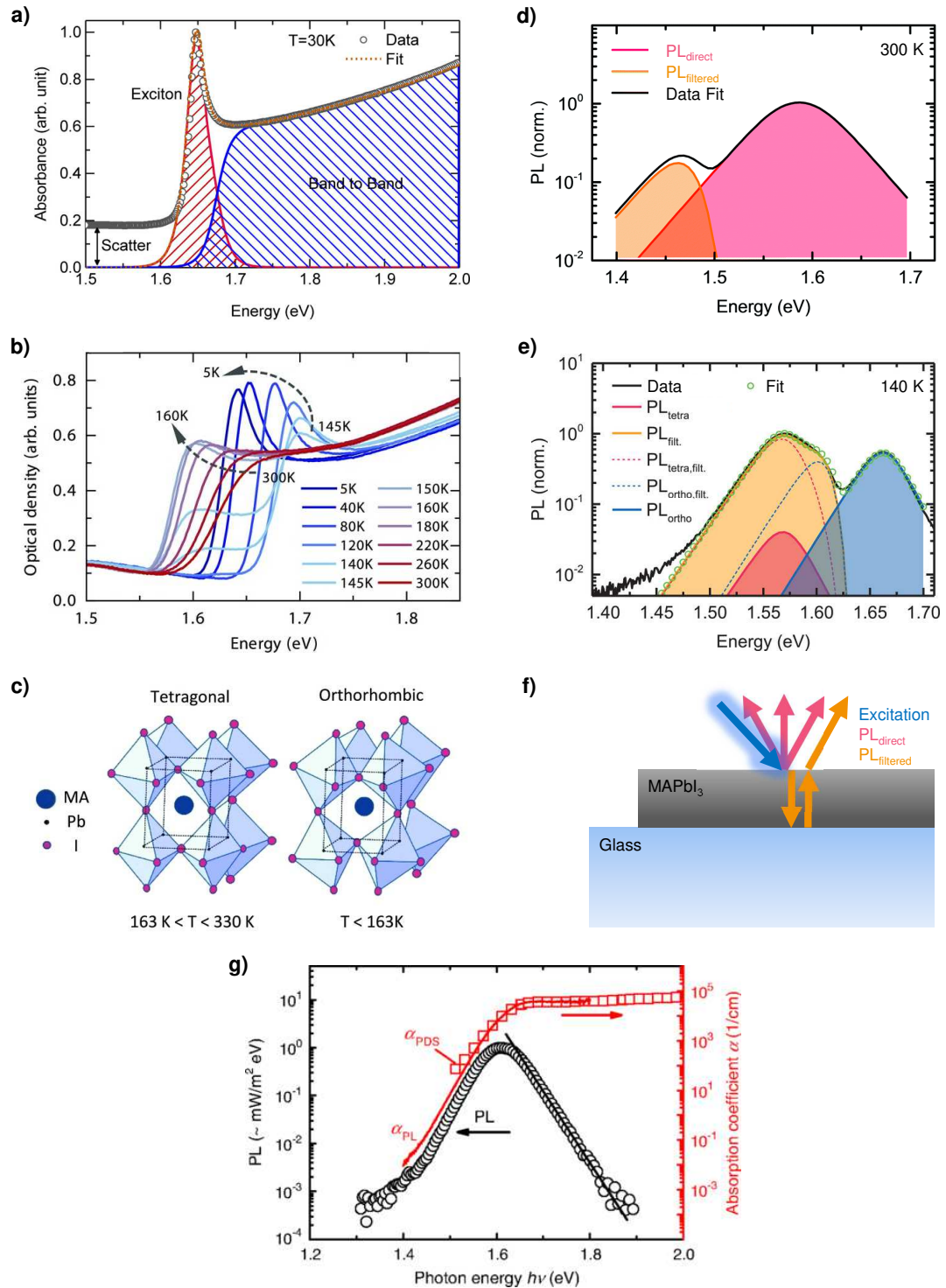
Figure 2.4: a) Absorption spectrum of a MAPbI$_3$ thin film measured at 30 K, which is composed of band-to-band and excitonic contributions. Reprinted with permission from Singh et al.[93] Copyright 2016 American Chemical Society. b) Absorption spectra of a MAPbI$_3$ thin film measured between 300 K and 5 K.

c) MAPbI$_3$ crystal structure in tetragonal and orthorhombic phase. b), c) Reprinted as adapted version with permission from Panzer et al.[21] Copyright 2017 WILEY-VCH Verlag GmbH & Co. KGaA, Weinheim. d) Modeled MAPbI$_3$ single crystal PL at 300 K with contributions of direct and filtered PL. Reprinted as adapted version with permission from Schötz et al.[101] Copyright 2020 The Royal Society of Chemistry. Permission conveyed through Copyright Clearance Center, Inc. e) Modeling of single crystal PL measured at 140 K with direct and filtered contributions of tetragonal and orthorhombic phase. Reprinted as adapted version with permission according to the CC BY 4.0 license from Schötz et al.[104] Copyright 2020 The Authors. Published by WILEY-VCH Verlag GmbH & Co. KGaA, Weinheim. f) Scetch of direct and filtered PL after photoexcitation of a MAPbI$_3$ thin film. Reprinted as adapted version with permission from Witt et al.[73] Copyright 2023 The Authors. Published by American Chemical Society. g) Measured PL (black symbols) and absorption (red symbols) together with calculated absorption from PL (red line) of a MAPbI$_{3-x}$Cl$_x$ thin film. Reprinted with permission from Staub et al.[103] (DOI: 10.1103/PhysRevApplied.6.044017). Copyright 2016 American Physical Society.

Besides radiative recombination, non-radiative recombination also occurs.[39,91] Recombination rates are accessible via time-resolved, i.e. transient PL measurements.[39] The as measured PL decay curves can be described with $\mathrm{PL}(t) \approx -k_2[n(t)]^2$, i.e. with the decay of the charge carrier density $\frac{\mathrm{d}n}{\mathrm{d}t} = -k_1 n - k_2 n^2 - k_3 n^3$ (rate equation).[39] Here k_1 describes non-radiative recombination at defects and non-radiative excitonic recombination and thus indicates the defect concentration and quality of the investigated sample. The rate k_2 describes radiative recombination of electrons and holes and is an intrinsic material constant. Also an intrinsic material constant is the rate k_3, which describes non-radiative Auger recombination (electron and hole recombine under energy transfer to third charge carrier) which becomes relevant only at higher excitation fluences.[39] At low excitation fluences, i.e. low charge carrier densities, the PL decay is mainly dominated by k_1, allowing the measured transient PL to be described approximately as monoexponential decay with $\mathrm{PL}(t) \approx -k_2 n_0^2 \exp\left(-2k_1 t\right)$.[39,103]

Temperature-dependent optical measurements (PL and absorption) from room temperature down to cryogenic temperatures of 5 K are a valuable tool to access MHPs structural properties, since e.g. the relevance of defect-related processes as well as the relevance of structural and dynamic contributions to the energetic disorder changes depending on the temperature. In addition, temperature-dependent optical measurements can be used to induce and observe structural dynamics in the form of crystallographic phase transitions, which enables conclusions to be drawn regarding e.g. strain.[21,105]
For example, cooling MAPbI$_3$ down from room temperature, a phase transition from the tetragonal phase (above ≈ 163 K up to ≈ 330 K) to the orthorhombic phase (below ≈ 163 K) occurs reflected in the shift of the absorption edge by ≈ 0.1 eV to higher energies (Fig. 2.4b,c).[21] In general, the band edge of MHPs such as MAPbI$_3$ shifts to lower energies with decreasing temperature (Fig. 2.4b), which is opposite to the behavior of classical inorganic semiconductors. The reason for this behavior is the high thermal expansion coefficient of MHPs such as MAPbI$_3$ in combination with a positive deformation

potential, so that the negative electron-phonon coupling contribution does not dominate the temperature behavior of the band edge as in classical inorganic semiconductors.[21, 93] In accordance with the bandgap-shift in absorption due to the phase transition from tetragonal to orthorhombic phase, two peaks (PL_{tetra} and PL_{ortho} in Fig. 2.4e) appear in corresponding PL spectra in the temperature range of the phase transition (between $\approx$160 and 120 K for $MAPbI_3$), which can be assigned to these two crystallographic phases.[104] In addition to these two peaks, which stem from direct PL, i.e. PL coming directly from (near) the sample surface, a second peak based on filtered PL occurs respectively ($PL_{tetra,filt.}$ and $PL_{ortho,filt.}$ in Fig. 2.4e). Filtered PL results from PL which is internally reflected in the sample and filtered by the sample intrinsic absorption (sketch for thin film sample in Fig. 2.4f). This effect is called self-absorption and results in red-shifted PL compared to direct PL (Fig. 2.4d for pure tetragonal phase at 300 K). In single crystal samples the filtered PL peak is more pronounced than in thin film samples (where it appears rather as a shoulder at the low energy edge of the direct PL), since in single crystals the light can travel longer path lengths due to larger sample thicknesses and less barriers in the form of grain boundaries and defects.[101] At low temperatures below $\approx$ 150 K, additional defect-related PL and PL due to exciton recombination become relevant as described above.[100, 102] These two PL contributions are also red-shifted to direct PL and are more pronounced in thin film samples than in single crystals due to the higher defect density in films.[73, 100, 102, 104] Both, the less pronounced filtered PL and the increased defect PL, pose challenges for description and evaluation of the entire PL shape of thin film samples analogous to single crystals (Fig. 2.4e green circles).

Interestingly, PL spectrum $PL(E)$ and absorption spectrum $\alpha(E)$ are linked via the so-called reciprocity theorem[103, 104]

$$PL(E) \propto \alpha(E) \cdot E^2 \cdot \exp\left(-\frac{E}{k_B T}\right). \tag{2.2}$$

According to this theorem, information contained in the absorption edge is also contained in the low energy edge of the PL, as shown in Fig. 2.4g.[103, 104]

2.4.2 Urbach Energy

The energetic disorder, a structural characteristic in semiconductor materials, is represented by the Urbach energy.[107–109] For crystalline semiconductors like MHPs, the Urbach energy is the sum of temperature-dependent dynamic disorder (i.e. electron-phonon interaction) and temperature-independent static disorder (i.e. defect-induced disorder and zero-point phonon energy).[32,94,110,111] The Urbach energy is a popular figure of merit for the performance potential of semiconductor materials and for the quality of processed semiconductor samples, as it is correlated to structural and optoelectronic properties,[31,108,109,112–117] e.g. to the minimum open-circuit-voltage (V_{OC}) deficit of solar cells (Fig. 2.5a).[31,107–109]
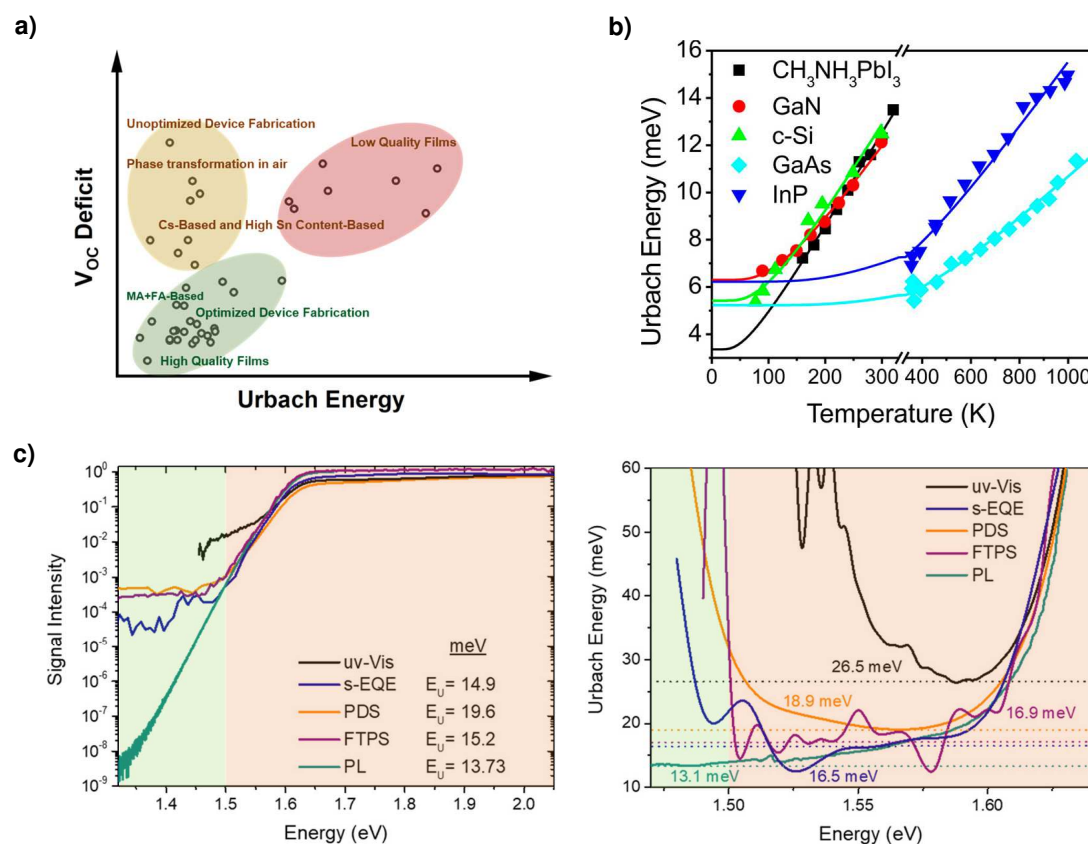
Figure 2.5: a) Relationship between Urbach energy, V_{OC} deficit and film quality illustrated for MHPs. Reprinted with permission from Subedi et al.[106] Copyright 2022 American Chemical Society. b) Temperature-dependent Urbach energy values and modelling down to 0 K according to Eq. 2.3 for classic inorganic semiconductors and MAPbI$_3$. Reprinted with permission from Ledinsky et al.[32] Copyright 2019 American Chemical Society. c) Evaluation of Urbach energies for MAPbI$_3$ thin films using different measurement methods: Evaluation of absorption tail (left) and evaluation from the horizontal part of the apparent Urbach energy calculated from absorption taking the derivative (right). Reprinted as adapted version with permission from Ugur et al.[31] Copyright 2022 American Chemical Society.

The Urbach energy can be derived from optical measurements such as PL and absorption measurements.[31,32,104,108] As already mentioned in Section 2.4.1, energetic disorder results in so-called Urbach tail states, which lead to Urbach tail absorption below the bandgap energy.[32,91,93,94] The Urbach tail absorption appears in a characteristic exponential absorption edge, whose steepness is inverse to the Urbach energy.[31,32,93,94,108,111] Thus, a steeper absorption edge reflects a lower Urbach energy and thus a higher electronic quality.[31,94] Since absorption and PL are linked by the reciprocity theorem (Eq. 2.2), the Urbach energy can also be extracted from the low energy edge of PL spectra.[32,103,104]

Temperature-dependent optical measurements from room temperature down to lower temperatures enable the determination of the Urbach energy as a function of decreasing temperature, i.e., with reducing fraction of dynamic disorder. By modeling the temperature-dependent Urbach energies down to 0 K according to

$$E_U(T) = E_U^{stat} + E_U^{dyn} = E_U^{stat} + 2 \cdot E_U^{stat} \left[\exp\left(\frac{\theta_E}{T} \right) - 1 \right]^{-1} \qquad (2.3)$$

the pure static disorder E_U^{stat} can be quantified (Einstein temperature θ_E represents charge carrier - phonon interaction).[32,94,104,110] Using such modeling, surprisingly low static disorder values below 4 meV have been determined for MHPs such as $MAPbI_3$, which are lower than corresponding values for classical inorganic semiconductors (Fig. 2.5b) and thus demonstrate the high potential of MHPs for efficient optoelectronic devices such as solar cells.[32,104] One reason for the remarkably low static disorder in MHPs could be the high defect tolerance compared to classical inorganic semiconductors, rendering defect-induced static disorder negligible, so that significant contribution to static disorder is only given by zero-point phonon energy.[110] However, a comprehensive understanding of the energetic disorder in MHPs is still missing. Even the reliable determination of Urbach energy values is still a challenge, because of the fact that different measurement and analysis methods yield different Urbach energy values (Fig. 2.5c).[31,32] The origin of these discrepancies is not yet understood. Only the assumption was raised that for the determination of the physically true value of the Urbach energy a sufficiently low evaluation energy range (at least 0.1 eV below the bandgap) must be considered,[31] but without showing solid evidence for this. Consequently, although the Urbach energy is a popular figure of merit, up to now it is not possible to meaningfully interpret the extracted Urbach energy values because of only poor understanding of Urbach analyses. This poor understanding motivates me in this work to investigate the origin of the discrepancies in Urbach energy values and to sensitize for reliable and profound interpretation and comparison of extracted Urbach energy values.

2.4.3 Role of Morphology on Structural and Optoelectronic Properties

Morphology of MHP samples includes properties such as density and compactness, surface roughness, grain size and crystallite size, as well as crystallographic orientation, which can be characterized using, e.g., a profilometer or LSM, SEM, XRD and GIWAXS measurements.

So far, studies concerning the influence of MHP film morphology on resulting structural and optoelectronic properties have mainly focused on grain size.[30, 118] The reason for this focus is the direct visualization of grain sizes in SEM images and rather simple methods to induce specific grain sizes during or after film formation. In solution-based MHP film processing methods, the grain size can be adjusted by changing the precursor concentration, by adding additives or by hot casting or annealing (i.e. by increased temperature).[30] Furthermore, hot-pressing also induces increased grain sizes with increasing temperature.[87, 119] An increased grain size and thus a lower fraction of grain boundaries has often been shown to lead to increased charge carrier lifetimes, i.e. lower defect densities and thus higher solar cell efficiencies (PCEs) (Fig. 2.6a).[30, 118] An et al. also observed a decrease in Urbach energy with increasing grain size and related this to a lower defect density.[118] Yet, as discussed in Section 2.4.2, a profound understanding of
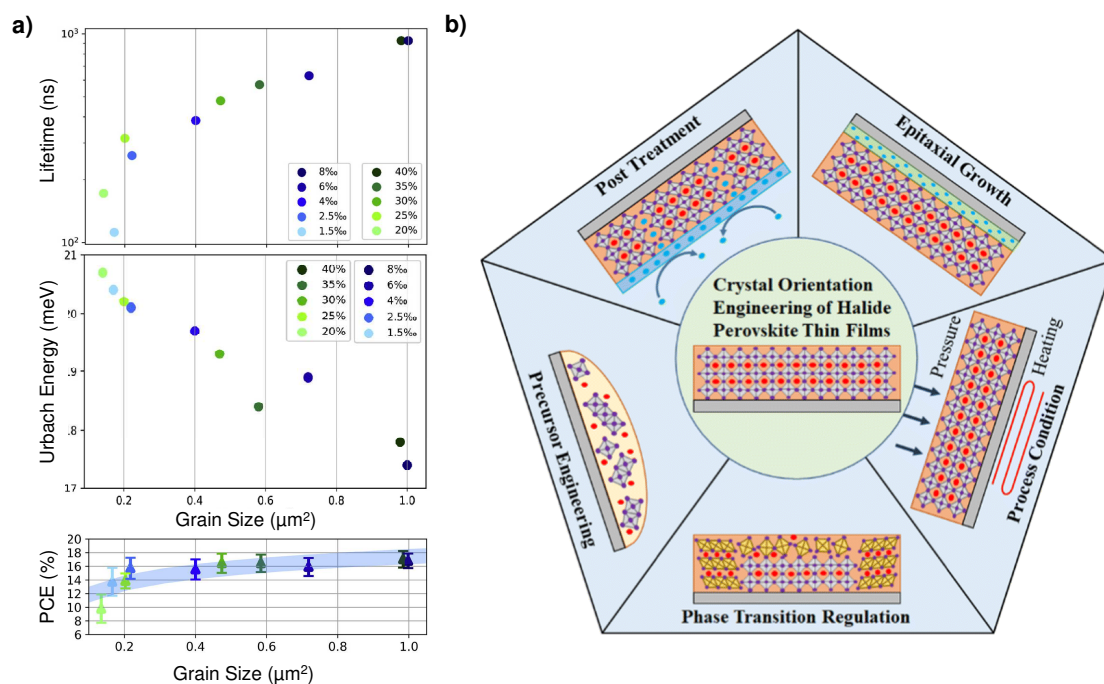

Figure 2.6: a) Charge carrier lifetime, Urbach Energy and power conversion efficiency (PCE) as function of grain size for MAPbI$_3$ thin films. Reprinted as adapted version from An et al.[118] with permission from Elsevier. Copyright 2021 Elsevier Inc. b) Concepts of crystallographic orientation engineering in MHP films. Reprinted with permission from Li et al.[120] Copyright 2023 The Royal Society of Chemistry. Permission conveyed through Copyright Clearance Center, Inc.

Urbach analyses is still missing, since even the origin of discrepancies in Urbach energy values determined by different measurement and analysis methods is still unsolved.[31,32] In addition, a comprehensive consideration of the influence of the overall film morphology on structural and optoelectronic properties is still missing. Recently, the importance of orientation, i.e. orientation of individual grains as well as crystallographic orientation (orientation of unit cells), for further improvement of device efficiencies has been recognized.[120,121] However, studies specifically addressing the role of orientation have only recently begun, so developing a solid understanding of orientation is still in its early stages.[118,120–123] For example, while different preferred crystallographic orientation is observed in MHP films, its influence is not yet comprehensively understood. One reason for this is, that, although orientation can be induced by methods such as precursor engineering or hot-pressing (Fig. 2.6b), it is much more difficult to control and to quantify than grain size.[120]

In this work, film morphology, i.e. grain size and preferred crystallographic orientation, is specifically induced by (hot-)pressing. Using this approach, comprehensive analyses are performed regarding the influence of film morphology on structural properties (phase transition, strain, energetic disorder and defects) and resulting optoelectronic functionality. For these analyses, temperature-dependent optical measurements and solar cell characterizations are performed with the (hot-)pressed MHP films. Special attention is devoted to how only small differences in film morphology affect structural and optoelectronic properties in order to evaluate the significance of individual film properties for device functionality and optimization.

2.5 MHP Optoelectronic Device Applications

In Section 2.2, the beneficial optoelectronic properties of MHPs, that make them attractive for integration in optoelectronic devices, were presented. In this work, MHP thick film pellets are investigated, which are of interest for photodetectors (especially X-ray detectors due to high absorption coefficient based on high atomic number elements).[59,124] In addition, MHP thin films are investigated and integrated in solar cell configuration.

2.5.1 X-ray Detectors and Solar Cells

Both, solar cells and photodetectors, are light harvesting devices, whose most common device architecture is the so-called planar heterojunction, i.e. a vertical structure (Fig. 2.7a).[13,16] Here, the perovskite active layer is sandwiched between an electron transport layer (ETL) and a hole transport layer (HTL), which direct generated free charge carriers to the electrodes.[16] Free charge carriers are generated in the perovskite active layer through incident light (i.e. incident photons). Generated electrons are discharged via the ETL to the cathode and holes are discharged via the HTL to the anode (Fig. 2.7b), resulting in a current that is dependent on the number of induced free charge carriers and the charge carrier losses on the way to the electrodes.[13,125]
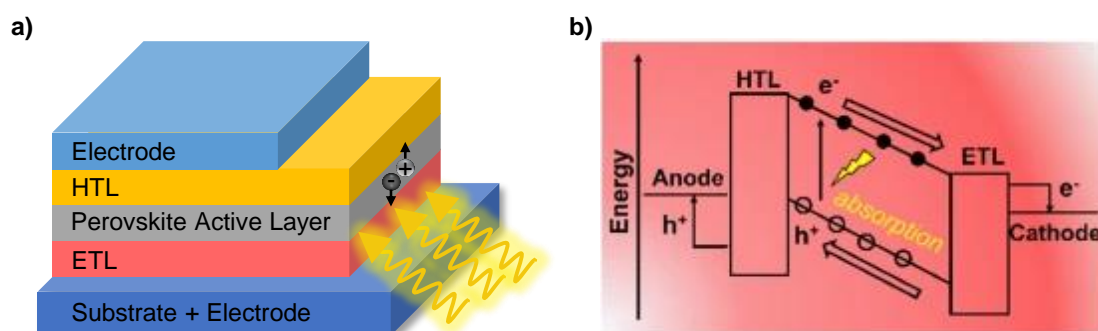

Figure 2.7: Perovskite solar cell and photodetector devices: a) Common device architecture. b) Illustration of photophysical processes in the device in an energy level diagram. Reprinted as adapted version with permission according to the CC BY 4.0 license from Dong et al.[13] Copyright The Author(s) 2023.

2.5.2 Upscaling and Commercialization

Both, solar cells and X-ray detectors, achieve efficiencies or sensitivities on laboratory scale that are on par with established technologies based on classical inorganic semiconductors.[3,5,9,19,20] For X-ray detectors, the present hurdles to commercialization are current instabilities and high dark currents due to ion migration, which is dominant at grain boundaries in polycrystalline films. Therefore, passivation approaches are applied to limit ion migration.[62,126] Furthermore, upscaling of MHP thick film pellets to at least 10 x 10 cm^2 (better to 30 x 40 cm^2) remains a challenge.[18] However, upscaling approaches such as blade-coating and pressing are already being investigated,[18] and the assembly of

individual MHP pellets to form a larger area is also being tested.[69] The integration of MAPbI$_3$ pellets on pixelated backplanes for MHP based flat-panel X-ray detector arrays has already been demonstrated successfully.[17,18]

For solar cells, current hurdles to commercialization are mainly instabilities, i.e., instabilities of perovskite active phases (in e.g. FAPbI$_3$) and degradation of perovskite by light, humidity, and oxygen.[23,45] In order to impove stability, passivation approaches and the incorporation of additives are investigated.[23] Solution-based upscaling approaches are available, such as blade coating, spray coating or slot-die coating, which allow continuous roll-to-roll processing.[127] However, since film formation in upscaling methods such as slot-die coating is different from that in e.g. lab-scale spincoating,[128] there is still research potential for understanding and optimizing solution-based large-scale processing methods, especially since process control in general still needs to be improved. Solar modules are fabricated by dividing the active layer into connected subcells to minimize resistive losses,[129] where commercial-sized solar cells have an area of around 16 x 16 cm^2.[7] Despite the remaining hurdles, the beneficial optoelectronic properties of MHPs, their cost-effective processing and the possibility for new applications (e.g. tandem or flexible devices)[3,10,11,13,38,47] are attractive and responsible for tandem cells (silicon-MHP active layer) being already close to commercialization. In addition, more and more startups and companies are working on MHP based solar cells.[7,130–132]

Lead (Pb), contained in MHP films like FAPbI$_3$ or MAPbI$_3$ in efficient solar cells, has been discussed critically with regard to commercialization due to its toxicity.[38,44,45,127] While lead-free stoichiometries are also being investigated, so far they seem promising only for X-ray detector applications but cannot compete with high-efficiency lead-based solar cells yet.[62,133–135] However, the lead issue is already being dealt with in established silicon-based solar cells, where it is present in the solder for solar modules. Special safety protocolls exist for established solar cell technologies throughout the entire product chain from processing until the end of life.[45] The lead content in MHP-based solar cells is considered relatively low, so that successful safety measures should be feasible.[127] In addition to the toxicity of lead, toxic solvents are also used in solution-based MHP processing,[127] where, e.g. the use of DMF is restricted by the european union.[136] Thus, avoiding such toxic solvents seems inevitable on the way to commercialization. For this reason, research is now being done on so-called alternative green solvents, i.e. less toxic solvents for MHP processing.[127,137]

In this work, thick and thin film MHP processing methods are used that are completely dry, i.e., without any use of solvents, avoiding the issue of solvent toxicity. Furthermore, these dry MHP processing methods are potentially upscalable and enable improved process control by separating material synthesis and film formation. Hence, these dry MHP processing methods are also valuable tool to get away from often used try and error optimization attempts and instead gain a comprehensive understanding of the relationship between morphological, structural and optoelectronic film properties, which is currently still missing. Thus, understanding this structure-properties relationship is the aim of this work to identify and overcome current issues regarding MHP material quality and optimize functionality of MHP-based devices.

2.6 References

[1] Federal Ministry for Economic Cooperation and Development. Energy and climate. `https://www.bmz.de/en/issues/climate-change-and-development/energy-and-climate`. Last modified 22.09.2020, Accessed 01.08.2023.

[2] IRENA International Renewable Energy Agency. Global Renewables Outlook: Energy transformation 2050. `https://www.irena.org/publications/2020/Apr/Global-Renewables-Outlook-2020`. Last modified 04.2020, Accessed 01.08.2023.

[3] Office of Energy Efficiency and Renewable Energy. Solar Photovoltaic Cell Basics. `https://www.energy.gov/eere/solar/solar-photovoltaic-cell-basics`. Accessed 01.08.2023.

[4] Fraunhofer ISE. Silicon Photovoltaics. `https://www.ise.fraunhofer.de/en/business-areas/photovoltaics/silicon-photovoltaics.html`. Accessed 01.08.2023.

[5] NREL Transforming ENERGY. Best Research-Cell Efficiency Chart. `https://www.nrel.gov/pv/cell-efficiency.html`. Last modified 10.07.2023, Accessed 01.08.2023.

[6] NREL Transforming ENERGY. Champion Photovoltaic Module Efficiency Chart. `https://www.nrel.gov/pv/module-efficiency.html`. Last modified 06.07.2023, Accessed 01.08.2023.

[7] Oxford Photovoltaics. Oxford PV sets new solar cell world record. `https://www.oxfordpv.com/news/oxford-pv-sets-new-solar-cell-world-record`. Last modified 24.05.2023, Accessed 01.08.2023.

[8] Fraunhofer ISE. Perovskite Silicon Tandem Photovoltaics. `https://www.ise.fraunhofer.de/en/business-areas/photovoltaics/perovskite-and-organic-photovoltaics/perovskite-silicon-tandem-photovoltaics.html`. Accessed 01.08.2023.

[9] Akihiro Kojima, Kenjiro Teshima, Yasuo Shirai, and Tsutomu Miyasaka. Organometal Halide Perovskites as Visible-Light Sensitizers for Photovoltaic Cells. *Journal of the American Chemical Society*, 131(17):6050–6051, 2009.

[10] Ajay Kumar Jena, Ashish Kulkarni, and Tsutomu Miyasaka. Halide Perovskite Photovoltaics: Background, Status, and Future Prospects. *Chemical Reviews*, 119(5):3036–3103, 2019.

[11] Hao Chen, Hao Wang, Jiang Wu, Feng Wang, Ting Zhang, Yafei Wang, Detao Liu, Shibin Li, Richard V. Penty, and Ian H. White. Flexible optoelectronic devices based on metal halide perovskites. *Nano Research*, 13(8):1997–2018, 2020.

[12] Kevin Fischer NETZMEDIEN AG. netzwoche: Das bringt die Zukunft des IoT - Interview mit Angela Nicoara. `https://www.netzwoche.ch/news/`

2022-10-04/das-bringt-die-zukunft-des-iot. Last modified 04.10.2022, Accessed 10.08.2023.

[13] He Dong, Chenxin Ran, Weiyin Gao, Mingjie Li, Yingdong Xia, and Wei Huang. Metal Halide Perovskite for next-generation optoelectronics: progresses and prospects. *eLight*, 3(1):3, 2023.

[14] Lata Chouhan, Sushant Ghimire, Challapalli Subrahmanyam, Tsutomu Miyasaka, and Vasudevanpillai Biju. Synthesis, optoelectronic properties and applications of halide perovskites. *Chemical Society Reviews*, 49(10):2869–2885, 2020.

[15] Samuel D. Stranks and Henry J. Snaith. Metal-halide perovskites for photovoltaic and light-emitting devices. *Nature Nanotechnology*, 10(5):391–402, 2015.

[16] Yuhui Dong, Yousheng Zou, Jizhong Song, Xiufeng Song, and Haibo Zeng. Recent progress of metal halide perovskite photodetectors. *Journal of Materials Chemistry C*, 5(44):11369–11394, 2017.

[17] Sarah Deumel, Albert van Breemen, Gerwin Gelinck, Bart Peeters, Joris Maas, Roy Verbeek, Santhosh Shanmugam, Hylke Akkerman, Eric Meulenkamp, Judith E. Huerdler, Manognya Acharya, Marisé García-Batlle, Osbel Almora, Antonio Guerrero, Germà Garcia-Belmonte, Wolfgang Heiss, Oliver Schmidt, and Sandro F. Tedde. High-sensitivity high-resolution X-ray imaging with soft-sintered metal halide perovskites. *Nature Electronics*, 4(9):681–688, 2021.

[18] Yuki Haruta, Mioko Kawakami, Yuui Nakano, Soumya Kundu, Shinji Wada, Takumi Ikenoue, Masao Miyake, Tetsuji Hirato, and Makhsud I. Saidaminov. Scalable Fabrication of Metal Halide Perovskites for Direct X-ray Flat-Panel Detectors: A Perspective. *Chemistry of Materials*, 34(12):5323–5333, 2022.

[19] Mykhailo Sytnyk, Sarah Deumel, Sandro Francesco Tedde, Gebhard J. Matt, and Wolfgang Heiss. A perspective on the bright future of metal halide perovskites for X-ray detection. *Applied Physics Letters*, 115(19):190501, 2019.

[20] Haotong Wei and Jinsong Huang. Halide lead perovskites for ionizing radiation detection. *Nature Communications*, 10(1):1066, 2019.

[21] Fabian Panzer, Cheng Li, Tobias Meier, Anna Köhler, and Sven Huettner. Impact of Structural Dynamics on the Optical Properties of Methylammonium Lead Iodide Perovskites. *Advanced Energy Materials*, 7(16):1700286, 2017.

[22] Naveen Kumar Tailor, Mojtaba Abdi-Jalebi, Vinay Gupta, Hanlin Hu, M. Ibrahim Dar, Gang Li, and Soumitra Satapathi. Recent progress in morphology optimization in perovskite solar cell. *Journal of Materials Chemistry A*, 8(41):21356–21386, 2020.

[23] Abd. Rashid bin Mohd Yusoff, Maria Vasilopoulou, Dimitra G. Georgiadou, Leonidas C. Palilis, Antonio Abate, and Mohammad Khaja Nazeeruddin. Passivation and process engineering approaches of halide perovskite films for high efficiency and stability perovskite solar cells. *Energy & Environmental Science*, 14(5):2906–2953, 2021.

[24] Jinxin Li, Basudev Pradhan, Surya Gaur, and Jayan Thomas. Predictions and Strategies Learned from Machine Learning to Develop High-Performing Perovskite Solar Cells. *Advanced Energy Materials*, 9(46):1901891, 2019.

[25] Hongfei Chen, Hejin Yan, and Yongqing Cai. Recipe for the design of mixed cation lead halide perovskites: adsorption and charge transfer from A-site cations to PbI_2. *Journal of Materials Chemistry A*, 11:19349–19359, 2023.

[26] Shahram Moradi, Soumya Kundu, Milad Rezazadeh, Vishal Yeddu, Oleksandr Voznyy, and Makhsud I. Saidaminov. High-throughput exploration of halide perovskite compositionally-graded films and degradation mechanisms. *Communications Materials*, 3(1):13, 2022.

[27] Meghna Srivastava, Abigail R. Hering, Yu An, Juan-Pablo Correa-Baena, and Marina S. Leite. Machine Learning Enables Prediction of Halide Perovskites' Optical Behavior with >90% Accuracy. *ACS Energy Letters*, 8(4):1716–1722, 2023.

[28] Shijing Sun, Armi Tiihonen, Felipe Oviedo, Zhe Liu, Janak Thapa, Yicheng Zhao, Noor Titan P. Hartono, Anuj Goyal, Thomas Heumueller, Clio Batali, Alex Encinas, Jason J. Yoo, Ruipeng Li, Zekun Ren, I. Marius Peters, Christoph J. Brabec, Moungi G. Bawendi, Vladan Stevanovic, John Fisher, and Tonio Buonassisi. A data fusion approach to optimize compositional stability of halide perovskites. *Matter*, 4(4):1305–1322, 2021.

[29] Jin-Wook Lee, Seongrok Seo, Pronoy Nandi, Hyun Suk Jung, Nam-Gyu Park, and Hyunjung Shin. Dynamic structural property of organic-inorganic metal halide perovskite. *iScience*, 24(1):101959, 2021.

[30] Kun Chen, Stefan Schünemann, Seulki Song, and Harun Tüysüz. Structural effects on optoelectronic properties of halide perovskites. *Chemical Society Reviews*, 47(18):7045–7077, 2018.

[31] Esma Ugur, Martin Ledinský, Thomas G. Allen, Jakub Holovský, Aleš Vlk, and Stefaan De Wolf. Life on the Urbach Edge. *The Journal of Physical Chemistry Letters*, 13(33):7702–7711, 2022.

[32] Martin Ledinsky, Tereza Schönfeldová, Jakub Holovský, Erkan Aydin, Zdeňka Hájková, Lucie Landová, Neda Neyková, Antonín Fejfar, and Stefaan De Wolf. Temperature Dependence of the Urbach Energy in Lead Iodide Perovskites. *The Journal of Physical Chemistry Letters*, 10(6):1368–1373, 2019.

[33] S.-R. Bae, D.Y. Heo, and S.Y. Kim. Recent progress of perovskite devices fabricated using thermal evaporation method: Perspective and outlook. *Materials Today Advances*, 14:100232, 2022.

[34] Konstantin Schötz and Fabian Panzer. Using In Situ Optical Spectroscopy to Elucidate Film Formation of Metal Halide Perovskites. *The Journal of Physical Chemistry A*, 125(11):2209–2225, 2021.

[35] Finn Babbe and Carolin M. Sutter-Fella. Optical Absorption-Based In Situ Characterization of Halide Perovskites. *Advanced Energy Materials*, 10(26):1903587, 2020.

[36] Vladimir Held, Nada Mrkyvkova, Peter Nádaždy, Karol Vegso, Aleš Vlk, Martin Ledinský, Matej Jergel, Andrei Chumakov, Stephan V. Roth, Frank Schreiber, and Peter Siffalovic. Evolution of Structure and Optoelectronic Properties During Halide Perovskite Vapor Deposition. *The Journal of Physical Chemistry Letters*, 13(51):11905–11912, 2022.

[37] Eugene A. Katz. Perovskite: Name Puzzle and German-Russian Odyssey of Discovery. *Helvetica Chimica Acta*, 103(6):e2000061, 2020.

[38] Ahmed Waseem Faridi, Muhammad Imran, Ghulam Hasnain Tariq, Sana Ullah, Syed Farhan Noor, Sabah Ansar, and Farooq Sher. Synthesis and Characterization of High-Efficiency Halide Perovskite Nanomaterials for Light-Absorbing Applications. *Industrial & Engineering Chemistry Research*, 62(11):4494–4502, 2023.

[39] Laura M. Herz. Charge-Carrier Dynamics in Organic-Inorganic Metal Halide Perovskites. *Annual Review of Physical Chemistry*, 67(1):65–89, 2016.

[40] Tianzhao Dai, Qiaojun Cao, Lifeng Yang, Mahmoud H. Aldamasy, Meng Li, Qifeng Liang, Hongliang Lu, Yiming Dong, and Yingguo Yang. Strategies for High-Performance Large-Area Perovskite Solar Cells toward Commercialization. *Crystals*, 11(3), 2021.

[41] Nan Zhang, Quanxin Na, Qijie Xie, and Siqi Jia. Development of Solution-Processed Perovskite Semiconductors Lasers. *Crystals*, 12(9), 2022.

[42] Riley E. Brandt, Jeremy R. Poindexter, Prashun Gorai, Rachel C. Kurchin, Robert L. Z. Hoye, Lea Nienhaus, Mark W. B. Wilson, J. Alexander Polizzotti, Raimundas Sereika, Raimundas Žaltauskas, Lana C. Lee, Judith L. MacManus-Driscoll, Moungi Bawendi, Vladan Stevanović, and Tonio Buonassisi. Searching for "Defect-Tolerant" Photovoltaic Materials: Combined Theoretical and Experimental Screening. *Chemistry of Materials*, 29(11):4667–4674, 2017.

[43] Jin-Wook Lee, Sang-Hoon Bae, Nicholas De Marco, Yao-Tsung Hsieh, Zhenghong Dai, and Yang Yang. The role of grain boundaries in perovskite solar cells. *Materials Today Energy*, 7:149–160, 2018.

[44] Luis K. Ono, Emilio J. Juarez-Perez, and Yabing Qi. Progress on Perovskite Materials and Solar Cells with Mixed Cations and Halide Anions. *ACS Applied Materials & Interfaces*, 9(36):30197–30246, 2017.

[45] Timothy D. Siegler, Andrew Dawson, Peter Lobaccaro, David Ung, Markus E. Beck, Garrett Nilsen, and Leonard L. Tinker. The Path to Perovskite Commercialization: A Perspective from the United States Solar Energy Technologies Office. *ACS Energy Letters*, 7(5):1728–1734, 2022.

[46] Siqi Sun, Min Lu, Xupeng Gao, Zhifeng Shi, Xue Bai, William W. Yu, and Yu Zhang. 0D Perovskites: Unique Properties, Synthesis, and Their Applications. *Advanced Science*, 8(24):2102689, 2021.

[47] Guan-Woo Kim and Annamaria Petrozza. Defect Tolerance and Intolerance in Metal-Halide Perovskites. *Advanced Energy Materials*, 10(37):2001959, 2020.

[48] David A. Egger, Achintya Bera, David Cahen, Gary Hodes, Thomas Kirchartz, Leeor Kronik, Robert Lovrincic, Andrew M. Rappe, David R. Reichman, and Omer Yaffe. What Remains Unexplained about the Properties of Halide Perovskites? *Advanced Materials*, 30(20):1800691, 2018.

[49] Zhendong Guo, Jing Wang, and Wan-Jian Yin. Atomistic origin of lattice softness and its impact on structural and carrier dynamics in three dimensional perovskites. *Energy & Environmental Science*, 15:660–671, 2022.

[50] Nico Leupold, Anna Lena Seibel, Ralf Moos, and Fabian Panzer. Electrical Conductivity of Halide Perovskites Follows Expectations from Classical Defect Chemistry. *European Journal of Inorganic Chemistry*, 2021(28):2882–2889, 2021.

[51] Peng Gao, Michael Grätzel, and Mohammad K. Nazeeruddin. Organohalide lead perovskites for photovoltaic applications. *Energy & Environmental Science*, 7:2448–2463, 2014.

[52] Farhad Fouladi Targhi, Yousef Seyed Jalili, and Faramarz Kanjouri. $MAPbI_3$ and $FAPbI_3$ perovskites as solar cells: Case study on structural, electrical and optical properties. *Results in Physics*, 10:616–627, 2018.

[53] Bruno Ehrler, Esther Alarcón-Lladó, Stefan W. Tabernig, Tom Veeken, Erik C. Garnett, and Albert Polman. Photovoltaics Reaching for the Shockley–Queisser Limit. *ACS Energy Letters*, 5(9):3029–3033, 2020.

[54] Anna Amat, Edoardo Mosconi, Enrico Ronca, Claudio Quarti, Paolo Umari, Md. K. Nazeeruddin, Michael Grätzel, and Filippo De Angelis. Cation-Induced Band-Gap Tuning in Organohalide Perovskites: Interplay of Spin–Orbit Coupling and Octahedra Tilting. *Nano Letters*, 14(6):3608–3616, 2014.

[55] Shreetu Shrestha, René Fischer, Gebhard Matt, Patrick Feldner, Thilo Michel, Andres Osvet, Ievgen Levchuk, Benoit Merle, Saeedeh Golkar, Haiwei Chen, Sandro Tedde, Oliver Schmidt, Rainer Hock, Manfred Rührig, Mathias Göken, Wolfgang Heiss, Gisela Anton, and Christoph Brabec. High-performance direct conversion X-ray detectors based on sintered hybrid lead triiodide perovskite wafers. *Nature Photonics*, 11:436–441, 06 2017.

[56] Wiley A. Dunlap-Shohl, Yuanyuan Zhou, Nitin P. Padture, and David B. Mitzi. Synthetic Approaches for Halide Perovskite Thin Films. *Chemical Reviews*, 119(5):3193–3295, 2019.

[57] Helge Eggers, Fabian Schackmar, Tobias Abzieher, Qing Sun, Uli Lemmer, Yana Vaynzof, Bryce S. Richards, Gerardo Hernandez-Sosa, and Ulrich W. Paetzold. Inkjet-Printed Micrometer-Thick Perovskite Solar Cells with Large Columnar Grains. *Advanced Energy Materials*, 10(6):1903184, 2020.

[58] Yong Kim, Kwang Kim, dae yong Son, Dong-Nyuk Jeong, Ja-Young Seo, Yeong Choi, In Han, Sang Lee, and Nam-Gyu Park. Printable organometallic perovskite enables large-area, low-dose X-ray imaging. *Nature*, 550:87–91, 10 2017.

[59] Yuki Haruta, Takumi Ikenoue, Masao Miyake, and Tetsuji Hirato. Fabrication of CsPbBr$_3$ Thick Films by Using a Mist Deposition Method for Highly Sensitive X-ray Detection. *MRS Advances*, 5:1–7, 01 2020.

[60] Laura Basiricò, Andrea Ciavatti, and Beatrice Fraboni. Solution-Grown Organic and Perovskite X-Ray Detectors: A New Paradigm for the Direct Detection of Ionizing Radiation. *Advanced Materials Technologies*, 6(1):2000475, 2021.

[61] Weicheng Pan, Bo Yang, Guangda Niu, Kan-Hao Xue, Xinyuan Du, Lixiao Yin, Muyi Zhang, Haodi Wu, Xiang-Shui Miao, and Jiang Tang. Hot-Pressed CsPbBr$_3$ Quasi-Monocrystalline Film for Sensitive Direct X-ray Detection. *Advanced Materials*, 31(44):1904405, 2019.

[62] Nico Leupold and Fabian Panzer. Recent Advances and Perspectives on Powder-Based Halide Perovskite Film Processing. *Advanced Functional Materials*, 31(14):2007350, 2021.

[63] Lei Gao and Qingfeng Yan. Recent Advances in Lead Halide Perovskites for Radiation Detectors. *Solar RRL*, 4(2):1900210, 2020.

[64] Erin G. Moloney, Vishal Yeddu, and Makhsud I. Saidaminov. Strain Engineering in Halide Perovskites. *ACS Materials Letters*, 2(11):1495–1508, 2020.

[65] Zhaoning Song, Suneth C. Watthage, Adam B. Phillips, and Michael J. Heben. Pathways toward high-performance perovskite solar cells: review of recent advances in organo-metal halide perovskites for photovoltaic applications. *Journal of Photonics for Energy*, 6(2):022001, 2016.

[66] Zhibin Yang, Chu-Chen Chueh, Fan Zuo, Jong H. Kim, Po-Wei Liang, and Alex K.-Y. Jen. High-Performance Fully Printable Perovskite Solar Cells via Blade-Coating Technique under the Ambient Condition. *Advanced Energy Materials*, 5(13):1500328, 2015.

[67] Christina Witt, Andreas Schmid, Nico Leupold, Maximilian Schultz, Julian Höcker, Andreas Baumann, Ralf Moos, and Fabian Panzer. Impact of Pressure and Temperature on the Compaction Dynamics and Layer Properties of Powder-Pressed Methylammonium Lead Halide Thick Films. *ACS Applied Electronic Materials*, 2(8):2619–2628, 2020.

[68] Nico Leupold, Konstantin Schötz, Stefania Cacovich, Irene Bauer, Maximilian Schultz, Monika Daubinger, Leah Kaiser, Amelle Rebai, Jean Rousset, Anna Köhler, Philip Schulz, Ralf Moos, and Fabian Panzer. High Versatility and Stability

of Mechanochemically Synthesized Halide Perovskite Powders for Optoelectronic Devices. *ACS Applied Materials & Interfaces*, 11(33):30259–30268, 2019.

[69] Sarah Deumel, Yvonne Reg, Judith E. Huerdler, Lukas Hussenether, Oliver Schmidt, Anastasia Barabash, Wolfgang Heiss, and Sandro F. Tedde. Laser Cutting of Metal-Halide-Perovskite Wafers for X-Ray Detector Integration. *Advanced Materials Interfaces*, 9(16):2200642, 2022.

[70] Tatiana Soto-Montero, Wiria Soltanpoor, and Monica Morales-Masis. Pressing challenges of halide perovskite thin film growth. *APL Materials*, 8(11):110903, 11 2020.

[71] Bahram Abdollahi Nejand, Saba Gharibzadeh, Vahid Ahmadi, and H. Reza Shahverdi. Novel Solvent-free Perovskite Deposition in Fabrication of Normal and Inverted Architectures of Perovskite Solar Cells. *Scientific Reports*, 6(33649):1–14, 2016.

[72] Simon Biberger, Nico Leupold, Christina Witt, Christopher Greve, Paul Markus, Philipp Ramming, Daniel Lukas, Konstantin Schötz, Frank-Julian Kahle, Chenhui Zhu, Georg Papastavrou, Anna Köhler, Eva M. Herzig, Ralf Moos, and Fabian Panzer. First of Their Kind: Solar Cells with a Dry-Processed Perovskite Absorber Layer via Powder Aerosol Deposition and Hot-Pressing. *Solar RRL*, 7:2300261.

[73] Christina Witt, Konstantin Schötz, Meike Kuhn, Nico Leupold, Simon Biberger, Philipp Ramming, Frank-Julian Kahle, Anna Köhler, Ralf Moos, Eva M. Herzig, and Fabian Panzer. Orientation and Grain Size in MAPbI$_3$ Thin Films: Influence on Phase Transition, Disorder, and Defects. *The Journal of Physical Chemistry C*, 127(22):10563–10573, 2023.

[74] Nico Leupold, Philipp Ramming, Irene Bauer, Christina Witt, Jennifer Jungklaus, Ralf Moos, Helen Grüninger, and Fabian Panzer. How Methylammonium Iodide Reactant Size Affects Morphology and Defect Properties of Mechanochemically Synthesized MAPbI$_3$ Powder. *European Journal of Inorganic Chemistry*, 26(8):e202200736, 2023.

[75] Christina Witt, Nico Leupold, Philipp Ramming, Konstantin Schötz, Ralf Moos, and Fabian Panzer. How the Microstructure of MAPbI$_3$ Powder Impacts Pressure-Induced Compaction and Optoelectronic Thick-Film Properties. *The Journal of Physical Chemistry C*, 126(36):15424–15435, 2022.

[76] Priyabrata Sadhukhan, Dibyendu Ghosh, Payal Sengupta, Sayan Bhattacharyya, and Sachindranath Das. Unraveling the Charge Transport Mechanism in Mechanochemically Processed Hybrid Perovskite Solar Cell. *Langmuir*, 37(18):5513–5521, 2021.

[77] Zonghan Hong, Davin Tan, Rohit Abraham John, Yong Kang Eugene Tay, Yan King Terence Ho, Xin Zhao, Tze Chien Sum, Nripan Mathews, Felipe García, and Han Sen Soo. Completely Solvent-free Protocols to Access Phase-Pure, Metastable Metal Halide Perovskites and Functional Photodetectors from the Precursor Salts. *iScience*, 16:312–325, 2019.

[78] Francisco Palazon, Yousra El Ajjouri, and Henk J. Bolink. Making by Grinding: Mechanochemistry Boosts the Development of Halide Perovskites and Other Multinary Metal Halides. *Advanced Energy Materials*, 10(13):1902499, 2020.

[79] Khachatur Manukyan, Armenuhi Yeghishyan, Dmitry Moskovskikh, James Kapaldo, Alexander Mintairov, and A. Mukasyan. Mechanochemical synthesis of methylammonium lead iodide perovskite. *Journal of Materials Science*, 51:9123–9130, 10 2016.

[80] Francisco Palazon, Yousra El Ajjouri, Paz Sebastia-Luna, Simone Lauciello, Liberato Manna, and Henk J. Bolink. Mechanochemical synthesis of inorganic halide perovskites: evolution of phase-purity, morphology, and photoluminescence. *Journal of Materials Chemistry C*, 7:11406–11410, 2019.

[81] Bo Yang, Weicheng Pan, Haodi Wu, Guangda Niu, Yuan Junhui, Kan-Hao Xue, Lixiao Yin, Xinyuan Du, X. S. Miao, Xiaoquan Yang, Qingguo Xie, and Jiang Tang. Heteroepitaxial passivation of $Cs_2AgBiBr_6$ wafers with suppressed ionic migration for X-ray imaging. *Nature Communications*, 10(1989):1–10, 2019.

[82] Toshinori Matsushima, Takashi Fujihara, Chuanjiang Qin, Shinobu Terakawa, Yu Esaki, Sunbin Hwang, Atula S. D. Sandanayaka, William J. Potscavage, and Chihaya Adachi. Morphological control of organic-inorganic perovskite layers by hot isostatic pressing for efficient planar solar cells. *Journal of Materials Chemistry A*, 3(34):17780–17787, 2015.

[83] Mingxin Hu, Shanshan Jia, Yucheng Liu, Jian Cui, Yunxia Zhang, Han Su, Shuqing Cao, Lihong Mo, Depeng Chu, Guangtao Zhao, Kui Zhao, Zhou Yang, and Shengzhong Frank Liu. Large and Dense Organic–Inorganic Hybrid Perovskite $CH_3NH_3PbI_3$ Wafer Fabricated by One-Step Reactive Direct Wafer Production with High X-ray Sensitivity. *ACS Applied Materials & Interfaces*, 12(14):16592–16600, 2020.

[84] Christina Witt. *Untersuchung der pulverbasierten Herstellung von Dickschichten sowie Dünnschichten aus dem Halogenperowskit MAPbI3 mittels Druck- und Temperaturbehandlung.* Masterarbeit Fakultät für Mathematik, Physik und Informatik Lehrstuhl für Optoelektronik weicher Materie, Universität Bayreuth, 2020.

[85] Shunyong Wei, Shujie Tie, Kai Shen, Hui Sun, Xiaojia Zheng, Hao Wang, Wenqing Liang, Jihua Zou, Yixuan Huang, Lingzhi Luo, Xiangyu Zhou, Tixian Zeng, Aobo Ren, Dewei Zhao, and Jiang Wu. Enhanced Carrier Transport in X-Ray Detector Based on $Cs_3Bi_2I_9$/MXene Composite Wafers. *Advanced Optical Materials*, 10(23):2201585, 2022.

[86] Shujie Tie, Wei Zhao, Deyu Xin, Min Zhang, Jidong Long, Qi Chen, Xiaojia Zheng, Jianguo Zhu, and Wen-Hua Zhang. Robust Fabrication of Hybrid Lead-Free Perovskite Pellets for Stable X-ray Detectors with Low Detection Limit. *Advanced Materials*, 32(31):2001981, 2020.

[87] Andre Mayer, Maximilian Buchmüller, Si Wang, Christian Steinberg, Marc Papenheim, Hella-Christin Scheer, Neda Pourdavoud, Tobias Haeger, and Thomas Riedl.

Thermal nanoimprint to improve the morphology of MAPbX$_3$ (MA = methylammonium, X = I or Br). *Journal of Vacuum Science & Technology B*, 35(6):06G803, 2017.

[88] Junyan Xiao, Yueyong Yang, Xin Xu, Jiangjian Shi, Lifeng Zhu, Songtao Lv, Huijue Wu, Yanhong Luo, Dongmei Li, and Qingbo Meng. Pressure-assisted CH$_3$NH$_3$PbI$_3$ morphology reconstruction to improve the high performance of perovskite solar cells. *Journal of Materials Chemistry A*, 3:5289–5293, 2015.

[89] Ding-Jiang Xue, Yi Hou, Shunchang Liu, Mingyang Wei, Bin Chen, Ziru Huang, Z.B. Li, Bin Sun, Andrew Proppe, Yitong Dong, Makhsud Saidaminov, Shana Kelley, Jin-Song Hu, and Edward Sargent. Regulating strain in perovskite thin films through charge-transport layers. *Nature Communications*, 11:1514, 2020.

[90] Albert These, Neamul H. Khansur, Osbel Almora, Larry Luer, Gebhard J. Matt, Udo Eckstein, Anastasia Barabash, Andres Osvet, Kyle G. Webber, and Christoph J. Brabec. Characterization of Aerosol Deposited Cesium Lead Tribromide Perovskite Films on Interdigited ITO Electrodes. *Advanced Electronic Materials*, 7(3):2001165, 2021.

[91] Karl W. Böer and Udo W. Pohl. *Semiconductor Physics*, pages 1–1299. Springer International Publishing, Cham, 2018.

[92] U. Lemmer and E. O. Göbel. *Photoluminescence Spectroscopy as a Probe for Disorder and Excitonic Effects in Organic and Inorganic Semiconductors*, chapter 9, pages 211–253. 1998.

[93] Shivam Singh, Cheng Li, Fabian Panzer, K. L. Narasimhan, Anna Graeser, Tanaji P. Gujar, Anna Köhler, Mukundan Thelakkat, Sven Huettner, and Dinesh Kabra. Effect of Thermal and Structural Disorder on the Electronic Structure of Hybrid Perovskite Semiconductor CH$_3$NH$_3$PbI$_3$. *The Journal of Physical Chemistry Letters*, 7(15):3014–3021, 2016.

[94] G. D. Cody, T. Tiedje, B. Abeles, B. Brooks, and Y. Goldstein. Disorder and the Optical-Absorption Edge of Hydrogenated Amorphous Silicon. *Physical Review Letters*, 47(20):1480–1483, 1981.

[95] Michal Baranowski and Paulina Plochocka. Excitons in Metal-Halide Perovskites. *Advanced Energy Materials*, 10(26):1903659, 2020.

[96] Jenya Tilchin, Dmitry N. Dirin, Georgy I. Maikov, Aldona Sashchiuk, Maksym V. Kovalenko, and Efrat Lifshitz. Hydrogen-like Wannier-Mott Excitons in Single Crystal of Methylammonium Lead Bromide Perovskite. *ACS Nano*, 10(6):6363–6371, 2016.

[97] Anna Yu. Samsonova, Vsevolod I. Yudin, Anna V. Shurukhina, and Yury V. Kapitonov. Excitonic Enhancement and Excited Excitonic States in CsPbBr$_3$ Halide Perovskite Single Crystals. *Materials*, 16(1), 2023.

[98] Fabian Ruf, Alice Magin, Moritz Schultes, Meltem F. Aygüler, Pablo Docampo, Erik Ahlswede, Heinz Kalt, and Michael Hetterich. Temperature-Dependent Electromodulation Spectroscopy of Excitons in Perovskite Solar Cells. *2018 IEEE 7th World Conference on Photovoltaic Energy Conversion (WCPEC) (A Joint Conference of 45th IEEE PVSC, 28th PVSEC & 34th EU PVSEC)*, pages 1550–1554, 2018.

[99] Christopher Davies, Marina Filip, Jay Patel, Timothy Crothers, Carla Verdi, Adam Wright, Rebecca Milot, Feliciano Giustino, Michael Johnston, and Laura Herz. Bimolecular recombination in methylammonium lead triiodide perovskite is an inverse absorption process. *Nature Communications*, 9, 01 2018.

[100] Adrián Francisco-López, Bethan Charles, M. Isabel Alonso, Miquel Garriga, Mark T. Weller, and Alejandro R. Goñi. Photoluminescence of Bound-Exciton Complexes and Assignment to Shallow Defects in Methylammonium/Formamidinium Lead Iodide Mixed Crystals. *Advanced Optical Materials*, 9(18):2001969, 2021.

[101] Konstantin Schötz, Abdelrahman M. Askar, Wei Peng, Dominik Seeberger, Tanaji P. Gujar, Mukundan Thelakkat, Anna Köhler, Sven Huettner, Osman M. Bakr, Karthik Shankar, and Fabian Panzer. Double peak emission in lead halide perovskites by self-absorption. *Journal of Materials Chemistry C*, 8(7):2289–2300, 2020.

[102] Le Quang Phuong, Yumi Nakaike, Atsushi Wakamiya, and Yoshihiko Kanemitsu. Free Excitons and Exciton–Phonon Coupling in $CH_3NH_3PbI_3$ Single Crystals Revealed by Photocurrent and Photoluminescence Measurements at Low Temperatures. *The Journal of Physical Chemistry Letters*, 7(23):4905–4910, 2016.

[103] Florian Staub, Hannes Hempel, Jan-Christoph Hebig, Jan Mock, Ulrich W. Paetzold, Uwe Rau, Thomas Unold, and Thomas Kirchartz. Beyond Bulk Lifetimes: Insights into Lead Halide Perovskite Films from Time-Resolved Photoluminescence. *Physical Review Applied*, 6(4):044017, 2016.

[104] Konstantin Schötz, Abdelrahman M. Askar, Anna Köhler, Karthik Shankar, and Fabian Panzer. Investigating the Tetragonal-to-Orthorhombic Phase Transition of Methylammonium Lead Iodide Single Crystals by Detailed Photoluminescence Analysis. *Advanced Optical Materials*, 8(17):2000455, 2020.

[105] Rebecca L. Milot, Giles E. Eperon, Henry J. Snaith, Michael B. Johnston, and Laura M. Herz. Temperature-Dependent Charge-Carrier Dynamics in $CH_3NH_3PbI_3$ Perovskite Thin Films. *Advanced Functional Materials*, 25(39):6218–6227, 2015.

[106] Biwas Subedi, Chongwen Li, Cong Chen, Dachang Liu, Maxwell M. Junda, Zhaoning Song, Yanfa Yan, and Nikolas J. Podraza. Urbach Energy and Open-Circuit Voltage Deficit for Mixed Anion–Cation Perovskite Solar Cells. *ACS Applied Materials & Interfaces*, 14(6):7796–7804, 2022.

[107] Stefaan De Wolf, Jakub Holovsky, Soo-Jin Moon, Philipp Löper, Bjoern Niesen, Martin Ledinsky, Franz-Josef Haug, Jun-Ho Yum, and Christophe Ballif. Organometallic Halide Perovskites: Sharp Optical Absorption Edge and Its Relation to

Photovoltaic Performance. *The Journal of Physical Chemistry Letters*, 5(6):1035–1039, 2014.

[108] Joel Jean, Thomas S. Mahony, Deniz Bozyigit, Melany Sponseller, Jakub Holovský, Moungi G. Bawendi, and Vladimir Bulović. Radiative Efficiency Limit with Band Tailing Exceeds 30% for Quantum Dot Solar Cells. *ACS Energy Letters*, 2(11):2616–2624, 2017.

[109] Chujun Zhang, Sudhi Mahadevan, Jun Yuan, Johnny Ka Wai Ho, Yaxin Gao, Wei Liu, Hui Zhong, He Yan, Yingping Zou, Sai-Wing Tsang, and Shu Kong So. Unraveling Urbach Tail Effects in High-Performance Organic Photovoltaics: Dynamic vs Static Disorder. *ACS Energy Letters*, 7(6):1971–1979, 2022.

[110] Stefan Zeiske, Oskar J. Sandberg, Nasim Zarrabi, Christian M. Wolff, Meysam Raoufi, Francisco Peña-Camargo, Emilio Gutierrez-Partida, Paul Meredith, Martin Stolterfoht, and Ardalan Armin. Static Disorder in Lead Halide Perovskites. *The Journal of Physical Chemistry Letters*, 13(31):7280–7285, 2022.

[111] Ihor Studenyak, M. Kranjčec, and Mykhailo Kurik. Urbach Rule in Solid State Physics. *International Journal of Optics and Applications*, 4(3):76–83, 2014.

[112] Kyle Frohna, Miguel Anaya, Stuart Macpherson, Jooyoung Sung, Tiarnan Doherty, Yu-Hsien Chiang, Andrew Winchester, Kieran Orr, Julia Parker, Paul Quinn, Keshav Dani, Akshay Rao Ananth, and Samuel Stranks. Nanoscale chemical heterogeneity dominates the optoelectronic response of alloyed perovskite solar cells. *Nature Nanotechnology*, 17:1–7, 2022.

[113] Gwisu Kim, Hanul Min, Kyoung Su Lee, Do Yoon Lee, So Me Yoon, and Sang Il Seok. Impact of strain relaxation on performance of α-formamidinium lead iodide perovskite solar cells. *Science*, 370(6512):108–112, 2020.

[114] Hooman Mehdizadeh-Rad and Jai Singh. Influence of Urbach Energy, Temperature, and Longitudinal Position in the Active Layer on Carrier Diffusion Length in Perovskite Solar Cells. *ChemPhysChem*, 20(20):2712–2717, 2019.

[115] Lu Qiao, Wei-Hai Fang, Run Long, and Oleg. V. Prezhdo. Elimination of Charge Recombination Centers in Metal Halide Perovskites by Strain. *Journal of the American Chemical Society*, 143(26):9982–9990, 2021.

[116] Adharsh Rajagopal, Po-Wei Liang, Chu-Chen Chueh, Zhibin Yang, and Alex K.-Y. Jen. Defect Passivation via a Graded Fullerene Heterojunction in Low-Bandgap Pb–Sn Binary Perovskite Photovoltaics. *ACS Energy Letters*, 2(11):2531–2539, 2017.

[117] E. Regalado-Pérez, Evelyn B. Díaz-Cruz, J. Landa-Bautista, N. R. Mathews, and X. Mathew. Impact of Vertical Inhomogeneity on the Charge Extraction in Perovskite Solar Cells: A Study by Depth-Dependent Photoluminescence. *ACS Applied Materials & Interfaces*, 13(10):11833–11844, 2021.

[118] Qingzhi An, Fabian Paulus, David Becker-Koch, Changsoon Cho, Qing Sun, Andreas Weu, Sapir Bitton, Nir Tessler, and Yana Vaynzof. Small grains as recombination hot spots in perovskite solar cells. *Matter*, 4(5):1683–1701, 2021.

[119] Wiley A. Dunlap-Shohl, Tianyang Li, and David B. Mitzi. Interfacial Effects during Rapid Lamination within MAPbI$_3$ Thin Films and Solar Cells. *ACS Applied Energy Materials*, 2(7):5083–5093, 2019.

[120] Bo Li, Ting Shen, and Sining Yun. Recent progress of crystal orientation engineering in halide perovskite photovoltaics. *Materials Horizons*, 10(1):13–40, 2023.

[121] Chunqing Ma, Michael Grätzel, and Nam-Gyu Park. Facet Engineering for Stable, Efficient Perovskite Solar Cells. *ACS Energy Letters*, 7(9):3120–3128, 2022.

[122] Chunqing Ma, Felix T. Eickemeyer, Sun-Ho Lee, Dong-Ho Kang, Seok Joon Kwon, Michael Grätzel, and Nam-Gyu Park. Unveiling facet-dependent degradation and facet engineering for stable perovskite solar cells. *Science*, 379(6628):173–178, 2023.

[123] Mathias Uller Rothmann, Judy S. Kim, Juliane Borchert, Kilian B. Lohmann, Colum M. O'Leary, Alex A. Sheader, Laura Clark, Henry J. Snaith, Michael B. Johnston, Peter D. Nellist, and Laura M. Herz. Atomic-scale microstructure of metal halide perovskite. *Science*, 370(6516):eabb5940, 2020.

[124] Gebhard J. Matt, Ievgen Levchuk, Judith Knüttel, Johannes Dallmann, Andres Osvet, Mykhailo Sytnyk, Xiaofeng Tang, Jack Elia, Rainer Hock, Wolfgang Heiss, and Christoph J. Brabec. Sensitive Direct Converting X-Ray Detectors Utilizing Crystalline CsPbBr$_3$ Perovskite Films Fabricated via Scalable Melt Processing. *Advanced Materials Interfaces*, 7(4):1901575, 2020.

[125] Jarla Thiesbrummel, Vincent M. Le Corre, Francisco Peña-Camargo, Lorena Perdigón-Toro, Felix Lang, Fengjiu Yang, Max Grischek, Emilio Gutierrez-Partida, Jonathan Warby, Michael D. Farrar, Suhas Mahesh, Pietro Caprioglio, Steve Albrecht, Dieter Neher, Henry J. Snaith, and Martin Stolterfoht. Universal Current Losses in Perovskite Solar Cells Due to Mobile Ions. *Advanced Energy Materials*, 11(34):2101447, 2021.

[126] Philipp Ramming, Nico Leupold, Konstantin Schötz, Anna Köhler, Ralf Moos, Helen Grüninger, and Fabian Panzer. Suppressed ion migration in powder-based perovskite thick films using an ionic liquid. *Journal of Materials Chemistry C*, 9(35):11827–11837, 2021.

[127] Dong Hoe Kim, James B. Whitaker, Zhen Li, Maikel F.A.M. van Hest, and Kai Zhu. Outlook and Challenges of Perovskite Solar Cells toward Terawatt-Scale Photovoltaic Module Technology. *Joule*, 2(8):1437–1451, 2018.

[128] Konstantin Schötz, Christopher Greve, Arjan Langen, Harrie Gorter, Ilker Dogan, Yulia Galagan, Albert J. J. M. van Breemen, Gerwin H. Gelinck, Eva M. Herzig, and Fabian Panzer. Understanding Differences in the Crystallization Kinetics between One-Step Slot-Die Coating and Spin Coating of MAPbI$_3$ Using Multimodal In Situ Optical Spectroscopy. *Advanced Optical Materials*, 9(21):2101161, 2021.

[129] José Maria C. da Silva Filho, Agnaldo D. Gonçalves, Francisco C. Marques, and Jilian N. de Freitas. A Review on the Development of Metal Grids for the Upscaling of Perovskite Solar Cells and Modules. *Solar RRL*, 6(8):2100865, 2022.

[130] VDI Verlag GmbH INGENIEUR.de. Bill Gates setzt auf Perowskit: Neue Technologie für Solarzellen? `https://www.ingenieur.de/technik/fachbereiche/energie/bill-gates-setzt-auf-perowskit-neue-technologie-fuer-solarzellen/`. Last modified 24.05.2023, Accessed 18.09.2023.

[131] PEROSOL. A BRIGHT FUTURE FOR SOLAR POWER. `https://www.perosol.com/`. Accessed 18.09.2023.

[132] Perovskite-info. Microquanta Semiconductor. `https://www.perovskite-info.com/microquanta-semiconductor`. Last modified 06.03.2023, Accessed 18.09.2023.

[133] Xin Zhang, Shouwu Yu, Xianguang Meng, and Shujuan Xiao. A Review on Lead-Free Perovskites for X-Ray Detection and Imaging. *Crystal Research and Technology*, 58(5):2200232, 2023.

[134] Umar Farooq, Muhammad Ishaq, Usman Ali Shah, Shuo Chen, Zhuang-Hao Zheng, Muhammad Azam, Zheng-Hua Su, Rong Tang, Ping Fan, Yang Bai, and Guang-Xing Liang. Bandgap engineering of lead-free ternary halide perovskites for photovoltaics and beyond: Recent progress and future prospects. *Nano Energy*, 92:106710, 2022.

[135] Weijun Ke and Mercouri Kanatzidis. Prospects for low-toxicity lead-free perovskite solar cells. *Nature Communications*, 10:1–4, 2019.

[136] KFT The CHEMICAL COMPLIANCE Company. EU schränkt Verwendung von Dimethylformamid ein. `https://www.kft.de/eu-schraenkt-verwendung-von-dimethylformamid-ein/`. Last modified 01.12.2021, Accessed 18.09.2023.

[137] Hui-Seon Kim, Youn-Joo An, Jin Il Kwak, Hee Jung Kim, Hyun Suk Jung, and Nam-Gyu Park. Sustainable Green Process for Environmentally Viable Perovskite Solar Cells. *ACS Energy Letters*, 7(3):1154–1177, 2022.

3 Thesis Summary

3.1 Overview Thesis Structure

This thesis aims to understand the morphology and optoelectronic properties of powder-based pressure-processed lead halide perovskites to improve their functionality. This issue is addressed by six paper publications (research articles) divided into two parts, as illustrated in the overview of the thesis structure in Figure 3.1.
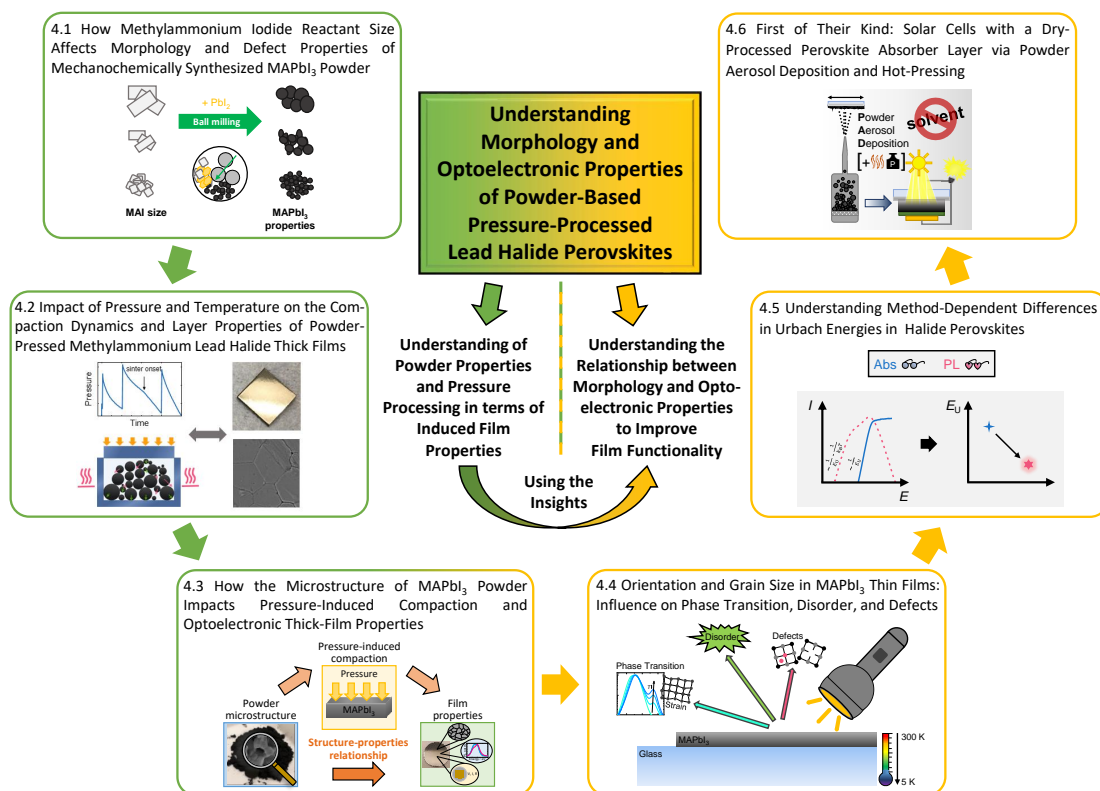
Figure 3.1: Overview of the thesis structure including six paper publications.

The first part including three paper publications (presented in Sections 4.1 - 4.3) focuses on the understanding of the powder properties and the pressure processing and how both impacts the final film properties. Here, the publication in Section 4.1 investigates the MAPbI₃ powder microstructure and their relation to defect properties, while the publication in Section 4.2 describes the impact of pressure, pressing temperature and pressing time on the compaction dynamics and resulting film properties of powder-pressed lead halide perovskite thick films. Insights from both publications in Sections 4.1 and 4.2 are

used to reveal how the MAPbI$_3$ powder microstructure impacts pressure-induced compaction and resulting morphological and optoelectronic thick film properties relevant for e.g., application in X-ray detectors (publication in Section 4.3).

The latter aspect hands over to the second part of the thesis (also including three paper publications presented in Sections 4.4 - 4.6), investigating the relationship between morphology and optoelectronic properties of halide perovskites. For this purpose, thin films are considered with regard to the most popular halide perovskite device application, solar cells. Using insights from the publication in Section 4.2, the publication in Section 4.4 investigates how small differences in crystallographic orientation and grain size influence structural and optoelectronic thin film properties, i.e., the phase transition, strain, defects and energetic disorder. For the energetic disorder, characterized by the so-called Urbach energy, discrepancies occur from different measurement and analysis methods, whose origin is analyzed and revealed in the publication in Section 4.5. The gained fundamental understanding of the Urbach energy is important, as it is a figure of merit for the performance potential of semiconductor samples and related to solar cell functionality. In the publication in Section 4.6, the first successful integration of powder-based pressure-processed MAPbI$_3$ films in a solar cell configuration is demonstrated. Here, using insights from the publications in Sections 4.2, 4.4 and 4.5, pressure-treatment is applied to induce improved film morphology for improved optoelectronic properties and thus improved device functionality.

3.2 Individual Publications and Their Contribution to the Thesis Aim

In the following a more detailed summary is given of what I investigated and found in the six individual paper publications presented in Sections 4.1 - 4.6 and how these publications contribute to the overall aim of the thesis.

How Methylammonium Iodide Reactant Size Affects Morphology and Defect Properties of Mechanochemically Synthesized MAPbI$_3$ Powder

In the publication in Section 4.1 we investigated how differences in the mechanochemical powder synthesis, i.e. different MAI reactant sizes, affect resulting MAPbI$_3$ powder properties. For this, we precipitated crystalline MAI by dropping diethyl ether to MAI dissolved in ethanol. By reducing the amount of diethyl ether and the solution temperature we precipitated smaller MAI reactant sizes, which we further reduced by milling in a planetary ball mill. In this way, we prepared three different MAI powders named Large, Medium and Small, whose average MAI reactant sizes were evaluated from SEM images to cover about two orders of magnitude (Fig. 3.2a-c).

Using these three MAI powders we mechanochemically synthesized three different MAPbI$_3$ powders. From SEM images of MAI reactant powders and corresponding mechanochemically synthesized MAPbI$_3$ powders we observed larger MAI reactant sizes to
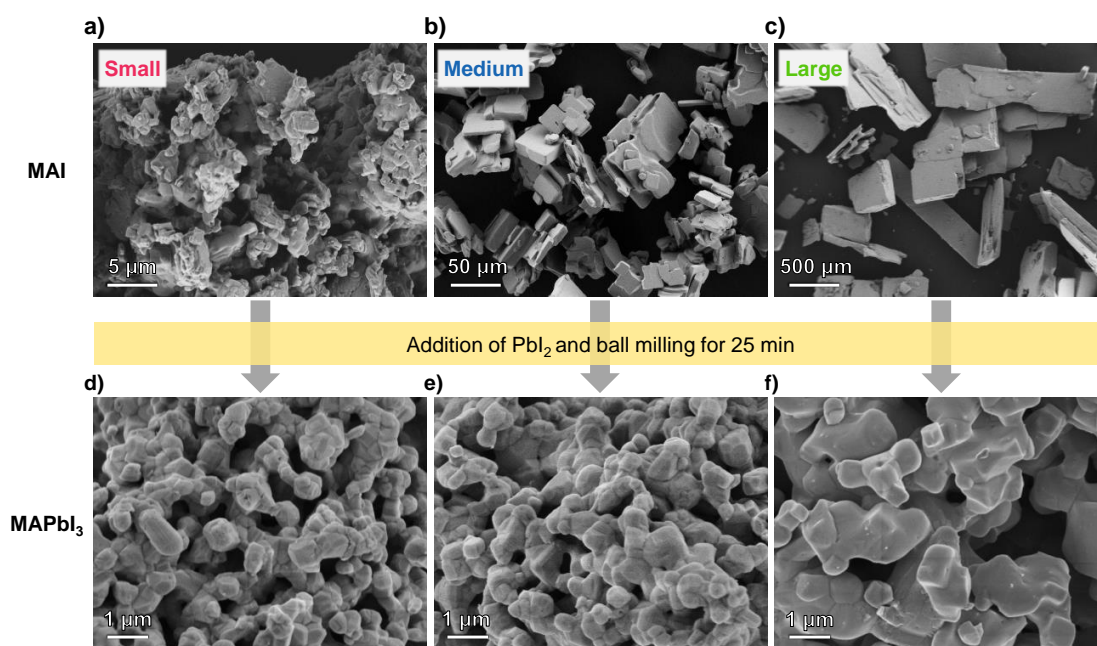
Figure 3.2: Top row: SEM images of MAI reactant powders with a) small, b) medium and c) large particle sizes. Bottom row: SEM images of MAPbI$_3$ powders synthesized via mechanochemical synthesis using the MAI reactant powders d) small, e) medium and f) large. Reproduced from Section 4.1.

result in larger MAPbI$_3$ powder particle sizes (Fig. 3.2 and Fig. 3.3a). Furthermore, we found decreased reflex widths in XRD patterns of MAPbI$_3$ powders synthesized from larger MAI reactant sizes, indicating larger crystallite sizes and/or reduced microstrain, which are both typically related to lower defect densities.

To confirm this relation, we performed nuclear quadrupole resonance (NQR) measurements on the MAPbI$_3$ powders to investigate the local structural environment of the iodide in the MHP crystal lattice. We found narrower peak widths and increased integrated signal intensity for MAPbI$_3$ powders synthesized from larger MAI reactant sizes, indicating less perturbation of the iodide environment by defects. In addition, from TRPL measurements of the MAPbI$_3$ powders we extracted lower defect-related recombination rates k_1 for MAPbI$_3$ powders synthesized from larger MAI reactant sizes (Fig. 3.3b). Thus, we revealed larger MAI reactant sizes to correlate with larger MAPbI$_3$ powder particle sizes and reduced defect densities.

To explain this correlation, I contributed to the interpretation of the mechanochemical synthesis mechanism. Here, I associated larger MAI sizes with a longer duration of perovskite synthesis and a delayed MAPbI$_3$ crushing stage during ball milling resulting in larger MAPbI$_3$ particle sizes, as proven by XRD and SEM analyses. Besides less fragmentation of MAPbI$_3$ powder particles I also associated the shortened crushing stage with reduced defect creation due to less impacting mechanical energy, fully in line with lower defect densities found for larger powder particle sizes from NQR and TRPL analyses.
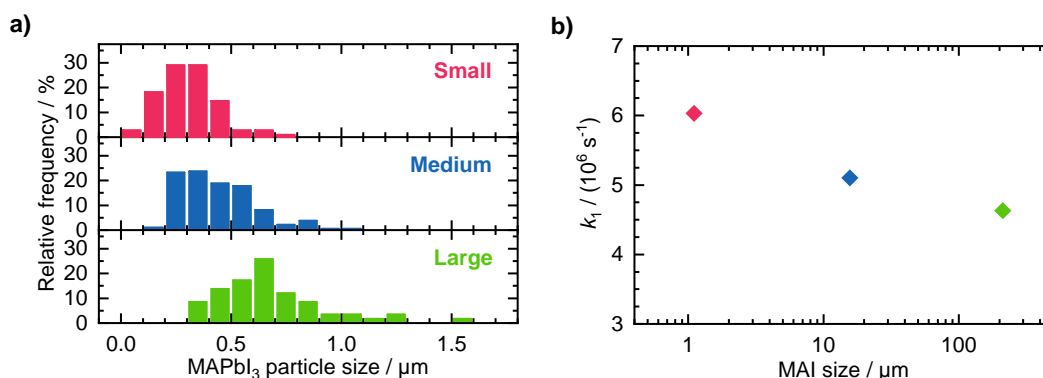
Figure 3.3: a) Particle size distribution of MAPbI$_3$ powders synthesized via mechanochemical synthesis using the MAI reactant powders with small (top), medium (middle) and large (bottom) particle sizes. b) Defect-related recombination rate k_1 etracted from TRPL measurements of MAPbI$_3$ powders synthesized via mechanochemical synthesis using MAI reactant powders with small, medium and large particle sizes. Reproduced from Section 4.1.

Impact of Pressure and Temperature on the Compaction Dynamics and Layer Properties of Powder-Pressed Methylammonium Lead Halide Thick Films

To bring perovskite powders into use for application in devices, they must be processed into a film. Accordingly, in the publication in Section 4.2 I examined in detail the compaction dynamics during pressing of halide perovskite powders into thick film pellets and their resulting morphology.

By means of time-resolved pressure monitoring, I investigated pressure relaxations in terms of temporal width and shape. Here, I described pressure relaxations taken at room-temperature by satisfying fits with a biexponential decay function (Fig. 3.4a). The two corresponding characteristic relaxation times indicated two relaxation processes occurring at room-temperature, where I observed the longer one to get more important
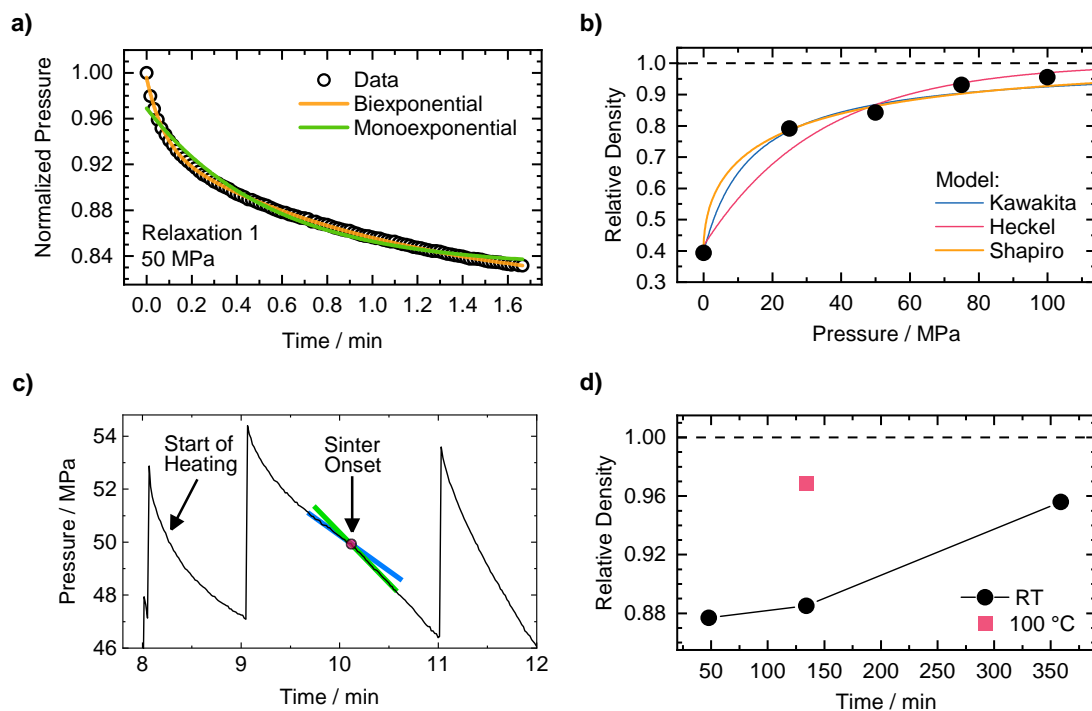
Figure 3.4: a) Normalized first pressure relaxation from pressing MAPbI$_3$ powder with 50 MPa at room-temperature (black circles) together with insufficient monoexponential fit (green line) and satisfying biexponential fit (orange line). b) Pressure-dependent relative densities of MAPbI$_3$ thick film pellets pressed from MAPbI$_3$ powder at room-temperature (black circles) together with fits according to models of Kawakita, Heckel and Shapiro. c) Temporal evolution of pressure during pressing of MAPbI$_3$ powder with ≈ 50 MPa and heating up from room-temperature. A few minutes after the start of heating, the pressure relaxation accelerates, indicating the sinter onset. d) Relative density of thick film pelllets pressed from MAPbI$_3$ powder with 100 MPa as a function of pressing time for pressing at room-temperature (black circles) and 100 °C (red square). Reproduced from Section 4.2.

with increasing number of pressure regulations and thus increasing compaction. By modeling pressure-dependent relative densities of powder pressed thick film pellets (Fig. 3.4b) I identified the shorter relaxation process to be associated to particle rearrangement and the longer one to plastic deformation (including crushing). Here, a fit according to the Heckel model, considering only plastic deformation of powder particles as compaction process, described the pressure-dependent relative densities only in an upper pressure range ≥ 50 MPa. A fit according to the Shapiro model, considering not only plastic deformation but also rearrangement dynamics of powder particles, described the pressure-dependent relative densities well in the entire pressure range (similar to the fit of the empirically derived Kawakita model). From this I concluded that at pressures < 50 MPa particle rearrangement dominates the pressure induced compaction process, while at pressures ≥ 50 MPa plastic deformation gets more significant.

Regarding the influence of pressing parameters, I found increased pressure and pressing time to result in increased pellet densities (Fig. 3.4b,d). Furthermore, via time-resolved pressure monitoring, I observed that the compaction during pressing can be accelerated significantly by hot-pressing, i.e., by using an elevated pressing temperature (Fig. 3.4c,d). This acceleration is reflected in concavely curved pressure relaxations, (Fig. 3.4c), from which I identified the onset of this temperature-induced accelerated compaction to occur already at temperatures as low as 30 °C. I associated this temperature-induced third compaction process with a sinter process. The sintering is supported by SEM images of pellet top surface (Fig. 3.5a) and cross-section, that show increased pressing temperature to result in increased grain sizes and reduced surface roughness in line with increased pellet density. Consequently, for a high pressure-temperature combination of 100 MPa and 100 °C I obtained relative pellet densities above 97%. In addition, from intensity analyses of reflexes in XRD patterns, we observed a temperature-induced preferred crystallographic orientation of the (002) plane (parallel to the press punch area) increasing with pressing temperature (Fig. 3.5b).
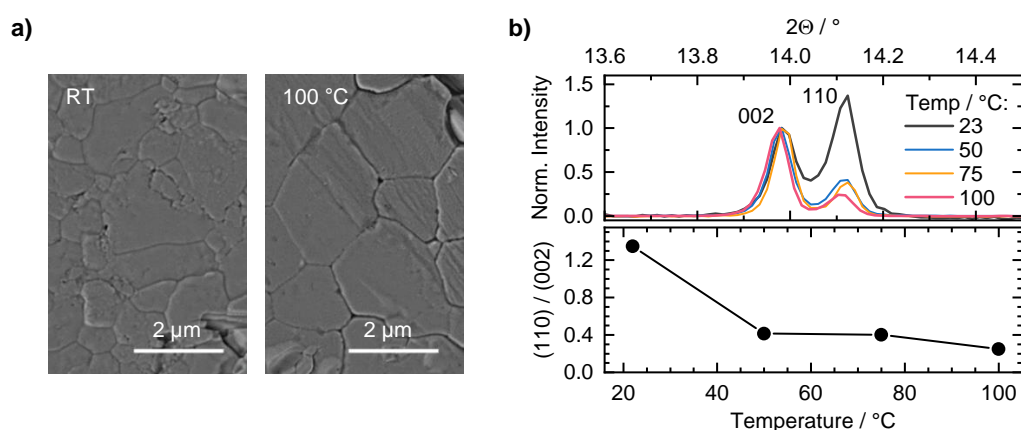
Figure 3.5: a) Top view SEM images of powder pressed MAPbI$_3$ thick film pellets with 100 MPa at room-temperature (RT) and at 100 °C. b) XRD pattern of MAPbI$_3$ thick film pellets pressed with 100 MPa and temperatures between 23 °C and 100 °C normalized to the (002) reflex (top) and temperature-dependent (110)/(002) intensity ratio (bottom). Reproduced from Section 4.2.

How the Microstructure of MAPbI$_3$ Powder Impacts Pressure-Induced Compaction and Optoelectronic Thick-Film Properties

Using the insights about powder properties from the publication in Section 4.1, as well as about pressing parameters and compaction processes during powder pressing from the publication in Section 4.2, I investigated how the powder microstructure impacts pressure-induced compaction and resulting morphological and optoelectronic film properties in the publication in Section 4.3.

Therefore, MAPbI$_3$ powders with different microstructure (Fig. 3.6a), i.e., different MAPbI$_3$ powder particle size and degree of sintered particle connections between neighboring particles were synthesized via mechanochemical synthesis using different MAI and PbI$_2$ reactant sizes. In accordance with the insights from Section 4.1 we found larger MAI reactant sizes to result in larger MAPbI$_3$ powder particle sizes due to a longer duration of the perovskite synthesis along with a reduced subsequent crushing stage during ball milling (Fig. 3.6a top and middle). In addition, we observed exceptional
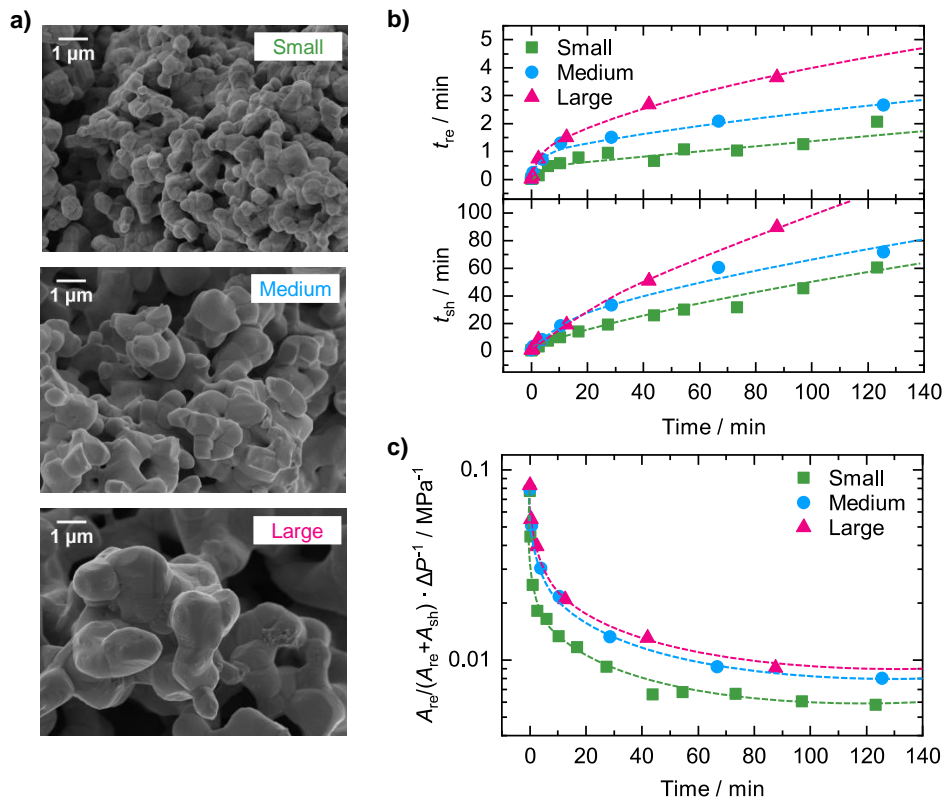
Figure 3.6: a) SEM images of MAPbI$_3$ powders with small (top), medium (middle) and large (bottom) powder particle sizes and sintered connections. b) Characteristic relaxation times t_{re} (top) and t_{sh} (bottom) and c) evolution of the ΔP-corrected amplitude ratio as a function of pressing time from biexponential fits of pressure relaxations during pressing MAPbI$_3$ powders with small (green squares), medium (blue dots), and large (red triangles) powder particle sizes at 25 MPa (dashed lines serve as a guide for the eye). Reproduced from Section 4.3.

growth of MAPbI$_3$ powder particles during ball milling small reactant sizes (Fig. 3.6a bottom). I attributed this observation to a prompt perovskite conversion of the reactants in the milling process followed by the growth of the synthesized MAPbI$_3$ powder particles via a ponounced sintering effect, which is favored by the limited heat dissipation capability of small MAPbI$_3$ particles. Overall, we found powders with larger synthesized MAPbI$_3$ powder particles to exhibit larger sintered particle connections between neighboring particles (Fig. 3.6). According to the described powder microstructure, we named the powders "Small", "Medium" and "Large".

In order to investigate the compaction behavior of these three powders as well as resulting thick film pellet properties, I pressed the powders. Using the gained knowledge about analyzing time-resolved pressure relaxations from Section 4.2, I identified decreased compaction dynamic for larger powder particles with stronger sintered connections, which I quantified by longer characteristic relaxation times t_{re} and t_{sh} (Fig. 3.6b). I extracted these relaxation times, which represent the compaction due to particle rearrangement and shape changing processes (i.e., plastic deformation and crushing), via biexponential decay fits to the pressure relaxations. The identified decreased compaction for larger powder particles is in line with a lower visible compaction in SEM images, higher surface roughness and lower densities of resulting thick film pellets. From the biexponential fits to the pressure relaxations, I also derived the corresponding pressure-corrected amplitude ratio decreasing with pressing time (Fig. 3.6c). I associated this decrease with reduced significance of rearrangement processes with increasing pressing time. From the overall lower amplitude ratio of the MAPbI$_3$ powder with small particle sizes I concluded crushing to be the more relevant compaction process among the shape changing compaction processes in line with the shortest t_{sh} (green symbols in Fig. 3.6b,c). In addition, I identified increased contribution of plastic deformation to the overall compaction process for powders with larger particle sizes. Besides that I also observed increased plastic deformation with increasing MAPbI$_3$ powder particle sizes to be reflected in a higher degree of crystallite size reduction characterized by XRD measurements of final films. From fitting the rate equation (describing the decay of charge carrier density) to corresponding TRPL curves (Fig. 3.7a), I found the crystallite size reduction
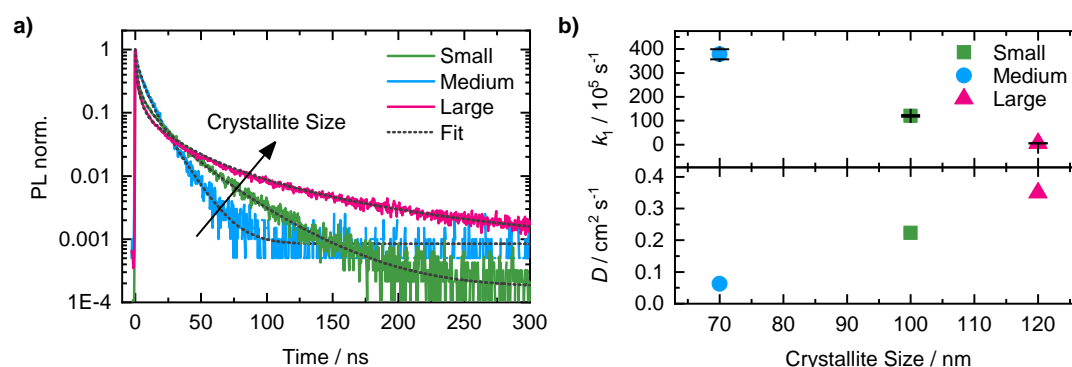
Figure 3.7: a) Normalized transient PL curves with fits according to the rate equation and b) corresponding rate constant k_1 (top) and diffusion constant D (bottom) as a function of crystallite size for pellets pressed at 100 MPa using MAPbI$_3$ powders with small (green), medium (blue), and large (red) powder particle sizes. Reproduced from Section 4.3.

to go along with increased nonradiative, defect-associated excited state recombination and decreased charge carrier diffusion (Fig. 3.7b). Moreover, we found that increased plastic deformation also deteriorates the grain boundary quality, facilitating ion migration as observed by higher electrical dark conductivities from impedance spectroscopy measurements. Thus, I elucidated the many-faceted structure-properties relationship in powder pressed halide perovskite thick film pellets, which will advance their processing and resulting functionality when integrated in optoelectronic devices such as X-ray detectors.

Orientation and Grain Size in MAPbI$_3$ Thin Films: Influence on Phase Transition, Disorder, and Defects

Besides thick film devices, thin film devices, in particular solar cells, have attracted much attention due to achieved lab-scale efficiencies on par with commercially established silicon devices. For this reason, in the publication in Section 4.4, I also in detail investigated the structure-properties relationship, i.e., the relationship between morphology (grain size and crystallographic orientation) and structural and optoelectronic properties (phase transition, strain, defects, energetic disorder) in MAPbI$_3$ thin films.

Therefore, I used the insights from the publication in Section 4.2 to induce slightly different morphologies in MAPbI$_3$ thin films deposited via PAD method by pressing these films with different pressing temperatures (CP: Cold-pressed film pressed at room-temperature, HP: Hot-pressed film pressed at 100 °C). Here, SEM and XRD analyses confirmed, that increased pressing temperature induces larger grain sizes and increased preferred crystallographic orientation and thus improved morphological properties.

Via temperature-dependent absorption and PL measurements, I revealed these improved morphological properties to be related to an increased phase transition temperature for the transition from tetragonal to orthorhombic phase (Fig. 3.8), which I attributed to less strain resulting from the reduced fraction of grain boundaries. Furthermore, via
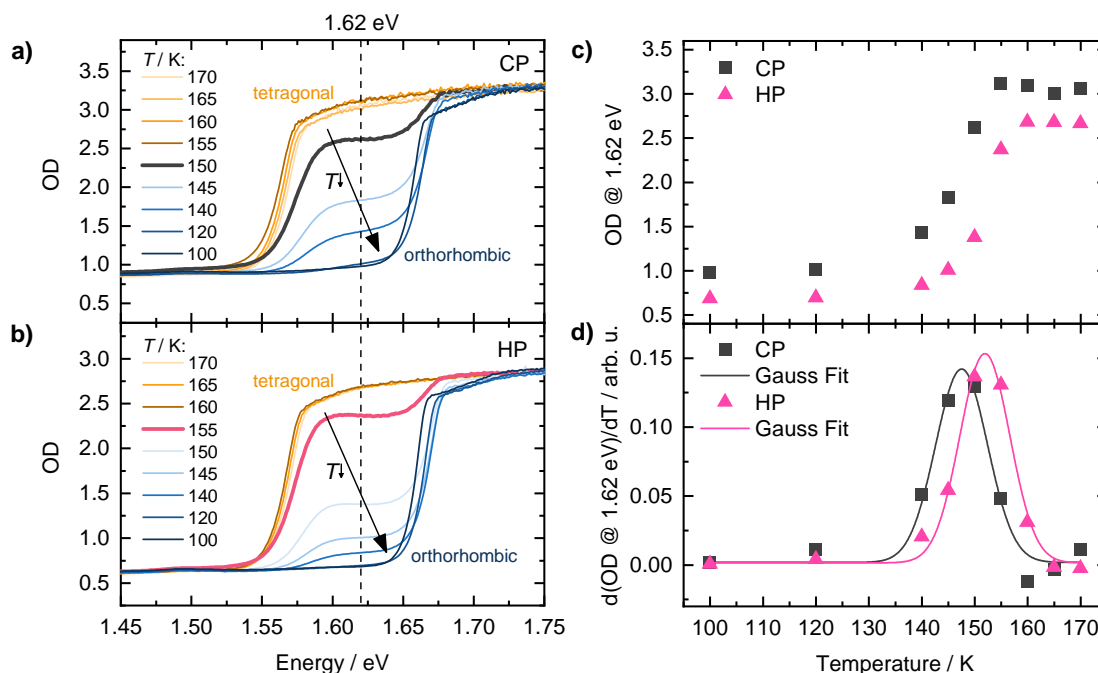
Figure 3.8: Absorption spectra of a) cold-pressed (CP) and b) hot-pressed (HP) MAPbI$_3$ thin films in the phase transition region between 170 and 100 K. c) Optical density at 1.62 eV for temperatures between 170 and 100 K extracted from absorption spectra in a,b for CP (gray) and HP (red) MAPbI$_3$ thin films. d) Derivative of c, where the peak position is associated with the critical phase transition temperature. Reproduced from Section 4.4.

temperature- and fluence-dependent PL analyses I related the morphological improvements to lower defect densities. In this regard, I found higher ASE peak intensities in PL spectra measured at 5 K for films with improved morphology (3.9a), which indicated higher crystallinity and longer charge carrier lifetimes. Via TRPL measurements, I indeed quantified the charge carrier lifetime to be longer for films with improved morphology (Fig. 3.9b right panel). Here, I observed that besides the often-considered grain size, also an increased preferred crystallographic orientation results in longer charge carrier lifetimes (Fig. 3.9b left panel). The identified reduced strain and lower defect densities
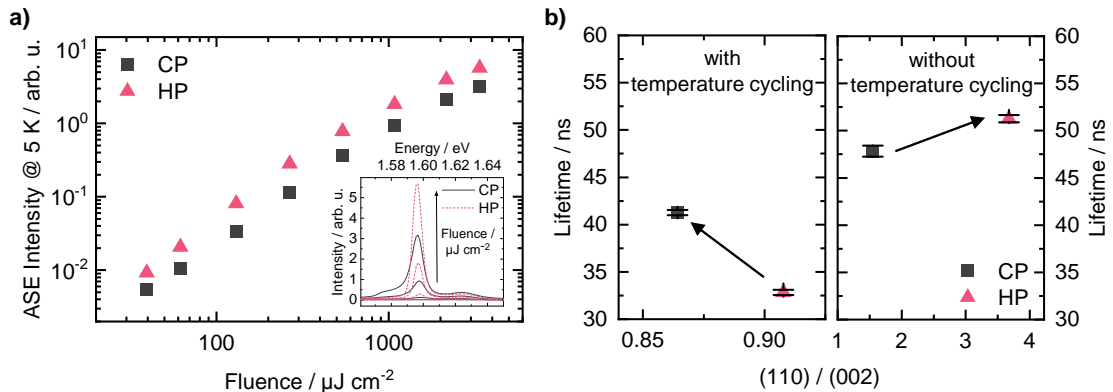
Figure 3.9: a) Fluence-dependent ASE peak intensity at 5 K and inset with corresponding exemplary PL spectra for CP (gray) and HP (red) MAPbI$_3$ thin films. b) Lifetimes dependent on 002-preferred orientation after temperature cycling, i.e., cooling the sample to 5 K and heating it back to room temperature (left panel), and lifetimes dependent on the 110-preferred orientation without temperature cycling measured at room temperature for CP (gray) and HP (red) MAPbI$_3$ thin films. Reproduced from Section 4.4.

for improved morphological properties indicated also less energetic disorder. However, as especially small morphological differences have been considered with regard to the optimization of high efficient perovskite-based devices, differences in energetic disorder could not be resolved by simple PL analyses of the characteristic Urbach energy. Yet, I resolved differences in energetic disorder from absorption, where I found lower Urbach energies for improved film morphology. The latter I showed in the publication in Section 4.5.

Understanding Method-Dependent Differences in Urbach Energies in Halide Perovskites

In the publication in Section 4.5, I aimed to understand the origin of present discrepancies in Urbach energy values extracted via different measurement and analyses methods. Therefore, we recorded temperature-dependent absorption and PL spectra quasi-simultaneously on the same MAPbI$_3$ thin film to ensure for reliable sample- and aging-independent investigations of both, the impact of measurement and analysis methods.

I carried out profound Urbach analyses in an extended energy range down to 0.2 eV below the bandgap (Fig. 3.11a). These Urbach analyses included Urbach Rule fits to measured absorption spectra (Fig. 3.10a) and calculations of the apparent Urbach energy $E_{\mathrm{U,app}}$ from measured absorption spectra where the Urbach energy E_{U} is given by the horizontal part of $E_{\mathrm{U,app}}$ representing the purely exponential disorder related part of the absorption edge (Fig. 3.10b). I also extracted the Urbach energy from measured
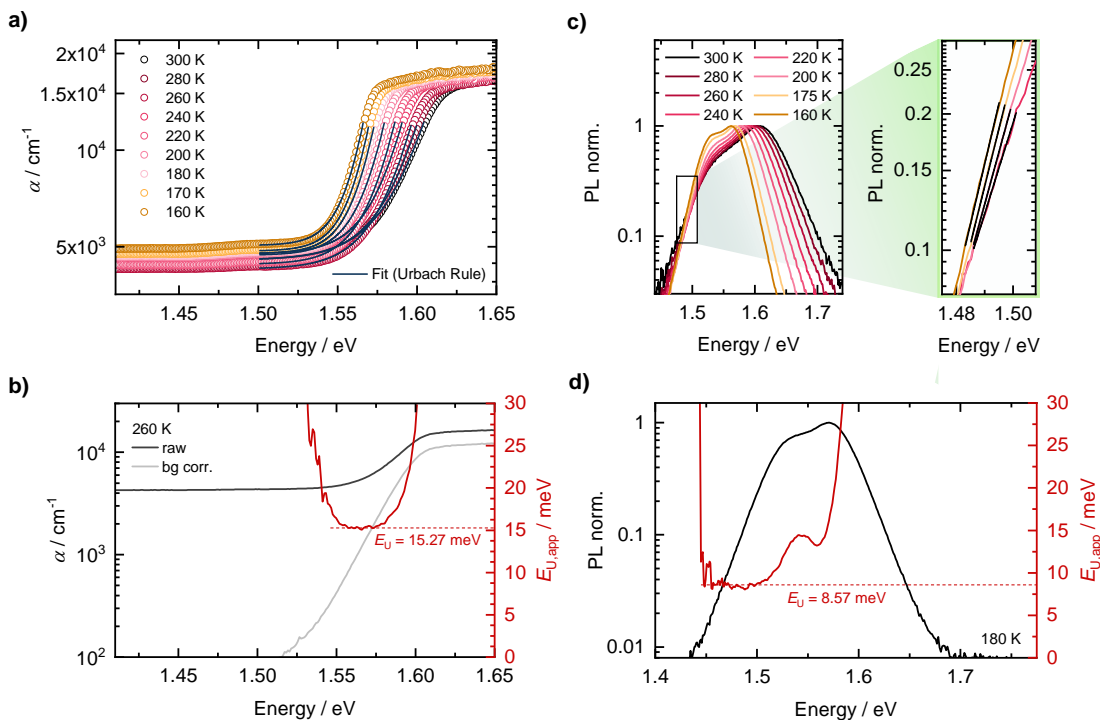
Figure 3.10: Extraction of Urbach energy values E_{U} from absorption and PL spectra of a MAPbI$_3$ thin film: a) Measured absorption spectra from 300 K down to 160 K (circles) with fits according to the Urbach Rule (solid lines). b) Absorption spectra as measured (black) and without scattering offset (grey) at 260 K and therefrom calculated apparent Urbach energy $E_{\mathrm{U,app}}$ (red). c) Measured PL spectra from 300 K down to 160 K (left) and exemplary fits of the low energy edge (right). d) Measured PL spectrum at 180 K (black) and therefrom calculated $E_{\mathrm{U,app}}$ (red). The Urbach energy E_{U} in b,d is given by the horizontal part of the $E_{\mathrm{U,app}}$ profile (red dashed line). Reproduced from Section 4.5.

PL spectra. Here, I performed low-energy-edge fits (Fig. 3.10c) as well as entire shape fits considering direct and filtered PL calculated via the Beer-Lambert law by using the intrinsic PL lineshape (Section 4.5). In addition I fitted the Urbach Rule to absorption spectra which I calculated from measured PL spectra via the reciprocity theorem (Section 4.5) and I also calculated the apparent Urbach energy $E_{U,app}$ from measured PL spectra where the Urbach energy E_U is given by the horizontal part of $E_{U,app}$ representing the purely exponential disorder related part of the low-energy PL edge (Fig. 3.10d). Applying these Urbach analyses methods for absorption and PL spectra between 300 K and 160 K of the same MAPbI$_3$ thin film, I observed that (1) The Urbach energies extracted from measured absorption spectra were higher than the Urbach energies extracted from measured PL spectra. (2) For measured absorption spectra, the apparent Urbach energy method gave lower Urbach energy values compared to corresponding values from Urbach Rule fits. In contrast for measured PL spectra all methods lead to similar Urbach energy values (Fig. 3.11b grey squares). From the latter, by considering the energy range used for Urbach energy extraction, I concluded that energy-range-dependent exaggeration effects on the Urbach energy due to non-Urbach absorption states are relevant only about 0.02 eV below the bandgap (Fig. 3.11a,b). To check if the overall lower Urbach energy values from measured PL compared to measured absorption originate from an additional energy range dependent effect which starts to contribute below 1.55 eV or
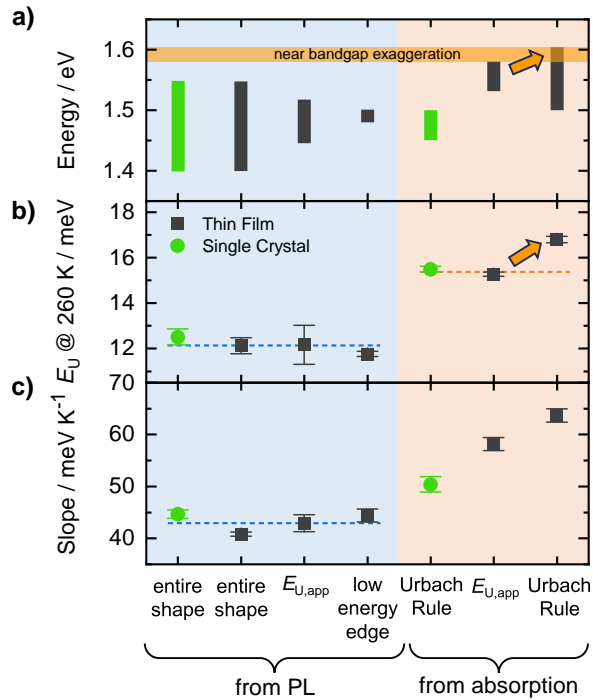
Figure 3.11: Comparison of Urbach analysis methods of measured PL (left) and absorption spectra (right) performed for a MAPbI$_3$ thin film (grey squares) and MAPbI$_3$ single crystal samples (green circles): a) Maximum E_U extraction energy range between 300 K and 160 K. b) Urbach energy E_U at 260 K. c) Slope of linear fitting to the temperature-dependence of the Urbach energy E_U. Reproduced from Section 4.5.

from a different sensitivity of the measurement methods for energetic disorder, we also evaluated absorption and PL spectra of single crystal samples. For single crystal samples the relevant energy range for Urbach energy extraction is below 1.55 eV for both absorption and PL (Fig. 3.11a). From the single crystal analyses, I observed that independent of the evaluated energy range above or below 1.55 eV from PL in general lower Urbach energies are derived (Fig. 3.11b). Besides in general lower Urbach energies I also identified a lower temperature-dependence of the Urbach energy from PL than from absorption quantified by the slope of linear fits to the temperature-dependent Urbach energies (Fig. 3.11c). Having excluded energy range dependent effects, I attributed these general discrepancies dependent on the measurement method to a preferential sensitivity of PL for sites with lower energetic disorder and thus sites of higher film quality. In addition, I discussed that the lower temperature-dependence of the Urbach energy from PL could also stem from higher phonon energies in the excited state geometry probed by PL.

First of Their Kind: Solar Cells with a Dry-Processed Perovskite Absorber Layer via Powder Aerosol Deposition and Hot-Pressing

The publication in Section 4.6 demonstrates fully working solar cells with dry-processed powder-based lead halide perovskite absorber layer – the first of their kind. Here, $MAPbI_3$ thin films deposited via PAD method were successfully integrated in solar cell configuration.

Using the insights from the publications in Sections 4.2, 4.4 and 4.5, I hot-pressed the $MAPbI_3$ PAD thin films to improve their morphological and optoelectronic properties. Via profilometer measurements, I quantified a reduction in surface roughness Ra by about 92% to a mean value of $\approx$18 nm and a reduction in film thickness by about 37% to $\approx$1 μm upon pressing, both indicating increased compaction of hot-pressed $MAPbI_3$ PAD thin films. This increased compaction is also visible in SEM images as well as in the shiny gray appearance of the films after hot-pressing compared to the matt black appearance before hot-pressing (Fig. 3.12a). We also found the hot-pressing to result in increased preferred crystallographic orientation. I attributed these morphology improvements resulting from the compaction upon hot-pressing to stem from a sinter effect fully in line with the publications in Sections 4.2 and 4.4.

Using insights from the publications in Sections 4.4 and 4.5 I investigated the impact of these morphology improvements on the optoelectronic film properties. From Urbach analyses, e.g. Urbach Rule fits to measured absorption spectra, I extracted significantly decreased Urbach energy for pressure-treated films (Fig. 3.12b). Moreover, from TRPL curves we found longer charge carrier lifetimes for pressed $MAPbI_3$ thin films, as expected from the publication in Section 4.4. Both, the decreased Urbach energy and the increased charge carrier lifetime of pressed $MAPbI_3$ thin films were on par with optoelectronic properties of common solution-processed films and thus confirmed the suitability of the pressed $MAPbI_3$ thin films for efficient solar cells.
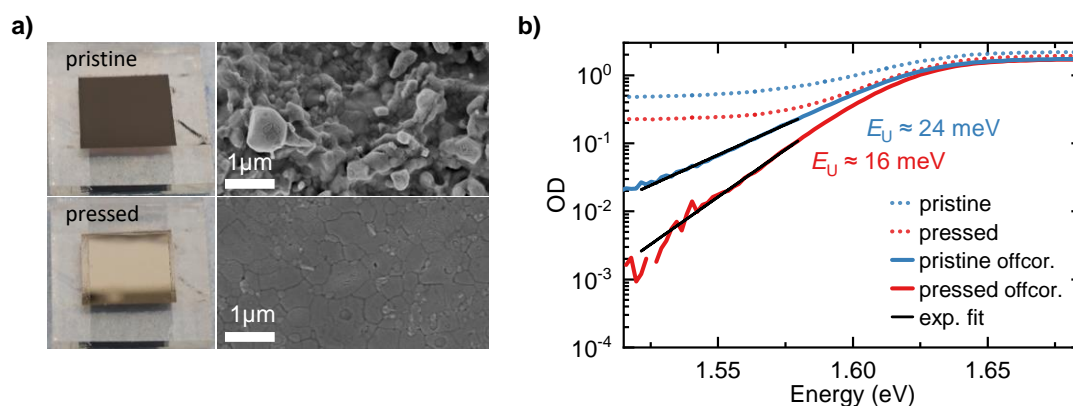
Figure 3.12: $MAPbI_3$ thin film properties: a) Photographs (left) and top-view SEM images (right) of pristine (top) and pressed (bottom) $MAPbI_3$ PAD thin films. b) Absorption spectra of pristine (blue) and pressed (red) $MAPbI_3$ PAD thin film as measured (dotted) and offset corrected (line). Exponential fits according to the Urbach Rule (black lines) are applied to extract thte respective Urbach energy. Reproduced from Section 4.6.

However, the efficiency of the devices lagged behind literature values due to issues at the interfaces between perovskite layer and charge transport layers. Here, using insights from the publication in Section 4.5, from absorption spectra of the electron transport layer (SnO_2 layer) I extracted increased Urbach energies, i.e., increased energetic disorder after PAD processing (Fig. 3.13a). We discussed that this increased energetic disorder could be associated with an increased defect density due to the mechanical energy impacting during PAD processing or attributed to the incorporation of Pb into the electron transport layer, both limiting the electrical functionality of the electron transport layer. Regarding the latter aspect, we indeed found enhanced Pb-related signals in the XPS spectra of electron transport layers that underwent PAD treatment (Fig. 3.13b). Furthermore, light-intensity-dependent *J-V* measurements indicated interface recombination, which we attributed to the formation of hydrates at the perovskite surface, i.e. at the interface between perovskite and hole transport layer.
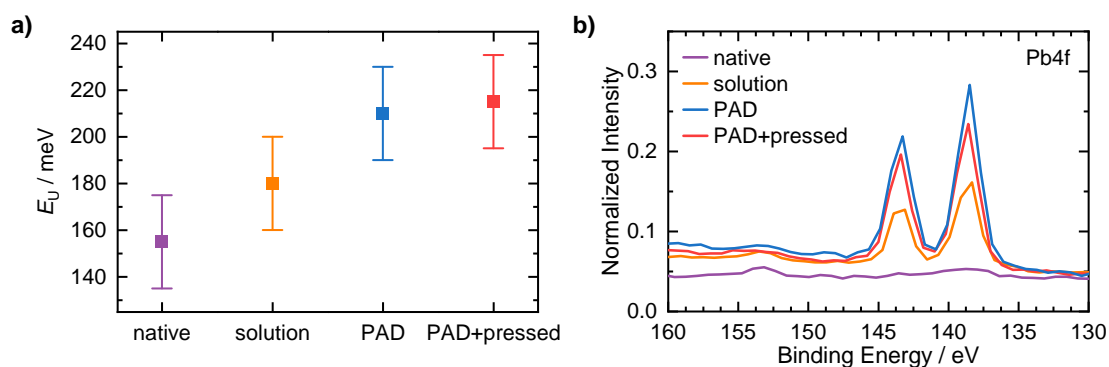
Figure 3.13: SnO_2 layer properties: a) Urbach energy of a native SnO_2 layer serving as reference (purple), a SnO_2 layer after removing a solution-processed $MAPbI_3$ film (orange), a SnO_2 layer after removing a pristine $MAPbI_3$ PAD film (blue), and a SnO_2 layer after removing a pressed $MAPbI_3$ PAD film (red). b) Pb4f signals in XPS spectra of the samples in a. Reproduced from Section 4.6.

Nevertheless, as promising approaches exist in literature to overcome the current hurdles (e.g. defect engineering and optimized preparation of the SnO_2 layer, moving all processing steps in dry athmosphere), we are confident that efficient halide perovskite solar cells can be achieved with our novel dry processing approach in the future and that in comparison to common solution processing methods, advantages like high process control and suitability for upscaling come into play.

Overall, my investigations in the six paper publications provide a profound understanding of morphology and related optoelectronic properties induced in powder-based lead halide perovskite films by pressure processing. This gained understanding of the structure-properties relationship enables targeted improvements in film processing and resulting functionality of corresponding optoelectronic devices such as X-ray detectors or solar cells.

3.3 Outlook

In this thesis I investigated the structure-properties relationship of MHPs by using powder-based pressure processing approaches for MHP thick films and thin films. These approaches, in which perovskite synthesis and film formation occur separately, enabled systematic investigations for a thorough understanding of MHP film morphology and related optoelectronic properties. The gained understanding is of interest not only for the powder-based MHP processing community but also for the MHP processing community in general as in common solution-based processing approaches uncovering the relationship between morphology and optoelectronic properties is difficult. This difficulty lies in the complexity of the interplay between perovskite synthesis and film formation occuring simultaneously. As I adressed both thick and thin film processing my results are also of interest for a wide range of applications (e.g. X-ray detectors and solar cells) and thus for large parts of the application oriented MHP community. Moreover, my investigations on discrepancies between multiple extraction methods of the Urbach energy, a popular figure of merit for the performance potential of semiconductors, are relevant for the crystalline semiconductor community.

My results push for some specific processing approach related follow-up studies as well as for some more general MHP related follow-up studies, which are not limited to the processing approaches presented in this thesis. Regarding the latter, based on the observed correlation between preferred crystallographic orientation and excited state properties, future research should disentangle the influence of different crystallographic orientations, not only out-of-plane but also in-plane. In addition, the extension of investigations on pressure-induced preferred orientation from 3D MHPs to e.g. 2D Ruddlesden-Popper perovskites could be exciting, as here, pressure also seems to be a promising stimulus to adjust the film properties and performance. Via Urbach energy analyses I extracted comparable low static disorder values for both single crystal and thin film MHP samples. These low values are desired in terms of optoelectronic performance, however further investigations to fundamentally understand the origin of these low values are needed. The identified correlation of strain with excited state properties forces the differentiation between types of strain and their respective impact, where an improved understanding of strain seems highly relevant not only in terms of performance but also stability.

Processing approach related follow-up studies include the transfer of the film processing to a humidity-controllable system in order to evaluate the effects of humidity and optimize performance and stability. In addition, for performance optimizations of dry-processed solar cells, the transfer to an inert atmosphere should be envisaged, as well as the use of a more robust ETL, defect engineering and passivation approaches. Moreover, other stoichiometries such as $FAPbI_3$ could be used, which enable higher efficiencies in accordance to the Shockley-Queisser limit. Here, investigations on phase transitions and stability would render optical in-situ measurements during pressing highly desirable.

In summary, all recommended follow-up studies aim for improved stability and performance optimization in order to enable the commercialization of MHP-based optoelectronic applications. The rising number of start-ups and companies focusing on the realization of solar cells with an integrated MHP layer underlines the potential of MHP based technologies and the relevance of my research work.

3.4 Authors' Contribution

How Methylammonium Iodide Reactant Size Affects Morphology and Defect Properties of Mechanochemically Synthesized MAPbI$_3$ Powder

This work is published in *European Journal of Inorganic Chemistry* **2023** 26, e202200736. The authors are:

Nico Leupold, Philipp Ramming, Irene Bauer, **Christina Witt**, Jennifer Jungklaus, Ralf Moos, Helen Grüninger, and Fabian Panzer.

Fabian Panzer supervised the project and Nico Leupold coordinated the measurements. Powders were manufactured by Irene Bauer and Jennifer Jungklaus. Angelika Mergner and Nicole Hall recorded SEM images, from which Nico Leupold evaluated particle sizes, all under supervision of Ralf Moos. Nico Leupold conducted XRD measurements and analyzed them. Helen Grüninger performed NMR and NQR measurements and carried out corresponding analyses. Philipp Ramming measured and analyzed PL spectra und TRPL curves. Nico Leupold and Fabian Panzer interpreted the results regarding the mechanochemical synthesis mechanism. **Christina Witt contributed to the interpretation of the mechanochemical synthesis mechanism and to the design of figures.** Fabian Panzer, Nico Leupold and Helen Grüninger wrote the manuscript, which was **proofread and edited** by all authors.

Impact of Pressure and Temperature on the Compaction Dynamics and Layer Properties of Powder-Pressed Methylammonium Lead Halide Thick Films

This work is published in *ACS Applied Electronic Materials* **2020** *2* (8), 2619-2628. The authors are:

Christina Witt, Andreas Schmid, Nico Leupold, Maximilian Schultz, Julian Höcker, Andreas Baumann, Ralf Moos, and Fabian Panzer.

Fabian Panzer initiated and planned the project. **The thick film pellet samples were pressed by** Andreas Schmid, Maximilian Schultz and **Christina Witt** from powders, which were synthesized by Nico Leupold, Monika Daubinger and Irene Bauer. XRD measurements were conducted by Julian Höcker under supervision of Andreas Baumann, and by Nico Leupold under supervision of Ralf Moos. SEM images were recorded by Angelika Mergner. Andreas Schmid measured the surface roughness of thick film pellet samples. Andreas Schmid and **Christina Witt determined relative densities of thick film pellets.** A small part of the measurement data shown in the paper (Figure 1c, S2, S11a,e) was generated by Christina Witt in the course of her master thesis. A very small part of the pressure relaxation analyses (Figure 2b) originates from this master thesis and was included in the paper with improved visualization and a new design. **All other pressure relaxation analyses** in the paper were conducted not in the framework of the master thesis and were performed by Fabian Panzer and **Christina**

Witt. Fabian Panzer and **Christina Witt developed the concept of the paper and carried out most of the data analyses and figure design** (except Figure 6a: Andreas Schmid, Figure S7: Maximilian Schultz, Figure S8, S10: Nico Leupold). Fabian Panzer and **Christina Witt discussed and interpreted the results and related them to existing literature reports.** Fabian Panzer and **Christina Witt wrote the manuscript,** which was revised by all authors.

How the Microstructure of MAPbI$_3$ Powder Impacts Pressure-Induced Compaction and Optoelectronic Thick-Film Properties

This work is published in *The Journal of Physical Chemistry C* **2022** *126* (36), 15424-15435.
The authors are:

Christina Witt, Nico Leupold, Philipp Ramming, Konstantin Schötz, Ralf Moos, and Fabian Panzer.

Fabian Panzer supervised the project. **The thick film pellet samples were pressed by Christina Witt** from powders, which were previously manufactured by Jennifer Jungklaus and Irene Bauer. Nico Leupold, under supervision of Ralf Moos, conducted XRD measurements and analyzed them via Rietveld Refinement Method. Angelika Mergner and Nicole Hall recorded SEM images, from which Nico Leupold evaluated particle sizes. Nico Leupold determined relative density and surface roughness of thick film pellets. Philipp Ramming measured TRPL curves and together with Konstantin Schötz measured steady-state PL. Konstantin Schötz developed a Python program to fit the rate equation to the TRPL curves. Nico Leupold did impedance spectroscopy measurements and evaluated dark conductivities. **Christina Witt carried out the analyses of the pressure relaxations, evaluated the TRPL curves by fitting the rate equation and analyzed the PL spectra with respect to peak positions, peak ratio and Urbach energy.** Fabian Panzer and **Christina Witt developed the concept of the paper and discussed and interpreted the results. Christina Witt created the design of all figures and tables** (except Figure S8). Fabian Panzer and **Christina Witt wrote the manuscript,** which was revised by all authors.

Orientation and Grain Size in MAPbI$_3$ Thin Films: Influence on Phase Transition, Disorder, and Defects

This work is published in *The Journal of Physical Chemistry C* **2023** *127* (22), 10563-10573.
The authors are:

Christina Witt, Konstantin Schötz, Meike Kuhn, Nico Leupold, Simon Biberger, Philipp Ramming, Frank-Julian Kahle, Anna Köhler, Ralf Moos, Eva M. Herzig, and Fabian Panzer.

Fabian Panzer supervised the project. **Christina Witt pressed the thin film samples,** which were deposited by Nico Leupold and Daniel Lukas vie PAD method under supervision of Ralf Moos by using powder prepared by Irene Bauer and Monika Daubinger. **Christina Witt determined surface roughness and film thickness of films.** Simon Biberger, under supervision of Fabian Panzer and Anna Köhler, recorded SEM images, where **Christina Witt analyzed corresponding grain sizes.** Nico Leupold, under supervision of Ralf Moos, conducted XRD measurements and analyzed them via Rietveld Refinement Method. Meike Kuhn, under supervision of Eva M. Herzig, contributed to the XRD analyses in terms of crystallographic orientation. Frank-Julian Kahle recorded and evaluated XPS spectra. Konstantin Schötz and **Christina Witt measured temperature- and fluence-dependent PL and absorption spectra** under supervision of Fabian Panzer and Anna Köhler. Philipp Ramming, under supervision of Fabian Panzer and Anna Köhler, measured TRPL curves, **assisted by** Konstantin Schötz and **Christina Witt.** Meike Kuhn took microscope images of a film during cooling in a LINKAM stage, **where temperature control was performed by** Frank-Julian Kahle and **Christina Witt. All analyses in the paper (i.e., morphological and optical analyses) were performed by Christina Witt,** except for the evaluation of the XRD measurements via Rietveld Refinement Method. Regarding the optical analyses, Christina Witt was advised by Konstantin Schötz and Fabian Panzer. Fabian Panzer, Konstantin Schötz and **Christina Witt developed the concept of the paper and discussed and interpreted the results. Christina Witt created the design of all figures and tables.** Fabian Panzer, Konstantin Schötz and **Christina Witt wrote the manuscript,** which was revised by all authors.

Understanding Method-Dependent Differences in Urbach Energies in Halide Perovskites

This work exists as draft and is in preparation for submission.
The authors are:

Christina Witt, Konstantin Schötz, Anna Köhler, Fabian Panzer.

Christina Witt initiated and planned the project, and Fabian Panzer supervised the project. Temperature-dependent steady-state PL and absorption spectra of thin films and single crystals were recorded in the course of previous works [C. Witt et al. The Journal of Physical Chemistry C 2023 127 (22), 10563-10573; K. Schötz et al. Journal of Materials Chemistry C 2020 8, 2289-2300; K. Schötz et al. Advanced Optical Materials 2020 8, 2000455] by Konstantin Schötz and Christina Witt. **Christina Witt did all analyses of thin film samples** under supervision of Fabian Panzer and Anna Köhler. Konstantin Schötz did the Urbach analyses of single crystal samples under supervision of Fabian Panzer and Anna Köhler. Konstantin Schötz and **Christina Witt developed the concept of the paper and discussed and interpreted the results by means of literature research. Christina Witt created the design of all figures.** Fabian Panzer and **Christina Witt wrote the manuscript,** which was revised by all authors.

First of Their Kind: Solar Cells with a Dry-Processed Perovskite Absorber Layer via Powder Aerosol Deposition and Hot-Pressing

This work is published in *Solar RRL* **2023**, 20232300261.
The authors are:

Simon Biberger*, Nico Leupold*, **Christina Witt***, Christopher Greve, Paul Markus, Philipp Ramming, Daniel Lukas, Konstantin Schötz, Frank-Julian Kahle, Chenhui Zhu, Georg Papastavrou, Anna Köhler, Eva M. Herzig, Ralf Moos, and Fabian Panzer.

<div align="right">

* Contributed equally

</div>

Fabian Panzer initiated and planned the project. Thin film samples were deposited by Nico Leupold and Daniel Lukas via PAD method under supervision of Ralf Moos by using powders prepared by Irene Bauer and Monika Daubinger. Information about PAD processing including developments were provided by Nico Leupold. **Christina Witt established hot-pressing of thin films deposited by PAD method and performed the hot-pressing of all pressed films for the paper.** Simon Biberger manufactured, measured and analyzed the solar cells (J-V curves, solar cell metrics including light-intensity-dependent measurements) based on a protocol initially introduced and tested by Philipp Ramming (device and mask layout design, processing procedures for electrodes and transporting layers), all under supervision of Fabian Panzer and Anna Köhler. **Christina Witt determined surface roughness and film thickness of films using a profilometer** and Nico Leupold measured film thickness and surface roughness with an LSM. Nico Leupold conducted XRD measurements, Frank-Julian Kahle did XPS measurements and Simon Biberger and Angelika Mergner recorded SEM images. Philipp Ramming measured TRPL curves and Simon Biberger measured absorption spectra under supervision of Fabian Panzer and Anna Köhler. **Christina Witt** and Konstantin Schötz **did the Urbach energy analyses** under supervision of Fabian Panzer. Christopher Greve, under supervision of Eva M. Herzig, analyzed the GIWAXS data, which he measured together with Chenhui Zhu. Paul Markus performed and interpreted conductive AFM measurements under supervision of Georg Papastavrou. Fabian Panzer, Simon Biberger, Nico Leupold and **Christina Witt developed the concept of the paper and** together with Konstantin Schötz and Frank-Julian Kahle **results were discussed and related to literature reports.** Fabian Panzer, Simon Biberger, Nico Leupold, **Christina Witt** and regarding the GIWAXS data Christopher Greve **wrote the manuscript,** which was revised by all authors.

4 Publications

4.1 How Methylammonium Iodide Reactant Size Affects Morphology and Defect Properties of Mechanochemically Synthesized MAPbI$_3$ Powder

Nico Leupold, Philipp Ramming, Irene Bauer, **Christina Witt**, Jennifer Jungklaus, Ralf Moos, Helen Grüninger, and Fabian Panzer.

How Methylammonium Iodide Reactant Size Affects Morphology and Defect Properties of Mechanochemically Synthesized MAPbI₃ Powder

Nico Leupold,[a] Philipp Ramming,[b] Irene Bauer,[b] Christina Witt,[b] Jennifer Jungklaus,[a] Ralf Moos,[a] Helen Grüninger,[c, d] and Fabian Panzer*[b]

Here, we investigate in detail the impact of the size of the methylammonium iodide (MAI) reactants in the mechanochemical powder synthesis of the halide perovskite methylammonium lead iodide (MAPbI₃). Morphology and structural characterizations by scanning electron microscopy and X-ray diffraction reveal that with increasing MAI reactant size, the particle size of the perovskite powder increases, while its defect density decreases, as suggested by nuclear quadrupole resonance spectroscopy and photoluminescence investigations. The reason for this behavior seems to be associated to the sensitive influence of the MAI size on the time durations of MAPbI₃ synthesis and delayed MAPbI₃ crushing stage during ball milling. Thus, our results emphasize the high importance the reactant properties have on the mechanochemical synthesis of halide perovskites and will contribute to enhance the reproducibility and control of the fabrication of halide perovskites in powder form.

Introduction

Halide perovskites with their ABX₃ composition have gained much attention in recent years due to their excellent optoelectronic properties and potential low-cost fabrication. Accordingly, a variety of highly functional optoelectronic devices based on halide perovskites, such as solar cells, light-emitting diodes and detectors for light, X-rays and gamma radiation have been demonstrated.[1]

A key aspect to achieve optimal optoelectronic properties of the perovskite is to ensure a high film quality, which in turn is largely determined by the film fabrication process. To fabricate perovskite films it is possible to process readily synthesized perovskite powders, for example, by powder pressing,[2] powder aerosol deposition,[3] or vapor deposition.[4] Especially in the past few years, these powder-based methods have emerged as a promising alternative to the solvent-based film fabrication methods, where in the latter the reactants (e.g. MAI and PbI₂ for the synthesis of MAPbI₃) are dissolved and then solution-processed to form the final perovskite film.[5] However, even for classic solvent-based processing routes, redissolving readily synthesized perovskite powders and using these solution for further film processing was demonstrated to exhibit advantages compared to the use of conventional precursor solutions where the individual educts are solved.[6,7] For example, thin films prepared from redissolved powder typically exhibit larger grain size, higher crystallinity, higher phase purity, and lower defect density.[8,9] In addition, the long shelf life[7,10] and increased reproducibility[11] make halide perovskites in powder form attractive for industrial processes.

The powders are usually prepared either by precipitation reactions or by mechanochemical synthesis approaches.[4,8] Here, mechanochemical synthesis has emerged as an attractive route for perovskite powder preparation in recent years, as the stoichiometry can be adjusted very precisely, no solvent is required, and the synthesis can easily be scaled up.[12,13] Besides these technologically relevant advantages, it also became clear that the properties of the final mechanochemically synthesized perovskites depend decisively on the precise synthesis conditions, such as humidity,[9,14] and the feed-in ratio of precursors.[15]

In addition, aspects that are not relevant in solution processing can play a crucial role in the mechanochemical synthesis of halide perovskites. For example, the presence of a liquid milling agent during the mechanochemical synthesis was found to allow for the preparation of formamidinium lead iodide (FAPbI₃) in its black perovskite phase with cubic crystal

[a] N. Leupold, J. Jungklaus, Prof. Dr. R. Moos
Department of Functional Materials
University of Bayreuth
Bayreuth 95440 (Germany)
[b] P. Ramming, I. Bauer, C. Witt, Dr. F. Panzer
Soft Matter Optoelectronics
University of Bayreuth
Bayreuth 95440 (Germany)
E-mail: fabian.panzer@uni-bayreuth.de
https://www.ep2-bayreuth.de
[c] Dr. H. Grüninger
Institute for Molecules and Materials
Radboud University
Nijmegen 6525 AJ (The Netherlands)
[d] Dr. H. Grüninger
Northern Bavarian NMR Centre (NBNC) and Inorganic Chemistry
University of Bayreuth
Bayreuth 95440 (Germany)

EurJIC
European Journal of Inorganic Chemistry

Research Article
doi.org/10.1002/ejic.202200736

**Chemistry
Europe**
European Chemical
Societies Publishing

structure, while without milling agent, it was only possible to obtain FAPbI$_3$ in its undesired yellow δ-phase.[9,13] Another aspect that is irrelevant for the solution-based preparation of perovskite films, yet impacts the properties of mechanochemically synthesized perovskite powders is the particle size of the organic and inorganic reactants. While they dissolve in typical precursor solutions, for example, based on DMF or DMSO,[16] the size of the precursor crystals or particles impacts the mechanochemical perovskite synthesis process. As such, the time needed to accomplish a complete mechanochemical synthesis of MAPbI$_3$ decreases with smaller MAI reactant size.[17] While this finding emphasizes the importance of developing a detailed understanding of the influence of MAI reactant size on MAPbI$_3$ powder properties, the exact quantitative influence of MAI reactant size on powder morphology and its optoelectronic properties has not been elucidated yet.

In this work, we investigate in detail how the MAI reactant size affects the morphology, as well as the optical properties of corresponding MAPbI$_3$ powder. For this purpose, we use MAI with three different sizes and mechanochemically synthesize MAPbI$_3$ powder using a planetary ball mill. We characterize the morphology of the synthesized powders by scanning electron microscopy (SEM) and observe structural changes by X-ray diffraction (XRD). Together with nuclear quadrupolar resonance spectroscopy (NQR) and time-resolved photoluminescence (TRPL) measurements, it is possible to correlate the influence of MAI reactant size on the particle size, defect densities and thus the optoelectronic functionality of the mechanochemically synthesized perovskite powders.

Results

For MAI synthesis, crystalline MAI is precipitated by adding diethyl ether to MAI dissolved in ethanol. Here, the temperature as well as the amount and rate of dropping ether to the MAI-ethanol solution determine the nucleation and growth of the crystalline MAI. Adding a small amount (<1 ml) of ether and ensuring slow crystallization by keeping the solution at −18 °C results in crystalline MAI in a rectangular shape with a size ranging from 25 to 1300 μm (mean size 213 μm, hereafter referred to as MAI-large), as extracted from analyses of corresponding SEM images (Figure 1c). Increasing the amount of added ether and increasing the solution temperature to about 0 °C yields rectangular MAI with a reduced size in the range of 5 to 44 μm (mean size 16 μm, hereafter referred to as MAI-medium, see also Figure 1b). To produce MAI with smaller particle size, MAI-medium was ground in a planetary ball mill. From the SEM image in Figure 1a (see Figure S1 for higher magnification), it becomes clear that a MAI powder results that consists of agglomerates of primary particles, with a size between 0.1 and 4.1 μm (mean size of 1.1 μm, hereafter referred to as MAI-small). Thus, with the different synthesis procedures, three MAI powders are available with average MAI sizes covering about two orders of magnitude.

Using these three MAI powders, we prepared MAPbI$_3$ in a planetary ball mill. To ensure comparability of the MAPbI$_3$ powders, the amounts of PbI$_2$ and cyclohexane and the milling parameters were kept the same (see experimental section and Figure S1).
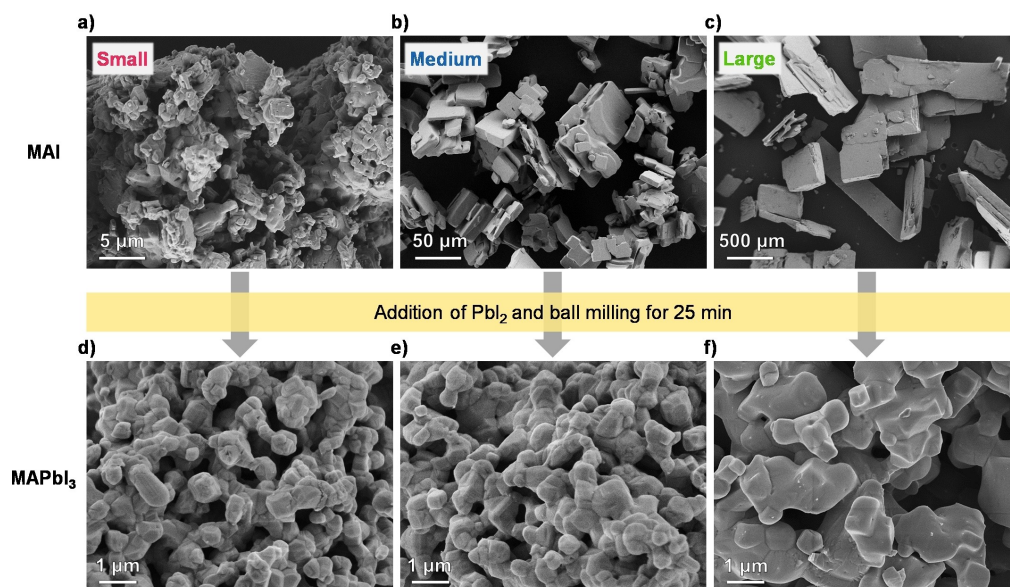

Figure 1. Top row: SEM images of the MAI reactant powders with different particle sizes covering two orders of magnitude, referred to as (a) MAI-small, (b) MAI-medium and (c) MAI-large. Bottom row: SEM images of the mechanochemically synthesized MAPbI$_3$ powders resulting from the different MAI reactants. (d) The resulting MAPbI$_3$ powder using MAI-small, (e) resulting MAPbI$_3$ powder using MAI-medium, and (f) resulting MAPbI$_3$ powder using MAI-large.

EurJIC
European Journal of Inorganic Chemistry

Research Article
doi.org/10.1002/ejic.202200736

Chemistry Europe
European Chemical
Societies Publishing

First, we examined the influence of the three different MAI sizes on the morphology of the resulting $MAPbI_3$ powders by SEM (Figure 1d–f). All three $MAPbI_3$ powders are composed of agglomerates, which in turn are composed of primary particles. The average agglomerate size is in the range of 20–30 μm and does not differ significantly between the samples (compare Figure S2). However, it becomes clear from Figure 1d–f that the particle size increases with increasing MAI reactant size.

For a more detailed analysis, we determined the mean particle sizes and the corresponding particle size distribution from the SEM images of the $MAPbI_3$ powders (Figure 2). Specifically, the $MAPbI_3$ particle sizes range from 0.05 to 0.75 μm for $MAPbI_3$ powder synthesized from MAI-small, from 0.15 to 1.05 μm for MAI-medium, and from 0.35 to 1.55 μm for MAI-large (Figure 2a), respectively. Figure 2b shows the mean $MAPbI_3$ particle size and their standard deviation as a measure

for the dispersion of the particle sizes resulting from the SEM analyses as a function of MAI reactant size. Here, the mean particle size increases from (0.31 ± 0.13) μm using MAI-small to (0.44 ± 0.17) μm using MAI-medium to (0.68 ± 0.24) μm using MAI-large. Accordingly, the observation of an increase in $MAPbI_3$ particle size with increasing MAI reactant size from the SEM images is also confirmed quantitatively.

To verify that the mechanochemical $MAPbI_3$ synthesis is complete for all three different MAI samples, XRD measurements were conducted. The corresponding diffractograms in Figure 3a show the typical reflections of tetragonal $MAPbI_3$ for all powders (see Figure S3 for indexed diffractograms).[18] Also, no reflections that are associated with crystalline PbI_2 reactant (e.g., at $2\Theta = 12.6°$) are found in the diffractograms,[19] suggesting complete synthesis of all three $MAPbI_3$ powders despite the different MAI sizes and morphologies. This is further supported by ^{207}Pb NMR measurements of the three $MAPbI_3$ powders (Figure S4), where alone the signal for $MAPbI_3$ at a chemical shift of about 1430 ppm and no signals corresponding to PbI_2 phase at a chemical shift between 0 and -30 ppm were detected.[20] Furthermore, the NMR intensities of all samples normalized to the largest integrated intensity under consideration of the sample mass are about unity, which strongly suggests the absence of impurity phases.

By considering the width of the reflections in the XRD patterns (Figure 3a), it is possible to gain insights about the influence of MAI reactant size on the $MAPbI_3$ crystallite size and microstrain. To this end, we fitted Pseudo-Voigt functions to the (220)-reflections at $2\Theta = 28.5°$ and extracted the corresponding full-width at half maximum (FWHM) for the $MAPbI_3$ powders produced from different MAI sizes. From this analysis, it becomes clear that the FWHM of the (220)-reflections decreases with increasing MAI reactant size from $0.053°$ using MAI-small, to $0.051°$ using MAI-medium, to $0.045°$ using MAI-large (Figure 3b). A decrease in FWHM typically results from a decrease in microstrain and/or an increase in crystallite size.[21] Both are strongly related to defects like grain boundaries, crystal twinning, the particle surface, orientation misfits, dislocations, and point defects, as defects may disturb the coherently scattering domains (crystallite size) and induce local variations in the lattice spacing (microstrain).[21,22,23] As the extracted FWHM of the powders is close to the instrumental resolution of $(0.0423 \pm 0.0003)°$, we did not extract the microstrain and crystallite size quantitatively, for example, by applying Williamson-Hall analysis, but focus on the FWHM. The decreasing FWHM with increasing MAI reactant size indicates that the resulting $MAPbI_3$ powders exhibit less microstrain and/or larger crystallites and thus a more uniform crystal lattice that is less disturbed by defects.

To confirm this correlation, we performed ^{127}I nuclear quadrupole resonance (NQR) measurements on the three $MAPbI_3$ powders (Figure 3c). The spectra show two peaks for the $3/2 \rightarrow 5/2$ spin transition for each $MAPbI_3$ powder as there are two different positions for the iodide (unequal axial and equatorial I ions) in the tetragonal crystal lattice.[24] Here, the FWHM of the peak at 164.1 MHz in the spectrum shows a decrease from 56.3 kHz (small) to 54.3 kHz (medium) and
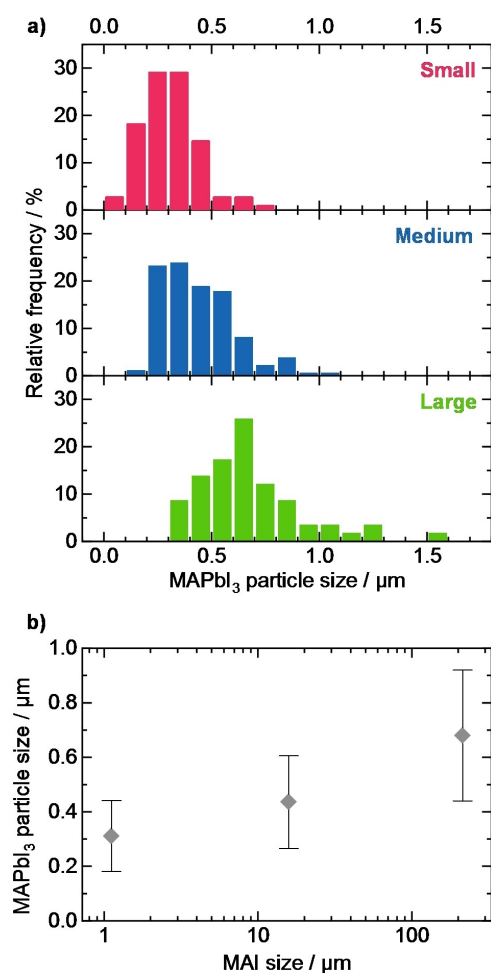

Figure 2. (a) Particle size distribution of the resulting $MAPbI_3$ powders using small, medium, and large MAI as reactant. (b) Mean particle size of the resulting $MAPbI_3$ as a function of the MAI reactant size. The bars indicate the standard deviation as a measure for the dispersion of the particle sizes.

Eur. J. Inorg. Chem. **2023**, e202200736 (3 of 8)

© 2022 The Authors. European Journal of Inorganic Chemistry published by Wiley-VCH GmbH

74

EurJIC
European Journal of Inorganic Chemistry

Research Article
doi.org/10.1002/ejic.202200736

**Chemistry
Europe**
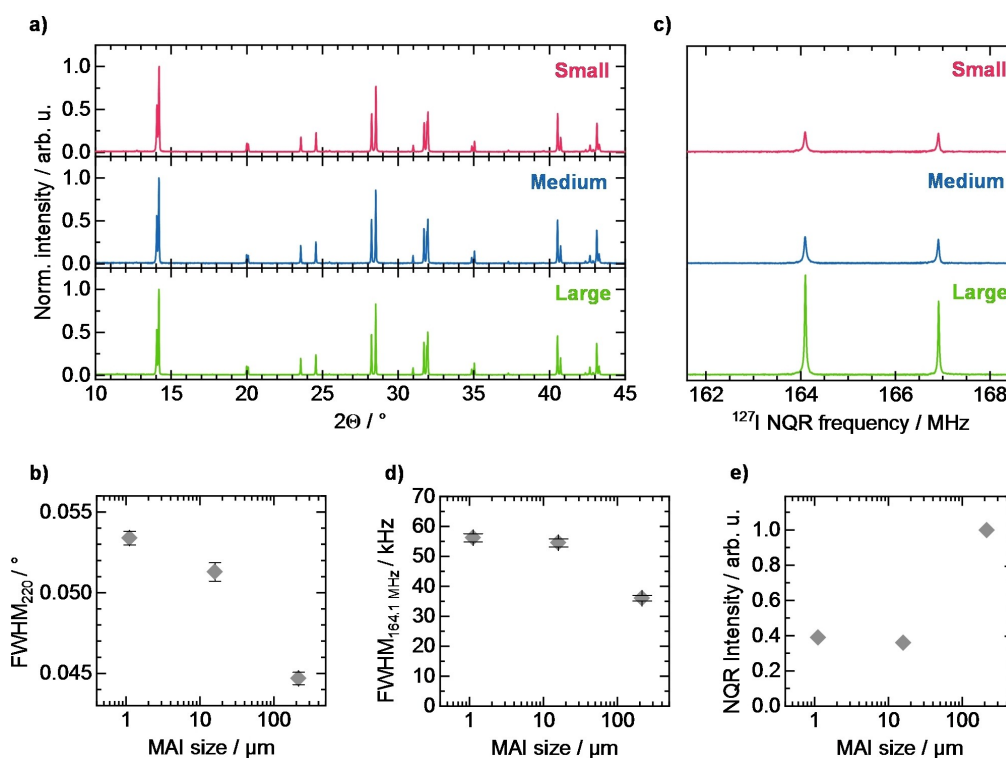European Chemical
Societies Publishing

Figure 3. (a) XRD patterns of MAPbI₃ powders synthesized with different MAI sizes. (b) FWHM of the (220) reflection from XRD measurement as a function of the MAI reactant size. (c) ¹²⁷I NQR measurement of MAPbI₃ powders synthesized with different MAI sizes. (d) FWHM of the Peak at 164.1 MHz and (e) sum of the integrated intensity of both Peaks from the ¹²⁷I NQR measurements as a function of the MAI size. The sum of the integrated intensity was divided by the sample mass to correct for small differences in the sample mass and normalized to the integrated intensity of the MAPbI₃ powder from MAI-large.

36.1 kHz (large) for increasing MAI reactant size (Figure 3d), while the integrated peak intensity under consideration of the respective sample mass increases (Figure 3e). Analogously, also the FWHM of the peak at 166.9 Hz decreases with increasing MAI reactant size (Figure S5).

In general, ¹²⁷I NQR measurements are sensitive to the local structural environments of the iodide in the halide perovskite crystal lattice and are influenced by the chemical composition and by, for example, microstrain and resulting distortions.[25] Consequently, if the ions surrounding the iodide are arranged uniformly (i.e., ordered) in the sample, narrow peaks result.[26] In contrast, defects change the associated iodide environments and induce distortions in the next-neighbor coordination shells, which in the case of MAPbI₃ was found to lead to peak broadening and to a reduction of the integrated signal intensity.[27] Thus, the decrease in FWHM and simultaneous increase in intensity observed in Figure 3 indicates that the iodide environment in the MAPbI₃ powder is less disturbed by defects with increasing MAI reactant size. From the decrease in FWHM of the reflections in XRD and peaks in NQR and from the increase in NQR intensity with increasing MAI reactant size, we conclude that the defect density in the synthesized MAPbI₃ powder decreases with increasing MAI reactant size.

To investigate how the observed differences in defect density in the MAPbI₃ powders affect their optical and excited state properties, we performed time-resolved photoluminescence (TRPL). Figure 4a shows the spectra of the time-integrated PL decay curves of the three perovskite powders. All spectra exhibit the typical PL peak for MAPbI₃ with a maximum at about 770 nm (Figure 4a and Figure S6).[28] In contrast, the PL intensities of the different MAPbI₃ powders deviate from each other, with MAPbI₃ made from MAI-large showing the lowest, from MAI-small showing a medium, and from MAI-medium showing the highest intensity (Figure 4a).

The normalized PL decay curves of the three MAPbI₃ powders exhibit a similar behavior, i.e., dropping to about 10^{-3} of their original PL intensity after a time t of 400 ns after the laser excitation (Figure 4b). In halide perovskites, the PL decay can be described with the rate Equation (1):[29]

$$-\frac{dn}{dt} = k_1 n + k_2 n^2 + k_3 n^3 \tag{1}$$

In this equation, n is the charge carrier density, t denotes the time, k_1 is the rate constant for the nonradiative monomolecular recombination, k_2 the rate constant for radiative
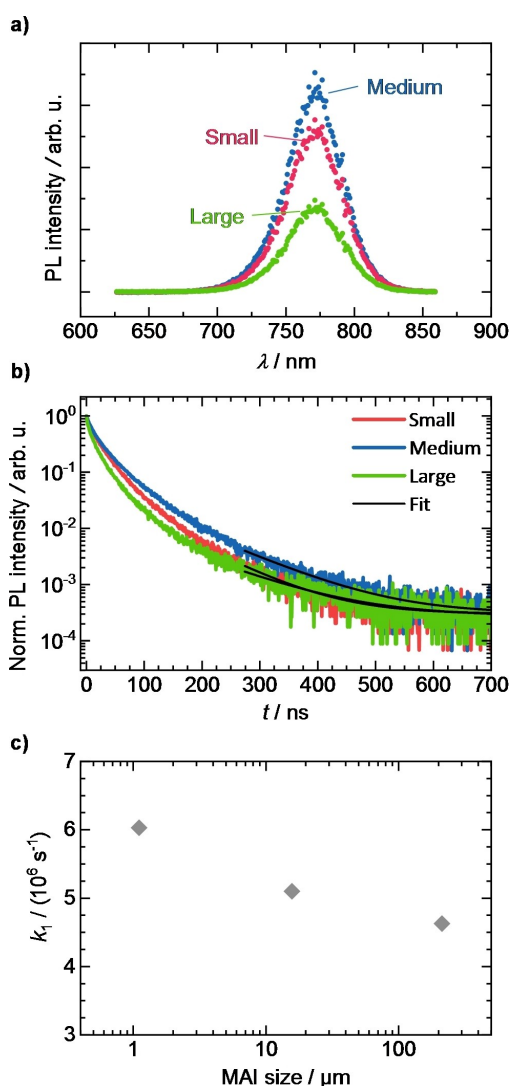
Figure 4. (a) PL spectra of the MAPbI$_3$ powders synthesized with different MAI reactant sizes. (b) Normalized time-resolved PL (TRPL) measurements of MAPbI$_3$ powders synthesized with different MAI reactant sizes together with exponential tail fits (black lines) as described in the text. (c) Rate constants k_1 extracted from the TRPL analyses as a function of MAI reactant size.

band-to-band recombination, and k_3 the rate constant for Auger recombination. At longer times, when the charge carrier density is low, the measured PL decay is thus dominated by the monomolecular recombination of the photoinduced charge carriers.[30] In particular, this nonradiative recombination channel has been associated with the recombination of charge carriers at defects (Shockley-Read-Hall recombination).[31] Hence, quantification of the monomolecular recombination rate k_1 allows to draw conclusions about the defect density within the perovskite. Using the relationship[32] (Eq. (2))

$$PL(t) \sim \exp(-2 \times k_1 \times t) \tag{2}$$

and considering the dark counts of the detector as a baseline, we quantify k_1, by fitting a monoexponential function to the measured PL decay curves for times longer than 275 ns (see solid lines in Figure 4b). From this analysis, we find the recombination rate k_1 of the MAPbI$_3$ powders to decrease from 6.0×10^6 s^{-1} (MAI-small) to 5.1×10^6 s^{-1} (MAI-medium) to 4.6×10^6 s^{-1} (MAI-large) with increasing MAI reactant size (Figure 4c). The decreasing monomolecular recombination rate with increasing MAI reactant size (or particle size of the final MAPbI$_3$ powder respectively), again indicates a decreasing defect density in the larger sized perovskite powder, in agreement with the results from the XRD and NQR analyses.

In general, under constant measurement conditions, a reduction in defect density and thus k_1 in halide perovskites leads to an increase in their measured PL intensity as the PL quantum yield Φ is proportional to[30,32,33] (Eq. (3))

$$\Phi \sim \frac{k_2 n}{k_1 + k_2 n + k_3 n^2} \tag{3}$$

This is consistent with the PL intensity of the MAPbI$_3$ powder made from MAI-small being lower than the intensity of the powder made from MAI-medium (Figure 4a). However, the fact that the perovskite powder made from MAI-large exhibits the lowest PL intensity even though this sample has the lowest k_1 value appears surprising. While a detailed investigation of the origin of this behavior is beyond the scope of this work, we speculate that due to the larger average particle size in the perovskite powder made from MAI-large (compared to the other two powders) a more pronounced charge carrier diffusion after photoexcitation is present. This is consistent with the initial PL decay of the powder large being faster than for the other two powders as is noticeable in Figure 4b. A more pronounced diffusion leads to an overall lower charge carrier density during recombination, which according to equation (3) results in a lower PL intensity. A similar effect was observed for thin films, where the PL intensity of large grains was significantly reduced compared to small grains of the same film.[34]

Discussion

In the following, we first summarize the findings about the mechanism and possible pathways of mechanochemical synthesis of halide perovskites that have been published in the past, before discussing our results in the context of the literature findings.

Manukyan et al. studied the mechanochemical synthesis of MAI and PbI$_2$ to MAPbI$_3$ and concluded that during the mechanochemical synthesis the MAI plastically deforms, creating cracks and pores in the MAI particles. PbI$_2$, on the other hand, is brittle, so it is mainly crushed during synthesis.[35] In addition, the PbI$_2$ is forced into the MAI during synthesis, so

that both MAI and PbI_2 are in close contact, which enables the interdiffusion of MAI and PbI_2. Here, an increased surface area of the PbI_2 reactant (given for lower PbI_2 reactant sizes) enhances and accelerates the interdiffusion. The introduced mechanical energy is also expected to create point defects and dislocations in the reactants.[35,36] The presence of such defects facilitates the interdiffusion of MAI and PbI_2.[36,37] As the Gibbs free energy to form $MAPbI_3$ from MAI and PbI_2 is negative at room temperature, a facilitated reactant interdiffusion also fosters the subsequent perovskite reaction.[38] This is consistent with the Study of Gil-Gonzáles et al. on the mechanochemical synthesis of $MAPbCl_3$, where the authors find a steep increase in the fraction of formed perovskite at the beginning of the synthesis. This slows down at a later stage of the mechanochemical synthesis process, as the diffusion paths become longer and the probability of unreacted PbI_2 encountering MAI decreases.[39]

The sequence of the mechanochemical synthesis was also studied in detail by Palazon et al. using $CsPbBr_3$. Here, three distinct synthesis stages could be identified.[22] In the first stage, which extended over the first 5 minutes, the reactants CsBr and $PbBr_2$ form $CsPbBr_3$, as well as non-stoichiometric intermediate phases. These intermediate phases and remaining reactants completely convert into $CsPbBr_3$ in the second stage. After the complete conversion to perovskite, the $CsPbBr_3$ powder gets crushed in a third stage, which is accompanied by a decrease in crystallite size. This also leads to a general trend of decreasing PL intensity with longer milling times, although the trend is interrupted at some milling times where the PL intensity is larger for the longer milling time than at the time before, indicating a more complex relationship between the PL intensity and the milling time. In a previous work, we also observed a decrease in particle size with increasing milling time after complete mechanochemical synthesis of $MAPbI_3$.[17] Overall, it thus becomes clear that in the mechanochemical synthesis of halide perovskites via ball milling, an initial synthesis stage, in which the perovskite forms, is followed by a stage of crushing the perovskite powder.

The insights from literature can be transferred to our results to understand the influence of MAI reactant size on the properties of the synthesized $MAPbI_3$ powders. The larger the MAI reactant powder, the more energy is required for plastic deformation and the introduction of defects during the synthesis stage. Also, more energy is required to crush the MAI, increasing the general diffusion lengths for perovskite formation. As a consequence, the initial perovskite synthesis stage is longer for increasing MAI reactant size. During the synthesis, from a certain point onwards, the crushing stage of the synthesized $MAPbI_3$ starts, during which the perovskite particle and crystallite size decreases.[17,22] For a constant overall milling time (as it is the case in the present study), a reduction of the duration of the initial perovskite synthesis stage for smaller MAI reactant size goes along with an extension of the crushing stage duration. Prolonged dwelling in the crushing stage results in final perovskite powders that exhibit a reduced particle size (Figure 2b), increased defect density (Figure 3d), and an

increased non-radiative decay rate of excited states (Figure 4c), fully in line with our experimental results.

Conclusion

By detailed characterization of $MAPbI_3$ powders, mechanochemically synthesized from MAI of different sizes, we identified a clear influence of the MAI reactant size on the final $MAPbI_3$ powder properties. In particular, with increasing MAI reactant size, we observed an increase in particle size in the perovskite powder as deduced from SEM images. The increase in particle size is accompanied by a decrease in defect density in the $MAPbI_3$ powder, which was inferred from NQR and TRPL analyses.

Our results thus emphasize the importance for precise control of the organohalide reactant size to ensure a reproducible, well-defined perovskite powder morphology and optoelectronic functionality. The precise properties of perovskite powders are known to directly impact the properties of films that are made from these powders, for example, via pressing, powder aerosol deposition, or suspension deposition.[4] Consequently, our results will contribute to advance the development of efficient perovskite powder-based optoelectronic devices in the future.

Experimental Section

MAI synthesis: 20 mL of methylamine (160 mmol, 33 wt% in ethanol, Sigma Aldrich) were dissolved in 170 mL of ethanol under argon atmosphere. Then, 22.18 mL (168 mmol) of HI (57 wt% in H_2O, Alfa Aesar) were added dropwise under constant stirring within 30 min, while the solution was cooled with an ice bath. After stirring the solution overnight, the solvent was removed by a rotary evaporator and the powder was washed with a diethyl ether-ethanol mixture. In the final step, the powder was again dissolved in 50 ml ethanol and 250 ml diethyl ether were dropped into the concentrated solution of MAI at room temperature to crystallize the final white MAI powder. In this step, the rate of ether addition determines the crystallization rate and thus the MAI size. The ether was added within 1 to 2 min, after which the MAI was separated by filtration and washed with diethyl ether. The process of redissolution and crystallization was repeated before the MAI powder was dried. The resulting powder was called MAI-medium.

To prepare MAI-large, 5 g MAI-medium were dissolved in 25 ml ethanol and a few drops ($<$ 1 ml) of diethyl ether were added. Slow crystallization was first carried out in a refrigerator at 7 °C for 5 h and then in a freezer at −18 °C overnight. Finally, the powder was filtered and dried. To obtain MAI-small, 5.5 g of MAI-medium were milled in the planetary ball mill using the same procedure as for the mechanochemical synthesis.

Mechanochemical synthesis: For the mechanochemical synthesis of $MAPbI_3$, 1.55 g of the respective MAI reactant powders and 4.5 g of PbI_2 (99.99 %, TCI) were added to 80 ml ZrO_2 milling jars together with 5 mL cyclohexane and 25 ZrO_2 milling balls with a diameter of 10 mm. During weighing-in, the relative humidity was about 45 % at a temperature of 21 to 25 °C. A Fritsch "Pulverisette 5/4" planetary ball mill with 400 rpm was used for synthesis. After 5 min of milling, a pause of 20 min was implemented to prevent excessive heating of the milling jar. The process was repeated until a total

milling time of 25 min was achieved. Afterwards, the cyclohexane was evaporated in air and the obtained black $MAPbI_3$ powder was sieved using a mesh size of 63 μm.

Sample Characterization: For morphology studies, SEM images of the perovskite and MAI powders were taken with a Zeiss Leo 1530 scanning electron microscope (FE-SEM with Schottky-field-emission cathode, SE2 detector and In-lens detector) using an accelerating voltage of 3.0 kV. The powders were fixed on a sample holder with conductive graphite pads (Plano) and sputtered with a 1.5 nm thin platinum layer. To calculate the area of the MAI particles, their lengths and widths were determined manually using the SEM images. The MAI size was then recalculated as the equivalent edge length of a square with the same area. For MAI-small 53 particles, for MAI-medium 54 particles, and for MAI-large 39 particles were used to calculate the average size. The particle size of the $MAPbI_3$ powders was determined from SEM images. Here, the particle boundaries were manually retraced before the area of each particle was calculated using imageJ. The particle size was then calculated from the area of the particles as the equivalent diameter of a circle with the same area. The average particle size and the standard deviation as a parameter for dispersion were obtained using 110 particles for the $MAPbI_3$ powder made from MAI-small, 185 for the $MAPbI_3$ powder made from MAI-medium, and 58 for the $MAPbI_3$ powder made from MAI-large.

XRD patterns were acquired under ambient conditions by reflection mode XRD using a Bruker "D8 Discover A25" with Cu-$K_{\alpha 1}$ radiation ($\lambda = 0.15406$ nm) and Ge-$K_{\alpha 1}$ monochromator. The X-ray source was operated with 40 kV and 40 mA. Diffractograms were recorded with a 2θ step size of 0.008° in the 2θ range from 10° to 45°. To determine the instrumental resolution and the measurement error, a standard alumina sample (SRM 1976c, provided by Bruker) was measured 6 times and the FWHM was determined by fitting a Pseudo-Voigt function to the (104)-reflex.

^{127}I NQR spectra (3/2→5/2) were recorded on a 300 MHz Varian V NMRS system with a Varian 3.2 mm T3 HXY probe head placed far away from the magnet. The NQR frequencies were 164.1 and 166.9 MHz (3/2→5/2) at room temperature. As the T_1 relaxation was extremely short (~30 μs) a fast recycle delay was used (0.1 s) with 8192 scans using a Hahn-echo experiment with as short delays as possible. ^{207}Pb MAS NMR spectra were recorded on Varian V NMRS systems operating at a magnetic field strength of 14.1 T using a Varian 3.2 mm T3 HXY probe head at room temperature. The ^{207}Pb MAS NMR spectra were recorded at 5 kHz spinning speed with a recycle delay of 0.5 s. The chemical shift was referenced using lead nitrate for ^{207}Pb (-3494 ppm) as secondary reference.

Time-resolved PL measurements of the perovskite powders were recorded using time-correlated single-photon counting (TCSPC) on a PicoQuant MT200 confocal fluorescence microscope. Excitation was performed using a 560 nm diode laser (PicoQuant LDH-D-TA-560) at a frequency of 1.0 MHz, with a pulse width of 68 ps, and a fluence of about 100 nJ/cm^2. The laser light was focused on the powder sample with an Olympus objective (4x magnification, numerical aperture of 0.1). The emitted light was filtered with a 561 nm long pass filter and detected with a PMA Hybrid PMT 40 photomultiplier tube (PicoQuant). The Signal was processed using a Picoquant TimeHarp 260 Pico TCPSC board. The PL spectra were also acquired with this setup using a Shamrock SR163 spectrograph and a Newton 970 EMCCD camera (Andor).

Conflict of Interest

The authors declare no conflict of interest.

Data Availability Statement

The data that support the findings of this study are available from the corresponding author upon reasonable request.

Keywords: Ball milling · Lead halide perovskites · Methylammonium lead iodide · Optical properties · Semiconductors

[1] a) M. Ahmadi, T. Wu, B. Hu, *Adv. Mater.* **2017**, *29*, 1605242; b) K. Ji, M. Anaya, A. Abfalterer, S. D. Stranks, *Adv. Opt. Mater.* **2021**, 2002128; c) G. Kakavelakis, M. Gedda, A. Panagiotopoulos, E. Kymakis, T. D. Anthopoulos, K. Petridis, *Adv. Sci.* **2020**, *7*, 2002098; d) NREL, "Research Cell Record Efficiency Chart", can be found under https://www.nrel.gov/pv/cell-efficiency.html.
[2] C. Witt, A. Schmid, N. Leupold, M. Schultz, J. Höcker, A. Baumann, R. Moos, F. Panzer, *ACS Appl. Electron. Mater.* **2020**, *2*, 2619.
[3] M. Schubert, D. Hanft, T. Nazarenus, J. Exner, M. Schubert, P. Nieke, P. Glosse, N. Leupold, J. Kita, R. Moos, *Funct. Mater. Lett.* **2019**, *12*, 1930005.
[4] N. Leupold, F. Panzer, *Adv. Funct. Mater.* **2021**, *31*, 2007350.
[5] W. A. Dunlap-Shohl, Y. Zhou, N. P. Padture, D. B. Mitzi, *Chem. Rev.* **2019**, *119*, 3193.
[6] D. Prochowicz, P. Yadav, M. Saliba, M. Saski, S. M. Zakeeruddin, J. Lewiński, M. Grätzel, *ACS Appl. Mater. Interfaces* **2017**, *9*, 28418.
[7] Y. Zhang, Y. Wang, X. Yang, L. Zhao, R. Su, J. Wu, D. Luo, S. Li, P. Chen, M. Yu, Q. Gong, R. Zhu, *Adv. Mater.* **2022**, *34*, e2107420.
[8] W. Feng, J.-F. Liao, X. Chang, J.-X. Zhong, M. Yang, T. Tian, Y. Tan, L. Zhao, C. Zhang, B.-X. Lei, L. Wang, J. Huang, W.-Q. Wu, *Mater. Today* **2021**, *50*, 199.
[9] W. Fan, K. Deng, Y. Shen, Y. Bai, L. Li, *Angew. Chem. Int. Ed.* **2022**, *61*, e202211259.
[10] B. Dou, L. M. Wheeler, J. A. Christians, D. T. Moore, S. P. Harvey, J. J. Berry, F. S. Barnes, S. E. Shaheen, M. F. van Hest, *ACS Energy Lett.* **2018**, *3*, 979.
[11] Y. Zhang, S.-G. Kim, D.-K. Lee, N.-G. Park, *ChemSusChem* **2018**, *11*, 1813.
[12] F. Palazon, Y. El Ajjouri, H. J. Bolink, *Adv. Energy Mater.* **2019**, *48*, 1902499.

EurJIC
European Journal of Inorganic Chemistry

Research Article
doi.org/10.1002/ejic.202200736

Chemistry
Europe
European Chemical
Societies Publishing

[13] Z. Hong, D. Tan, R. A. John, Y. K. E. Tay, Y. K. T. Ho, X. Zhao, T. C. Sum, N. Mathews, F. García, H. S. Soo, *iScience* **2019**, *16*, 312.

[14] a) G. E. Eperon, S. N. Habisreutinger, T. Leijtens, B. J. Bruijnaers, J. J. van Franeker, D. W. deQuilettes, S. Pathak, R. J. Sutton, G. Grancini, D. S. Ginger, R. A. J. Janssen, A. Petrozza, H. J. Snaith, *ACS Nano* **2015**, *9*, 9380; b) D. Tsvetkov, M. Mazurin, I. Ivanov, D. Malyshkin, V. Sereda, A. Zuev, *Chem. Eur. J.* **2020**, *26*, 12549.

[15] P. Fassl, V. Lami, A. Bausch, Z. Wang, M. T. Klug, H. J. Snaith, Y. Vaynzof, *Energy Environ. Sci.* **2018**, *11*, 3380.

[16] a) J. Li, J. Dagar, O. Shargaieva, M. A. Flatken, H. Köbler, M. Fenske, C. Schultz, B. Stegemann, J. Just, D. M. Többens, A. Abate, R. Munir, E. Unger, *Adv. Energy Mater.* **2021**, *11*, 2003460; b) Y. Vaynzof, *Adv. Energy Mater.* **2020**, *10*, 2003073.

[17] N. Leupold, K. Schötz, S. Cacovich, I. Bauer, M. Schultz, M. Daubinger, L. Kaiser, A. Rebai, J. Rousset, A. Köhler, P. Schulz, R. Moos, F. Panzer, *ACS Appl. Mater. Interfaces* **2019**, *11*, 30259.

[18] T. Baikie, Y. Fang, J. M. Kadro, M. Schreyer, F. Wei, S. G. Mhaisalkar, M. Graetzel, T. J. White, *J. Mater. Chem. A* **2013**, *1*, 5628.

[19] T. P. Gujar, T. Unger, A. Schönleber, M. Fried, F. Panzer, S. van Smaalen, A. Köhler, M. Thelakkat, *Phys. Chem. Chem. Phys.* **2018**, *20*, 605.

[20] a) A. M. Askar, G. M. Bernard, B. Wiltshire, K. Shankar, V. K. Michaelis, *J. Phys. Chem. C* **2017**, *121*, 1013; b) A. Senocrate, I. Moudrakovski, G. Y. Kim, T.-Y. Yang, G. Gregori, M. Grätzel, J. Maier, *Angew. Chem. Int. Ed.* **2017**, *56*, 7755.

[21] D. Liu, D. Luo, A. N. Iqbal, K. W. P. Orr, T. A. S. Doherty, Z.-H. Lu, S. D. Stranks, W. Zhang, *Nat. Mater.* **2021**, *20*, 1337.

[22] F. Palazon, Y. El Ajjouri, P. Sebastia-Luna, S. Lauciello, L. Manna, H. J. Bolink, *J. Mater. Chem. C* **2019**, *7*, 11406.

[23] a) S. Jariwala, H. Sun, G. W. Adhyaksa, A. Lof, L. A. Muscarella, B. Ehrler, E. C. Garnett, D. S. Ginger, *Joule* **2019**, *3*, 3048; b) T. W. Jones, A. Osherov, M. Alsari, M. Sponseller, B. C. Duck, Y.-K. Jung, C. Settens, F. Niroui, R. Brenes, C. V. Stan, Y. Li, M. Abdi-Jalebi, N. Tamura, J. E. Macdonald, M. Burghammer, R. H. Friend, V. Bulović, A. Walsh, G. J. Wilson, S. Lilliu, S. D. Stranks, *Energy Environ. Sci.* **2019**, *12*, 596; c) X. Xiao, W. Li, Y. Fang, Y. Liu, Y. Shao, S. Yang, J. Zhao, X. Dai, R. Zia, J. Huang, *Nat. Commun.* **2020**, *11*, 2215.

[24] a) Q. Xu, T. Eguchi, H. Nakayama, N. Nakamura, M. Kishita, *Z. Naturforsch. A* **1991**, *46*, 240; b) A. Senocrate, I. Moudrakovski, J. Maier, *Phys. Chem. Chem. Phys.* **2018**, *20*, 20043.

[25] a) M. Aebli, N. Porenta, N. Aregger, M. V. Kovalenko, *Chem. Mater.* **2021**, *33*, 6965; b) E. M. Mozur, M. A. Hope, J. C. Trowbridge, D. M. Halat, L. L. Daemen, A. E. Maughan, T. R. Prisk, C. P. Grey, J. R. Neilson, *Chem. Mater.* **2020**, *32*, 6266.

[26] T. A. S. Doherty, S. Nagane, D. J. Kubicki, Y.-K. Jung, D. N. Johnstone, A. N. Iqbal, D. Guo, K. Frohna, M. Danaie, E. M. Tennyson, S. Macpherson, A. Abfalterer, M. Anaya, Y.-H. Chiang, P. Crout, F. S. Ruggeri, S. Collins, C. P. Grey, A. Walsh, P. A. Midgley, S. D. Stranks, *Science* **2021**, *374*, 1598.

[27] a) W. M. J. Franssen, S. G. D. van Es, R. Dervişoğlu, G. A. de Wijs, A. P. M. Kentgens, *J. Phys. Chem. Lett.* **2017**, *8*, 61; b) L. Piveteau, V. Morad, M. V. Kovalenko, *J. Am. Chem. Soc.* **2020**, *142*, 19413.

[28] K. Schötz, A. M. Askar, W. Peng, D. Seeberger, T. P. Gujar, M. Thelakkat, A. Köhler, S. Huettner, O. M. Bakr, K. Shankar, F. Panzer, *J. Mater. Chem. C* **2020**, *8*, 2289.

[29] D. W. deQuilettes, K. Frohna, D. Emin, T. Kirchartz, V. Bulovic, D. S. Ginger, S. D. Stranks, *Chem. Rev.* **2019**, *119*, 11007.

[30] S. D. Stranks, V. M. Burlakov, T. Leijtens, J. M. Ball, A. Goriely, H. J. Snaith, *Phys. Rev. Appl.* **2014**, *2*, 34007.

[31] L. M. Herz, *Annu. Rev. Phys. Chem.* **2016**, *67*, 65.

[32] S.-G. Kim, J.-H. Kim, P. Ramming, Y. Zhong, K. Schötz, S. J. Kwon, S. Huettner, F. Panzer, N.-G. Park, *Nat. Commun.* **2021**, *12*, 1554.

[33] M. B. Johnston, L. M. Herz, *Acc. Chem. Res.* **2016**, *49*, 146.

[34] M. Yang, Y. Zeng, Z. Li, D. H. Kim, C.-S. Jiang, J. van de Lagemaat, K. Zhu, *Phys. Chem. Chem. Phys.* **2017**, *19*, 5043.

[35] K. V. Manukyan, A. V. Yeghishyan, D. O. Moskovskikh, J. Kapaldo, A. Mintairov, A. S. Mukasyan, *J. Mater. Sci.* **2016**, *51*, 9123.

[36] X. Liu, Y. Li, L. Zeng, X. Li, N. Chen, S. Bai, H. He, Q. Wang, C. Zhang, *Adv. Mater.* **2022**, e2108327.

[37] E. Aleksanyan, A. Aprahamian, A. S. Mukasyan, V. Harutyunyan, K. V. Manukyan, *J. Mater. Sci.* **2020**, *55*, 8665.

[38] a) I. L. Ivanov, A. S. Steparuk, M. S. Bolyachkina, D. S. Tsvetkov, A. P. Safronov, A. Zuev, *J. Chem. Thermodyn.* **2018**, *116*, 253; b) A. Senocrate, G. Y. Kim, M. Grätzel, J. Maier, *ACS Energy Lett.* **2019**, *4*, 2859.

[39] E. Gil-González, L. A. Pérez-Maqueda, P. E. Sánchez-Jiménez, A. Perejón, *J. Phys. Chem. Lett.* **2021**, *12*, 5540.

RESEARCH ARTICLE

Methylammonium iodide (MAI) of different sizes is used to mechanochemically synthesize MAPbI$_3$ powder by planetary ball milling. Morphology and structural characterization reveal a clear trend of an increasing particle size and decreasing defect density in the perovskite powder with increasing MAI reactant size, which also affects the optoelectronic properties.

MAI size

\+ PbI$_2$

Ball milling
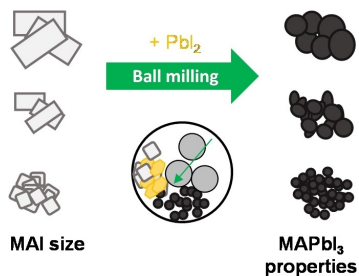
MAPbI$_3$ properties

N. Leupold, P. Ramming, I. Bauer, C. Witt, J. Jungklaus, Prof. Dr. R. Moos, Dr. H. Grüninger, Dr. F. Panzer*

1 – 9

How Methylammonium Iodide Reactant Size Affects Morphology and Defect Properties of Mechanochemically Synthesized MAPbI$_3$ Powder

80

European Journal of Inorganic Chemistry

Supporting Information

How Methylammonium Iodide Reactant Size Affects Morphology and Defect Properties of Mechanochemically Synthesized MAPbI$_3$ Powder

Nico Leupold, Philipp Ramming, Irene Bauer, Christina Witt, Jennifer Jungklaus, Ralf Moos, Helen Grüninger, and Fabian Panzer*
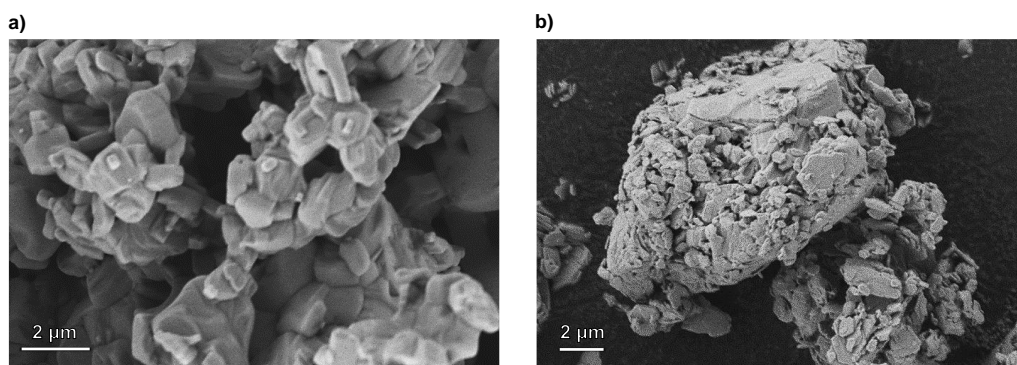
Figure S1: (a) Magnified SEM image of milled MAI-powder (MAI-small) (b) SEM image of the lead iodide powder used for mechanochemical synthesis.
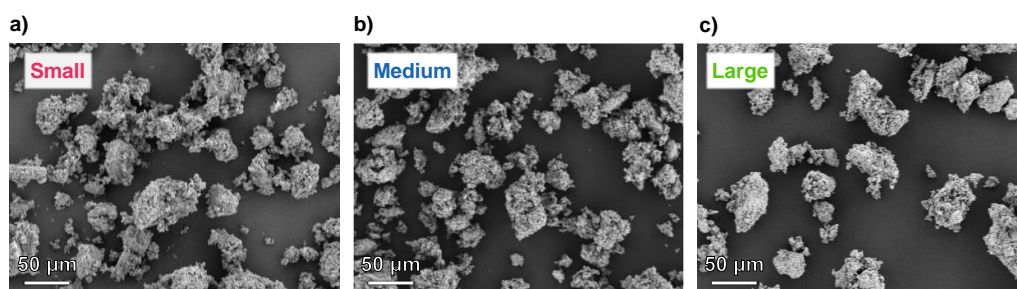
Figure S2: SEM images of MAPbI$_3$ powders resulting from the use of different MAI sizes as reactants in the mechanochemical synthesis: (a) MAI-small, (b) MAI-medium, (c) MAI-large.

S1
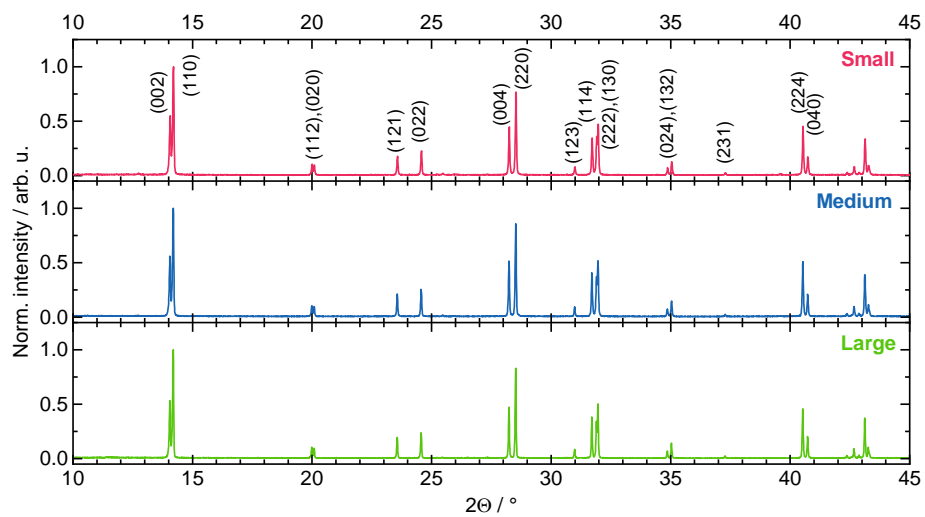
Figure S3: XRD patterns of MAPbI₃ powders synthesized with different MAI sizes. The corresponding lattice planes are indexed according to the tetragonal I4cm space group (PDF #01-083-7582).
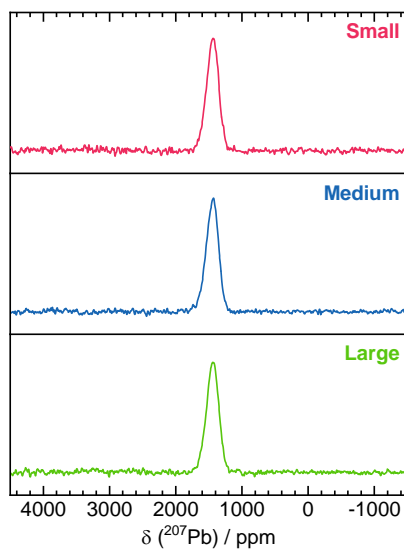
Figure S4: ²⁰⁷Pb MAS NMR spectra of MAPbI₃ powders synthesized with small, medium, and large MAI. The spectra were corrected for slightly different sample masses.

S2
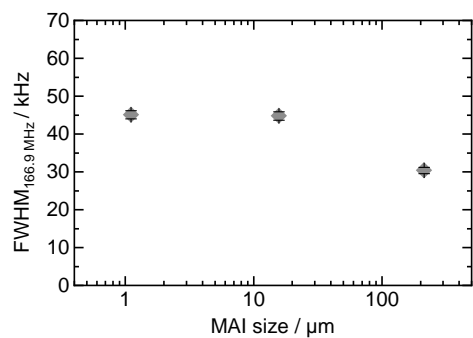
Figure S5: MAI reactant size dependence of the Peak FWHM at 166.9 MHz in the ^{127}I NQR measurement shown in Figure 3c.
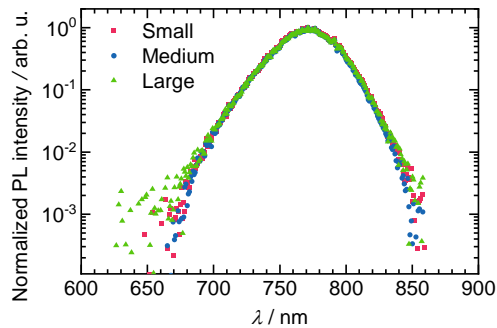
Figure S6: Logarithmic representation of the normalized PL spectra of MAPbI$_3$ powders synthesized with different MAI reactant sizes obtained by integrating the TRPL decay curves.

S3

4.2 Impact of Pressure and Temperature on the Compaction Dynamics and Layer Properties of Powder-Pressed Methylammonium Lead Halide Thick Films

Christina Witt, Andreas Schmid, Nico Leupold, Maximilian Schultz, Julian Höcker, Andreas Baumann, Ralf Moos, and Fabian Panzer.

Article

Impact of Pressure and Temperature on the Compaction Dynamics and Layer Properties of Powder-Pressed Methylammonium Lead Halide Thick Films

Christina Witt, Andreas Schmid, Nico Leupold, Maximilian Schultz, Julian Höcker, Andreas Baumann, Ralf Moos, and Fabian Panzer*

Cite This: *ACS Appl. Electron. Mater.* 2020, 2, 2619−2628

Read Online

ACCESS | Metrics & More | Article Recommendations | Supporting Information

ABSTRACT: While halide perovskite X-ray detectors based on single crystals could achieve extraordinary sensitivities, detectors based on polycrystalline thick films lag behind in efficiency. This is unfortunate since the processing methods for producing polycrystalline thick films, especially by pressure treatment of powders, are suitable for upscaling. Here, we investigate in detail the pressing of readily prepared powders of methylammonium lead halide perovskites $MAPbI_3$ and $MAPbBr_3$ to thick layers. By time-dependent pressure measurements, we monitor the occurring compaction dynamics, identifying two relaxation processes with different timescales. When pressing at elevated temperatures from room temperature (RT) to 100 °C, the pressure relaxations change drastically. While the layer properties such as relative density and surface roughness only improve to a certain degree by increasing the pressure at RT, we observe relative densities >97%, considerable reduction in surface roughness, and a significant increase in grain size with tempered pressing. Analyses regarding time-dependent pressure relaxations of tempered pressing allow attributing the dynamics to a sintering process, where we find the sinter onset to be surprisingly low at about 30 °C, mainly independent of the applied pressure (10−100 MPa). Our results will allow for an improved and more targeted powder processing of halide perovskite thick films as they are promising candidates for efficient X-ray detectors.

KEYWORDS: *halide perovskites, MAPbI₃, sintering, hot pressing, pellets, X-ray detectors*
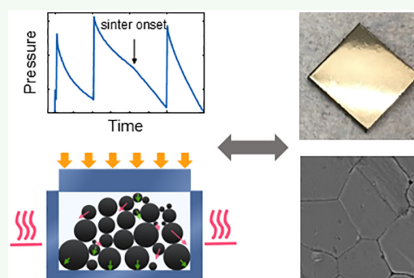
1. INTRODUCTION

The remarkable rise of perovskite solar cells within the last decade has astonished the research community with laboratory device efficiencies now even on par with those of the commercially established silicon-based solar cells.[1] Other perovskite-based optoelectronic devices such as light detectors,[2] lasers,[3,4] or LEDs[5] also showed a fast increase in usage, with efficiencies of perovskite LEDs now even exceeding 21%.[5−7] No less remarkable, however, are the developments of perovskite-based X-ray detectors, which, in the meantime, are close to (cadmium zinc telluride—CdZnTe), or even surpass (amorphous selenium—a-Se) their commercially established competitors in terms of sensitivity on a laboratory scale.[8,9] However, these outstanding sensitivities have so far only been achieved using high-quality perovskite single crystals.[10] Even though studies regarding the upscaling of perovskite single crystals to industrially relevant scales were carried out, this remains a challenging and still unsolved aspect.[11] To ensure full absorption of the impinging X-ray irradiation, perovskite thicknesses in the range of up to several millimeters are required.[8] However, when it comes to the processing of perovskite thick films by methods that are suitable for

upscaling, the established methods for perovskite thin-film processing (solution processing or evaporation) quickly lose their advantages and reach their limits.

Therefore, in the past, other approaches to produce perovskite thick films have been demonstrated, which were then used in X-ray detector devices. For example, Kim et al. showed the fabrication of a viscous $MAPbI_3$ paste, with which 830 μm thick films were produced on a 10 cm × 10 cm flat panel detector module via doctor blade coating, thereby achieving efficient X-ray detectors.[12] Alternatively, studies have shown the fabrication of perovskite thick films using a melting process, where the perovskite in a powder form is heated to melt and then cooled in a controlled manner, resulting in the recrystallization of the perovskite into a layer.[13−16] Regarding ternary halide perovskites, this approach is currently limited to
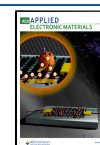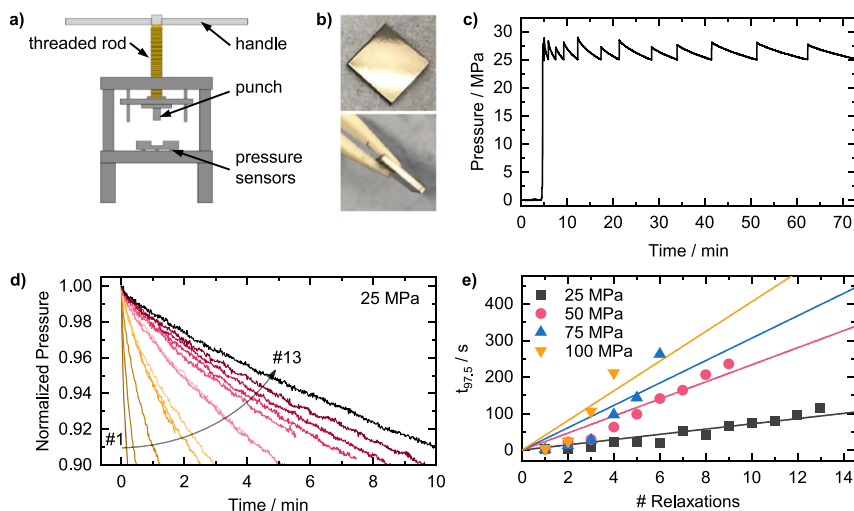
Figure 1. (a) Schematic illustration of the used screw press with individual components as indicated. (b) Image of a pressed 1 cm × 1 cm MAPbI$_3$ pellet, exhibiting a shiny surface. (c) Temporal evolution of the applied pressure, during pressing of MAPbI$_3$ powders at a target pressure of 25 MPa. The pressure was adjusted 13 times manually to keep the target pressure level during the shown time span. (d) Normalized pressure relaxations from (c), with the peak value of the relaxation set as time zero. (e) $t_{97.5}$ time as a function of consecutive pressure relaxations for target pressure levels of 25 MPa (black squares), 50 MPa (red dots), 75 MPa (blue triangles), and 100 MPa (orange triangles) together with linear fits.

cesium lead tribromide (CsPbBr$_3$) as it exhibits a melting temperature slightly below its decomposition temperature. Furthermore, halide perovskite thick films could be achieved by compressing source powder with or without heating into a thick film tablet using a simple press.[17−19] The dry processing of perovskite powders into a layer is a potential cold process that decouples material synthesis and layer formation and, in addition, no solvent has to be used.[20] Furthermore, when pressing MAPbI$_3$ powders to thick films, Shrestha et al. also reported signatures of a pressure-induced sintering process and achieved X-ray sensitivities comparable to the state-of-the art cadmium telluride (CdTe) single crystals.[17] Nevertheless, all the thick-film processing approaches described above result in polycrystalline perovskite films with nonoptimal densification so that there is still potential for their optimization allowing their optoelectronic properties to come closer to their single-crystal counterparts.

Pressure-assisted sintering processes typically occur when pressing powders at elevated temperatures but still well below the melting temperature of the material.[21] In such a case, the material starts to flow, which can lead to improved densification, increase in grain size, and hence an improvement in the optoelectronic layer properties.[22] In this context, an increase in grain size was achieved in the past by tempered pressure treatment of solution-processed perovskite films,[23−30] sometimes accompanied by changes in the optoelectronic material properties, for example, by a reduction of the threshold for amplified spontaneous emission.[31] However, until now, detailed investigations on the pressing process and the associated compression dynamics of halide perovskites are still missing; hence, also the influence of different pressing parameters on the material or layer properties has not yet been identified.

To address this, in this work, we systematically investigate the influence of pressure, temperature, and pressing time on the pressing process as well as on the final layer properties of thick-film pellets made of a perovskite powder. By means of

time-resolved transient pressure measurements during the pressing process, we investigate the different pressure relaxation processes that occur. This allows us to understand the different particle rearrangements and plastic deformation dynamics of the material during pressing and relate them to the process parameters pressure level, temperature, and pressing time.

2. IMPACT OF PRESSURE ON COMPACTION DYNAMICS AND THICK-FILM PROPERTIES

2.1. Results. To produce perovskite pellets investigated in this work, we used mechanochemically synthesized perovskite powders, described in more detail elsewhere.[32] To prepare a pellet, the powder was first weighed and placed in a metal sleeve (base 1 cm × 1 cm) of a homemade mechanical screw press. By turning a threaded rod via a handle, pressure was applied to the powder (see Figure 1a). Four pressure sensors located below the sample recorded the time-dependent pressure. During pressing, either the metal punch was used or two pieces of glass with a thickness of 10 mm were placed directly above and below the powder. After the pressing process, free-standing, compact perovskite layers were obtained, whereby their thickness could be realized in a range of approximately 0.3−2 mm, depending on the weighed powder quantity. When using glass as the press die, the pellets exhibit a shiny surface (Figure 1b). For more information on the exact process of powder and pellet preparation, see Figure S1 in Supporting Information.

Figure 1c shows a typical pressure profile, where a target pressure of about 25 MPa was directly applied. After that, the pressure decreased with time, which made it necessary to readjust it to maintain a certain pressure level over time. The pressure was adjusted 13 times within a pressing time of ∼70 min. From Figure 1c, it also becomes clear that the time lengths of the relaxations change with the number of consecutive pressure regulations. To investigate this change in more detail, we plot the normalized pressure relaxations on a

common time axis where $t = 0$ s corresponds to the initial peak pressure of each pressure relaxation (Figure 1d). It becomes clear that the pressure relaxations become longer with increasing number of pressure adjustments. In the first analysis step, we quantify this behavior by extracting the time $t_{97.5}$, which corresponds to the time it takes for the pressure to drop to 97.5% of its peak value. Here, we choose this value as it still allowed to consider the majority of measured pressure relaxations. Figure 1e shows $t_{97.5}$ as a function of the number of pressure relaxations, for different target pressure levels between 25 and 100 MPa (see Figure S2 for further pressure curves), together with linear fits.

We find that $t_{97.5}$ increases by about 7.2 s per consecutive relaxation for a pressure level of 25 MPa from 2.0 s for the 1st relaxation to 114.0 s for the 13th relaxation. Furthermore, the increase of $t_{97.5}$ becomes steeper for higher target pressures, with an increase in $t_{97.5}$ of ~40.5 s per consecutive relaxation at a target pressure level of 100 MPa (also see Figure S3). However, it also becomes clear that the linear fits in Figure 1e deviate more for the evolution of $t_{97.5}$ values at higher target pressures, which rather increase in a superlinear fashion. An increase in pressure relaxation times with increasing number of pressure adjustments indicates a powder compaction process,[22] which seems to saturate for high pressure levels. In addition to the deceleration of the pressure relaxations, it also can be observed from Figure 1d that the shape of the pressure relaxation changes with the number of pressure adjustments, where the relaxations initially have a more curved shape, appearing less pronounced for higher numbers of relaxations. To characterize the changes in the qualitative shape of the pressure relaxations, we first fitted the relaxations using single exponential decay, where especially the pressure drop in the early time range cannot be well reproduced (see Figure 2a and Figure S4). In contrast, satisfying fits are achieved using biexponential decay of the form

$$P(t) = P_0 + A_1 e^{-t/t_1} + A_2 e^{-t/t_2} \tag{1}$$

where A_1, A_2 are amplitudes and t_1, t_2 are characteristic pressure-decay times (Figure 2a). This indicates that two relaxation processes take place during pressure decrease. Figure 2b shows $A_1/(A_1 + A_2)$, that is, the proportion of A_1 to the total intensity and the decay times t_1 and t_2 as a function of the number of consecutive relaxations. $A_1/(A_1 + A_2)$ decreases for all target pressure levels with the number of relaxations, where the values are in the range of 0.2−0.3 for the first relaxation and, for example, for the 25 MPa measurement series, they drop to <0.05 after the sixth relaxation. While there is no significant influence of the absolute pressure level on the evolution of $A_1/(A_1 + A_2)$, it nonetheless exhibits a certain fluctuation. This may be due to the limited degree of control when adjusting the pressure manually. Interestingly, no shorter pressure relaxation time can be found when the pressing process is regulated toward lower pressures, for example, from 100 to 50 MPa, after the pressure has been kept at a constant level for a certain time (Figure S5).

Both extracted relaxation times t_1 and t_2 increase with the number of relaxations, with t_1 generally exhibiting values one order of magnitude smaller than t_2 (Figure 2b mid and bottom panel). Furthermore, the dependence of relaxation times on the absolute pressure level can be observed. For instance, both t_1 and t_2 at 25 MPa (black squares in Figure 2b) are generally smaller and increase less rapidly than, for example, at 100 MPa
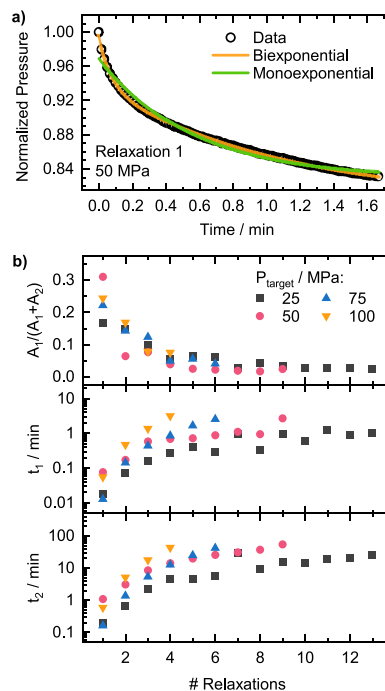
Figure 2. (a) Normalized first pressure relaxation (black circles), with a target pressure of 50 MPa, together with fits using monoexponential (green) and biexponential (orange) decay. (b) Extracted values of $A_1/(A_1 + A_2)$ (top), t_1 (middle), and t_2 (bottom), when fitting the pressure relaxations using biexponential decay as a function of the number of consecutive relaxations for target pressure levels of 25 MPa (black squares), 50 MPa (red dots), 75 MPa (blue triangles), and 100 MPa (orange triangles).

(orange triangles), where at the fourth pressure relaxation, t_1 and t_2 reach values of 3.2 and 43.1 min, respectively.

We also performed pressing of MAPbBr$_3$ powders with a directly applied target pressure of about 25 MPa and analyzed pressure relaxations analogous to Figures 1 and 2 for the MAPbI$_3$ powders (Figure S6). When comparing the evolution of $t_{97.5}$, t_1, and t_2 as well as $A_1/(A_1 + A_2)$ with the number of consecutive pressure relaxations between MAPbI$_3$ and MAPbBr$_3$ powders, we find the same qualitative behavior. However, $t_{97.5}$, t_1 and t_2 of MAPbBr$_3$ in general exhibit values about one order of magnitude lower than MAPbI$_3$.

After controlling the pressure at the respective target pressure level for a certain time, the pressure was removed completely and instantly from the samples. The resulting MAPbI$_3$ thick films pressed at different pressure levels were weighed, and their thickness was quantified using a micrometer caliper. Considering the known base area of 1 cm × 1 cm and taking into account the density of an MAPbI$_3$ single crystal of 4.159 g/cm^3,[33] finally allows calculating the relative density of the pressed layers.

Figure 3a shows the relative density of MAPbI$_3$ thick films as a function of the target pressure level during pressing. To calculate the value at 0 MPa, a known amount of MAPbI$_3$ powder was filled into the mold and the resulting filling level H_0 was determined and compared with the height H_{SC} that one would expect in the case of a single crystal with identical weight and base area. The relative density increases
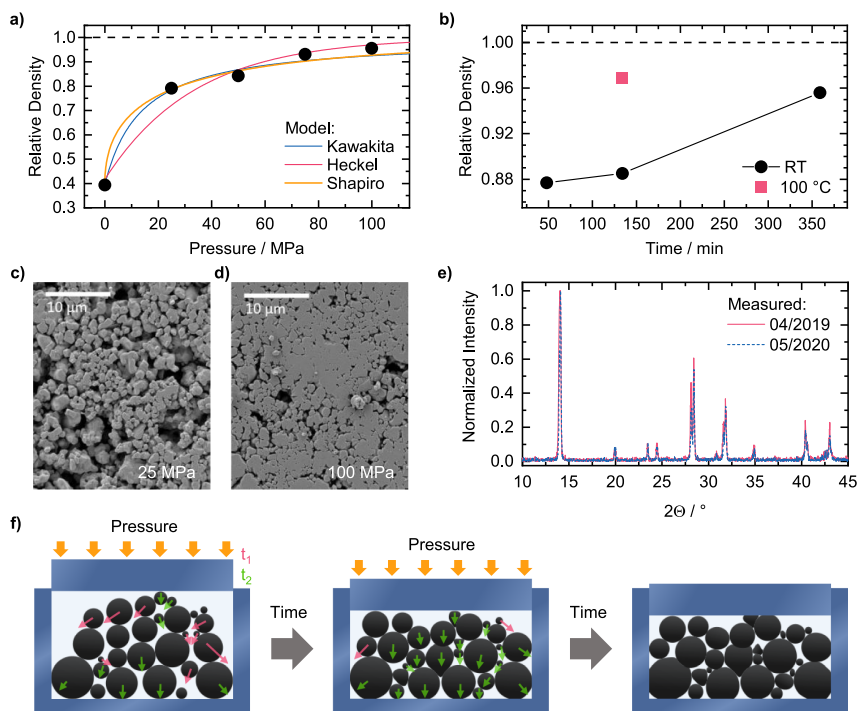
Figure 3. (a) Relative density (black dots) of powder-pressed MAPbI$_3$ pellets as a function of target pressure, together with best fits using different models as indicated. (b) Relative density of powder-pressed MAPbI$_3$ pellets as a function of pressing time at 100 MPa target pressure, for pressing at room temperature (black dots) and at 100 °C (red square). Top view SEM images of the pellets pressed at (c) 25 MPa and (d) 100 MPa. (e) Normalized XRD patterns of an MAPbI$_3$ pellet measured 6 months (red line) and 18 months (blue dashed line) after pressing. (f) Illustration of the powder compaction dynamics during pressing. Dynamics corresponding to the relaxation times t_1 (red arrows) and t_2 (green arrows) are also indicated.

significantly with pressure from 0.4 at 0 MPa to ~0.8 at 25 MPa, reaching a value of 0.95 at 100 MPa after a total pressing time of ~360 min. However, when stopping the pressing process earlier, the relative densities decrease to 0.89 and 0.88 for total pressing times of 134 and 47 min, respectively (Figure 3b).

In the past, various models have been used to analyze the measured pressure dependence on relative density for powder pressing of pellets. Often used is the model developed by Kawakita, where the compressibility $C(P)$ is assumed to follow a saturation function of the form:

$$C(P) = C_{max} \frac{P}{K_m + P} \tag{2}$$

where P is the applied pressure, C_{max} is the maximum compressibility, and K_m is a saturation constant that expresses the compression resistance of the material.[34] As the base area of the pellets is constant, compressibility can be written as $C = 1 - H/H_0$, with H being thickness of the pellet after pressing. Thus, the pressure dependence on the relative density $\rho_{rel} = H_{SC}/H$ is

$$\rho_{rel} = \frac{H_{SC}}{\left(1 - C_{max} \frac{P}{K_m + P}\right) H_0} \tag{3}$$

Fitting eq 3 to the data in Figure 3a yields a reasonable fit with fit parameters $C_{max} = 0.61 \pm 0.02$ and $K_m = 5.4 \pm 1.8$ MPa. While the Kawakita model was derived empirically, the

Heckel model follows from the assumption that compression is a first-order kinetic process between porosity E and pressure P, that is, $\frac{dE}{dP} = -kE$. Thus, the well-known relationship between E and P is given as

$$\ln \frac{1}{E} = kP + B \tag{4}$$

with k corresponding to the relative porosity change per unit pressure step.[34] From it, P_y, the so-called Heckel plasticity parameter, follows via $1/k$.[32] B relates to the initial conditions at zero pressure and is an empirical quantity. Using $E = 1 - \rho_{rel}$, eq 4 can be written as

$$\rho_{rel} = 1 - E = 1 - e^{-(kP + B)} \tag{5}$$

The fit of eq 5 to the relative densities in Figure 3a agrees well in the range ≥ 50 MPa but deviates from the measured data for lower pressures. We find $k = (0.03 \pm 0.01)$ MPa^{-1} (i.e., $P_y = 33.7$ MPa) and $B = 0.54 \pm 0.10$. To be able to describe the measured behavior of ρ_{rel} or E also for low pressure values, eq 4 can be extended by a term $f\sqrt{P}$. It takes into account higher-order kinematic processes (the so-called Shapiro model) so that eq 6 is given as

$$\ln \frac{1}{E} = \ln \frac{1}{E_0} + kP + f\sqrt{P} \tag{6}$$

wherein $E_0 = 1 - H_{SC}/H_0$ is the porosity at zero pressure, and the parameter f is referred to as the Shapiro compression
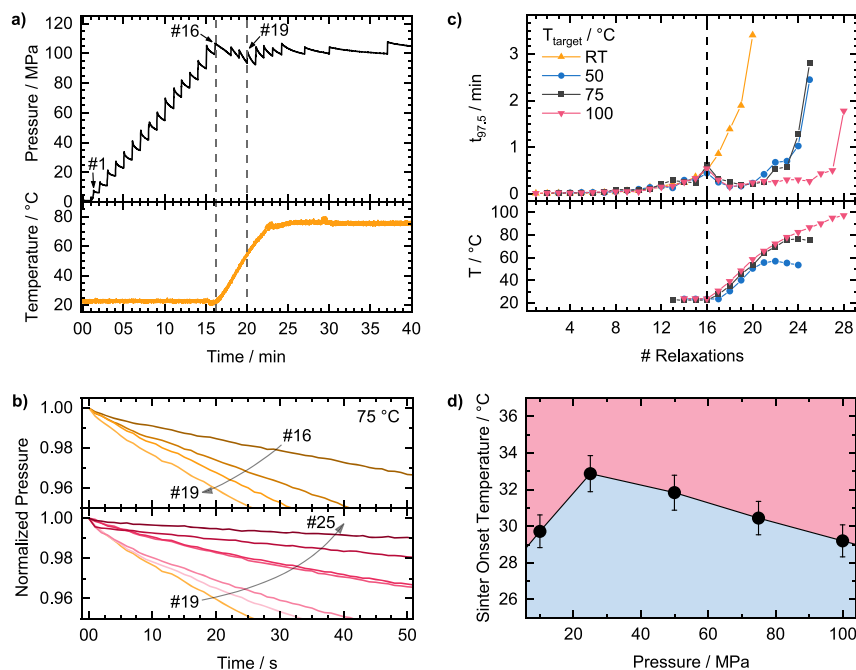
Figure 4. (a) Evolution of the applied pressure, during pressing MAPbI$_3$ powders at a target pressure of 100 MPa (top), together with corresponding temperature evolution (bottom), where heating to ~75 °C started after pressure relaxation 16. (b) Normalized pressure relaxations from (a), with the peak value of the relaxation set as time zero, for relaxations 16 to 19 (top) and for relaxations 19 to 25 (bottom). (c) $t_{97.5}$ time as a function of consecutive pressure relaxations following the pressure evolution from (a) for different target temperatures of room temperature (orange triangles), 50 °C (blue dots), 75 °C (black squares), and 100 °C (red triangles). (d) Sinter onset temperature determined from the pressure relaxations as a function of pressure level, where above T_{Sint} pressure relaxations showed accelerated decay (light red shaded area), while being absent below (blue shaded area).

parameter.[34] Analogous to the Heckel model, the relationship of ρ_{rel} and P is given as

$$\rho_{rel} = 1 - E = 1 - E_0 e^{-(kP + f\sqrt{P})} \tag{7}$$

Using eq 7, the experimentally determined pressure dependence of the relative densities can be fitted satisfyingly in the entire pressure range investigated here (Figure 3a), with values of $(6.53 \pm 0.01)10^{-4}$ MPa^{-1} and (0.21 ± 0.06) MPa$^{-0.5}$ for k and f, respectively.

The increase in relative density with the pressing pressure is also reflected in the morphology of the layers. Figure 3c shows the surface scanning electron microscopy (SEM) image of a pellet pressed at 25 MPa. In contrast to previous measurements, a glass substrate was used as a press die (upper) with a surface roughness of ~3 nm. To minimize the risk of glass breakage at higher target pressures due to very high abrupt pressure increases, the pressure was manually regulated upward following a fixed rate of 6.67 MPa/min (also see Figure S7 for further details).

Figure 3c shows that the surface of the pellets is not compact but that there are clear gaps distributed over the surface. Furthermore, the primary particles and aggregates of the initial powder are clearly visible. They occasionally appear to have a flattened character. In contrast, the surface of a layer formed at 100 MPa looks significantly more compact (Figure 3d), that is, the proportion and size of the gaps is reduced in contrast to that shown in Figure 3c. However, even at 100 MPa, it is not possible to achieve a gap-free surface over a larger area. Furthermore, the primary particles of the powder are still

visible (Figure S8). From X-ray diffraction (XRD) patterns of the pellets, it becomes clear that they only show the characteristic features of MAPbI$_3$ in a tetragonal structure, that is, the pressure processing obviously has no harmful effect on the perovskite (Figure 3e). Furthermore, XRD measurements on the same pellet repeated more than 1.5 years after its production (stored in a nitrogen-filled glovebox) show no change, indicating good temporal stability of the MAPbI$_3$ thick films (Figure 3e), similar to what we could observe in the past for halide perovskites in a powder form.[32]

2.2. Discussion. The processes that generally occur when compressing powders under pressure can be classified into rearrangement of powder particles and their plastic as well as elastic deformation.[32,34,35] Here, one expects that the rearrangement of particles is particularly relevant at low pressures and that plastic deformation becomes more important at higher pressures and the effect of elastic deformation of the material finally dominates at even higher pressures. To identify which processes are relevant during the pressing of MAPbI$_3$ powders, one can take advantage of the fact that the Heckel model only takes into account the plastic deformation of the powder particles, whereas densification due to the rearrangement of the particles are not considered.[34] From the deviations of the fit from eq 5 to the data in Figure 3a, we can thus conclude that in the pressure range < 50 MPa, the rearrangement of the powder particles dominates the compaction process, whereas the plastic deformation process contributes more significantly at pressures ≥50 MPa. This interpretation is also supported by a good fit using the Shapiro

model shown in Figure 3a, which considers higher-order kinetics due to powder rearrangement dynamics.[34] Furthermore, it appears obvious that a high proportion of gaps, as it is the case for the pellets pressed at low pressures (Figure 3c), facilitates particle rearrangement dynamics. In contrast, due to the significantly lower proportion of gaps in the layer produced at 100 MPa, the powder particles can no longer rearrange very easily, but they can rather reduce the applied pressure via plastic deformation. The two identified relaxation processes further support these findings, where we generally associate the shorter time t_1, which dominates pressure relaxation especially directly after the pressure regulation, with the rearrangement dynamics. Correspondingly, the decrease of $A_1/(A_1 + A_2)$ (A_1, A_2 being the amplitudes of the two exponential functions given in eq 1) with the number of pressure regulations means that the proportion of particle rearrangement continuously reduces, and in turn, plastic deformation dynamics, associated with t_2, become more important (illustrated in Figure 3f). This is also consistent with the found decrease in relative density for shorter pressure times (Figure 3b) and the absence of t_1 when decreasing the overall pressure level so that the relaxation processes are fully due to plastic deformation dynamics of the powder particles (Figure S5).

The fact that we observed the same relaxation behaviors also in the case of MAPbBr$_3$ suggests that the identified pressing dynamics are general to halide perovskites. We speculate that the differences in the relaxation time values between MAPbI$_3$ and MAPbBr$_3$ might stem from differences in the powder properties, such as shape and size of the agglomerates, aggregates, and/or primary particles, as well as from possible differences in the initial powder distribution within the press die.

To the best of our knowledge, only Shrestha et al. have so far reported the relative density of halide perovskite pellets to be $\sim$0.9, when pressing MAPbI$_3$ powders at 300 MPa for 5 min.[17] Their data fits well with the value we obtained at 100 MPa for a pressing time of 134 min (Figure 3b).

Regarding the influence of pressing time on the final densification of perovskites, Nejand et al. observed a qualitative decrease of the layer thickness (i.e., an increase of density) with increasing pressing time when hot pressing MAPbI$_3$ thin films produced by spray coating.[36] This fits well with the relationship between relative density and pressing time we observed in Figure 3b and further emphasizes the importance of pressing time regarding the achievable relative densities and final layer properties of powder-pressed perovskites.

3. IMPACT OF TEMPERATURE ON COMPACTION DYNAMICS AND THICK-FILM PROPERTIES

3.1. Results. To be able to heat the sample during pressing, a heating mat is installed surrounding the press mold (see Figure S1). Initially, pressure is applied to the perovskite powder using the same 6.67 MPa/min increase as used above until a certain target pressure (e.g., 100 MPa) is reached. Upon reaching the target pressure for the first time, the heating element is switched on causing the mold and thus the powder to heat up continuously at a rate of $\sim$8.5 °C/min. After reaching the set temperature, the setup is kept at the set temperature for 25 min. During this period, the pressure is manually adjusted to maintain the targeted pressure level (Figure 4a). Afterward, the heating mat is switched off, allowing the mold to cool down so that after removing the

remaining pressure, the perovskite layer can be taken out of the press.

Analogous to the first analysis approach of the pressure relaxations during pressing at RT (Figure 1d), Figure 4b shows the normalized pressure curves starting from relaxation 16, that is, from the first readjustment after reaching a target pressure of 100 MPa. It becomes clear that the pressure relaxations accelerate until relaxation 19 (Figure 4b top panel), while from there onwards, they decelerate (Figure 4b bottom panel).

Within the time range from relaxation 16 to relaxation 19, the sample temperature increases continuously from RT to $\sim$50 °C. Due to the changing influence of temperature over time, the shape of the pressure relaxations also changes, even leading sometimes to concavely curved pressure relaxations (Figure S9). Therefore, an analysis like the one shown in Figure 2, that is, applying exponential decays on the data shown in Figure 4b is not easily possible. To still be able to quantify the changes in the relaxations that occur in the course of the temperature increase, we analyze, analogous to the approach shown in Figure 1e, the time $t_{97.5}$, after which the pressure has dropped to 97.5% of its maximum value. Figure 4c shows $t_{97.5}$ as a function of the number of relaxations at RT and when the sample was heated to 50, 75, and 100 °C, respectively, in each case for a target pressure of 100 MPa. Also shown (bottom panel of Figure 4c) are the temperatures at the end of each relaxation. During the phase of pressure increase, that is, within the first 16 relaxations, $t_{97.5}$ increases similarly for all measurement series reaching a value of $\sim$30 s. In the RT measurement series, $t_{97.5}$ further increases exponentially also for relaxations >16, up to a value of 204 s at relaxation 20. In contrast, the $t_{97.5}$ time starts to decrease to $\sim$10 s at relaxations 18−19, for all measurement series at elevated temperatures, independently of the target temperature. This is not surprising considering the very similar temperature increase within the first 20 relaxations for all tempered processes (Figure 4c bottom panel). Depending on the target temperature, $t_{97.5}$ remains at values in the range of 10 s for several consecutive pressure regulations before rising significantly again for further pressure regulations (Figure 4c top panel). This behavior is particularly pronounced for a target temperature of 100 °C, where a significant increase of $t_{97.5}$ is only observed after relaxation 27.

We performed further hot pressings with different target pressure levels to identify the influence of pressure on the threshold temperature T_{Sint}, at which the pressure relaxations start to show accelerated decay. For each of these pressings, the heating mat was switched on directly after reaching the target pressure for the first time and T_{Sint} was determined by either considering the temperature in the moment the pressure relaxation exhibited a kink or considering the temperature at the beginning of the first pressure relaxation that shows accelerated decay (see Figure S9 for details). Figure 4d shows the resulting values of T_{Sint} as a function of target pressure, where we find an increase from 30 °C at 10 MPa to 33 °C at 20 MPa followed by a continuous decrease of T_{Sint} for increasing pressure values up to <30 °C at 100 MPa.

After having analyzed the influence of temperature on the pressing process, we next investigate the influence of temperature on the final layer properties. Figure 5 shows the top view and the cross-sectional SEM images of the final MAPbI$_3$ thick films, pressed with 100 MPa at RT and at 100 °C.
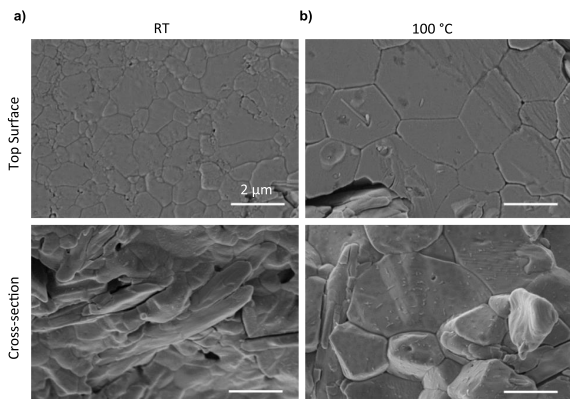
Figure 5. Top view (top) and cross-sectional (bottom) SEM images of powder-pressed MAPbI$_3$ pellets with a target pressure of 100 MPa (a) at RT and (b) at 100 °C. The scale bar for all images is 2 μm.

It becomes clear that the layer pressed at RT exhibits a mean grain size in the range of 0.6 μm and, as already observed in Figure 3c, the primary particles of the source powder (Figure S8) can be recognized. This also applies in a similar way to the morphology in the bulk, as can be seen from the cross-sectional SEM images shown in Figure 5a. In contrast, the grain sizes of the thick film pressed at 100 MPa and 100 °C are significantly larger, both at the surface and in the bulk with an average grain size of 1.9 μm (Figure 5b). It is also noticeable that no primary particles can be observed anymore, and the grain boundaries appear more distinct. However, a pellet pressed at 10 MPa and 100 °C shows a noncompact surface, similar to the morphology shown in Figure 3c (Figure S10). The more compact appearance of the layers pressed at 100 MPa and higher temperatures is also reflected in the surface roughness that decreases from 70 nm at RT to 24 nm at 100 °C (Figure 6a top), and in an increase in relative density, where we could achieve a relative density of >0.97 for 100 °C and 100 MPa target pressure (Figure 6a bottom).

We note that compared to the corresponding value shown in Figure 3c, the lower relative density of 0.86 at RT shown in Figure 6a is caused by the use of the glass die, where, due to its specifications, a gap of ~200−300 μm between the glass and the surrounding mold was present. Powder particles can flow into these gaps, leading to a decreased height of the main pellet and affecting the relaxation dynamics (see Figure S11 for more details on the differences between metal and glass die pressing). In addition, the flow of powder particles into the gaps between the glass and the mold in many cases led to a noticeable ridge formation, which made it more difficult to obtain a complete layer. This effect occurs mainly when pressing at higher temperatures, so in corresponding cases, the layer characterizations were performed on the largest and most trustworthy fragments (see Figure S11 for further details).

The thick films produced at different temperatures were also characterized by XRD. Figure 6b shows the two Bragg reflexes at 14.0°, associated to the (002) plane, and 14.1°, associated to the (110) plane, normalized to the intensity of the (002) reflex for different temperatures during pressing. A clear reduction of the (110)/(002) intensity ratio from 1.35 at RT to 0.25 at 100 °C can be seen (Figure 6b bottom).

3.2. Discussion. Based on the discussion of relaxation dynamics at RT in Section 2.2, we have associated shorter and
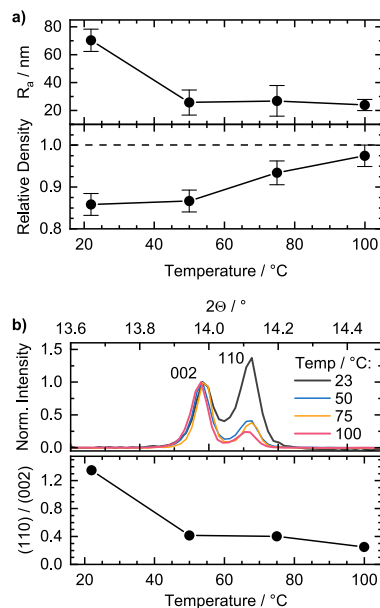
Figure 6. (a) Temperature dependence of the surface roughness R_a (top) and the relative density of the pellets (bottom). (b) XRD pattern of MAPbI$_3$ pellets pressed at 100 MPa with different temperatures between 23 and 100 °C as indicated, normalized to the (002) reflex (top) and the corresponding temperature dependence of the (110)/(002) intensity ratio (bottom).

longer relaxation times with the occurrence of particle rearrangement and plastic deformation dynamics, respectively. Correspondingly, we are associating the accelerated pressure relaxation upon temperature increase shown in Figure 4 to a more pronounced particle rearrangement dynamics, where the higher temperature makes it easier for the powder particles to reduce the applied pressure by filling the remaining pores, so that we assume the occurrence of a sintering process. This is clearly supported by the grain growth and disappearance of the primary particle structures and clearer grain boundaries as observed in Figure 5, which are typical for a sintering process.[21,37]

The effect of grain coalescence and coarsening and the associated disappearance of primary particle structures was also observed by Xiao et al. and Mayer et al., when hot pressing solution-processed MAPbI$_3$ thin films for 5 min at 0.5 MPa and 100 °C,[24] and 10 MPa and 100 °C and 150 °C.[23]

The average grain size of our thick films of 1.9 μm, pressed at 100 MPa at 100 °C (see Figure S10), is higher than the grain sizes reported by Mayer et al. for a thin film pressed at 10 MPa and 150 °C.[23] Furthermore, Hu et al. were able to produce MAPbI$_3$ thick films with grain sizes over 1.9 μm when hot pressing mixed methylammonium iodide (MAI) and lead iodide (PbI$_2$) powders at 10 MPa and 150 °C.[38] These thick films still exhibited clearly visible holes at the grain boundaries and in the grains, which is in good agreement with the porous morphology of our layer pressed at 10 MPa and 100 °C. This underlines the need for a minimum pressure (>10 MPa) to achieve high compaction of perovskite thick films made from powders, which obviously cannot be compensated by increasing the temperature.

With increasing pressing temperature, we could observe a reduction of surface roughness from 70 nm at RT to 24 nm at 100 °C when using a glass die and pressing with 100 MPa (Figure 6a). The value at RT agrees well with the root-mean-square surface roughness of about 75 nm documented by Shrestha et al., which was measured for thick films pressed from MAPbI$_3$ powders at 300 MPa for 5 min using polished stainless steel punches.[17] The reduction of surface roughness with temperature as shown in Figure 6 is in line with the results of Pourdavoud et al., who found a root-mean-square surface roughness of 0.6 nm, only limited by the roughness of the punch, when pressing perovskite thin films with a pressure of 10 MPa for 30 min at 150 °C using a silicon punch.[25]

Due to the grain growth, the reduction of pinholes, and the decrease in surface roughness, occurring during hot pressing, we were able to achieve high powder compaction when pressing at 100 MPa and 100 °C. This also resulted in the formation of clear grain boundaries with good grain boundary interconnection (Figure 5). High-quality grain boundaries were also observed by Mayer et al. when hot pressing thin films at 10 MPa and at a temperature of 150 °C,[23] and Hu et al. also obtained clear grain boundaries when pressing powder thick films at 10 MPa and 150 °C.[38] In contrast, a lower grain boundary quality was observed when perovskite thin films were pressed at 100 °C and 0.5 MPa or 10 MPa.[23,24] Thus, it can be concluded that a sufficiently high combination of pressure and temperature is required to achieve high densification and improved crystallinity with good grain−boundary interconnection.

Our results shown in Figure 4d imply that the start of sintering (sinter onset) already occurs at about 30 °C. Together with the accelerating effect of temperature on the pressing time (Figure 3b) and by choosing a suitable combination of pressure, temperature, and pressing time, our results demonstrate the potential to produce highly densified powder-based perovskite layers efficiently under technologically easily accessible conditions. The low value of the sintering temperature at 10 MPa shown in Figure 4d can be explained by the very low compression of the powder particles (Figure S10), which makes it easier for the powder particles to flow into gaps. At 25 MPa, the powder is considerably better compacted, which makes it more difficult for the powder particles to flow into gaps and the sintering process therefore only starts at about 33 °C.

In passing, we note that we did not observe any changes of the pressure relaxation dynamics in the range of about 60 °C. In this temperature range, it is known that MAPbI$_3$ undergoes a phase transition from tetragonal to a cubic crystal structure,[39] which seems not to have any influence on the particle rearrangement and plastic deformation dynamics.

From the XRD patterns of our hot-pressed MAPbI$_3$ thick films, the temperature dependence of the intensity ratio of the peaks associated with perpendicular crystal planes could be observed (see Figure 6b). This clearly indicates that the sintering process induces a preferential orientation in the thick films and thus recrystallization occurs.[40]

4. CONCLUSIONS

In summary, we investigated in detail the process of pressing perovskite powders to thick films. By time-resolved pressure monitoring during pressing at RT, we could identify two pressure relaxation processes due to plastic deformation and particle rearrangement, the latter becoming especially important for pressing at pressures below 50 MPa. We find these compaction dynamics to occur for MAPbI$_3$ and MAPbBr$_3$, suggesting their general nature. In addition to the high temporal stability of the MAPbI$_3$ pellets (>1.5 years), we could for the first time systematically quantify the impact of pressure, temperature, and pressing time on the relative density of the pressed pellets. We found an increasing relative density with pressing time, which can be significantly accelerated when the pressing happens at elevated temperatures. Using a suitable combination of pressure and temperature of 100 MPa and 100 °C, pellets with a relative density of >97% could be obtained. Furthermore, from time-resolved transient pressure monitoring during pressing at elevated temperatures, we demonstrate that the onset for temperature-induced accelerated particle rearrangement, that is, the sinter process, already starts at temperatures as low as about 30 °C. When pressing at higher temperatures, we observed a decrease of surface roughness and a significant increase of grain size at the pellet surface and also throughout the entire layer thickness, leading to R_a = 24 nm and an average grain size of 1.9 μm for pressing at 100 MPa and 100 °C. Furthermore, XRD analysis suggests a temperature-induced orientation of the MAPbI$_3$ crystal lattice. These improved layer properties have the potential to not only facilitate charge extraction due to the compact and smooth surface morphology but also can lead to improved charge transport properties throughout the bulk. This is an important aspect to further push the X-ray sensitivity of polycrystalline perovskite thick films in a detector configuration towards the sensitivities of single-crystal-based X-ray detectors.

5. EXPERIMENTAL SECTION

5.1. Powder Preparation. For ball milling, MAI and PbI$_2$ for the synthesis of MAPbI$_3$ or MABr and PbBr$_2$ for the synthesis of MAPbBr$_3$ were weighed to the desired stoichiometry and transferred into an 80 mL ZrO$_2$ milling jar containing ZrO$_2$ milling balls with a 10 mm diameter (a ball-to-powder ratio of 10:1). Then, 11 mL of cyclohexane was added as the milling agent. The powders were milled in a Fritsch "Pulverisette 5/4" planetary ball mill at 400 rpm for 5 min and then the milling was paused for 20 min to cool down the jar. The procedure was repeated until the desired milling time was reached.

5.2. Pellet Characterizations. The structural characterization of the perovskite pellets pressed at different temperatures was carried out by reflection mode XRD using a Bruker "D8 Discover A25" with Cu K$_{\alpha1}$ radiation (λ = 0.15406 nm), whereby the K$_{\alpha\text{II}}$-rays were removed by a Ge-K$_{\alpha1}$-monochromator. The device was operated at 40 kV and 40 mA. The diffractograms were recorded in a 2θ range from 10 to 45° with a 2θ step size of 0.016°. Long-term XRD stability tests of the MAPbI$_3$ pellet were carried out using an X-ray diffraction system General Electric XRD 3003 TT using a Cu(Copper)-K$_{\alpha1}$ radiation source with a wavelength λ of 1.5406 Å (V = 40 kV, I = 40 mA). The measurements were made under ambient conditions. The surface roughness of the pellets was determined using a profilometer (Dektak 150, Veeco). The powder and pellet morphology was characterized by SEM using a Zeiss Leo 1530 instrument with an accelerating voltage of 3.0 kV.

■ ASSOCIATED CONTENT

Ⓢ Supporting Information

The Supporting Information is available free of charge at https://pubs.acs.org/doi/10.1021/acsaelm.0c00493.

> Details of the press setup, additional P−t data for pressing at RT, evaluation of exponential fits to pressure relaxations, SEM images of pellets pressed at different compression rates, SEM images of the source powder, details of the determination of the sinter onset

temperature, grain size distribution for pellets pressed at different temperatures, details of differences in the pressing process when using glass dies or metal punches (PDF)

■ AUTHOR INFORMATION

Corresponding Author

Fabian Panzer − *Soft Matter Optoelectronics, University of Bayreuth, Bayreuth 95440, Germany;* ● orcid.org/0000-0002-2191-9011; Email: fabian.panzer@uni-bayreuth.de

Authors

Christina Witt − *Soft Matter Optoelectronics, University of Bayreuth, Bayreuth 95440, Germany*

Andreas Schmid − *Soft Matter Optoelectronics, University of Bayreuth, Bayreuth 95440, Germany*

Nico Leupold − *Department of Functional Materials, University of Bayreuth, Bayreuth 95440, Germany*

Maximilian Schultz − *Soft Matter Optoelectronics, University of Bayreuth, Bayreuth 95440, Germany*

Julian Höcker − *Experimental Physics 6, Julius Maximilian University of Würzburg, D-97074 Würzburg, Germany*

Andreas Baumann − *Bavarian Center for Applied Energy Research (ZAE Bayern), D-97074 Würzburg, Germany*

Ralf Moos − *Department of Functional Materials, University of Bayreuth, Bayreuth 95440, Germany*

Complete contact information is available at:
https://pubs.acs.org/10.1021/acsaelm.0c00493

Notes

The authors declare no competing financial interest.

■ REFERENCES

(1) NREL Solar efficiency chart, accessed 04.05.2020; Available from: http://www.nrel.gov/pv/assets/images/efficiency-chart.png.

(2) Xu, Y.; Lin, Q. Photodetectors based on solution-processable semiconductors: Recent advances and perspectives. *Appl. Phys. Rev.* **2020**, *7*, No. 011315.

(3) Tiguntseva, E.; Koshelev, K.; Furasova, A.; Tonkaev, P.; Mikhailovskii, V.; Ushakova, E. V.; Baranov, D. G.; Shegai, T.; Zakhidov, A. A.; Kivshar, Y.; Makarov, S. V. Room-Temperature Lasing from Mie-Resonant Nonplasmonic Nanoparticles. *ACS Nano* **2020**, DOI: 10.1021/acsnano.0c01468.

(4) Zhu, H.; Fu, Y.; Meng, F.; Wu, X.; Gong, Z.; Ding, Q.; Gustafsson, M. V.; Trinh, M. T.; Jin, S.; Zhu, X. Y. Lead halide perovskite nanowire lasers with low lasing thresholds and high quality factors. *Nat. Mater.* **2015**, *14*, 636−642.

(5) Xu, W.; Hu, Q.; Bai, S.; Bao, C.; Miao, Y.; Yuan, Z.; Borzda, T.; Barker, A. J.; Tyukalova, E.; Hu, Z.; Kawecki, M.; Wang, H.; Yan, Z.; Liu, X.; Shi, X.; Uvdal, K.; Fahlman, M.; Zhang, W.; Duchamp, M.; Liu, J.-M.; Petrozza, A.; Wang, J.; Liu, L.-M.; Huang, W.; Gao, F. Rational molecular passivation for high-performance perovskite light-emitting diodes. *Nat. Photonics* **2019**, *13*, 418−424.

(6) Cao, Y.; Wang, N.; Tian, H.; Guo, J.; Wei, Y.; Chen, H.; Miao, Y.; Zou, W.; Pan, K.; He, Y.; Cao, H.; Ke, Y.; Xu, M.; Wang, Y.; Yang, M.; Du, K.; Fu, Z.; Kong, D.; Dai, D.; Jin, Y.; Li, G.; Li, H.; Peng, Q.; Wang, J.; Huang, W. Perovskite light-emitting diodes based on spontaneously formed submicrometre-scale structures. *Nature* **2018**, *562*, 249−253.

(7) Lin, K.; Xing, J.; Quan, L. N.; de Arquer, F. P. G.; Gong, X.; Lu, J.; Xie, L.; Zhao, W.; Zhang, D.; Yan, C.; Li, W.; Liu, X.; Lu, Y.; Kirman, J.; Sargent, E. H.; Xiong, Q.; Wei, Z. Perovskite light-emitting diodes with external quantum efficiency exceeding 20 per cent. *Nature* **2018**, *562*, 245−248.

(8) Wei, H.; Huang, J. Halide lead perovskites for ionizing radiation detection. *Nat. Commun.* **2019**, *10*, 1066.

(9) Sytnyk, M.; Deumel, S.; Tedde, S. F.; Matt, G. J.; Heiss, W. A perspective on the bright future of metal halide perovskites for X-ray detection. *Appl. Phys. Lett.* **2019**, *115*, 190501.

(10) Gao, L.; Yan, Q. Recent Advances in Lead Halide Perovskites for Radiation Detectors. *Solar RRL* **2020**, *4*, 1900210.

(11) Murali, B.; Kolli, H. K.; Yin, J.; Ketavath, R.; Bakr, O. M.; Mohammed, O. F. Single Crystals: The Next Big Wave of Perovskite Optoelectronics. *ACS Mater. Lett.* **2020**, *2*, 184−214.

(12) Kim, Y. C.; Kim, K. H.; Son, D.-Y.; Jeong, D.-N.; Seo, J.-Y.; Choi, Y. S.; Han, I. T.; Lee, S. Y.; Park, N.-G. Printable organometallic perovskite enables large-area, low-dose X-ray imaging. *Nature* **2017**, *550*, 87−91.

(13) Matt, G. J.; Levchuk, I.; Knüttel, J.; Dallmann, J.; Osvet, A.; Sytnyk, M.; Tang, X.; Elia, J.; Hock, R.; Heiss, W.; Brabec, C. J. Sensitive Direct Converting X-Ray Detectors Utilizing Crystalline CsPbBr$_3$ Perovskite Films Fabricated via Scalable Melt Processing. *Adv. Mater. Interfaces* **2020**, *7*, 1901575.

(14) Li, T.; Zeidell, A. M.; Findik, G.; Dunlap-Shohl, W. A.; Euvrard, J.; Gundogdu, K.; Jurchescu, O. D.; Mitzi, D. B. Phase-Pure Hybrid Layered Lead Iodide Perovskite Films Based on a Two-Step Melt-Processing Approach. *Chem. Mater.* **2019**, *31*, 4267−4274.

(15) Stoumpos, C. C.; Malliakas, C. D.; Peters, J. A.; Liu, Z.; Sebastian, M.; Im, J.; Chasapis, T. C.; Wibowo, A. C.; Chung, D. Y.; Freeman, A. J.; Wessels, B. W.; Kanatzidis, M. G. Crystal Growth of the Perovskite Semiconductor CsPbBr$_3$: A New Material for High-Energy Radiation Detection. *Cryst. Growth Des.* **2013**, *13*, 2722−2727.

(16) Li, T.; Dunlap-Shohl, W. A.; Han, Q.; Mitzi, D. B. Melt Processing of Hybrid Organic−Inorganic Lead Iodide Layered Perovskites. *Chem. Mater.* **2017**, *29*, 6200−6204.

(17) Shrestha, S.; Fischer, R.; Matt, G. J.; Feldner, P.; Michel, T.; Osvet, A.; Levchuk, I.; Merle, B.; Golkar, S.; Chen, H.; Tedde, S. F.; Schmidt, O.; Hock, R.; Rührig, M.; Göken, M.; Heiss, W.; Anton, G.; Brabec, C. J. High-performance direct conversion X-ray detectors based on sintered hybrid lead triiodide perovskite wafers. *Nat. Photonics* **2017**, *11*, 436.

(18) Pan, W.; Yang, B.; Niu, G.; Xue, K.-H.; Du, X.; Yin, L.; Zhang, M.; Wu, H.; Miao, X.-S.; Tang, J. Hot-Pressed CsPbBr$_3$ Quasi-Monocrystalline Film for Sensitive Direct X-ray Detection. *Adv. Mater.* **2019**, *31*, 1904405.

(19) Kiyek, V. M.; Birkhölzer, Y. A.; Smirnov, Y.; Ledinsky, M.; Remes, Z.; Momand, J.; Kooi, B. J.; Koster, G.; Rijnders, G.; Morales-Masis, M. Single-Source, Solvent-Free, Room Temperature Deposition of Black γ-CsSnI$_3$ Films. *Adv. Mater. Interfaces* **2020**, *7*, 2000162.

(20) Panzer, F.; Hanft, D.; Gujar, T.; Kahle, F.-J.; Thelakkat, M.; Köhler, A.; Moos, R. Compact Layers of Hybrid Halide Perovskites Fabricated via the Aerosol Deposition Process—Uncoupling Material Synthesis and Layer Formation. *Materials* **2016**, *9*, 277.

(21) German, R. M., *Sintering Theory and Practice*; Wiley, 1996.

(22) Carter, C. B.; Norton, M. G., Sintering and Grain Growth, in *Ceramic Materials: Science and Engineering*. 2013, Springer New York: New York, NY. p. 439−456.

(23) Mayer, A.; Buchmüller, M.; Wang, S.; Steinberg, C.; Papenheim, M.; Scheer, H.-C.; Pourdavoud, N.; Haeger, T.; Riedl, T. Thermal nanoimprint to improve the morphology of MAPbX$_3$ (MA = methylammonium, X = I or Br). *J. Vac. Sci. Technol. B* **2017**, *35*, No. 06G803.

(24) Xiao, J.; Yang, Y.; Xu, X.; Shi, J.; Zhu, L.; Lv, S.; Wu, H.; Luo, Y.; Li, D.; Meng, Q. Pressure-assisted CH$_3$NH$_3$PbI$_3$ morphology reconstruction to improve the high performance of perovskite solar cells. *J. Mater. Chem. A* **2015**, *3*, 5289−5293.

(25) Pourdavoud, N.; Mayer, A.; Buchmüller, M.; Brinkmann, K.; Häger, T.; Hu, T.; Heiderhoff, R.; Shutsko, I.; Görrn, P.; Chen, Y.; Scheer, H.-C.; Riedl, T. Distributed Feedback Lasers Based on MAPbBr$_3$. *Adv. Mater. Technol.* **2018**, *3*, 1700253.

(26) Chen, H.; Ye, F.; Tang, W.; He, J.; Yin, M.; Wang, Y.; Xie, F.; Bi, E.; Yang, X.; Grätzel, M.; Han, L. A solvent- and vacuum-free route to large-area perovskite films for efficient solar modules. *Nature* **2017**, *550*, 92−95.

(27) Abdollahi Nejand, B.; Gharibzadeh, S.; Ahmadi, V.; Shahverdi, H. R. New Scalable Cold-Roll Pressing for Post-treatment of Perovskite Microstructure in Perovskite Solar Cells. *J. Phys. Chem. C* **2016**, *120*, 2520−2528.

(28) Dunlap-Shohl, W. A.; Li, T.; Mitzi, D. B. Interfacial Effects during Rapid Lamination within MAPbI$_3$ Thin Films and Solar Cells. *ACS Appl. Energy Mater.* **2019**, *2*, 5083−5093.

(29) Dunfield, S. P.; Moore, D. T.; Klein, T. R.; Fabian, D. M.; Christians, J. A.; Dixon, A. G.; Dou, B.; Ardo, S.; Beard, M. C.; Shaheen, S. E.; Berry, J. J.; van Hest, M. F. A. M. Curtailing Perovskite Processing Limitations via Lamination at the Perovskite/Perovskite Interface. *ACS Energy Lett.* **2018**, *3*, 1192−1197.

(30) Matsushima, T.; Fujihara, T.; Qin, C.; Terakawa, S.; Esaki, Y.; Hwang, S.; Sandanayaka, A. S. D.; Potscavage, W. J.; Adachi, C. Morphological control of organic−inorganic perovskite layers by hot isostatic pressing for efficient planar solar cells. *J. Mater. Chem. A* **2015**, *3*, 17780−17787.

(31) Pourdavoud, N.; Haeger, T.; Mayer, A.; Cegielski, P. J.; Giesecke, A. L.; Heiderhoff, R.; Olthof, S.; Zaefferer, S.; Shutsko, I.; Henkel, A.; Becker-Koch, D.; Stein, M.; Cehovski, M.; Charfi, O.; Johannes, H.-H.; Rogalla, D.; Lemme, M. C.; Koch, M.; Vaynzof, Y.; Meerholz, K.; Kowalsky, W.; Scheer, H.-C.; Görrn, P.; Riedl, T. Room-Temperature Stimulated Emission and Lasing in Recrystallized Cesium Lead Bromide Perovskite Thin Films. *Adv. Mater.* **2019**, *31*, 1903717.

(32) Leupold, N.; Schötz, K.; Cacovich, S.; Bauer, I.; Schultz, M.; Daubinger, M.; Kaiser, L.; Rebai, A.; Rousset, J.; Köhler, A.; Schulz, P.; Moos, R.; Panzer, F. High Versatility and Stability of Mechanochemically Synthesized Halide Perovskite Powders for Optoelectronic Devices. *ACS Appl. Mater. Interfaces* **2019**, *11*, 30259−30268.

(33) Stoumpos, C. C.; Malliakas, C. D.; Kanatzidis, M. G. Semiconducting Tin and Lead Iodide Perovskites with Organic Cations: Phase Transitions, High Mobilities, and Near-Infrared Photoluminescent Properties. *Inorg. Chem.* **2013**, *52*, 9019−9038.

(34) Penkavova, V.; Kulaviak, L.; Ruzicka, M. C.; Puncochar, M.; Grof, Z.; Stepanek, F.; Schongut, M.; Zamostny, P. Compression of anisometric granular materials. *Powder Technol.* **2019**, *342*, 887−898.

(35) Oberacker, R., Powder Compaction by Dry Pressing, in *Ceramics Science and Technology*, Riedel, R.; Chen, I. W., Eds.; 2012. pp. 1−37.

(36) Nejand, B. A.; Gharibzadeh, S.; Ahmadi, V.; Shahverdi, H. R. Novel Solvent-free Perovskite Deposition in Fabrication of Normal and Inverted Architectures of Perovskite Solar Cells. *Sci. Rep.* **2016**, *6*, 33649.

(37) Kang, S. J. L., Sintering. In *Ceramics Science and Technology*, Riedel, R.; Chen, I. W., Eds.; 2012. pp 141−169.

(38) Hu, M.; Jia, S.; Liu, Y.; Cui, J.; Zhang, Y.; Su, H.; Cao, S.; Mo, L.; Chu, D.; Zhao, G.; Zhao, K.; Yang, Z.; Liu, S. F. Large and Dense Organic−Inorganic Hybrid Perovskite CH$_3$NH$_3$PbI$_3$ Wafer Fabricated by One-Step Reactive Direct Wafer Production with High X-ray Sensitivity. *ACS Appl. Mater. Interfaces* **2020**, *12*, 16592−16600.

(39) Baikie, T.; Fang, Y.; Kadro, J. M.; Schreyer, M.; Wei, F.; Mhaisalkar, S. G.; Graetzel, M.; White, T. J. Synthesis and crystal chemistry of the hybrid perovskite (CH$_3$NH$_3$)PbI$_3$ for solid-state sensitised solar cell applications. *J. Mater. Chem. A* **2013**, *1*, 5628−5641.

(40) Yang, B.; Xie, Y.; Zeng, P.; Dong, Y.; Ou, Q.; Zhang, S. Tightly Compacted Perovskite Laminates on Flexible Substrates via Hot-Pressing. *Appl. Sci.* **2020**, *10*, 1917.

Supporting Information to

Impact of Pressure and Temperature on the Compaction Dynamics and Layer Properties of Powder Pressed Methylammonium Lead Halide Thick Films

Christina Witt[1], Andreas Schmid[1], Nico Leupold[2], Maximilian Schultz[1], Julian Höcker[3], Andreas Baumann[4], Ralf Moos[2], Fabian Panzer[1*]

[1] Soft Matter Optoelectronics, University of Bayreuth, Bayreuth 95440, Germany.

[2] Department of Functional Materials, University of Bayreuth, Germany

[3] Experimental Physics 6, Julius Maximillian University of Würzburg, Am Hubland, D-97074 Würzburg, Germany

[4] Bavarian Center for Applied Energy Research (ZAE Bayern), Magdalene-Schoch-Str. 3, D-97074 Würzburg, Germany

Corresponding Author:

[*]E-Mail: fabian.panzer@uni-bayreuth.de

96
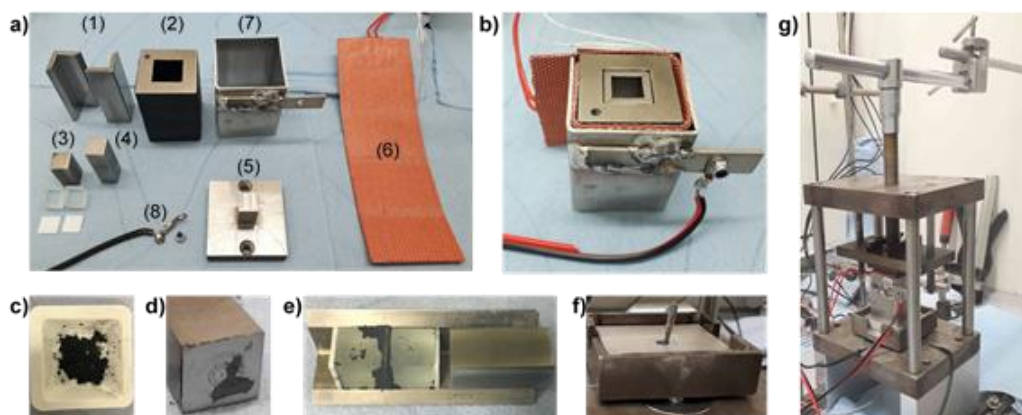
Figure S1: Details on the powder based processing of 1 cm² perovskite pellets: **(a)** Pressing tool consisting of **(1)** two angled moulds (inner length 1 cm), **(2)** a press mould, **(3)** a metal block for pressing with two glass dies using two Teflon plates to compensate pressure differences and reduce tensions, **(4)** a metal block for direct pressing with metal punch and **(5)** a press punch that can be screwed into the press, as well as components of the heating installation consisting of **(6)** a heating mat with a PT 100 temperature sensor and **(7)** a metal frame for fixing the heating mat, including **(8)** electrical ground connection. **(b)** Prepared press tool for hot pressing: The heating mat is placed around the press mould and fixed with a metal frame to which a grounding can be attached so that the temperature data recorded with a type K thermocouple does not contain any disturbances. **(c)** MAPbI₃ powder weighed in a weighing pan. **(d)** Metal punch with a circular pattern on the pressing surface caused by its manufacture. **(e)** Layer extraction of a MAPbI₃ thick film pressed with glass dies. **(f)** Thermocouple type K for temperature measurement can be introduced to the press tool through a hole in the base plate of the press and inserted into holes in the metal blocks. **(g)** Press which is operated manually via a handle.
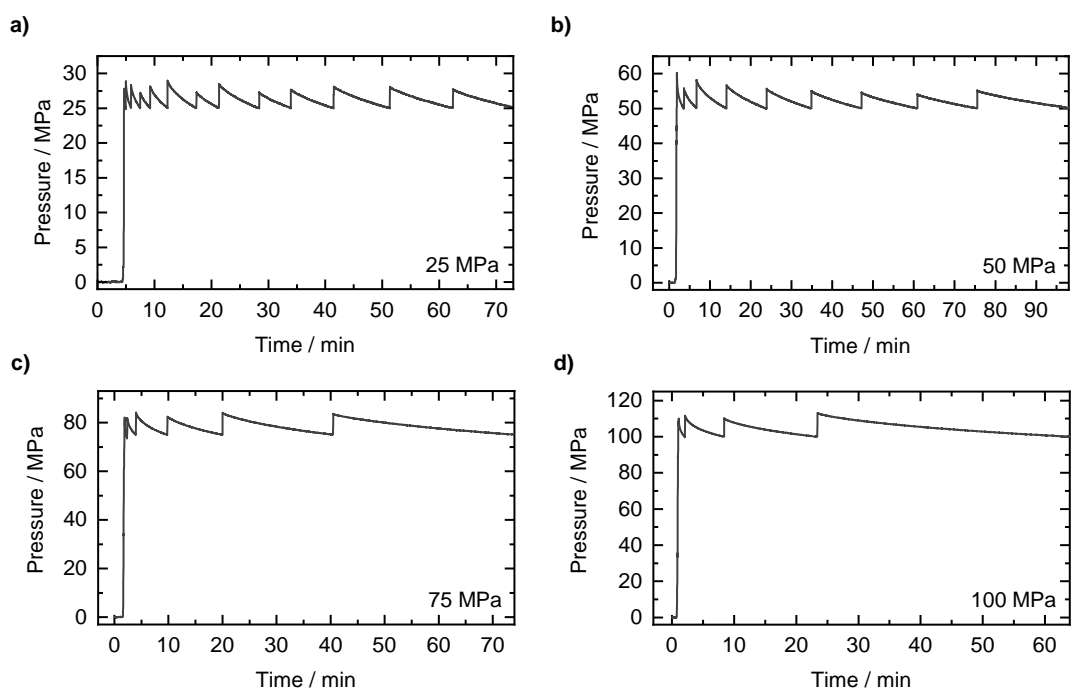
Figure S2: Temporal evolution of the applied pressure during pressing MAPbI₃ powder at a target pressure of (a) 25 MPa, (b) 50 MPa, (c) 75 MPa and (d) 100 MPa.
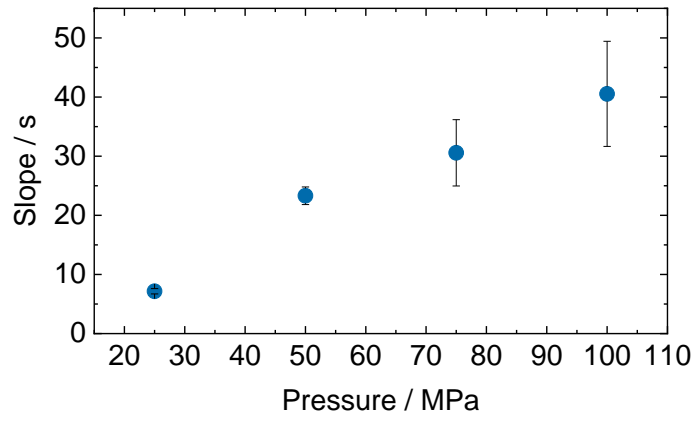
Figure S3: Slope of the linear fits from $t_{97.5}$ times from Figure 1e in the main text, as a function of the number of relaxations for different pressures.

S4
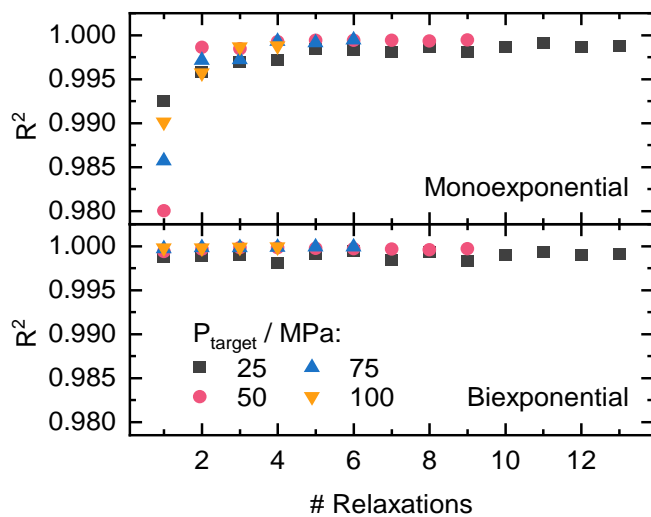
Figure S4: R^2 value of monoexponential (top panel) and biexponential (bottom panel) fits as a function of consecutive pressure relaxations for target pressure levels of 25 MPa (black squares), 50 MPa (red dots), 75 MPa (blue triangles) and 100 MPa (orange triangles).
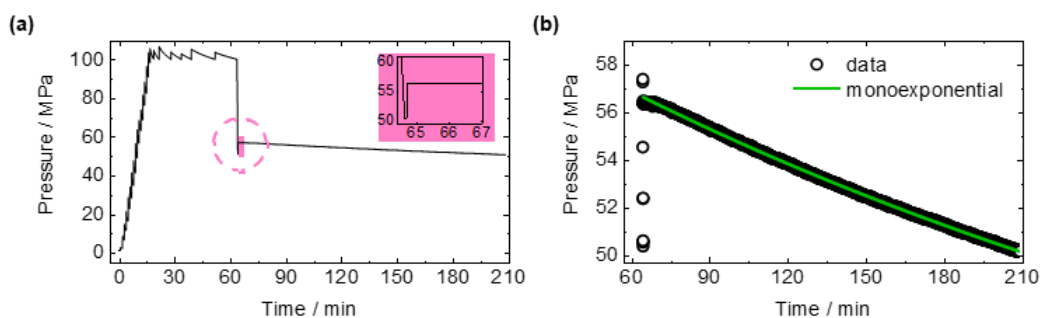
Figure S5: Evolution of the applied pressure during pressing MAPbI₃ powder: (a) After adjusting the pressure at a target pressure of 100 MPa, the pressure was deliberately reduced to 50 MPa. From there, the pressure was regulated again (see inset) (b) Pressure evolution of the pressure regulation at 50 MPa from (a), together with a monoexponential fit.

The pressure was gradually regulated to 100 MPa when pressing a MAPbI₃ thick film and several relaxations were carried out at this high pressure level. Afterwards the pressure was deliberately reduced to a lower level of 50 MPa. From there, another relaxation was induced by an increase of pressure of about 10 % of this lower pressure level (i.e. from ~50 MPa to ~55 MPa) (Figure S5a). The relaxation at the 50 MPa level can be fitted monoexponentially (Figure S5b), with a fit parameter t_2 of (371 ± 1) min and an adjusted R^2 value of 0.99965. This high quality of fit shows that the monoexponential fit describes the relaxation very well and that therefore no shorter pressure relaxation time t_1 occurs at this relaxation.
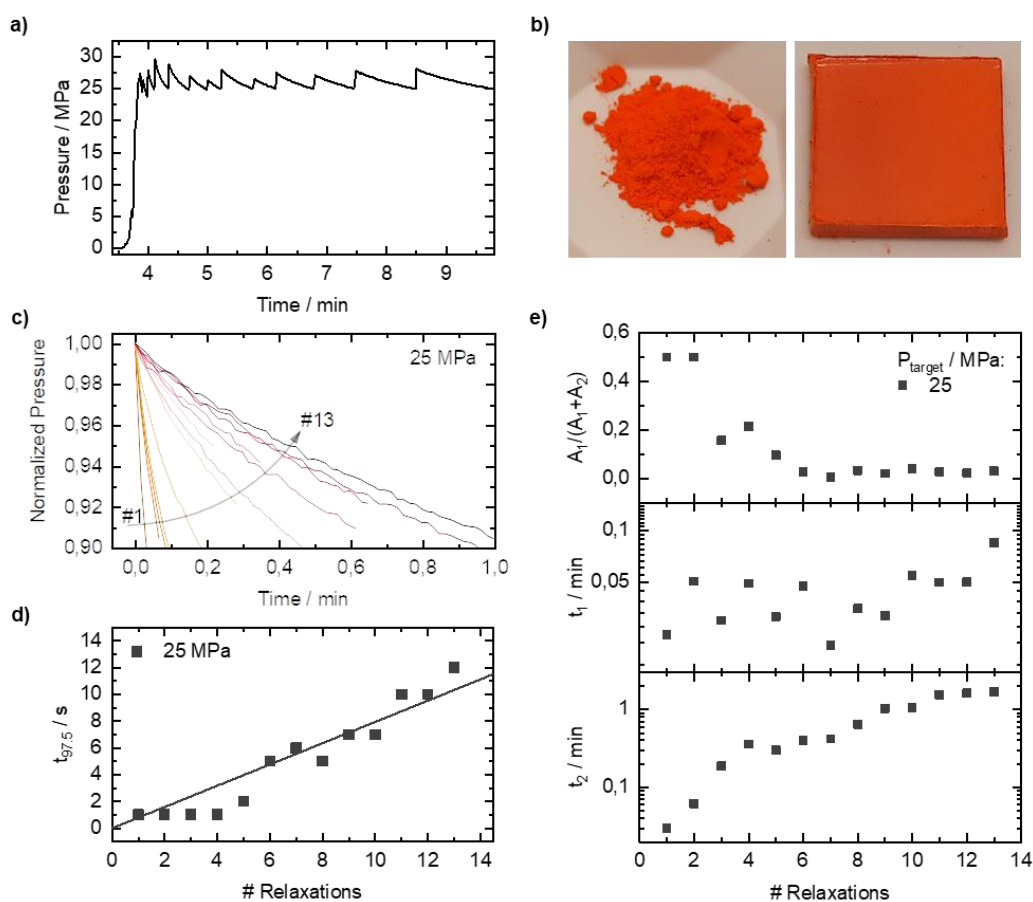
Figure S6: (a) Temporal evolution of the applied pressure, during pressing MAPbBr$_3$ powder at a target pressure of 25 MPa. The pressure was adjusted 13 times manually to keep the target pressure level during the shown time span. **(b)** Image of MAPbBr$_3$ powder and a pressed 1 cm x 1 cm MAPbBr$_3$ pellet. **(c)** Normalized pressure relaxations from (a), with the peak value of a relaxation set as time zero. **(d)** t$_{97.5}$ time as a function of consecutive pressure relaxations for the pressure relaxations from (a) together with a linear fit. **(e)** Extracted values of A$_1$/(A$_1$+A$_2$) (top), t$_1$ (middle) and t$_2$ (bottom), when fitting the pressure relaxations from (a) using a biexponential as given in Equation 1 in the main text as a function of the number of consecutive relaxations.
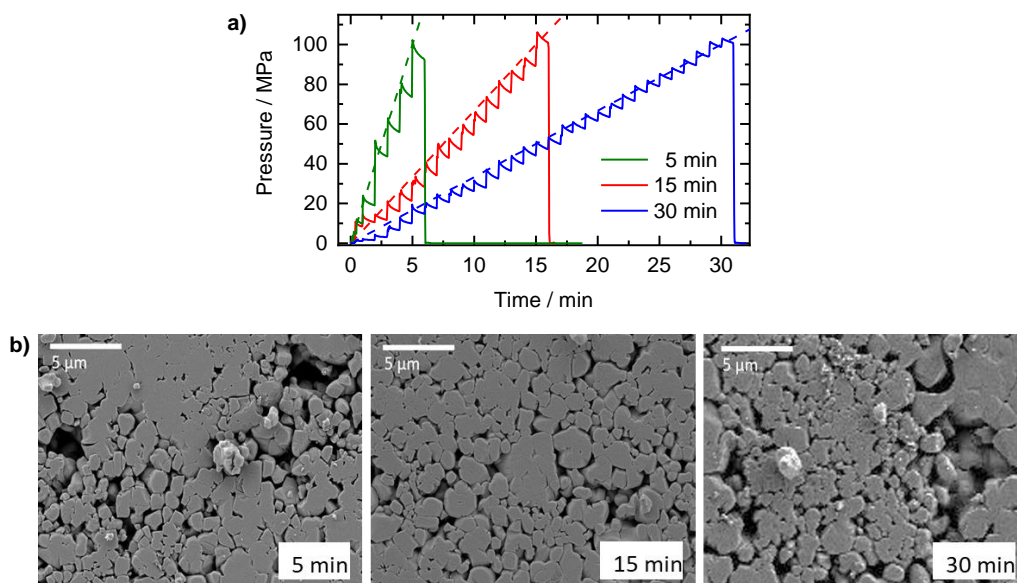
Figure S7: MAPbI$_3$ thick film pressing with three different compression rates using glass dies: (a) Evolution of the applied pressure with stepwise pressure readjustment, showing an increase to 100 MPa in 5 min (green), 15 min (red) and 30 min (blue). (b) Surface SEM images of three pellets, each produced with one of the pressing patterns shown in (a).

Due to strong abrupt pressure increases during the pressing of MAPbI$_3$ pellets, glass breakage as well as pellet breakage can occur. To reduce the risk of these unwanted effects when using glass dies, the pressure is not regulated directly to the specified target value, but is instead increased stepwise, following a linear increase guideline to the target pressure level. MAPbI$_3$ thick films were pressed with three different pressure increase ramps, reaching a pressure of 100 MPa within 5 min, 15 min and 30 min respectively (Figure S7a). That means the pressure regulation to the target level of 100 MPa was performed at three fixed rates of 20.00 MPa/min, 6.67 MPa/min and 3.33 MPa/min. Figure S7b shows surface SEM images of pellets produced with the three different pressure increase ramps. No differences in compaction and particle size can be identified, so that no pressure increase ramp can be preferred. However, to minimize the risk for glass breakage, we use 6.67 MPa/min as the standard pressure increase rate.

S8
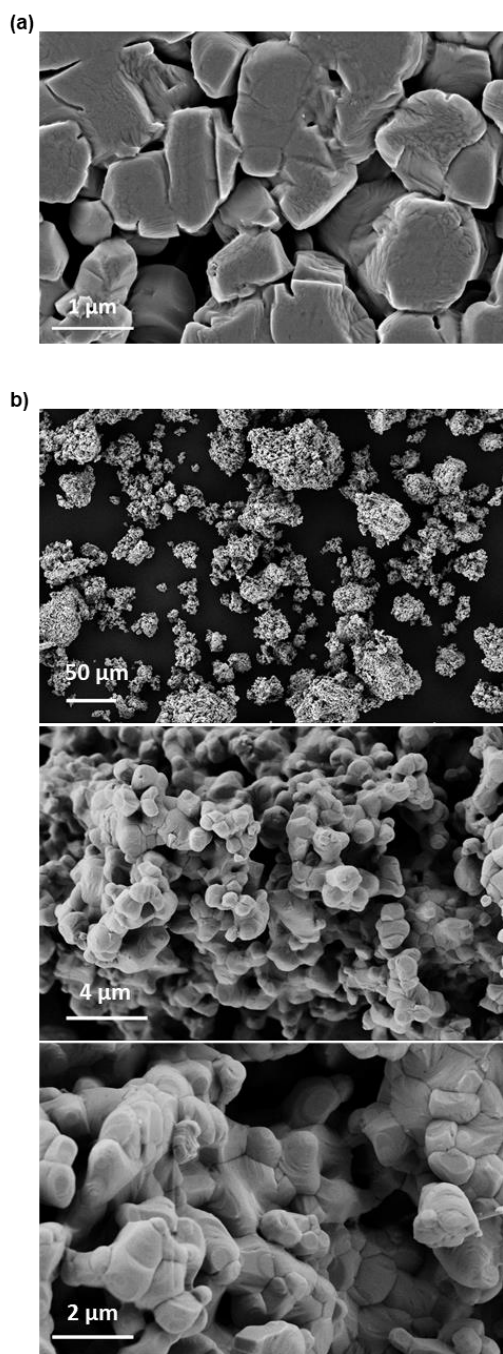
Figure S8: (a) Top view SEM image of a powder pressed MAPbI$_3$ pellet pressed at 100 MPa at RT. **(b)** SEM images of the source MAPbI$_3$ powder at different magnifications as indicated.
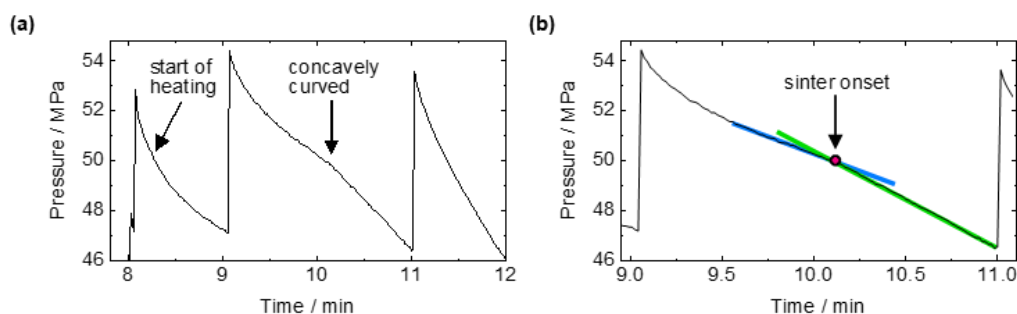
Figure S9: (a) The first full pressure relaxation after the start of heating, showing a concave shape. (b) For concavely curved pressure-relaxations, the time of the start of sintering (sinter onset) is determined by the intersection of two straight lines applied to the relaxation.

Due to the increasing temperature during hot pressing of MAPbI$_3$ thick films, concave curves can occur in pressure relaxations after the start of heating (Figure S9a). These concave curves are caused by an accelerating pressure decrease, which is associated with the beginning of a sintering process. The start of sintering is defined at the transition from the initially flattened pressure drop to the pressure drop with a visibly stronger negative gradient. The point of intersection of two straight lines, which are applied to the pressure relaxation before and after the negative gradient appears, is used to determine the time of the start of sintering and thus the sintering temperature T$_{sint}$ (see Figure S9b).

For pressure relaxations of hot-pressed MAPbI$_3$ thick films without concavely curved shape, the start of sintering is associated with the maximum of the first relaxation which has become faster after the start of heating. Taking into account the offset and the noise in the temperature measurements, an error of 3 % was estimated for the determined sintering temperatures. Several measurements were evaluated at 10 MPa and 100 MPa, from which the average value was calculated.

S10
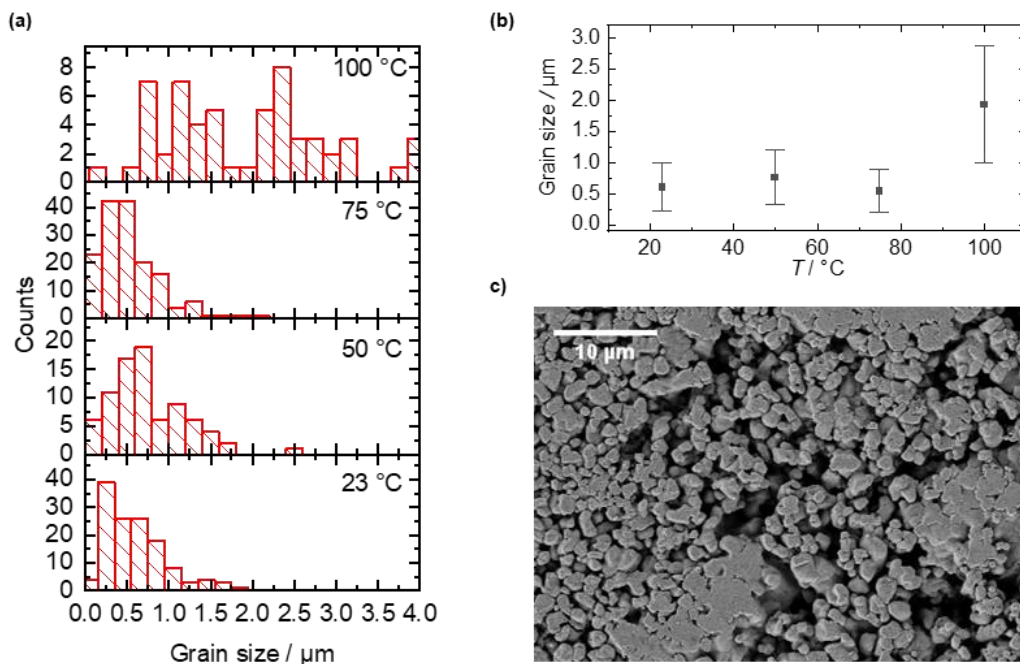
Figure S10: (a) Histogram of the grain size distribution of MAPbI₃ pellets pressed at different temperatures as indicated. (b) Temperature evolution of the average grain size, extracted from (a). (c) Top view SEM image of a powder pressed MAPbI₃ pellet with a target pressure of 10 MPa at 100 °C.

Figure S11a,b show the time-dependent pressure curves of MAPbI$_3$ thick films pressed at RT with metal and glass dies. Both measurements were carried out following the same pressing procedure and pressure increase ramp up to a target pressure level of 100 MPa, at which several relaxations were carried out. The relaxation time t_2 extracted from biexponential fits according to Equation 1 to the individual relaxations in Figure S11a, b, is plotted in Figure S11c as a function of the number of relaxations. After reaching the target pressure with relaxation 16, t_2 increases rapidly when using metal punch. In contrast, t_2 remains small at first after reaching the target pressure level and becomes significantly longer only at later relaxations when using a glass die. Figure S11d shows $t_{97.5}$ of the relaxations from Figure S11a, b, as a function of the number of relaxations. After reaching the target pressure level with relaxation 16, $t_{97.5}$ quickly increases for the pressing with metal stamps. A different behavior is shown for the measurement with glass dies, where $t_{97.5}$ remains small even after several relaxations at the target pressure level. Here, a slight increase of $t_{97.5}$ can only be seen for the last few relaxations. The described differences in the relaxation dynamics of MAPbI$_3$ thick films pressed with metal punches or glass dies can be explained by their geometry. Since the glass die could only be manufactured with a lower accuracy than the metal punches, there are gaps between the glass dies and the press mould into which powder can flow. When pressing with a metal punch, on the other hand, the gaps are very small, so that considerably less powder can get into the sides between the punch and the mould. As the number of relaxations increases, the powder becomes more compacted so that there are less gaps for powder particles or powder agglomerates to flow into and the relaxation times increase. When pressing with glass dies, the powder moves into the gaps between the die and the mould, thus compressing more slowly and the relaxation times do not increase as quickly as when pressing with metal punches.

When pressing with metal punches and glass dies, there are also differences in the layer properties. Due to the slower compaction of the powder when pressing with a glass die, corresponding layers tend to have a lower density. However, this difference can be

compensated by a sufficiently long pressing time compared to pressing with metal punches. Thick layers pressed with metal punches have a rough and rather matt surface due to their production method (inset in Figure S11a). In contrast, thick layers with a smooth and shiny surface can be produced when pressing with glass punches (inset in Figure S11b). This is due to the significantly lower surface roughness of the glass stamps compared to the metal stamps used.

Figure S11e, f show the temporal pressure curves of $MAPbI_3$ thick films hot-pressed with metal and glass stamps. Both measurements were carried out according to the same pressing procedure with a pressure increase ramp to a target pressure level of 100 MPa, as well as a temperature increase from room temperature to 100 °C. At the target pressure level, several relaxations were performed. To analyze the pressure relaxations, $t_{97.5}$ was evaluated and plotted as a function of the number of relaxations, together with the corresponding temperature T_{Peak}, which is the measured temperature in the moment of the maximum pressure value of a relaxation (Figure S11g). Due to the increasing compaction of the powder with the number of relaxations, $t_{97.5}$ increases initially. However, after the start of heating, $t_{97.5}$ decreases due to the start of a sintering process in which powder particles and powder agglomerates further densify, until there are hardly any flow possibilities for powder particles left, so that $t_{97.5}$ increases again.

In the measurements with metal punches, the increase of $t_{97.5}$ due to the sintering process starts earlier and more clearly than in the measurements with glass dies, because during pressing with metal dies there are hardly any gaps between the press die and the press mould into which powder could move. In contrast, for the measurements with glass stamps, an increase of $t_{97.5}$ only occurs at a higher number of relaxations, since the powder can flow more strongly into the mould due to the larger gaps between glass stamp and mould.
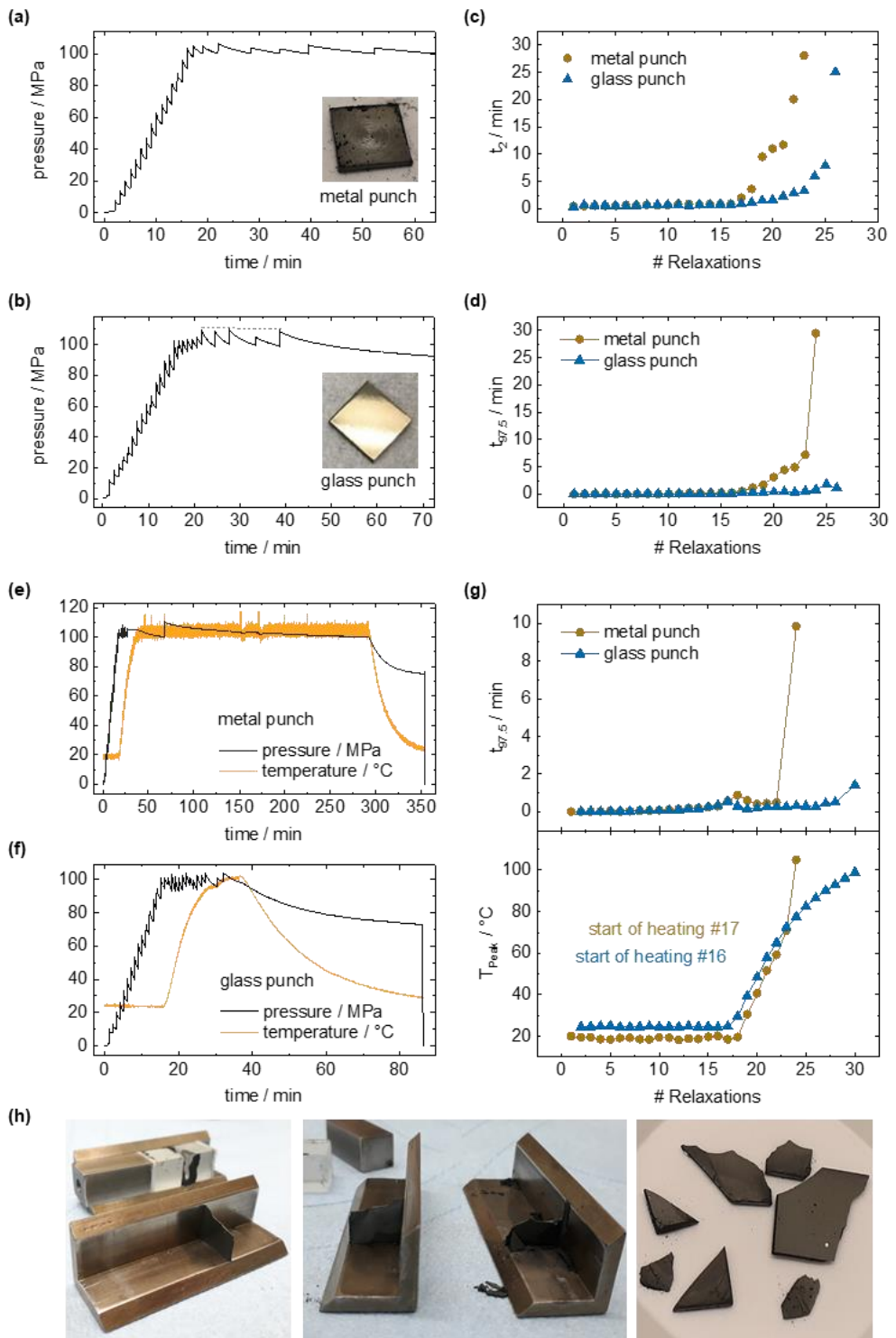
Figure S11: Pressing of halide perovskite thick films with 100 MPa at RT: (a), (b) Temporal pressure profile with pressure increase ramp to a target pressure level of 100 MPa for pressing with (a) metal punch and (b) glass die. The insets show exemplary pellets. (c) t_2 extracted from biexponential fits according to Equation 1 in the main text to the pressure relaxations of (a) and (b). (d) Evolution of $t_{97.5}$ for the measurements with metal die (a) and glass die (b). (e-g): Hot pressing of MAPbI$_3$ thick films at 100 MPa and 100 °C: Temporal pressure and temperature evolution with rise ramps to a target level of 100 MPa and 100 °C respectively, for pressing with (e) metal and (f) glass die. (g) Evolution of $t_{97.5}$ for the measurements shown in (e) and (f), together with the corresponding temperature T_{Peak} extracted at the maximum pressure value of the relaxations. (h) Extraction of a MAPbI$_3$ thick film pressed with 50 MPa at RT using a glass die: Web formation in both angled moulds (left and middle) and fragments of the incompletely removed thick film (right).

4.3 How the Microstructure of MAPbI$_3$ Powder Impacts Pressure-Induced Compaction and Optoelectronic Thick-Film Properties

Christina Witt, Nico Leupold, Philipp Ramming, Konstantin Schötz, Ralf Moos, and Fabian Panzer.

Article

How the Microstructure of MAPbI₃ Powder Impacts Pressure-Induced Compaction and Optoelectronic Thick-Film Properties

Christina Witt, Nico Leupold, Philipp Ramming, Konstantin Schötz, Ralf Moos, and Fabian Panzer*

Read Online

ACCESS | 📊 Metrics & More | 📰 Article Recommendations | ⓢ Supporting Information

ABSTRACT: Within the last few years, applying pressure to improve and alter the structural and optoelectronic properties of halide perovskite thin films and powder-based thick-film pellets has emerged as a promising processing method. However, a detailed understanding of the relationship between perovskite microstructure, pressing process, and final film properties is still missing. Here, we investigate the impact of powder microstructure on the compaction processes during pressure treatment and on the final properties of powder-pressed thick films, using the model halide perovskite methylammonium lead iodide (MAPbI₃). Analyzing pressure relaxations together with XRD and SEM characterizations, we find that larger powder particles result in less compact thick films with higher surface roughness. Furthermore, larger particles exhibit stronger sintered connections between individual powder particles, resulting in less crushing and particle rearrangement but in more pronounced plastic deformation during pressure treatment. Moreover, plastic deformation of the powder particles leads to a reduction of crystallite size in the final film. This reduction results in increased nonradiative, defect-associated excited state recombination, as confirmed by photoluminescence investigations. More plastic deformation also deteriorates the grain boundary quality and consequently facilitates ion migration, which is reflected in higher electrical dark conductivities of the thick films. Thus, our work elucidates how important the design of the perovskite powder microstructure is for the pressure-induced compaction behavior and for the resulting structural, optical, and electrical thick-film properties. These insights will pave the way for tailored pressure processing of halide perovskite films with improved optoelectronic properties.
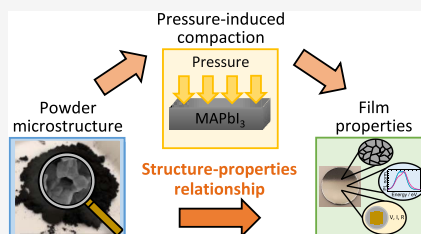
1. INTRODUCTION

In recent years, the application of halide perovskite thin films in solar cells with amazingly fast increasing power conversion efficiencies has attracted much attention in the field of optoelectronics.[1] Moreover, other halide perovskite-based applications such as LEDs[2] as well as photo- and X-ray detectors were also demonstrated.[3−5] In the case of perovskite X-ray detectors, especially single-crystal-based devices showed remarkably high sensitivities.[4,5] However, as the integration of perovskite single crystals in industry-relevant length scales and geometries remains challenging, perovskite powder-based thick films represent an attractive alternative for a versatile realization of perovskite X-ray detectors.[6−12]

The perovskite powders for such thick films can be produced, e.g., by mechanochemical approaches, thermal annealing, or by solution-based precipitation reactions.[13] By applying pressure, the perovskite powders are then either pressed directly on a (functional) substrate or in a suitable press mold to form a free-standing pellet wafer. However, compared to their single-crystalline counterparts, polycrystalline powder thick films exhibit deteriorated optoelectronic performance and higher dark currents, still limiting their overall device sensitivity.[4,9,13]

Improvements in powder pellet properties and the associated optoelectronic performance have so far been achieved in particular by the following two strategies: On the one hand, additives to passivate perovskite defects were used. The additives were either added directly in the powder synthesis[14] or during the powder pressing step.[9] On the other hand, using an optimized elevated temperature during pressing was found to increase perovskite crystallinity and pellet compactness due to sintering effects.[15−18]

Nevertheless, due to its technological simplicity, decreased setup wear, and thus its potential for lower costs, room temperature pressing of powders is still considered a promising processing approach for manufacturing perovskite thick films. From the field of ceramics, it is known that in room temperature powder pellet pressing, not only the pressing parameters but also the precise microstructure of the powders play a decisive role determining the final pellet properties.[19] Thus, for processing optimized halide perovskite powder pellets, it is crucial to understand the impact of the powder
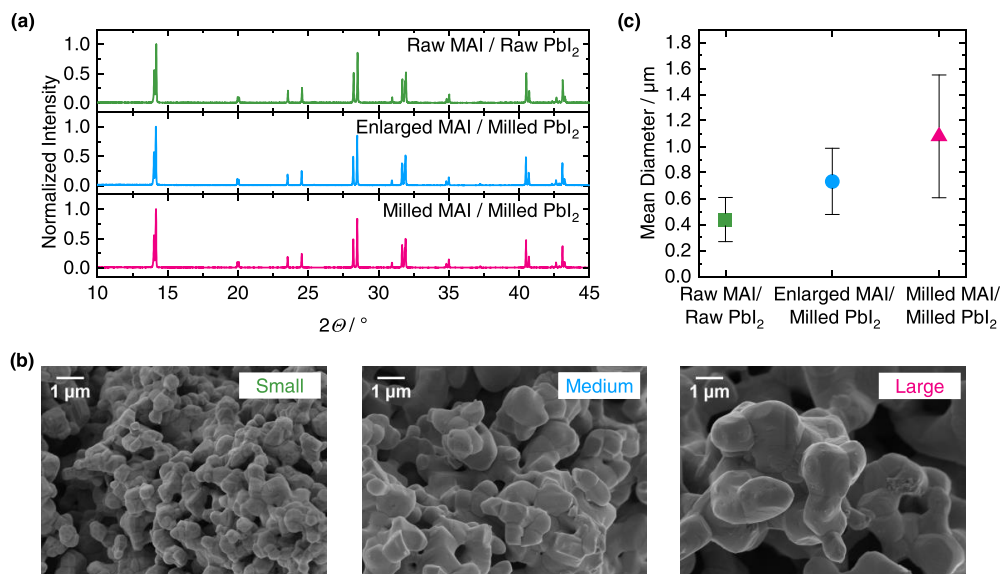
Figure 1. Synthesis of MAPbI$_3$ powders with different powder particle sizes (each color indicates data belonging to one sample): (a) XRD patterns of MAPbI$_3$ powders manufactured via mechanochemical synthesis using different MAI and PbI$_2$ precursor powders, as described in the main text. (b) SEM images of the MAPbI$_3$ powders with small (left), medium (middle), and large (right) powder particle sizes. (c) Mean diameter of MAPbI$_3$ powder particles extracted from SEM images.

microstructure on the pressure-induced compaction dynamics and the resulting pellet properties. However, this understanding has not evolved yet.

In this work, we investigate the influence of the perovskite powder microstructure on the pressure-induced compaction and structural and optoelectronic properties of the resulting pellets using the model halide perovskite MAPbI$_3$. By tailored mechanochemical synthesis, we prepare MAPbI$_3$ powders with different particle sizes and degrees of sintered connections between individual particles. In-depth analyses of pressure relaxations during powder pressing allow identifying the influence of the powder microstructure on rearrangement, plastic deformation, and crushing of sintered connections. These compaction processes directly affect the final pellet morphology, surface roughness, and density. In addition, from XRD measurements of powders and pellets, conclusions about the change of microstrain and crystallite size upon pressure treatment can be drawn, where the extent of pressure-induced crystallite size reduction depends decisively on the specific powder microstructure. Finally, we assess the optoelectronic properties of the pellets using time-resolved and steady-state photoluminescence (PL) spectroscopy, as well as impedance spectroscopy. This enables us to identify a dependence between the defect-assisted excited state recombination and the MAPbI$_3$ crystallite size in the pellets, whereas the dark conductivity depends on the powder particle size. Our results thus illustrate the complex relationship between the powder microstructure and the optoelectronic properties in perovskite powder pellets and also show the importance of pressure treatment in this context.

2. EXPERIMENTAL SECTION

2.1. Sample Preparation. Precursor powders MAI and PbI$_2$ were used to synthesize MAPbI$_3$ powders mechanochemically. The MAPbI$_3$ powders were pressed into pellets using a

homebuilt mechanical press and a circular pressing tool (diameter 13 mm) from Maassen (for details, see SI Section S1–S3).

2.2. Sample Characterizations. For morphology studies, SEM images of the perovskite powders and pellets were taken with a Zeiss Leo 1530 scanning electron microscope (FE-SEM with Schottky-field-emission cathode, SE2 detector, and In-lens detector) using an accelerating voltage of 3.0 kV. Therefore, the powders and the pellets were fixed on a sample holder with conductive adhesion graphite pads (Plano) and sputtered with a 1.5 nm thin platinum layer. The perovskite powders and the pellets were characterized under ambient conditions by reflection mode XRD using a Bruker "D8 Discover A25" with Cu-K$_{\alpha I}$ radiation (λ = 0.15406 nm). The K$_{\alpha II}$ rays were removed with a Ge-K$_{\alpha I}$ monochromator. The instrument was operated with 40 kV and 40 mA. Diffractograms were recorded with a 2θ step size of 0.016° or less in the 2θ range from 10 to 45°. The relative density of the pressed pellets was calculated based on the pellet area, the pellet mass, and the pellet thickness. The surface roughness Sz (maximum height of the surface) of the pellets was determined using a 3D laser scanning microscope ZEISS LSM 800 Mat (for more details, see SI Section S4).

2.3. Optical and Electrical Pellet Characterizations. The transient time-resolved PL measurements of the perovskite pellets were measured using time-correlated single-photon counting (TCSPC) in a PicoQuant MT200 confocal fluorescence microscope. For excitation, a 561 nm diode laser (PicoQuant LDH-D-TA-560) with a frequency of 1.0 MHz and a pulse width of 68 ps was used. The excitation fluence was set to 100 nJ/cm^2. An Olympus objective (4× magnification, numerical aperture of 0.1) was used to focus the laser beam on the pellet samples, giving a spot diameter of about 6 μm in the focal plane. In the optical detection path, a 561 nm long-pass filter was used to remove the scattered excitation light. The
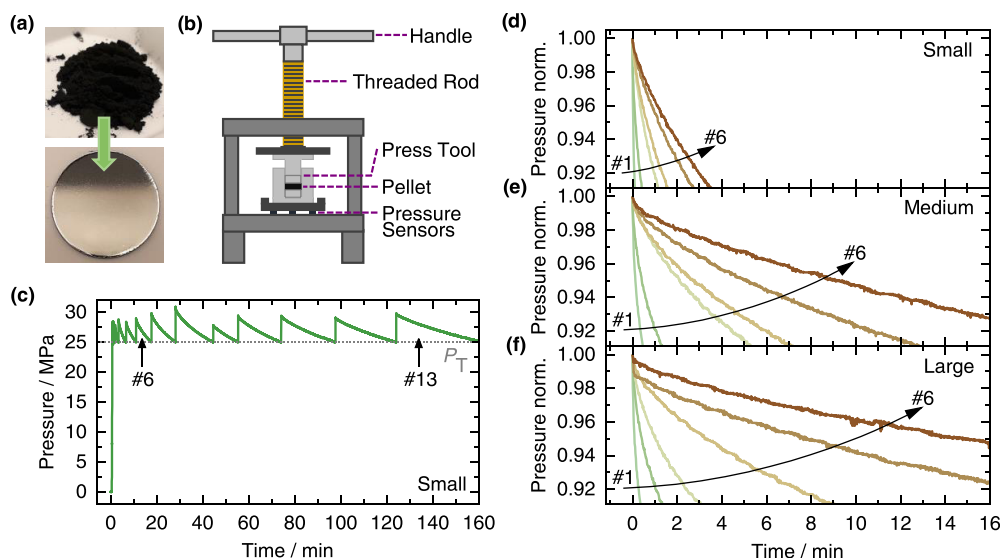
113

Figure 2. (a) Photographs of a MAPbI$_3$ powder and corresponding powder pellet (13 mm diameter). (b) Schematic illustration of the mechanical press setup used to prepare MAPbI$_3$ powder pellets. (c) Time evolution of the applied pressure when pressing a MAPbI$_3$ powder with small particles. To maintain the target pressure level of 25 MPa, the pressure was manually readjusted. (d)−(f) First 6 pressure relaxations (normalized), where the individual maximum values are set to a common time zero for MAPbI$_3$ powders with (d) small, (e) medium, and (f) large powder particle sizes.

remaining emission from the pellet sample was detected with a PMA Hybrid PMT 40 photomultiplier tube (PicoQuant), and the signal was processed with a TimeHarp 260 Pico TCSPC board (PicoQuant). The steady-state PL spectra were measured using a homebuilt setup. For excitation, a 337 nm nitrogen laser (LTB MNL 100) was used. The photoluminescence from the pellet samples was focused into a spectrograph (Andor Shamrock SR303i) and recorded with a CCD camera (Andor iDus DU420a-OE). The recorded spectra were corrected for transmission and detection efficiency of the setup.

The electrical properties of the perovskite pellets were investigated in darkness by impedance spectroscopy. Two-wire measurements were performed with an Alpha-A High-performance-frequency analyzer (Novocontrol Technologies). At the beginning of each measurement, a DC voltage of 0.5 V was applied for 60 min to avoid temporal drifts. Then, in addition to the already applied DC voltage of 0.5 V, an AC voltage with an amplitude of 30 mV was applied, whose frequency was varied between 1 Hz and 1 MHz. All measurements were carried out in a dry and oxygen-free argon atmosphere (for more details, see SI Section S5).

3. RESULTS AND DISCUSSION

3.1. Powder Microstructure. To obtain MAPbI$_3$ powders with different microstructures, we used a mechanochemical synthesis approach by ball milling MAI and PbI$_2$ precursor powders that exhibit different sizes. To achieve the different precursor sizes, we varied the time for the final crystallization step in the MAI synthesis, resulting in MAI with two different sizes (hereafter called "Raw MAI" and "Enlarged MAI") and also ball-milled the "Raw" compound to obtain a third MAI batch with smaller sizes ("Milled MAI"). Similarly, we used commercial PbI$_2$ powder as purchased ("Raw PbI$_2$") and produced a second PbI$_2$ batch with smaller particle sizes

("Milled PbI$_2$") by ball milling "Raw PbI$_2$." For the mechanochemical synthesis of the three MAPbI$_3$ powders fabricated in this work, we used the precursor combinations "Raw MAI/Raw PbI$_2$," "Enlarged MAI/Milled PbI$_2$," and "Milled MAI/Milled PbI$_2$" (see SI Section S1 and S2 for details of the precursor and MAPbI$_3$ preparation).

The total milling time for all three syntheses was 25 min, and all lead to phase-pure MAPbI$_3$ powder as confirmed by X-ray diffractometry (XRD) (Figure 1a, reflexes indexed in Figure S2). All mechanochemically synthesized powders consist of agglomerates of aggregates of individual particles (see scanning electron microscopy (SEM) images in Figure S3a−c for details), which is in agreement with the literature.[20,21] SEM images at higher magnification further demonstrate that the three different MAPbI$_3$ powders exhibit different particle sizes (Figure 1b). From the analysis of the SEM images (see SI Section S2 for details), we find that the "Raw MAI/Raw PbI$_2$" combination leads to small MAPbI$_3$ particles with a mean diameter of 0.4 μm (referred to as "Small"), whereas the "Enlarged MAI/Milled PbI$_2$" and "Milled MAI/Milled PbI$_2$" combinations result in larger MAPbI$_3$ particles with mean diameters of 0.7 μm ("Medium") and 1.1 μm ("Large"), respectively (Figure 1c).

From the SEM images, it also becomes clear that individual MAPbI$_3$ particles are tightly connected with neighboring particles, suggesting a soft sintering process occurring during the mechanochemical synthesis.[6,7] Furthermore, the size of these sintered connections appears to increase with the mean diameter of the MAPbI$_3$ particles (see Figure S3d−f for detailed images).

The final MAPbI$_3$ particle sizes can be understood by considering the differences in size and material properties of the MAI and PbI$_2$ precursors. Using XRD investigations, Manukyan et al. demonstrated that significant differences in the size of PbI$_2$ precursors do not influence the resulting

particle sizes of mechanochemical synthesized MAPbI$_3$ powders, as the brittle PbI$_2$ gets fully crushed quickly during milling.[22] Consequently, we assume the properties of the MAI precursors to play a major role determining the final MAPbI$_3$ particle sizes. While a detailed investigation of the influence of MAI size on MAPbI$_3$ particle sizes is beyond the scope of this paper and will be addressed in detail in subsequent work, we note that, in general, the milling time required for full perovskite conversion increases with larger MAI crystals.[23] Consequently, for a constant overall milling time, the milling duration after full perovskite conversion becomes shorter for larger MAI crystals. As the milling duration after full perovskite conversion is associated with a reduction of the MAPbI$_3$ particle size,[21,23,24] larger MAI crystals result in larger final MAPbI$_3$ particles. This explains the particle sizes found for the MAPbI$_3$ powders "Small" and "Medium," where "Raw MAI" and "Enlarged MAI" precursors were used, respectively.

However, surprisingly, using "Milled MAI" results in the MAPbI$_3$ powder with the largest particle sizes. In this case, due to the small MAI crystals and small PbI$_2$ particles, we expect a prompt perovskite conversion during ball milling,[22,23] where small MAPbI$_3$ particles form already after a rather short time of ball milling. During the remaining time of ball milling, a subsequent growth of the MAPbI$_3$ particles occurs, as observed by López et al.[25] This subsequent growth might be associated with the limited heat dissipation capability of small MAPbI$_3$ particles, facilitating a more pronounced sintering effect and thus growth of the MAPbI$_3$ particles during milling. The presence of such a sintering effect is easily conceivable, as, in MAPbI$_3$, sintering occurs already below 34 °C at 10 MPa,[15] and local temperatures around 40 °C are known to be present during mechanochemical synthesis due to the friction between powder, milling balls, and the vessel wall.[26] Furthermore, it is known from the field of ceramics that the sintering temperature decreases for powders with smaller powder particle sizes,[27] which further supports our explanation.

In summary, we successfully synthesized MAPbI$_3$ powders that exhibit different microstructures, i.e., different particle sizes and corresponding sizes of sintered connections, by appropriate choice of the precursor properties. These MAPbI$_3$ powders are the basis for the following investigations regarding the influence of the powder microstructure on the resulting pellet properties.

3.2. Pellet Pressing—Powder Compaction Dynamics.
Using the three MAPbI$_3$ powders "Small," "Medium," and "Large," we pressed pellets and investigated how the differences in the powder microstructure impact the compaction behavior upon applying pressure (see Figure 2a for photographs of representative MAPbI$_3$ powder and final pellet).

For producing the pellets, a homebuilt mechanical press was used, which is illustrated in Figure 2b and described in detail elsewhere (also see SI Section S3).[15] With our setup, it is possible to monitor the pressure as a function of time by means of pressure sensors that are located below the press tool. For the compaction of all three powders, we used the same pressing parameters, i.e., a target pressure P_T of 25 MPa and a pressing time of 160 min at the target pressure level.

After applying a certain pressure, the pressure decreases due to different compaction processes of the powder particles.[15] To investigate these compaction processes, we followed the approach from our previous work[15] and readjusted the pressure by a certain amount ΔP to prevent coming below

the target value P_T. In our experiments, we envisaged to realize ΔP to be in the range of about 4 MPa, where the accuracy to realize the targeted ΔP value was limited by our manual pressure readjustment procedure (Figure S4a). Figure 2c shows the temporal evolution of pressure for a pellet made from the powder "Small" (see Figure S4b for corresponding measurements of the other powders). For this powder "Small," 13 pressure readjustments were necessary to maintain the target pressure level of 25 MPa within the 160 min of pressing time.

From Figure 2c, it becomes clear that the relaxations decelerate with increasing number of pressure readjustments. To examine this behavior in more detail, it is useful to normalize all pressure relaxations and set each maximum pressure value to a common time zero (i.e., $t = 0$ min corresponds to the moment of pressure readjustment). This is shown in Figure 2d−f for the first six relaxations of the three powders pressed at 25 MPa (see Figure S4c for all relaxations). Qualitatively, it becomes clear that the deceleration of the relaxations with increasing number of pressure readjustments is more pronounced for larger powder particle sizes. Furthermore, the relaxations for lower numbers of readjustments appear more curved.

To quantify the observed changes in the length and shape of the relaxations, we fitted all normalized pressure relaxations using a biexponential function of the form

$$P(t) = P_0 + A_{re} \cdot e^{-t/t_{re}} + A_{sh} \cdot e^{-t/t_{sh}} \qquad (1)$$

with the amplitudes A_{re} and A_{sh} and the relaxation times t_{re} and t_{sh}. A_{re} and t_{re} represent the characteristic amplitude and time constant of particle rearrangement.[15] A_{sh} and t_{sh} are associated with compaction processes that change the shape of the connected powder particles, i.e., plastic deformation and crushing processes.[15,19] The corresponding fit results of t_{re} and t_{sh} are shown in Figure 3a as a function of pressing time for the three MAPbI$_3$ powders with small (green squares), medium (blue dots), and large (red triangles) particle sizes.

Both t_{re} and t_{sh} increase with time, with t_{re}, in general, being about one order of magnitude lower than t_{sh}. These observations are consistent with the results about the powder compaction behavior of MAPbI$_3$ and MAPbBr$_3$ powders from our previous work.[15] Furthermore, t_{re} and t_{sh} increase for larger powder particle sizes. Therefore, the more pronounced deceleration of the pressure relaxations for larger powder particle sizes and larger sintered connections (Figure 2d−f) is also reflected in Figure 3a. This implies that for the powder "Small" with small particle sizes and small sintered connections, the most prominent compaction dynamics is observed. Assuming that the crushing process takes place within a shorter period of time than the plastic deformation process, the lower values of t_{sh} for the powder "Small" indicate a more dominant crushing process to be present in this powder compared to the powders "Medium" and "Large." This is supported by the smallest sintered connections found for the powder "Small" (see Figure S3d−f), which might facilitate crushing into individual powder particles. Enhanced crushing for weaker connections between individual powder particles was also observed by Cai et al. for BaCeO$_3$ perovskites.[28]

From our analysis of the amplitudes extracted from the fits of the pressure relaxations, we find that the amplitude ratio $A_{re}/(A_{re} + A_{sh})$ is modulated by the variations in ΔP (Figure S4a). It is necessary to correct this modulation to derive reliable information from the amplitude ratios. Thus, Figure 3b
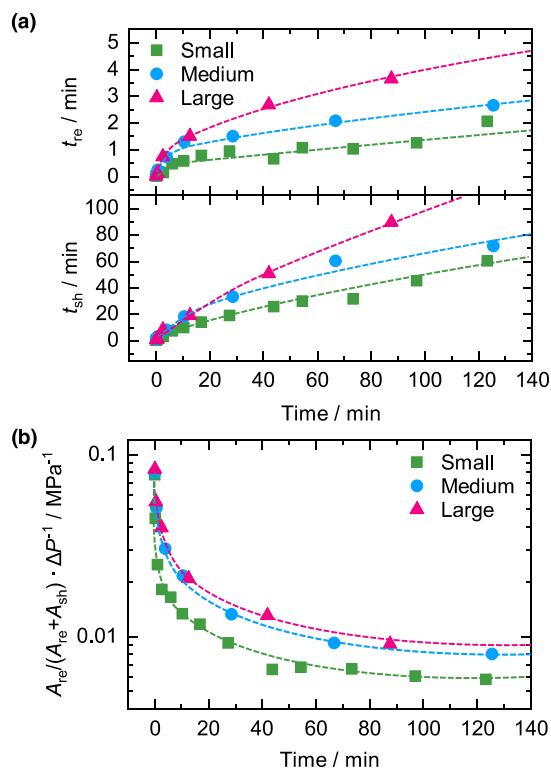
(a)

(b)

Figure 3. Quantitative pressure relaxation analysis for pellets pressed at P_T = 25 MPa using MAPbI$_3$ powders with small (green squares), medium (blue dots), and large (red triangles) powder particle sizes (dashed lines serve as a guide for the eye). (a) Resulting fitting parameters t_{re} (top) and t_{sh} (bottom) from fitting the pressure relaxations using a biexponential decay as a function of pressing time. (b) Temporal evolution of the ΔP-corrected amplitude ratio $A_{re}/(A_{re} + A_{sh}) \cdot \Delta P^{-1}$.

shows the amplitude ratio corrected for variations in ΔP, i.e., $A_{re}/(A_{re} + A_{sh}) \cdot \Delta P^{-1}$ as a function of pressing time for the three MAPbI$_3$ powders with small (green squares), medium (blue dots), and large (red triangles) particle sizes (see SI Section S3 and Figure S5 for details). For all powders, $A_{re}/(A_{re} + A_{sh}) \cdot \Delta P^{-1}$ decreases with pressing time, suggesting that most particle rearrangement occurs at the beginning of the pressing process, which is in line with the literature.[15,29] In contrast, the compaction processes associated with the second exponential, i.e., plastic deformation and crushing of connected particles seem to gain importance for the overall compaction process at longer times. It is noticeable that over the entire considered time range, the corrected amplitude ratio is lower for smaller particle sizes. Especially, the corrected amplitude ratio of the powder "Small" is clearly lower than that of the other powders "Medium" and "Large," indicating that plastic deformation and/or crushing contributes more to the overall pressure reduction in the powder "Small" compared to the other two powders. Overall, taking into account the above-discussed differences in the absolute values of t_{sh}, we conclude that among plastic deformation and/or crushing, crushing is the more relevant process for the powder "Small." In comparison, plastic deformation seems to be more important in the powders "Medium" and "Large," and its contribution to the

overall pressing process appears to increase with increasing particle size.

3.3. Pellet Morphology. Based on the findings in Section 3.2, we examined whether the different extents of the compaction processes in the three MAPbI$_3$ powders are also reflected in the resulting pellet properties, i.e., the pellet morphology and density. Figure 4a−c shows top view SEM images of the pellets pressed at 25 MPa using the three powders with small, medium, and large powder particle sizes. It becomes clear that an increasing powder particle size is also reflected in the morphology of the powder-pressed pellets, which was also observed, e.g., in the field of polycrystalline ceramics.[19] Furthermore, the size of voids and thus the porosity of the pellets increases with larger powder particles. Consequently, the corresponding relative densities decrease with increasing powder particle sizes (Figure 4d). Here, the highest relative density of ∼0.79 of the pellet made from the powder "Small" differs noticeably from the relative densities obtained with the powders "Medium" (∼0.77) and "Large" (∼0.76). All relative densities agree well with the relative density of ∼0.8 reported for a MAPbI$_3$ pellet pressed at the same pressure level in our previous work.[15] In addition, our observation that smaller powder particle sizes result in higher pellet densities agrees well, e.g., with the work of Cai et al., who investigated the densities of different BaCeO$_3$ perovskite powder pellets pressed at 130 MPa.[28] A higher compaction of the smaller powder particles compared to larger particle sizes is also reflected in the surface roughness Sz, which we find to increase with increasing powder particle sizes from ∼6.0 μm ("Small"), ∼8.6 μm ("Medium") to ∼10.8 μm ("Large") (Figure 4e).

Figure 4f shows normalized XRD patterns in the range of 27.7−29.0° for the powder "Medium" (solid line) and the corresponding 25 MPa pellet (dashed line). Here, a broadening of the (004) and (220) MAPbI$_3$ reflexes for the 25 MPa pellet becomes clear (see Figure S7 for patterns of the other powders and corresponding pellets). To further investigate the reflex broadening upon applying pressure, we pressed additional pellets at a pressure of 100 MPa (see SI Section S3 for details). The normalized XRD patterns of the 100 MPa pellets show an even stronger reflex broadening than for the 25 MPa pellets (Figures 4f and S7, dotted lines). In general, a reflex broadening in the XRD patterns could be caused by a reduction of the MAPbI$_3$ crystallite sizes due to the applied pressure. To evaluate this in more detail, we used the Rietveld refinement method to extract crystallite sizes and microstrain from the XRD patterns of all powders and pellets (see Figure S8 for details). The results are summarized in Table 1.

From the XRD analysis, it becomes clear that microstrain is induced, and it increases with increasing pressure, while the MAPbI$_3$ crystallite size in the final pellets reduces. The 25 MPa pellets exhibit 0.02−0.04%, and the 100 MPa pellets between 0.07 and 0.09% microstrain. This increase is reasonable, since the applied pressure can induce dislocations and stacking faults in the perovskite.[30−32] Here, the degree of microstrain induced in the pellets appears to be largely independent of the powder particle size. In the case of the powders, no significant microstrain could be found.

In contrast, the degree of crystallite size reduction induced by the applied pressure differs for the powders "Small," "Medium," and "Large." For the powder "Small," the crystallite size is reduced from 340 nm in the powder to 210 and 100 nm in the 25 and 100 MPa pellets, respectively. This corresponds
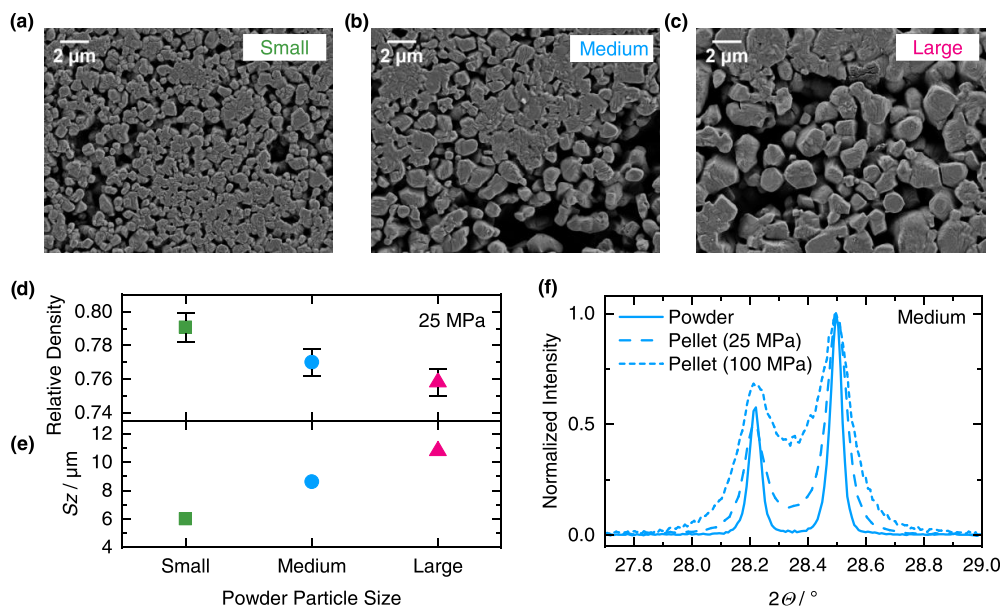
Figure 4. Top view SEM images of pellets pressed at P_T = 25 MPa using MAPbI$_3$ powders with (a) small, (b) medium, and (c) large powder particle sizes. (d) Relative density and (e) surface roughness Sz of pellets pressed at P_T = 25 MPa using MAPbI$_3$ powders with small (green squares), medium (blue dots), and large (red triangles) powder particle sizes. (f) XRD patterns showing the (004) and (220) MAPbI$_3$ reflexes of the powder "Medium" (solid line) and corresponding pellets pressed with 25 MPa (dashed line) and 100 MPa (dotted line) target pressure level.

Table 1. Microstrain and Crystallite Size of Samples from the Powders with Small, Medium, and Large Powder Particle Sizes Extracted via the Rietveld Refinement Method with Corresponding Relative Crystallite Size Reduction and Rate Constants k_1 from Time-Resolved Photoluminescence Measurements (see Section 3.4)

source powder	sample type	microstrain (%)	crystallite size (nm)	crystallite size reduction (%)	rate constant k_1 (10^5 s^{-1})
"Small"	powder	<0.01	340 ± 100		
				38	
	25 MPa pellet	0.04 ± 0.01	210 ± 45		
				52	
	100 MPa pellet	0.08 ± 0.01	100 ± 10		120.8 ± 3.5
"Medium"	powder	<0.01	>350		
				>54	
	25 MPa pellet	0.04 ± 0.01	160 ± 30		
				56	
	100 MPa pellet	0.09 ± 0.01	70 ± 15		377.6 ± 20.8
"Large"	powder	<0.01	>350		
				>14	
	25 MPa pellet	0.02 ± 0.01	300 ± 75		
				60	
	100 MPa pellet	0.07 ± 0.01	120 ± 25		5.8 ± 0.4

to a relative reduction of crystallite size of the powder "Small" by 38% for a pressure of 25 MPa and a further reduction by 52% when using 100 MPa to prepare a pellet (Table 1). Due to the very narrow reflexes in the XRD pattern of the powder "Medium," only a lower limit of >350 nm could be determined for the crystallite size. For the "Medium" compounds, the pressure-induced crystallite size reduction is at least 54% for a pressure of 25 MPa and comprises a reduction of another 56% when going to 100 MPa. Therefore, the pressure-induced crystallite size reduction is more pronounced for the powder

"Medium" than for the powder "Small." The powder "Large" shows the most significant reduction of crystallite size, reducing from 300 to 120 nm, i.e., by even 60%, when going from 25 to 100 MPa.

To understand the degree of pressure-induced crystallite size reduction, we recall that during the pressing process, rearrangement as well as crushing and plastic deformation of the powder particles take place. For crushing and rearrangement processes, powder particles typically break up at sintered connections and move without significantly reducing their

117
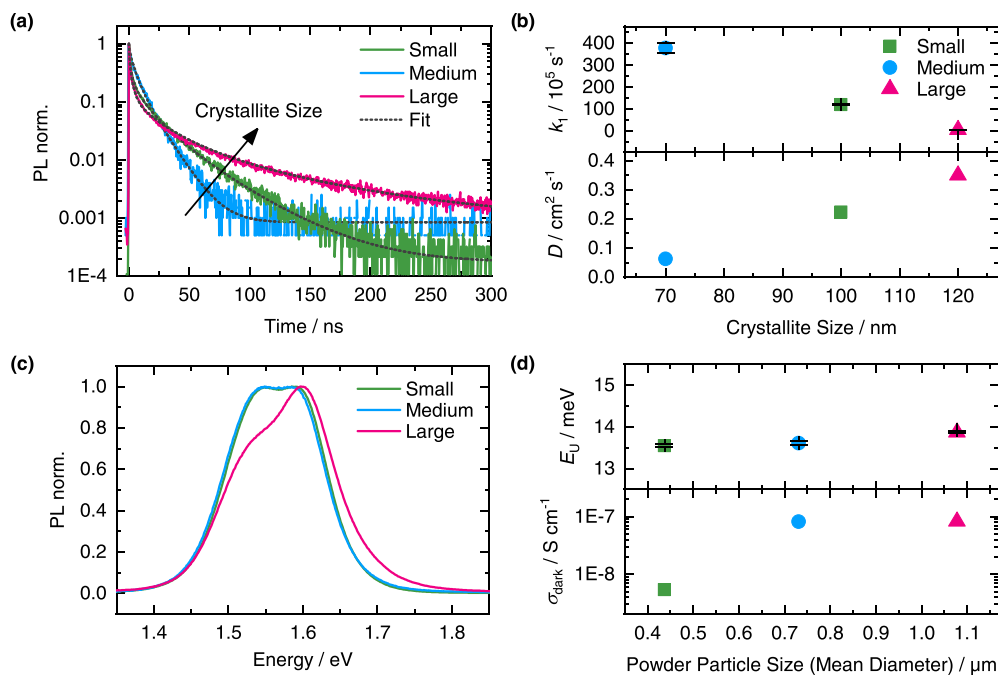
Figure 5. Analyses of optoelectronic properties for pellets pressed at 100 MPa target pressure level using MAPbI$_3$ powders with small (green), medium (blue), and large (red) powder particle sizes: (a) Normalized transient PL curves with fits. (b) Rate constant k_1 and diffusion constant D extracted from the fits in (a) as a function of crystallite size. (c) Normalized steady-state PL spectra. (d) Urbach energy E_U and dark conductivity σ_{dark} as a function of powder particle size.

crystallite size. In contrast, the crystallite size decreases clearly upon plastic deformation, e.g., due to the formation, movement, and accumulation of dislocations.[19,32,33] Here, Mayer et al. could also demonstrate recently that plastic deformation in halide perovskites proceeds by gliding of dislocations along well-defined crystallographic planes.[34] Accordingly, when pressing powders with larger particle sizes, the stronger reduction of the crystallite size (Table 1) indicates that the larger particles exhibit more plastic deformation. This is in good agreement with the conclusions drawn from the analysis of the compaction dynamics in Section 3.2. Furthermore, the stronger plastic deformation of larger powder particles appears reasonable, considering that within a defined volume, less rearrangement is possible for larger powder particles[35] and therefore, a higher fraction of the energy provided by the applied pressure transfers into plastic deformation. In addition, the size, and thus strength of the sintered connections between the individual powder particles, also seem to influence the extent of plastic deformation. Smaller thicknesses of the sintered connections between individual powder particles might allow them to break up more easily under a certain pressure, facilitating rearrangement processes of crushed particles. Indeed, such a relationship was reported for BaCeO$_3$ perovskites.[28] If the sintered connections are thicker so that a certain pressure is not sufficient to break these connections, the energy introduced by the pressure will be converted mainly into plastic deformation of the powder particles. The presence of thicker sintered connections for larger MAPbI$_3$ powder particle sizes, as observed in Figure S3d−f supports this scenario.

Overall, the morphology analyses of the pellets suggest a stronger compaction of smaller powder particles, as expected

from the analysis of the compaction dynamics (Section 3.2). Also, in line with the conclusions drawn in Section 3.2, the degree of pressure-induced crystallite size reduction indicates that larger powder particles exhibit more plastic deformation when pressure is applied, which is associated with the increasing size of the sintered connections for larger particles. This more pronounced crystallite size reduction for larger particle sizes finally results in lower absolute crystallite sizes in the pellets made from powder "Medium," compared to corresponding crystallite sizes in the pellets made from the powder "Small." Thus, the pressing process can significantly impact on the structural properties of MAPbI$_3$ powders.

3.4. Pellet Optoelectronic Functionality. After having determined the impact of the MAPbI$_3$ powder microstructure on the compaction dynamics and the morphology, i.e., density and crystallite size of the resulting pellets, we investigated the impact of the powder microstructure on the optoelectronic functionality of the final pellets. For all optoelectronic investigations, we used 100 MPa pellets due to their improved surface quality compared to the 25 MPa pellets (for details and supplementary morphology characterizations, see SI Section S4 and S5).

Time-resolved PL decay curves were measured to investigate the charge carrier recombination dynamics after exciting the pellet samples with a pulsed diode laser (excitation photon energy: 2.1 eV). Figure 5a shows the normalized time-resolved PL curves of the pellets made from powders with small (green), medium (blue), and large (red) powder particles. It becomes clear that the decay curves of the three pellets exhibit different shapes and decay dynamics. To investigate these differences in more detail, the rate equation

$$\frac{dn}{dt} = -k_1 n - k_2 n^2 - k_3 n^3 + D\frac{\partial^2 n}{\partial z^2} \tag{2}$$

describing the decay of the photoinduced free charge carrier density $n(t)$ due to different recombination processes was used to fit the time-resolved PL curves.[36] The rate equation considers three recombination processes with corresponding rate constants k_1, k_2, and k_3 that correspond to monomolecular, bimolecular, and Auger recombination, respectively. k_1 is determined by the nonradiative recombination due to traps[14,37] and thus correlates with the defect density in the pellet samples.[37] k_2 and k_3 are assumed to be material constants.[37] They were set to $k_2 = 6.8 \times 10^{-10}$ cm^3 s^{-1} and $k_3 = 1.0 \times 10^{-29}$ cm^6 s^{-1}, based on literature values.[36] The diffusion of the charge carriers after initial photoexcitation is considered by the term $D\frac{\partial^2 n}{\partial z^2}$, with the diffusion constant D and the thickness z over which charge carrier processes in the pellets are assumed to be relevant. To account for deviations in the initial charge carrier density caused by differences in the sample morphology, the fit parameter n_0 was allowed to deviate from the initial charge carrier density value one would expect based on the laser fluence used in our experiment, resulting in a range between $n_0 = 1.67 \times 10^{16}$ cm^{-3} and $n_0 = 5.14 \times 10^{17}$ cm^{-3} (see SI Section S5 for details).

Fits according to eq 2 to the measured time-resolved PL curves are shown in Figure 5a (gray dotted lines) and provide a good description of the measured data. The resulting rate constants are $k_{1,\text{Medium}} = (3.78 \pm 0.21) \times 10^7$ s^{-1}, $k_{1,\text{Small}} = (1.21 \pm 0.04) \times 10^7$ s^{-1}, and $k_{1,\text{Large}} = (5.77 \pm 0.40) \times 10^5$ s^{-1} for the pellets made from the powders "Medium," "Small," and "Large," respectively. Figure 5b shows k_1 as a function of crystallite sizes of the 100 MPa pellets (with corresponding values from Table 1). Even though the error ranges of the crystallite sizes for the powders "Small" and "Large" partly overlap, Figure 5b suggests that k_1 decreases with increasing crystallite size. This is in line with the transient PL results by D'Innocenzo et al. on MAPbI$_3$ thin films with different crystallite sizes.[38] The diffusion constants obtained from the fits according to eq 2 are in the range between 0.06 and 0.35 cm^2 s^{-1}, in good agreement with literature values of MAPbI$_3$ thin films.[39,40] Furthermore, D appears to be directly correlated with the MAPbI$_3$ crystallite size from Table 1 (Figure 5b, bottom). This is also in line with literature reports, where an increase of D with the crystallite size of MAPbI$_3$ was observed.[41,42] Overall, the time-resolved PL investigations demonstrate that larger crystallite sizes result in more charge carrier diffusion after photoexcitation and in prolonged charge carrier lifetimes, both aspects indicating a lower defect density in the perovskite.

We measured steady-state PL spectra of the 100 MPa pellets, with normalized spectra of the pellets made from powders with small (green), medium (blue), and large (red) powder particle sizes, as shown in Figure 5c. In addition to the main peak originating from direct PL of MAPbI$_3$ at about 1.6 eV,[43,44] all spectra show an additional shoulder at lower energies, which we attribute to stem from a filtered PL contribution due to self-absorption.[45–47] The pellets pressed from the powders "Medium," "Small," and "Large" exhibit direct PL peak positions of 1.58, 1.59, and 1.60 eV, respectively. Thus, the PL peak position shifts to higher energies with increasing crystallite size of the pellets (Table 1). This is accompanied by a decrease in the relative intensity of the filtered PL peak

contribution (Figure 5c). We associate the PL peak shift to higher energies with a decreasing density of defects near the interface toward air. The decreased defect density facilitates radiative recombination in this region. Thus, on average, more PL comes from near the interface than from the bulk, reducing the effect of self-absorption on the direct PL. This explanation is also supported by the finding that k_1 decreases with increasing crystallite size (Table 1). The lower contribution of filtered PL to the PL spectrum can be explained by the higher surface roughness of the pellet from the powder "Large" (Figure S9), leading to enhanced light outcoupling at the interfaces. Thereby, internal reflections contributing to the filtered PL become weaker, and additionally, more of the direct PL can leave the sample toward the detector.[48]

From the shape of the measured PL spectra, we extracted the Urbach energy E_U—a measure for the degree of disorder within the perovskite (for details, see SI Section S5, Figure S11). The extracted values of E_U increase slightly from 13.6 to 13.9 meV for the powder "Small" and "Medium" to the powder "Large," respectively, (Figure 5d, top) and are in line with reported E_U values for MAPbI$_3$ films and single crystals.[49,50]

Overall, our PL investigations demonstrate that the nondirect correlation between the MAPbI$_3$ powder particle size and the resulting crystallite size in corresponding pellets found in Section 3.3 is also reflected in the excited state properties and defect densities. Here, it is interesting to note that the increased extent of plastic deformation for larger particle sizes upon applying pressure appears to have no significant impact on the excited state recombination properties in the pellets, even though the Urbach energy extracted from the PL spectra increases with the MAPbI$_3$ particle size. This is in contrast to observations by, e.g., Frohna et al. on solution-processed halide perovskite thin films, where typically an increase in Urbach energy, i.e., disorder, is accompanied with an increase in nonradiative recombination rate.[51,52] We thus speculate that defects induced by plastic deformation exhibit different, more favorable energetic properties compared to the defects and associated type of disorder of, e.g., solution-processed perovskite films that are not subjected to pressure treatment.

Having investigated the impact of the powder microstructure on the optical properties, we finally consider the impact of the powder microstructure on the electronic functionality, i.e., charge carrier transport properties. Therefore, we evaporated top electrode structures on the 100 MPa pellets and conducted impedance spectroscopy measurements between 1 Hz and 1 MHz. All impedance measurements were performed in an argon atmosphere to exclude possible changes in the electrical properties due to oxygen and moisture.[53–55] The measured impedance spectra were plotted as Nyquist plots and fitted according to an equivalent circuit consisting of a resistance in series to an RC parallel element (see Figure S12 for details).

From the impedance spectra measured in the dark, the electrical dark conductivity σ_{dark} was calculated using the resistance of the MAPbI$_3$ pellets and a simulated geometry factor (for details, see SI Section S5). By doing so, we find electrical dark conductivities for the 100 MPa pellets to increase with the powder particle size, i.e., for the powders "Small," "Medium," and "Large," we find 5.4×10^{-9}, 8.2×10^{-8}, and 8.3×10^{-8} S cm^{-1}, respectively (Figure 5d, bottom). These values agree well with the dark conductivities in the

order of 10^{-8} S cm^{-1} found for MAPbI$_3$ thin films measured by galvanostatic polarization at 40 °C in argon atmosphere.[56]

Dark currents in MAPbI$_3$ powder-based thick films are caused by ion migration, in particular, by the vacancy-assisted migration of MA cations and iodine anions.[57−59] Literature reports indicate that due to the higher activation energy compared to iodine migration, the migration of MA cations plays a minor role.[14,60−62] Thus, we assume that the ionic conductivity is mainly determined by the iodine concentration [I$^-$] and their mobility μ_{I^-} to hop across vacancies, i.e., $\sigma_{ion,\ I^-} = \mu_{I^-} \cdot [I^-] \cdot e$.[60,62] Ion migration in polycrystalline halide perovskite films was found to typically take place at or in the grain boundaries, as the latter exhibit higher concentration of point defects (especially halide vacancies) than the perovskite bulk.[58,59,63,64] We assume that among the different pellets investigated in our study, the pellets made from the powder "Small" exhibit the highest density of grain boundaries, corresponding to the highest concentration of migrating ions. In this context, the mobility for ion migration in the pellet from the powder "Small" must be relatively low to explain the observed low dark conductivity (Figure 5d, bottom), i.e., here, a rather high activation energy for ion migration must be present. It is known that the microstructure of the perovskite has a significant impact on the activation energy for ion migration,[58] where higher activation energies were suggested to be linked to less lattice distortions[65] due to, e.g., dislocations, disorientated grains, wrong bonds, and excess volume at the grain boundaries.[66] This fits well with our results from Sections 3.2 and 3.3, where we find the powder "Small" to exhibit the lowest degree of plastic deformation due to the pressing process, possibly resulting in the highest "quality" of grain boundaries in the corresponding pellets.

In contrast, for the pellets made from the powders "Medium" and "Large," we assume a decreased ion concentration due to a lower grain boundary density. However, a reduced activation energy for ion migration due to, e.g., a rather high density of dislocations at the grain boundaries can be expected. The reduced activation energy seems to be the dominant aspect leading to the higher values of σ_{dark} for the pellets made from the powders "Medium" and "Large" in Figure 5d. A higher density of dislocations at the grain boundaries can be the result of the more pronounced plastic deformation of larger perovskite particles during the pressing process,[19] which we indeed identified from our analyses in Sections 3.2 and 3.3.

Consequently, we conclude that changes in activation energy for ion migration due to differences in the quality of the grain boundaries are likely to be the most crucial aspect determining the observed differences in dark conductivities in Figure 5d. Changes in ion concentration due to different densities of grain boundaries appear to be less important.

4. CONCLUSIONS

In summary, we investigate in detail the influence of powder microstructure on the properties of resulting powder-pressed pellets. To this end, MAPbI$_3$ powders with different microstructures, i.e., with different powder particle sizes and degrees of sintered particle connections, are manufactured by mechanochemical ball milling. From the analysis of the pressure relaxations during powder pressing, we identify that particle rearrangement, plastic deformation, and pressure-induced crushing of sintered connections are present, where

the importance of these processes to the overall compaction process depends on the particle size and the strength of the sintered connections. Here, we identify that MAPbI$_3$ powders with smaller powder particle sizes and thinner sintered connections result in more compact pellets.

From XRD patterns of powders and pellets, we find that the MAPbI$_3$ crystallite size of the powders decreases clearly when pressed to a pellet. Furthermore, the final crystallite size in the pellet does not directly correlate with the initial powder particle sizes. The extent of plastic deformation present during the pressing process is the dominant process that determines the magnitude of crystallite size reduction upon applying a certain pressure. Thereby, more plastic deformation during pressing of larger powder particles with higher sintered connection strength leads to a stronger reduction of crystallite size in the pellet. The extent of plastic deformation appears to depend decisively on the specific microstructure, especially the strength of sintered particle connections.

Finally, the optoelectronic functionality is examined by PL and impedance spectroscopy. While the nonradiative recombination rate constants determined from time-resolved PL spectroscopy decrease with the MAPbI$_3$ crystallite sizes in the pellets, the electrical dark conductivity of the pellets increases with the powder particle size. Changes of the activation energy for ion migration due to differences in the quality of the grain boundaries are likely to be the most crucial aspects determining the observed increase of dark conductivity with particle size.

Thus, our results demonstrate the importance of the powder microstructure on the compaction behavior upon pressure treatment and on the resulting pellet morphology as well as on optical and electric properties. Our work further sheds light on the many-faceted structure−properties relationship in halide perovskites, with pressure representing a suitable external stimulus to tune powder-based thick-film properties. Eventually, the understanding gained in this work will allow to further advance the pressure processing and thus the functionality of powder-based perovskite optoelectronic devices, such as X-ray detectors.

■ ASSOCIATED CONTENT

ⓢ Supporting Information

The Supporting Information is available free of charge at https://pubs.acs.org/doi/10.1021/acs.jpcc.2c03329.

Details on MAI and PbI$_2$ precursor preparation and mechanochemical synthesis of MAPbI$_3$ powders, including SEM images; details on pellet pressing; additional analyses of the pressure relaxations, including detailed analyses of the amplitude ratio; supplementary XRD patterns of powders and pellets; details concerning relative densities and surface roughness with values of the 100 MPa pellets; and details on optoelectronic measurements, including additional analyses of the time-resolved PL curves, extraction of Urbach energy, and an exemplary impedance spectrum with an equivalent circuit for corresponding fits (PDF)

■ AUTHOR INFORMATION

Corresponding Author

Fabian Panzer − *Soft Matter Optoelectronics, University of Bayreuth, Bayreuth 95440, Germany;* ⓞ orcid.org/0000-0002-2191-9011; Email: fabian.panzer@uni-bayreuth.de

Authors

Christina Witt − *Soft Matter Optoelectronics, University of Bayreuth, Bayreuth 95440, Germany*

Nico Leupold − *Department of Functional Materials, University of Bayreuth, Bayreuth 95440, Germany*

Philipp Ramming − *Soft Matter Optoelectronics, University of Bayreuth, Bayreuth 95440, Germany*

Konstantin Schötz − *Soft Matter Optoelectronics, University of Bayreuth, Bayreuth 95440, Germany*

Ralf Moos − *Department of Functional Materials, University of Bayreuth, Bayreuth 95440, Germany*

Complete contact information is available at:
https://pubs.acs.org/10.1021/acs.jpcc.2c03329

Notes

The authors declare no competing financial interest.

REFERENCES

(1) NREL Best Research-Cell Efficiency Chart, https://www.nrel.gov/pv/cell-efficiency.html (accessed April 14, 2022).

(2) Lin, K.; Xing, J.; Quan, L. N.; de Arquer, F. P. G.; Gong, X.; Lu, J.; Xie, L.; Zhao, W.; Zhang, D.; Yan, C.; et al. Perovskite Light-Emitting Diodes with External Quantum Efficiency Exceeding 20 Per Cent. *Nature* **2018**, *562*, 245−248.

(3) Miao, J.; Zhang, F. Recent Progress on Highly Sensitive Perovskite Photodetectors. *J. Mater. Chem. C* **2019**, *7*, 1741−1791.

(4) Wei, H.; Huang, J. Halide Lead Perovskites for Ionizing Radiation Detection. *Nat. Commun.* **2019**, *10*, No. 1066.

(5) Sytnyk, M.; Deumel, S.; Tedde, S. F.; Matt, G. J.; Heiss, W. A Perspective on the Bright Future of Metal Halide Perovskites for X-Ray Detection. *Appl. Phys. Lett.* **2019**, *115*, No. 190501.

(6) Shrestha, S.; Fischer, R.; Matt, G. J.; Feldner, P.; Michel, T.; Osvet, A.; Levchuk, I.; Merle, B.; Golkar, S.; Chen, H.; et al. High-Performance Direct Conversion X-Ray Detectors Based on Sintered Hybrid Lead Triiodide Perovskite Wafers. *Nat. Photon.* **2017**, *11*, 436−440.

(7) Deumel, S.; van Breemen, A.; Gelinck, G.; Peeters, B.; Maas, J.; Verbeek, R.; Shanmugam, S.; Akkerman, H.; Meulenkamp, E.; Huerdler, J. E.; et al. High-Sensitivity High-Resolution X-Ray Imaging with Soft-Sintered Metal Halide Perovskites. *Nat. Electron.* **2021**, *4*, 681−688.

(8) Hu, M.; Jia, S.; Liu, Y.; Cui, J.; Zhang, Y.; Su, H.; Cao, S.; Mo, L.; Chu, D.; Zhao, G.; et al. Large and Dense Organic−Inorganic Hybrid Perovskite $CH_3NH_3PbI_3$ Wafer Fabricated by One-Step Reactive Direct Wafer Production with High X-ray Sensitivity. *ACS Appl. Mater. Interfaces* **2020**, *12*, 16592−16600.

(9) Yang, B.; Pan, W.; Wu, H.; Niu, G.; Yuan, J.-H.; Xue, K.-H.; Yin, L.; Du, X.; Miao, X.-S.; Yang, X.; et al. Heteroepitaxial Passivation of $Cs_2AgBiBr_6$ Wafers with Suppressed Ionic Migration for X-Ray Imaging. *Nat. Commun.* **2019**, *10*, No. 1989.

(10) Tie, S.; Zhao, W.; Xin, D.; Zhang, M.; Long, J.; Chen, Q.; Zheng, X.; Zhu, J.; Zhang, W.-H. Robust Fabrication of Hybrid Lead-Free Perovskite Pellets for Stable X-Ray Detectors with Low Detection Limit. *Adv. Mater.* **2020**, *32*, No. 2001981.

(11) Hong, Z.; Tan, D.; John, R. A.; Tay, Y. K. E.; Ho, Y. K. T.; Zhao, X.; Sum, T. C.; Mathews, N.; García, F.; Soo, H. S. Completely Solvent-Free Protocols to Access Phase-Pure, Metastable Metal Halide Perovskites and Functional Photodetectors from the Precursor Salts. *iScience* **2019**, *16*, 312−325.

(12) Li, M.; Li, H.; Li, W.; Li, B.; Lu, T.; Feng, X.; Guo, C.; Zhang, H.; Wei, H.; Yang, B. Oriented 2D Perovskite Wafers for Anisotropic X-Ray Detection through a Fast Tableting Strategy. *Adv. Mater.* **2022**, *34*, No. 2108020.

(13) Leupold, N.; Panzer, F. Recent Advances and Perspectives on Powder-Based Halide Perovskite Film Processing. *Adv. Funct. Mater.* **2021**, *31*, No. 2007350.

(14) Ramming, P.; Leupold, N.; Schötz, K.; Köhler, A.; Moos, R.; Grüninger, H.; Panzer, F. Suppressed Ion Migration in Powder-Based Perovskite Thick Films Using an Ionic Liquid. *J. Mater. Chem. C* **2021**, *9*, 11827−11837.

(15) Witt, C.; Schmid, A.; Leupold, N.; Schultz, M.; Höcker, J.; Baumann, A.; Moos, R.; Panzer, F. Impact of Pressure and Temperature on the Compaction Dynamics and Layer Properties of Powder-Pressed Methylammonium Lead Halide Thick Films. *ACS Appl. Electron. Mater.* **2020**, *2*, 2619−2628.

(16) Xiao, J.; Yang, Y.; Xu, X.; Shi, J.; Zhu, L.; Lv, S.; Wu, H.; Luo, Y.; Li, D.; Meng, Q. Pressure-Assisted $CH_3NH_3PbI_3$ Morphology Reconstruction to Improve the High Performance of Perovskite Solar Cells. *J. Mater. Chem. A* **2015**, *3*, 5289−5293.

(17) Pourdavoud, N.; Haeger, T.; Mayer, A.; Cegielski, P. J.; Giesecke, A. L.; Heiderhoff, R.; Olthof, S.; Zaefferer, S.; Shutsko, I.; Henkel, A.; et al. Room-Temperature Stimulated Emission and Lasing in Recrystallized Cesium Lead Bromide Perovskite Thin Films. *Adv. Mater.* **2019**, *31*, No. 1903717.

(18) Mayer, A.; Buchmüller, M.; Wang, S.; Steinberg, C.; Papenheim, M.; Scheer, H.-C.; Pourdavoud, N.; Haeger, T.; Riedl, T. Thermal Nanoimprint to Improve the Morphology of MAPbX3 (MA = Methylammonium, X = I or Br). *J. Vac. Sci. Technol. B* **2017**, *35*, No. 06G803.

(19) Carter, C. B.; Norton, M. G. *Ceramic Materials - Science and Engineering*, 2nd ed.; Springer Science+Business Media: New York, 2013.

(20) Prochowicz, D.; Franckevičius, M.; Cieślak, A. M.; Zakeeruddin, S. M.; Grätzel, M.; Lewiński, J. Mechanosynthesis of the Hybrid Perovskite $CH_3NH_3PbI_3$: Characterization and the Corresponding Solar Cell Efficiency. *J. Mater. Chem. A* **2015**, *3*, 20772−20777.

(21) Bonomi, S.; Armenise, V.; Accorsi, G.; Colella, S.; Rizzo, A.; Fracassi, F.; Malavasi, L.; Listorti, A. The Effect of Extended Ball-Milling upon Three-Dimensional and Two-Dimensional Perovskite Crystals Properties. *Appl. Sci.* **2020**, *10*, 4775.

(22) Manukyan, K. V.; Yeghishyan, A. V.; Moskovskikh, D. O.; Kapaldo, J.; Mintairov, A.; Mukasyan, A. S. Mechanochemical Synthesis of Methylammonium Lead Iodide Perovskite. *J. Mater. Sci.* **2016**, *51*, 9123−9130.

(23) Leupold, N.; Schötz, K.; Cacovich, S.; Bauer, I.; Schultz, M.; Daubinger, M.; Kaiser, L.; Rebai, A.; Rousset, J.; Köhler, A.; et al. High Versatility and Stability of Mechanochemically Synthesized Halide Perovskite Powders for Optoelectronic Devices. *ACS Appl. Mater. Interfaces* **2019**, *11*, 30259−30268.

(24) Nejand, B. A.; Gharibzadeh, S.; Ahmadi, V.; Shahverdi, H. R. Novel Solvent-Free Perovskite Deposition in Fabrication of Normal and Inverted Architectures of Perovskite Solar Cells. *Sci. Rep.* **2016**, *6*, No. 33649.

(25) López, C. A.; Abia, C.; Rodrigues, J. E.; Serrano-Sánchez, F.; Nemes, N. M.; Martínez, J. L.; Fernandez-Díaz, M. T.; Biškup, N.; Alvarez-Galván, C.; Carrascoso, F.; et al. Enhanced Stability in $CH_3NH_3PbI_3$ Hybrid Perovskite from Mechano-Chemical Synthesis: Structural, Microstructural and Optoelectronic Characterization. *Sci. Rep.* **2020**, *10*, No. 11228.

121

(26) Sadhukhan, P.; Ghosh, D.; Sengupta, P.; Bhattacharyya, S.; Das, S. Unraveling the Charge Transport Mechanism in Mechanochemically Processed Hybrid Perovskite Solar Cell. *Langmuir* **2021**, *37*, 5513−5521.

(27) Rhodes, W. H. Agglomerate and Particle Size Effects on Sintering Yttria-Stabilized Zirconia. *J. Am. Ceram. Soc.* **1981**, *64*, 19−22.

(28) Cai, J.; Laubernds, K.; Galasso, F. S.; Suib, S. L.; Liu, J.; Shen, X.-F.; Begge, E.; Kunz, H. R.; Fenton, J. M. Preparation Method and Cation Dopant Effects on the Particle Size and Properties of BaCeO_3 Perovskites. *J. Am. Ceram. Soc.* **2005**, *88*, 2729−2735.

(29) Liu, J.; De, Lo. D. P. Particle Rearrangement during Powder Compaction. *Metall. Mater. Trans. A* **2001**, *32*, 3117−3124.

(30) Nisr, C.; Ribárik, G.; Ungár, T.; Vaughan, G. B. M.; Cordier, P.; Merkel, S. High Resolution Three-Dimensional X-Ray Diffraction Study of Dislocations in Grains of MgGeO_3 Post-Perovskite at 90 GPa. *J. Geophys. Res.* **2012**, *117*, No. B03201.

(31) Chen, Y.; Lei, Y.; Li, Y.; Yu, Y.; Cai, J.; Chiu, M.-H.; Rao, R.; Gu, Y.; Wang, C.; Choi, W.; et al. Strain Engineering and Epitaxial Stabilization of Halide Perovskites. *Nature* **2020**, *577*, 209−215.

(32) Moloney, E. G.; Yeddu, V.; Saidaminov, M. I. Strain Engineering in Halide Perovskites. *ACS Mater. Lett.* **2020**, *2*, 1495−1508.

(33) Zhang, K.; Alexandrov, I. V.; Kilmametov, A. R.; Valiev, R. Z.; Lu, K. The Crystallite-Size Dependence of Structural Parameters in Pure Ultrafine-Grained Copper. *J. Phys. D: Appl. Phys.* **1997**, *30*, 3008−3015.

(34) Mayer, A.; Haeger, T.; Runkel, M.; Staabs, J.; Rond, J.; van gen Hassend, F.; Görrn, P.; Riedl, T.; Scheer, H.-C. Direct Patterning of Methylammonium Lead Bromide Perovskites by Thermal Imprint. *Appl. Phys. A* **2022**, *128*, 399.

(35) Nordström, J.; Klevan, I.; Alderborn, G. A Particle Rearrangement Index Based on the Kawakita Powder Compression Equation. *J. Pharm. Sci.* **2009**, *98*, 1053−1063.

(36) Crothers, T. W.; Milot, R. L.; Patel, J. B.; Parrott, E. S.; Schlipf, J.; Müller-Buschbaum, P.; Johnston, M. B.; Herz, L. M. Photon Reabsorption Masks Intrinsic Bimolecular Charge-Carrier Recombination in CH_3NH_3PbI_3 Perovskite. *Nano Lett.* **2017**, *17*, 5782−5789.

(37) Herz, L. M. Charge-Carrier Dynamics in Organic-Inorganic Metal Halide Perovskites. *Annu. Rev. Phys. Chem.* **2016**, *67*, 65−89.

(38) D'Innocenzo, V.; Srimath Kandada, A. R.; De Bastiani, M.; Gandini, M.; Petrozza, A. Tuning the Light Emission Properties by Band Gap Engineering in Hybrid Lead Halide Perovskite. *J. Am. Ceram. Soc.* **2014**, *136*, 17730−17733.

(39) Ščajev, P.; Aleksiejūnas, Rn.; Miasojedovas, S.; Nargelas, S.; Inoue, M.; Qin, C.; Matsushima, T.; Adachi, C.; Juršėnas, S. Two Regimes of Carrier Diffusion in Vapor-Deposited Lead-Halide Perovskites. *J. Phys. Chem. C* **2017**, *121*, 21600−21609.

(40) Ščajev, P.; Qin, C.; Aleksiejūnas, Rn.; Baronas, P.; Miasojedovas, S.; Fujihara, T.; Matsushima, T.; Adachi, C.; Juršėnas, S. Diffusion Enhancement in Highly Excited MAPbI_3 Perovskite Layers with Additives. *J. Phys. Chem. Lett.* **2018**, *9*, 3167−3172.

(41) Adhyaksa, G. W. P.; Veldhuizen, L. W.; Kuang, Y.; Brittman, S.; Schropp, R. E. I.; Garnett, E. C. Carrier Diffusion Lengths in Hybrid Perovskites: Processing, Composition, Aging, and Surface Passivation Effects. *Chem. Mater.* **2016**, *28*, 5259−5263.

(42) Becker, M.; Wark, M. Controlling the Crystallization and Grain Size of Sequentially Deposited Planar Perovskite Films via the Permittivity of the Conversion Solution. *Org. Electron.* **2017**, *50*, 87−93.

(43) Panzer, F.; Baderschneider, S.; Gujar, T. P.; Unger, T.; Bagnich, S.; Jakoby, M.; Bässler, H.; Hüttner, S.; Köhler, J.; Moos, R.; et al. Reversible Laser-Induced Amplified Spontaneous Emission from Coexisting Tetragonal and Orthorhombic Phases in Hybrid Lead Halide Perovskites. *Adv. Opt. Mater.* **2016**, *4*, 917−928.

(44) Yamada, Y.; Nakamura, T.; Endo, M.; Wakamiya, A.; Kanemitsu, Y. Near-Band-Edge Optical Responses of Solution-Processed Organic−Inorganic Hybrid Perovskite CH_3NH_3PbI_3 on Mesoporous TiO_2 Electrodes. *Appl. Phys. Express* **2014**, *7*, No. 032302.

(45) Schötz, K.; Askar, A. M.; Peng, W.; Seeberger, D.; Gujar, T. P.; Thelakkat, M.; Köhler, A.; Huettner, S.; Bakr, O. M.; Shankar, K.; Panzer, F. Double Peak Emission in Lead Halide Perovskites by Self-Absorption. *J. Mater. Chem. C* **2020**, *8*, 2289−2300.

(46) Patel, J. B.; Wright, A. D.; Lohmann, K. B.; Peng, K.; Xia, C. Q.; Ball, J. M.; Noel, N. K.; Crothers, T. W.; Wong-Leung, J.; Snaith, H. J.; et al. Light Absorption and Recycling in Hybrid Metal Halide Perovskite Photovoltaic Devices. *Adv. Energy Mater.* **2020**, *10*, No. 1903653.

(47) Fassl, P.; Lami, V.; Berger, F. J.; Falk, L. M.; Zaumseil, J.; Richards, B. S.; Howard, I. A.; Vaynzof, Y.; Paetzold, U. W. Revealing the Internal Luminescence Quantum Efficiency of Perovskite Films via Accurate Quantification of Photon Recycling. *Matter* **2021**, *4*, 1391−1412.

(48) van der Pol, T. P. A.; Datta, K.; Wienk, M. M.; Janssen, R. A. J. The Intrinsic Photoluminescence Spectrum of Perovskite Films. *Adv. Opt. Mater.* **2022**, No. 2102557.

(49) Ledinsky, M.; Schönfeldová, T.; Holovský, J.; Aydin, E.; Hájková, Z.; Landová, L.; Neyková, N.; Fejfar, A.; De Wolf, S. Temperature Dependence of the Urbach Energy in Lead Iodide Perovskites. *J. Phys. Chem. Lett.* **2019**, *10*, 1368−1373.

(50) Schötz, K.; Askar, A. M.; Köhler, A.; Shankar, K.; Panzer, F. Investigating the Tetragonal-to-Orthorhombic Phase Transition of Methylammonium Lead Iodide Single Crystals by Detailed Photoluminescence Analysis. *Adv. Opt. Mater.* **2020**, *8*, No. 2000455.

(51) Frohna, K.; Anaya, M.; Macpherson, S.; Sung, J.; Doherty, T. A. S.; Chiang, Y.-H.; Winchester, A. J.; Orr, K. W. P.; Parker, J. E.; Quinn, P. D.; et al. Nanoscale Chemical Heterogeneity Dominates the Optoelectronic Response of Alloyed Perovskite Solar Cells. *Nat. Nanotechnol.* **2022**, *17*, 190−196.

(52) Mehdizadeh-Rad, H.; Singh, J. Influence of Urbach Energy, Temperature, and Longitudinal Position in the Active Layer on Carrier Diffusion Length in Perovskite Solar Cells. *Chemphyschem* **2019**, *20*, 2712−2717.

(53) Stoeckel, M.-A.; Gobbi, M.; Bonacchi, S.; Liscio, F.; Ferlauto, L.; Orgiu, E.; Samorì, P. Reversible, Fast, and Wide-Range Oxygen Sensor Based on Nanostructured Organometal Halide Perovskite. *Adv. Mater.* **2017**, *29*, No. 1702469.

(54) Haque, M. A.; Syed, A.; Akhtar, F. H.; Shevate, R.; Singh, S.; Peinemann, K.-V.; Baran, D.; Wu, T. Giant Humidity Effect on Hybrid Halide Perovskite Microstripes: Reversibility and Sensing Mechanism. *ACS Appl. Mater. Interfaces* **2019**, *11*, 29821−29829.

(55) Zhao, X.; Sun, Y.; Liu, S.; Chen, G.; Chen, P.; Wang, J.; Cao, W.; Wang, C. Humidity Sensitivity Behavior of CH_3NH_3PbI_3 Perovskite. *Nanomaterials* **2022**, *12*, 523.

(56) Kim, G. Y.; Senocrate, A.; Yang, T.-Y.; Gregori, G.; Grätzel, M.; Maier, J. Large Tunable Photoeffect on Ion Conduction in Halide Perovskites and Implications for Photodecomposition. *Nat. Mater.* **2018**, *17*, 445−449.

(57) Kwon, K. C.; Hong, K.; Van Le, Q.; Lee, S. Y.; Choi, J.; Kim, K.-B.; Kim, S. Y.; Jang, H. W. Inhibition of Ion Migration for Reliable Operation of Organolead Halide Perovskite-Based Metal/Semiconductor/Metal Broadband Photodetectors. *Adv. Funct. Mater.* **2016**, *26*, 4213−4222.

(58) Zhang, T.; Hu, C.; Yang, S. Ion Migration: A "Double-Edged Sword" for Halide-Perovskite-Based Electronic Devices. *Small Methods* **2020**, *4*, No. 1900552.

(59) Shao, Y.; Fang, Y.; Li, T.; Wang, Q.; Dong, Q.; Deng, Y.; Yuan, Y.; Wei, H.; Wang, M.; Gruverman, A.; et al. Grain Boundary Dominated Ion Migration in Polycrystalline Organic−Inorganic Halide Perovskite Films. *Energy Environ. Sci.* **2016**, *9*, 1752−1759.

(60) Futscher, M. H.; Lee, J. M.; McGovern, L.; Muscarella, L. A.; Wang, T.; Haider, M. I.; Fakharuddin, A.; Schmidt-Mende, L.; Ehrler, B. Quantification of Ion Migration in CH_3NH_3PbI_3 Perovskite Solar Cells by Transient Capacitance Measurements. *Mater. Horiz.* **2019**, *6*, 1497−1503.

(61) Tammireddy, S.; Reichert, S.; An, Q.; Taylor, A. D.; Ji, R.; Paulus, F.; Vaynzof, Y.; Deibel, C. Temperature-Dependent Ionic Conductivity and Properties of Iodine-Related Defects in Metal Halide Perovskites. *ACS Energy Lett.* **2022**, *7*, 310−319.

(62) Leupold, N.; Seibel, A. L.; Moos, R.; Panzer, F. Electrical Conductivity of Halide Perovskites Follows Expectations from Classical Defect Chemistry. *Eur. J. Inorg. Chem.* **2021**, *2021*, 2882−2889.

(63) Park, J.-S.; Calbo, J.; Jung, Y.-K.; Whalley, L. D.; Walsh, A. Accumulation of Deep Traps at Grain Boundaries in Halide Perovskites. *ACS Energy Lett.* **2019**, *4*, 1321−1327.

(64) Phung, N.; Al-Ashouri, A.; Meloni, S.; Mattoni, A.; Albrecht, S.; Unger, E. L.; Merdasa, A.; Abate, A. The Role of Grain Boundaries on Ionic Defect Migration in Metal Halide Perovskites. *Adv. Energy Mater.* **2020**, *10*, No. 1903735.

(65) Tan, S.; Yavuz, I.; De Marco, N.; Huang, T.; Lee, S.-J.; Choi, C. S.; Wang, M.; Nuryyeva, S.; Wang, R.; Zhao, Y.; et al. Steric Impediment of Ion Migration Contributes to Improved Operational Stability of Perovskite Solar Cells. *Adv. Mater.* **2020**, *32*, No. 1906995.

(66) Zhou, W.; Gu, J.; Yang, Z.; Wang, M.; Zhao, Q. Basis and Effects of Ion Migration on Photovoltaic Performance of Perovskite Solar Cells. *J. Phys. D: Appl. Phys.* **2020**, *54*, No. 063001.

📖 Recommended by ACS

Supporting Information to

How the Microstructure of MAPbI₃ Powder Impacts Pressure-Induced Compaction and Optoelectronic Thick-Film Properties

Christina Witt[1], Nico Leupold[2], Philipp Ramming[1], Konstantin Schötz[1], Ralf Moos[2], Fabian Panzer[1*]

[1] Soft Matter Optoelectronics, University of Bayreuth, Bayreuth 95440, Germany

[2] Department of Functional Materials, University of Bayreuth, Bayreuth 95440, Germany

Corresponding Author:

[*]E-Mail: fabian.panzer@uni-bayreuth.de

S1

124

1. Precursor preparation

MAI   PbI$_2$
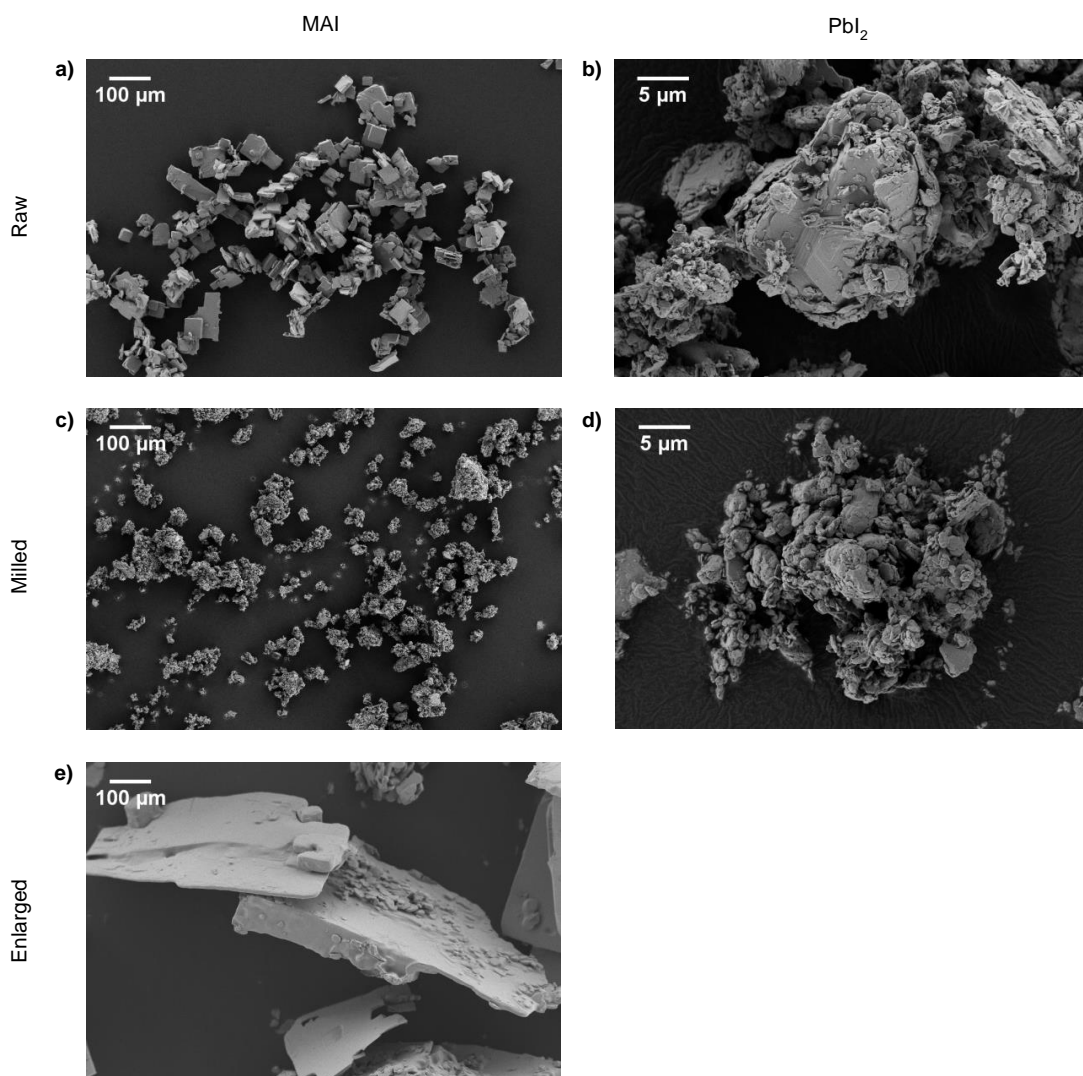
Figure S1: SEM images of the differently pre-treated precursors MAI and PbI$_2$ used for the preparation of MAPbI$_3$ powder by mechanochemical synthesis: (a) "Raw MAI". (b) "Raw PbI$_2$". (c) "Milled MAI". (d) "Milled PbI$_2$". (e) "Enlarged MAI".

Source Powder	MAI / mmol	PbI_2 / mmol	MAI : PbI_2
"Small"	9.75	9.76	1.00
"Medium"	9.75	9.78	1.00
"Large"	8.61	8.52	1.01

Table S1: Amounts of precursors MAI and PbI_2 and the ratio of precursors used for manufacturing MAPbI$_3$ powder with small, medium and large powder particle sizes by mechanochemical synthesis.

To prepare the MAI precursor powders, first 28.8 mL of methylamine (33 wt% in ethanol, Sigma Aldrich) were dissolved in 170 mL of ethanol under argon atmosphere. The solution was then cooled using an ice bath and 16 mL of HI (57 wt% in H_2O, Alfa Aesar) were added dropwise within 30 minutes of stirring. Stirring of the solution was continued overnight. Then the solvent was removed using a rotary evaporator and the remaining powder was washed with an ether-ethanol mixture. Finally, the powder was redissolved in ethanol and ether was dropped into the concentrated solution of MAI and ethanol for the crystallization to the final white MAI precursor powder. In this last process, the dropping rate of the ether into the concentrated solution of MAI and ethanol affects the size of the resulting MAI structures. For the MAI powder prepared by the standard procedure ("Raw MAI", Figure S1a), about 1 minute was taken for the ether to drop into the concentrated solution of MAI and ethanol. For the preparation of the MAI powder with larger crystals ("Enlarged MAI", Figure S1e), the time for dropping the ether in was increased to about 5-10 minutes.

The PbI_2 precursor powder was purchased from TCI (99.99% purity, "Raw PbI_2", Figure S1b). To obtain precursor powder with smaller particle size ("Milled PbI_2", Figure S1d), 18.5 g of the "Raw PbI_2" precursor powder were milled in the planetary ball mill for a total milling time of 30 min.

To obtain "Milled MAI" (Figure S1c), 5.5 g of the "Raw MAI" precursor powder were milled for 30 min in the planetary ball mill.

2. Mechanochemical synthesis of MAPbI₃ powders
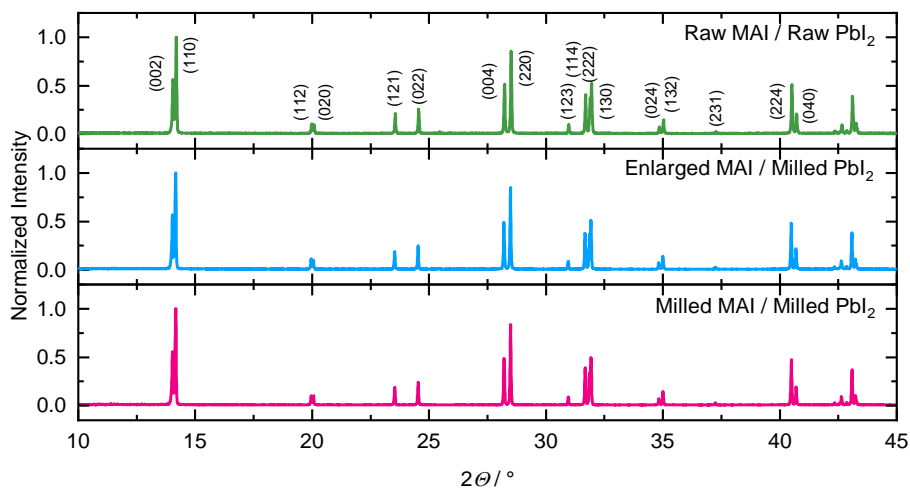
Figure S2: XRD patterns of MAPbI₃ powders manufactured via mechanochemical synthesis using different MAI and PbI₂ precursor powders with reflexes indexed (top).

The MAPbI₃ powders were manufactured from the precursor powders MAI and PbI₂ under ambient conditions via mechanochemical synthesis. For the powders with small and medium particle sizes (Figure S3a,b) 1.55 g MAI and 4.5 g PbI₂ were placed in a 80 mL ZrO₂ milling jar together with 5 mL cyclohexane as milling agent and 25 ZrO₂ milling balls with a diameter of 10 mm. For the milling process, a Fritsch "Pulverisette 5/4" planetary ball mill with 400 rpm was used. After 5 min of milling, a break of 20 min was taken to prevent the milling jar from becoming too hot as a result of rotation and friction. This procedure was repeated until a total milling time of 25 min was reached. For the powder with large particle sizes (Figure S3c) 1.37 g MAI and 4 g PbI₂ were used. After the milling process was completed, the cyclohexane was evaporated to obtain the final black MAPbI₃ powder.
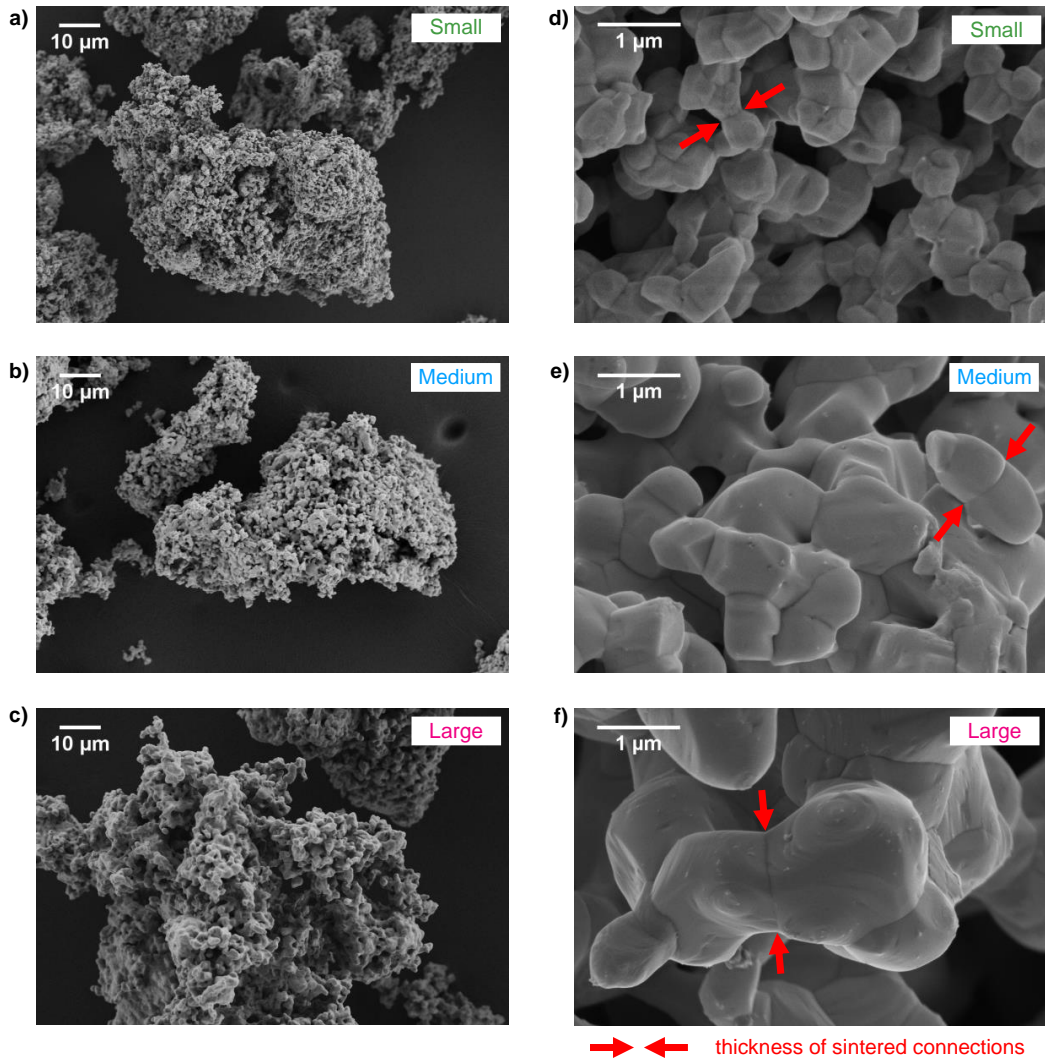
Figure S3: SEM images of the three different MAPbI₃ powders with (a) small, (b) medium and (c) large powder particle sizes showing agglomerates. Higher magnification SEM images of the MAPbI₃ powders with (d) small, (e) medium and (f) large powder particle sizes with thickness of sintered connections indicated by red arrows.

Determination of powder particle size: We considered SEM images with suitable magnification and highlighted the particle boundaries with a marker. Then the images were digitalized and the area of every single particle was determined using the Software imageJ. From the particle area, an equivalent diameter of a circle was calculated and considered as particle size. For the powder "Small" 185, for "Medium" 91, and for "Large" 147 particles were used to calculate the mean diameter and standard deviation.

3. Pellet pressing – Pressure relaxation analyses
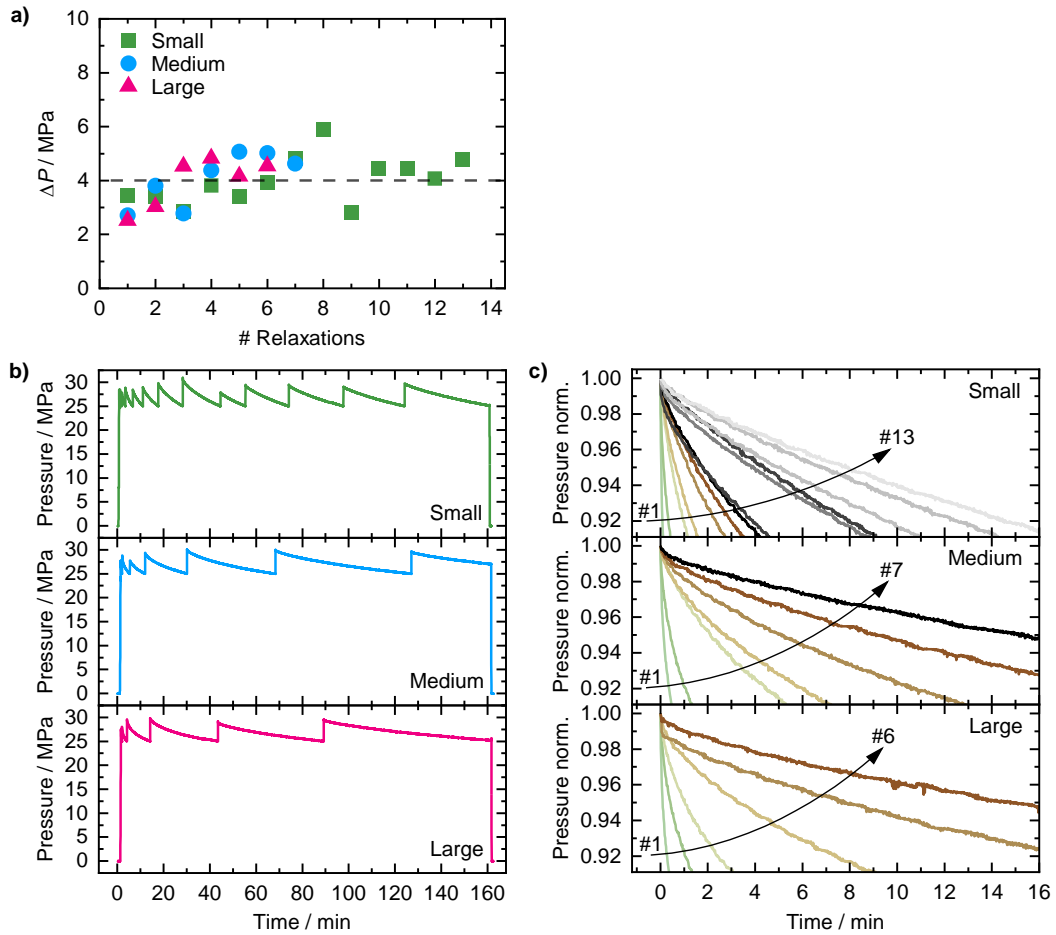
Figure S4: (a) Pressure difference ΔP of the pressure readjustments shown in (b) to maintain the target pressure level of 25 MPa as a function of consecutive pressure relaxations for MAPbI$_3$ powders with small (green squares), medium (blue dots) and large (red triangles) powder particle sizes. **(b)** Temporal evolution of the applied pressure during pressing of MAPbI$_3$ powders with small (top), medium (middle) and large (bottom) powder particle sizes at a target pressure level of 25 MPa. **(c)** Pressure relaxations from (b), shown normalized and with their maximum value at time zero for pressed MAPbI$_3$ powders with small (top), medium (middle) and large (bottom) powder particle sizes.

For pressing powders to pellets a home-built mechanical press was used (illustration in Figure 2b in the main text). By means of a handle mounted on a threaded rod, the press punch can be moved down onto the pressing tool in order to apply a pressure. The circular pressing tool

from Maassen with a diameter of 13 mm is placed on a carrier shell under which pressure sensors are mounted to record the applied pressure. The pressing tool contains two polished carbide KXF pressing plates to ensure a good quality of the pressed pellets. Free-standing pellets with thicknesses between about 0.83 mm and 0.95 mm were pressed from 0.4 g $MAPbI_3$ powder respectively. Pellet batches at room temperature with 160 min pressing time at a target pressure level of 25 MPa as well as with 20 min pressing time at a target pressure level of 100 MPa were produced for this work.
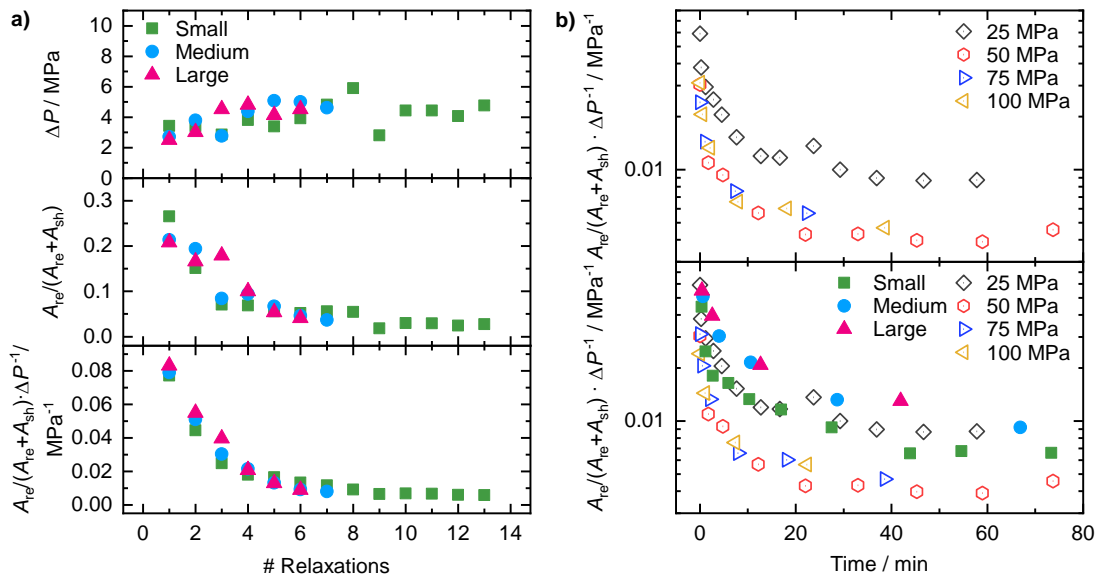
Figure S5: Analyses of the amplitude ratio extracted from the fits of the pressure relaxations according to eq. 1 in the main text for $MAPbI_3$ powders with small (green squares), medium (blue dots) and large (red triangles) powder particle sizes: (a) Pressure difference of the pressure readjustments (top), amplitude ratio $A_{re}/(A_{re}+A_{sh})$ (middle) and $A_{re}/(A_{re}+A_{sh}) \cdot \Delta P^{-1}$ (bottom) as a function of consecutive pressure relaxations. (b) ΔP corrected amplitude ratio $A_{re}/(A_{re}+A_{sh}) \cdot \Delta P^{-1}$ as a function of pressing time for one $MAPbI_3$ powder batch pressed with four different target pressures of 25 MPa (black diamond), 50 MPa (red hexagon), 75 MPa (blue triangle) and 100 MPa (yellow triangle) (top) and for $MAPbI_3$ powders with small (green squares), medium (blue dots) and large (red triangles) powder particle sizes pressed with 25 MPa (bottom).

The amplitude ratio $A_{re}/(A_{re}+A_{sh})$ (Figure S5a middle) extracted from the fits of the pressure relaxations according to eq. 1 in the main text is modulated by the pressure difference ΔP of the pressure readjustments (Figure S5a top). A correction of this modulation ($A_{re}/(A_{re}+A_{sh}) \cdot \Delta P^{-1}$, Figure S5a bottom) is necessary to derive reliable information from the amplitude ratios.

Furthermore, to analyze the role of the individual compaction processes, a plot of the corrected amplitude ratio as a function of pressing time is of interest, since the importance of the individual compaction processes changes with pressing time (see Section 3.2 in the main text). To gain a better understanding of the compaction processes from the amplitude ratio, Figure S5b (top) shows the corrected amplitude ratio of a MAPbI$_3$ powder batch pressed with different target pressures of 25 MPa, 50 MPa, 75 MPa and 100 MPa. The decrease of the corrected amplitude ratio with pressing time at a pressing pressure of 25 MPa is significantly lower than at the other pressing pressures ≥ 50 MPa. This indicates less plastic deformation and / or crushing processes at pressures below 50 MPa and is in line with the results from our previous work.[1] The corrected amplitude ratios of the three different MAPbI$_3$ powders "Small", "Medium" and "Large" pressed at 25 MPa fit well to the values of the reference batch pressed at 25 MPa (see Figure S5b bottom).
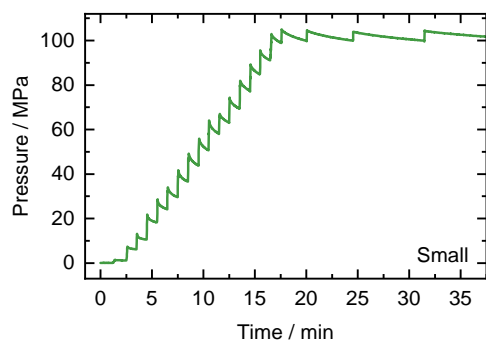
Figure S6: Temporal evolution of the applied pressure during pressing of the MAPbI$_3$ powder with small powder particle sizes at a target pressure level of 100 MPa.

At the beginning of the pressing process of the 100 MPa pellets, the pressure was increased following a linear pressure increase ramp with a rate of 6.67 MPa/min until the target pressure level was reached. Then, similar to the 25 MPa pellets (see Figure S4b), the target pressure level was maintained by readjusting the pressure as soon as the pressure value fell below 100 MPa. After the target pressure level was maintained for 20 min, the pressure was removed.

In contrast to the 25 MPa pellets (see Figure S4b), where the pressure was directly adjusted to the target pressure level, a pressure increase ramp was used for the 100 MPa pellets to ensure a smooth and successful pellet formation without cracking.

4. Additional pellet morphology analyses
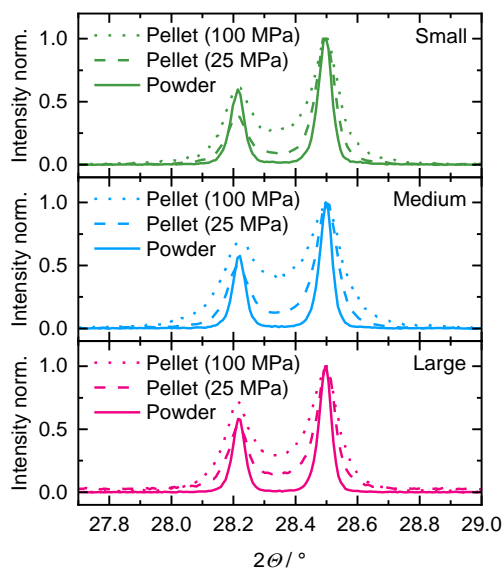
Figure S7: XRD patterns showing the (004) and (220) MAPbI$_3$ reflexes of powders and pellets pressed from them at a target pressure level of 25 MPa and 100 MPa for MAPbI$_3$ powders with small (top), medium (middle) and large (bottom) powder particle sizes.

Matching the XRD pattern of the powder "Large", all other XRD patterns were shifted along the x-axis to compensate for deviations owing to e.g., the measurement-related height error due to specimen surface displacement.[2]

We used the Rietveld refinement method to extract crystallite sizes and microstrain from the XRD patterns of all powders and pellets (see exemplary fits in Figure S8 and fit results in Table 1 in the main text). To determine the error range of crystallite size and microstrain, we considered the XRD-pattern that was measured for each sample. By varying the FWHM, while maintaining a satisfying fit quality, we considered the change in resulting crystallite size and microstrain values to estimate the error range.
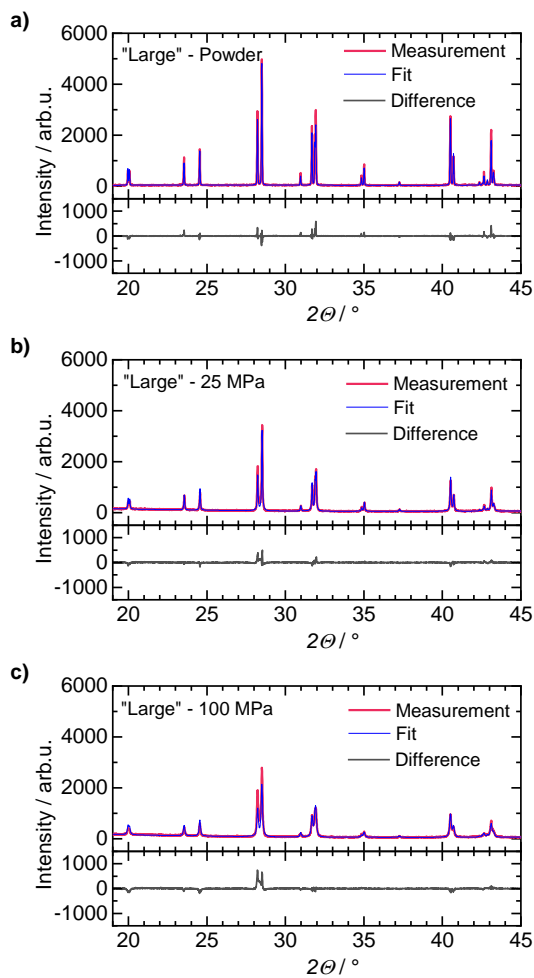
Figure S8: Measured XRD-Patterns (red), the fits from Rietveld refinement (blue) and the difference between measured and fitted intensity (dark grey): (a) Powder "Large". (b) Pellet pressed at 25 MPa from powder "Large". (c) Pellet pressed at 100 MPa from powder "Large".

S11
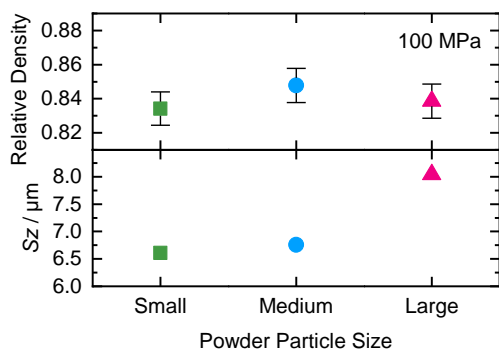
Figure S9: Relative density (top) and surface roughness *Sz* (bottom) of pellets pressed at 100 MPa target pressure level using MAPbI₃ powders with small (green squares), medium (blue dots) and large (red triangles) powder particle sizes.

The pellet properties density and surface roughness of the 100 MPa pellets were determined similar to the 25 MPa pellets (see Figure 4d,e) and are shown in Figure S9. The relative density of the pressed pellets was calculated based on the pellet area, the pellet mass, and the pellet thickness taking into account the density of a MAPbI₃ single crystal (4.159 g/cm³).[1] The pellet area defined by the pressing tool used was 1.327 cm², the pellet mass was determined with a laboratory balance, and the pellet thickness was measured using a micrometer screw. The relative density of the 100 MPa pellets made from the powders "Small", "Medium" and "Large" in Figure S9 (top) is the same for all three pellets within the experimental error. Moreover, the relative density of the 100 MPa pellets with an average of ~0.84 is clearly above the relative densities of the 25 MPa pellets (< 0.80).

The surface roughness *Sz* (maximum height of the surface) of the pellets was determined using a 3D laser scanning microscope ZEISS LSM 800 Mat. An area of 350 µm x 350 µm was measured in the center of each side of the pellets and the mean value was determined from the roughness of both sides. The surface roughness *Sz* of the 100 MPa pellets in Figure S9 (bottom) shows the same trend as for the 25 MPa pellets, that the surface roughness increases with particle size. However, due to the higher pressing pressure and the thus more pronounced plastic deformation and crushing processes, the surface roughness of the 100 MPa pellets appears to be lower (< 8.1 µm) than the surface roughness of the 25 MPa pellets. This is especially the case when using the powders "Medium" and "Large" for which the plastic deformation is particularly pronounced during pressing (according to Section 3.3 in the main text).

5. Analyses of optoelectronic properties

Since the pellets have to be contacted for the electrical measurements, i.e., electrodes have to be applied, smooth pellet surfaces are necessary. Considering the pellet surface properties of the pellets pressed at 25 MPa in Figure 4a-c,e, we used the pellets produced at 100 MPa (see Figure S9) for the optoelectronic investigations.
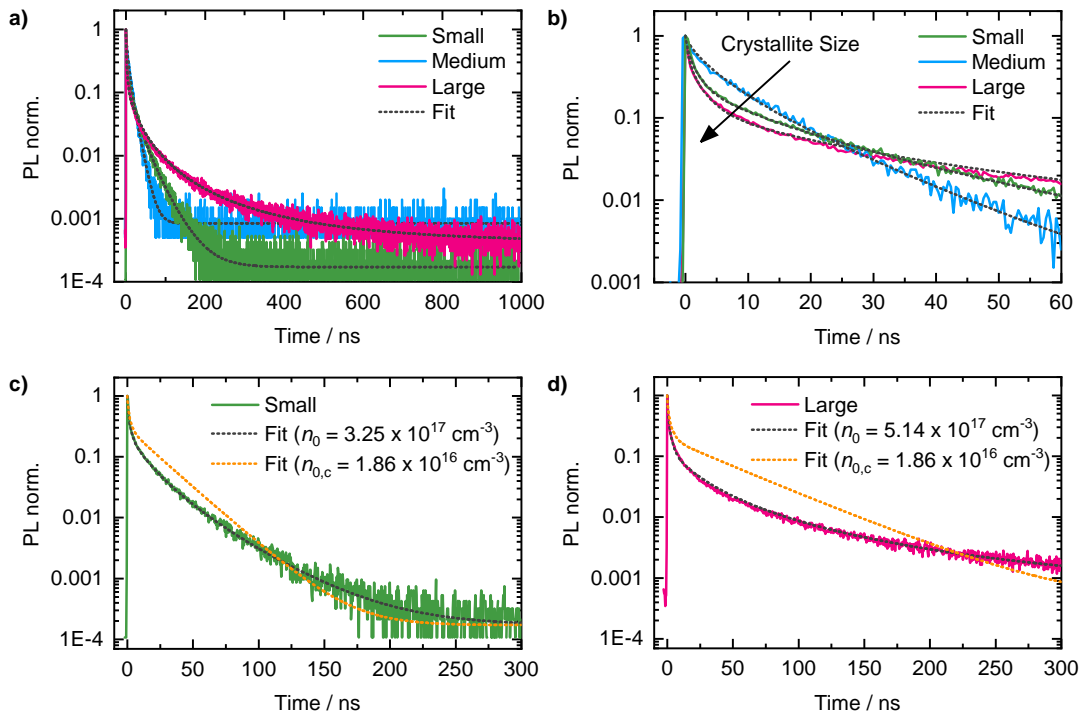
Figure S10: Time-resolved PL curves for 100 MPa pellets made from MAPbI$_3$ powders with small (green), medium (blue) and large (red) powder particle sizes: (a) Normalized time-resolved PL curves and corresponding fits according to eq. 2 in the main text (gray dotted lines). (b) Section from (a), showing in detail the first part of the PL decays. (c), (d) Normalized time-resolved PL curves and corresponding fits according to eq. 2 in the main text using the calculated charge carrier density ($n_{0,c}$ = 1.86 x 10^{16} cm^{-3}, see orange dotted lines) and a higher charge carrier density (see gray dotted lines).

The time-resolved PL curves of 100 MPa pellets in Figure 5a and S10a,b were fitted using eq. 2 in the main text according to the ABC model.[3] For the application of eq. 2 it is assumed that electron and hole density are equal.[3-4] In eq. 2 k_1 is the rate constant for monomolecular (non-radiative) recombination, k_2 is the rate constant for bimolecular (radiative) recombination and k_3 is the rate constant for Auger (non-radiative) recombination. Charge carrier diffusion is

S13

taken into account in the last term of eq. 2 with the diffusion constant D and the thickness z = 1.0 µm - 1.5 µm, in which the charge carrier processes are assumed to be relevant.[5] We used the intrinsic value of k_2 = 6.8 × 10^{-10} cm^3 s^{-1} from the work of Crothers et al.[5] for the fittings of the time-resolved PL curves to keep the fittings as simple as possible. The rate constant k_3 = 1.0 × 10^{-29} cm^6 s^{-1} was also fixed based on the literature value according to the work of Crothers et al.[5] As a starting value, the initial charge carrier density n_0 was estimated according to

$$n_0 = \frac{F}{E_{\text{Photon}}} \cdot \alpha \qquad\qquad\qquad (S1)$$

with the laser fluence F, the energy of the exciting photons E_{Photon} and the absorption coefficient α.[6] The calculated value of the initial charge carrier density is $n_{0,c}$ = 1.86 × 10^{16} cm^{-3}. For optimum fit results, however, the calculated initial charge carrier density was allowed to vary to a certain extent. Therefore, the initial charge carrier density used in the fits of the time-resolved PL curves is smaller (n_0 = 1.67 × 10^{16} cm^{-3}) than the calculated value for the pellet from the powder "Medium", and larger for the pellets from the powders "Small" (n_0 = 3.25 × 10^{17} cm^{-3}) and "Large" (n_0 = 5.14 × 10^{17} cm^{-3}).

For the pellets from the powders "Small" and "Large", in addition to the fits with variable larger charge carrier density (gray dotted lines), analogous fits using the smaller calculated initial charge carrier density (orange dotted lines) are shown in Figure S10c,d. The fits with the calculated initial charge carrier density (orange dotted lines) prove that the first drop of the time-resolved PL curves actually results from diffusion and not from the increased initial charge carrier density. Thus, our fit results in Figure 5a and S10a,b using slightly varying initial charge carrier densities are reliable.

A faster first drop of the time-resolved PL curves at short times indicates stronger diffusion.[5] In our work, the first drop of the transient PL curves at short times is the weakest for the pellet from the powder "Medium" and the strongest for the pellet from the powder "Large" (see Figure S10b). This is also reflected in the diffusion constants D_{Medium} = 0.06 cm^2 s^{-1}, D_{Small} = 0.22 cm^2 s^{-1}, and D_{Large} = 0.35 cm^2 s^{-1} obtained by fitting eq. 2 in the main text to the time-resolved PL curves. Both the strength of the first drop of the time-resolved PL curves and the diffusion constant increase with increasing crystallite size. Thus, the 100 MPa pellets exhibit an increased diffusion with increasing crystallite size.
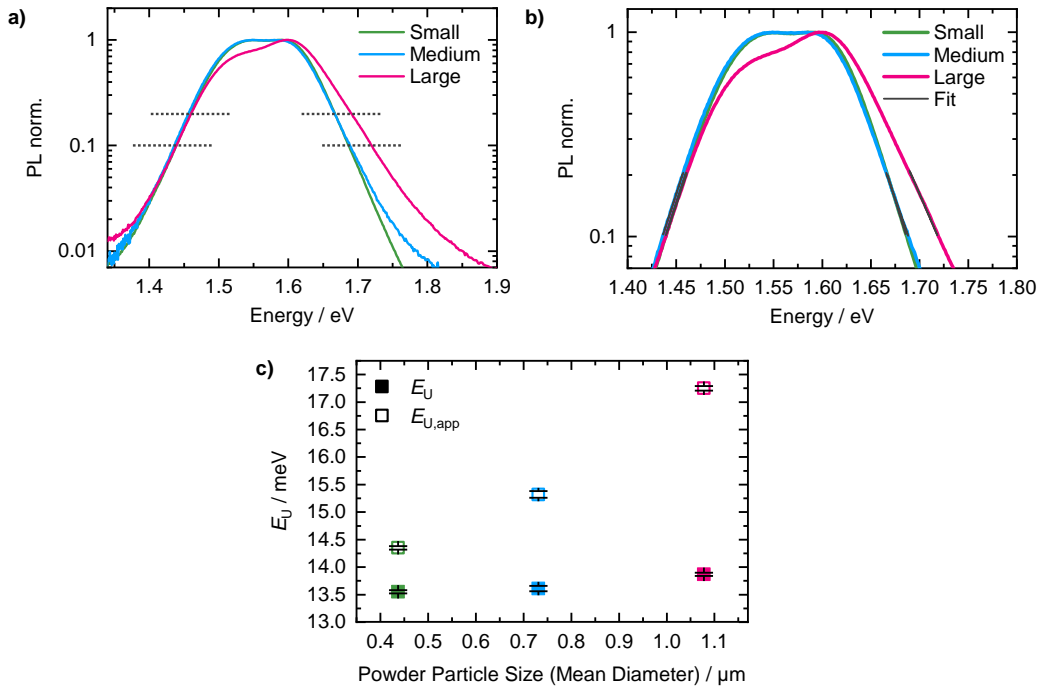
Figure S11: Extraction of Urbach energies from PL spectra of pellets pressed at 100 MPa target pressure level using MAPbI$_3$ powders with small (green), medium (blue) and large (red) powder particle sizes: (a) Normalized steady-state PL spectra with fit ranges indicated by gray dotted lines. (b) Section from (a) with applied fits. (c) Apparent Urbach energies $E_{U,app}$ (blank squares) and temperature-corrected Urbach energies E_U (full squares) as a function of powder particle size.

Below the bandgap, the absorption coefficient of MAPbI$_3$ decreases exponentially with decreasing energy. This exponential decrease is characteristic for the so-called Urbach tail absorption, which is attributed to absorbing states due to disorder. The extent of disorder is reflected in the slope of the Urbach tail and is described by the Urbach energy E_U.[7-9]

It is known, that the low energy edge in the PL spectra of MAPbI$_3$ perovskites is determined by the shape of the absorption coefficient.[10] For this reason, the Urbach energy can get extracted from the low energy edge of PL spectra, as already done by Fassl et al.[11] Therefore, first the high energy edge (fit range indicated in Figure S11a, fits in Figure S11b) is fitted according to $\mathrm{PL}(E) = c_1 \cdot \exp\left(-\frac{E}{k_B T_{app}}\right)$ to extract the temperature T_{app}, which is higher than the measurement temperature T and is assumed to be caused by self-absorption effects.[8] Next, this temperature T_{app} is used to fit the low energy edge (fit range indicated in Figure S11a, fits in Figure S11b) according to $\mathrm{PL}(E) = c_2 \cdot \exp\left(\frac{E-E_0}{E_{U,app}} - \frac{E}{k_B T_{app}}\right)$ to determine the

S15

138

apparent Urbach energy $E_{U,app}$ (see blank squares in Figure S11c). Finally, the temperature-corrected intrinsic Urbach energy E_U (full squares in Figure S11c) can be calculated according to $E_U = \left[\frac{1}{E_{U,app}} + \frac{1}{k_B}\left(\frac{1}{T} - \frac{1}{T_{app}} \right) \right]^{-1}$.[8] It is noted that in the above fit equations k_B is the Boltzmann constant, E is the energy, E_0 is a material constant, and c_1 and c_2 are prefactors. Figure S11c shows that the trend of the Urbach energy increasing with powder particle size is even more pronounced for the apparent Urbach energies than for the intrinsic Urbach energies.
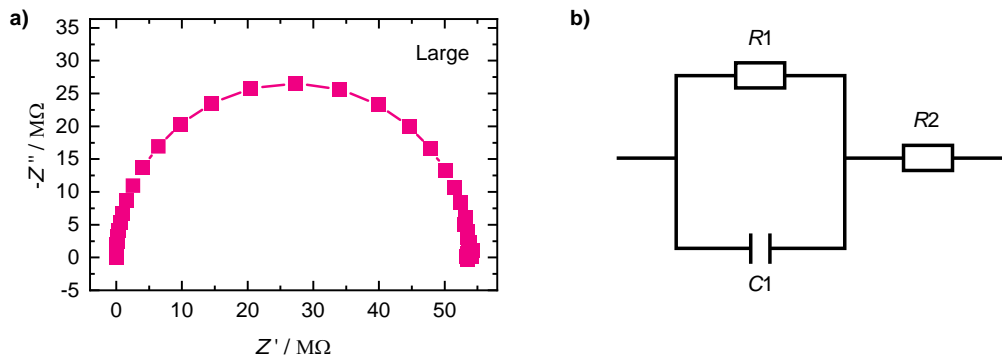
Figure S12: (a) Impedance spectrum as Nyquist plot of a 100 MPa pellet made from MAPbI$_3$ powder with large powder particle sizes. (b) Equivalent circuit for the fits of the impedance spectra.

For the electrical measurements, four pairs of gold electrodes were evaporated onto the pellet surfaces using a shadow mask. The gold was deposited using a rate of 0.02 nm/s until the desired electrode thickness of 100 nm was reached. The resulting electrode pairs formed a 1.0 mm wide channel with a distance between the electrodes of 150 μm.

The measured impedance spectra (exemplarily shown for the 100 MPa pellet made from the powder "Large" in Figure S12a) were fitted according to an equivalent circuit consisting of a resistance in series to an RC parallel element (see sketch in Figure S12b). From the fits, the resistance $R1$ of the MAPbI$_3$ pellets was extracted.

The electrical dark conductivity σ_{dark} was calculated according to

$$\sigma_{\text{dark}} = (R1 \cdot f)^{-1} \tag{S2}$$

with the resistance $R1$ of the MAPbI$_3$ pellets and a simulated geometry factor f = 0.00221 m. The geometry factor takes into account the shape of the top electrodes as well as the dependence of the electric field distribution on the pellet thickness.

Supporting References

1. Witt, C.; Schmid, A.; Leupold, N.; Schultz, M.; Höcker, J.; Baumann, A.; Moos, R.; Panzer, F. Impact of Pressure and Temperature on the Compaction Dynamics and Layer Properties of Powder-Pressed Methylammonium Lead Halide Thick Films. *ACS Appl. Electron. Mater.* **2020,** *2*, 2619-2628.
2. King, H. W.; Payzant, E. A. Error Corrections for X-Ray Powder Diffractometry. *Can. Metall. Q.* **2001,** *40*, 385-394.
3. Kiligaridis, A.; Frantsuzov, P. A.; Yangui, A.; Seth, S.; Li, J.; An, Q.; Vaynzof, Y.; Scheblykin, I. G. Are Shockley-Read-Hall and ABC Models Valid for Lead Halide Perovskites? *Nat. Commun.* **2021,** *12*, 3329.
4. Ramming, P.; Leupold, N.; Schötz, K.; Köhler, A.; Moos, R.; Grüninger, H.; Panzer, F. Suppressed Ion Migration in Powder-Based Perovskite Thick Films Using an Ionic Liquid. *J. Mater. Chem. C* **2021,** *9*, 11827-11837.
5. Crothers, T. W.; Milot, R. L.; Patel, J. B.; Parrott, E. S.; Schlipf, J.; Müller-Buschbaum, P.; Johnston, M. B.; Herz, L. M. Photon Reabsorption Masks Intrinsic Bimolecular Charge-Carrier Recombination in $CH_3NH_3PbI_3$ Perovskite. *Nano Lett.* **2017,** *17*, 5782-5789.
6. Schötz, K.; Askar, A. M.; Peng, W.; Seeberger, D.; Gujar, T. P.; Thelakkat, M.; Köhler, A.; Huettner, S.; Bakr, O. M.; Shankar, K., et al. Double Peak Emission in Lead Halide Perovskites by Self-Absorption. *J. Mater. Chem. C* **2020,** *8*, 2289-2300.
7. Ledinsky, M.; Schönfeldová, T.; Holovský, J.; Aydin, E.; Hájková, Z.; Landová, L.; Neyková, N.; Fejfar, A.; De Wolf, S. Temperature Dependence of the Urbach Energy in Lead Iodide Perovskites. *J. Phys. Chem. Lett.* **2019,** *10*, 1368-1373.
8. Schötz, K.; Askar, A. M.; Köhler, A.; Shankar, K.; Panzer, F. Investigating the Tetragonal-to-Orthorhombic Phase Transition of Methylammonium Lead Iodide Single Crystals by Detailed Photoluminescence Analysis. *Adv. Opt. Mater.* **2020,** *8*, 2000455.
9. Cody, G. D.; Tiedje, T.; Abeles, B.; Brooks, B.; Goldstein, Y. Disorder and the Optical-Absorption Edge of Hydrogenated Amorphous Silicon. *Phys. Rev. Lett.* **1981,** *47*, 1480-1483.
10. Staub, F.; Hempel, H.; Hebig, J.-C.; Mock, J.; Paetzold, U. W.; Rau, U.; Unold, T.; Kirchartz, T. Beyond Bulk Lifetimes: Insights into Lead Halide Perovskite Films from Time-Resolved Photoluminescence. *Phys. Rev. Appl.* **2016,** *6*, 044017.
11. Fassl, P.; Lami, V.; Berger, F. J.; Falk, L. M.; Zaumseil, J.; Richards, B. S.; Howard, I. A.; Vaynzof, Y.; Paetzold, U. W. Revealing the Internal Luminescence Quantum Efficiency of Perovskite Films via Accurate Quantification of Photon Recycling. *Matter* **2021,** *4*, 1391-1412.

4.4 Orientation and Grain Size in MAPbI$_3$ Thin Films: Influence on Phase Transition, Disorder, and Defects

Christina Witt, Konstantin Schötz, Meike Kuhn, Nico Leupold, Simon Biberger, Philipp Ramming, Frank-Julian Kahle, Anna Köhler, Ralf Moos, Eva M. Herzig, and Fabian Panzer.

Orientation and Grain Size in MAPbI₃ Thin Films: Influence on Phase Transition, Disorder, and Defects

Christina Witt, Konstantin Schötz, Meike Kuhn, Nico Leupold, Simon Biberger, Philipp Ramming, Frank-Julian Kahle, Anna Köhler, Ralf Moos, Eva M. Herzig, and Fabian Panzer*

ACCESS | Metrics & More | Article Recommendations | Supporting Information

ABSTRACT: In recent years, record efficiencies of halide perovskite-based devices have been achieved by processing high-quality thin films, where small morphology differences seem to be relevant for optimized optoelectronic functionality. However, a detailed understanding on how small morphological changes in perovskite films affect their structural and optoelectronic properties is still missing. Here, we investigate the influence of small morphology differences (i.e., increased grain size and crystallographic orientation), which are induced by hot-pressing methylammonium lead iodide (MAPbI₃) thin films, on the structural properties, phase transition behavior, energetic disorder, and defects. To this end, detailed temperature-dependent photoluminescence (PL) and absorption analyses from 300 K down to 5 K are performed. The morphology differences, confirmed by scanning electron microscopy and X-ray diffractometry analyses, result in an increased phase transition temperature for hot-pressed (HP) films, which we attribute to less strain. Moreover, fluence-dependent and transient PL measurements reveal a lower defect density in HP films. Here, besides grain size, also the degree of orientation appears to enhance the charge carrier lifetimes. The identified interdependence of strain and defect properties with film morphology suggests small differences in the perovskite's energetic disorder. Our work thus emphasizes the importance that even small structural differences in halide perovskites have on their optoelectronic functionality, spurring their further optimization.
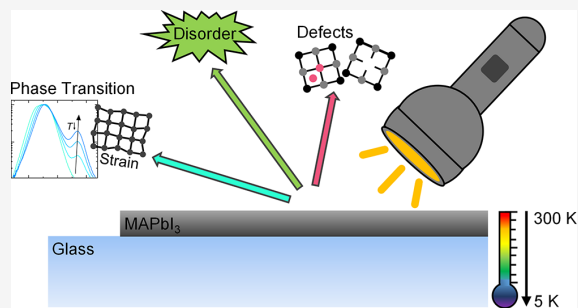
1. INTRODUCTION

Even though being relatively straightforward and inexpensive to produce, halide perovskites still exhibit remarkable semiconducting properties. Accordingly, they are currently considered one of the most promising candidates for the next generation of a variety of optoelectronic devices.[1,2] In contrast to conventional inorganic semiconductors, halide perovskites are exceptionally robust against the presence of defects as corresponding defect energy levels are typically located close to or in their conduction and valence bands, respectively.[3−5] That is why even with polycrystalline perovskite layers, remarkably high device efficiencies are achievable.[6−8]

However, to produce perovskite-based optoelectronic devices with record efficiencies, it is necessary to use perovskite films with optimized morphology. For example, large grain sizes and uniform crystallographic orientation are aimed for in the case of perovskite solar cells.[9−13] Various research reports indicate that even small improvements in the morphology of perovskites are important for further optimizing their optoelectronic functionality.[9,12−14]

Nevertheless, while various studies investigated the influence of distinct morphology changes on the resulting device

properties in the past,[9−15] only little is known about how small morphology changes of perovskite thin films affect structural and optoelectronic properties, especially with respect to changes in strain and correlated energetic disorder as well as defect properties.[16−23]

Using films of the model halide perovskite methylammonium lead iodide (MAPbI₃), we investigate in detail how a small increase in grain size and orientation induced by hot-pressing of polycrystalline thin films affects crystallographic phase transitions, energetic disorder, and the properties of the excited states. On the one hand, detailed analyses of temperature-dependent absorption and photoluminescence (PL) measurements allow us to identify differences in the critical transition temperature between tetragonal and orthorhombic crystal structures, indicating differences in strain, depending on the film morphology. On the other hand, our
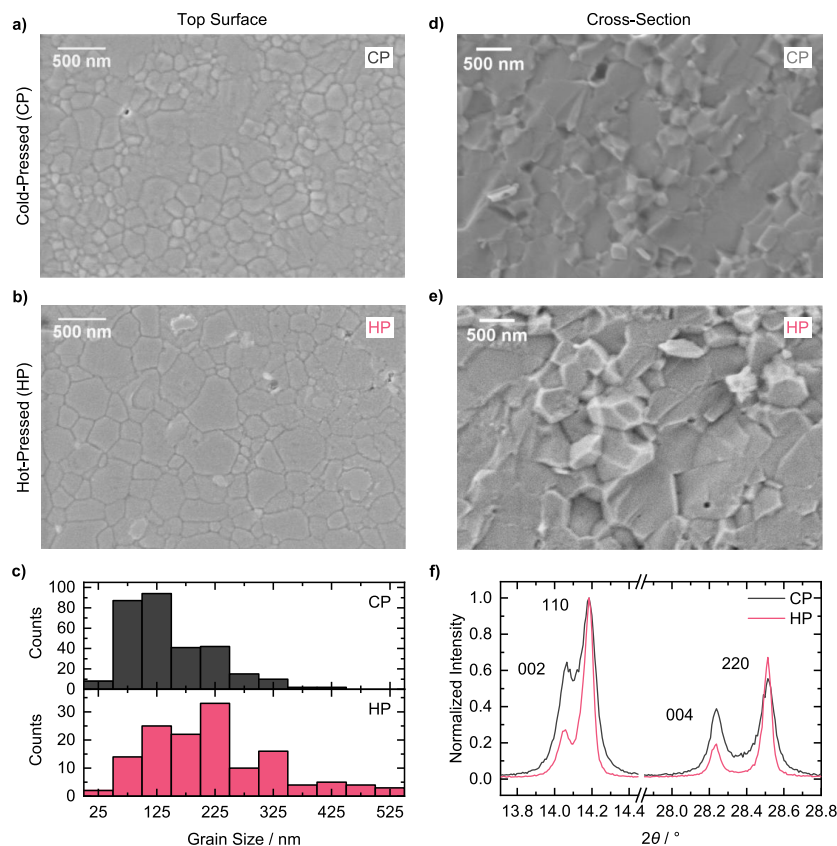
Figure 1. Morphology of CP (gray) and HP(red) MAPbI$_3$ thin films: (a,b) top-view SEM images and (c) corresponding grain size distributions. (d,e) Cross-sectional SEM images. (f) XRD patterns with 002, 110 and 004, 220 reflex pairs, normalized to the 110 reflex intensity.

analyses enable us to extract the Urbach energy—a measure for the energetic disorder in the semiconductor—from PL data, where within our error margins, no differences between the samples are observed. However, a clear impact of morphology changes induced by hot-pressing on the lifetimes of the photoexcited carriers is observed, which is investigated by means of transient PL measurements. Furthermore, a correlation between the lifetimes and changes in the preferred crystallographic orientation is observed.

2. EXPERIMENTAL SECTION

2.1. Film Preparation. MAPbI$_3$ powder was synthesized via mechanochemical synthesis using a Fritsch "Pulverisette 5/4" planetary ball mill with 400 rpm. Therefore, 1.900 g of MAI powder and 5.509 g of PbI$_2$ powder were put in a 80 mL ZrO$_2$ milling jar together with 25 ZrO$_2$ milling balls (diameter 10 mm) and 5 mL of cyclohexane as the milling agent. Milling was done for 5 min followed by a break of 20 min (to avoid too much heating due to rotation and friction) and both were repeated until a total milling time of 25 to 35 min was reached.

MAPbI$_3$ thin films with an area of about 1.0 cm × 1.4 cm were deposited onto 2 cm × 2 cm glass substrates (substrate thickness 3 mm) via the powder aerosol deposition method (PADM) using the mechanochemically synthesized MAPbI$_3$ powder and a custom-made apparatus for PAD. Then, these MAPbI$_3$ thin films were (hot-)pressed with a pressure of 25

MPa using a homebuilt mechanical press (for details, see Section S1).

2.2. Film Characterization. For morphology characterization of the MAPbI$_3$ thin films, SEM images were taken with a Zeiss Leo 1530 scanning electron microscope (with a Schottky-field-emission cathode, SE2 detector, and Inlens detector) using an accelerating voltage of 3.0 kV. Therefore, the thin films were fixed on a sample holder with conductive adhesion graphite pads (Plano) and sputtered with a 1.5 nm thin platinum layer. For details on grain size analysis from SEM images, see Section S1.

Structural characterization of the thin films was conducted by reflection mode XRD using a Bruker "D8 Discover A25" with Cu Kα_I radiation (λ = 0.15406 nm). The Kα_{II} rays were removed with a Ge Kα_I monochromator. The instrument was operated with 40 kV and 40 mA. Diffractograms were recorded with a 2θ step size of 0.008° in the 2θ range from 10 to 45° under ambient conditions. Details on XPS measurements are given in Section S1.

The surface roughness Ra and the average surface height of the thin films were determined using a profilometer (Dektak 150, Veeco).

2.3. PL and Absorption Measurements. The temperature- and fluence-dependent steady-state PL and absorption spectra were measured using a homebuilt setup: the MAPbI$_3$ thin films were placed in an electrically heatable continuous flow cryostat (Oxford Instruments, Optistat CF) with an

145

automated temperature controller (Oxford Instruments ITC503S), and the temperature was regulated between 300 and 5 K. A tungsten lamp was used as a white-light source for the absorption measurements. To obtain the optical density (OD), the transmission through the sample and a reference beam that did not pass through the sample were recorded. A 630 nm long-pass filter was placed in the optical detection path to remove the 2nd diffraction order of the spectrograph. For measuring PL spectra, a 337 nm nitrogen laser (LTB MNL 100) was used for excitation. In the optical detection path, a 400 nm long-pass filter was used to remove scattered excitation light. The PL of MAPbI$_3$ thin films when measuring PL spectra and the transmission and reference beams when measuring absorption spectra were focused into a spectrograph (Andor Shamrock SR303i), respectively, and recorded with a Si-CCD camera (Andor iDus DU420a-OE). All spectra were corrected for transmission and detection efficiency of the setup.

For the extraction of charge carrier lifetimes, time-resolved PL (TRPL) curves of the MAPbI$_3$ thin films were measured at room temperature using time-correlated single-photon counting (TCSPC) in a PicoQuant MT200 confocal fluorescence microscope. A 561 nm diode laser (PicoQuant LDH-D-TA-560) with a frequency of 1.0 MHz and a pulse width of 68 ps was used for excitation, and the excitation fluence was set to 300 nJ/cm^2. An Olympus objective (4× magnification, numerical aperture of 0.1) was used to focus the laser beam on the thin film surface with a spot diameter of about 6 μm in the focal plane. In the optical detection path, a 561 nm long-pass filter was installed in order to remove scattered excitation light. A PMA Hybrid PMT 40 photomultiplier tube (PicoQuant) was used to detect the remaining emission from the MAPbI$_3$ thin films. This emission signal was processed by a TimeHarp 260 Pico TCSPC board (PicoQuant).

3. RESULTS AND DISCUSSION

3.1. Preparation of Films with Different Morphologies. For investigating the influence of orientation and grain size on the phase transition behavior, energetic disorder, as well as defect properties, we first manufactured MAPbI$_3$ thin films with different morphologies. To do so, we used a dry powder-based two-step processing method comprising (i) film formation by spraying mechanochemically synthesized MAPbI$_3$ powder onto a glass substrate via the PADM and (ii) post-treatment by applying a pressure of 25 MPa for about 50 min to the perovskite films (for details, see Section S1). We chose this approach as producing MAPbI$_3$ films by PADM results in polycrystalline film morphologies,[2,24,25] while pressing polycrystalline halide perovskite films increases the degree of orientation and grain size, especially when the pressing process proceeds at an elevated temperature.[14,26] Therefore, we pressed PADM-processed thin films at room temperature (referred to as cold pressed, CP) and at an elevated temperature of about 100 °C (referred to as hot pressed, HP), producing films with well defined, yet different morphologies.

Following this processing approach, compact films with thicknesses of around ∼4 μm were obtained (see Figure S3a for the cross-sectional SEM image). Top-view SEM images in Figure 1a,b show an average grain size of (150 ± 75) nm for the CP film and (220 ± 110) nm for the HP film (see Figure 1c and Section S1 for details of grain size analysis). Furthermore, less and narrower grain boundaries can be

observed for the HP in contrast to the CP film (Figure 1a,b). Increased grain size and narrower grain boundaries in the HP film at the surface as well as throughout the layer thickness are also obvious in the corresponding cross-sectional SEM images (Figure 1d,e). Moreover, the HP film exhibits a reduced surface roughness of Ra_{HP} = 34 nm compared to the CP film with Ra_{CP} = 61 nm. The observed film morphology improvements are in line with previous literature reports about thermal pressure treatment of MAPbI$_3$ thin films.[26−29]

To investigate whether the increase in grain size is also accompanied by an increase in MAPbI$_3$ crystallite size, we measured XRD patterns of the HP and CP films. Figure 1f shows corresponding normalized XRD patterns in the 2θ range between 13.7 and 28.8°, which contain the reflex pairs 002, 110 and 004, 220 of MAPbI$_3$ in its tetragonal crystal structure.[30] From Figure 1f, it becomes clear that the HP film (red line) exhibits narrower reflexes compared to the CP film (gray line), indicating a larger crystallite size and/or reduced microstrain in the HP sample. Examining the reflex width by applying the Rietveld refinement method to the measured XRD patterns (Figure S3c), we extract crystallite size information from the width contribution changing with 1/cos(θ) and information on the microstrain in the sample from the width contribution changing with tan(θ) (Section S1). We find crystallite sizes of ∼(130 ± 25) and ∼(350 ± 150) nm for the CP and the HP films, respectively. Within the respective error ranges, these crystallite sizes are similar to the corresponding average grain sizes extracted from the SEM images, suggesting that the grains observed in Figure 1a,b for both films are essentially single crystalline. Applying the Rietveld refinement method, we also find that the extracted microstrain in the HP film (0.028% ± 0.015%) tends to be lower than the corresponding microstrain in the CP film (0.047% ± 0.015%). This reduction is in line with the work of Osherov et al., who suggested that the fraction of the strained perovskite material is higher for smaller grains than for larger grains as strain is predominantly present in the grain boundaries.[31]

In addition to differences in the width of the reflexes in the measured XRD patterns, we find their relative intensities to differ as well (Figure 1f). The 110/002 peak intensity ratio for the HP film (∼3.68) is clearly higher than for the CP film (∼1.55). This behavior also applies to the ratios of corresponding higher order reflexes, such as the 220/004 ratio (see Figure S3c for XRD patterns between 10 and 45°). Exploiting the geometric relationship between the individual scattering planes over the full measured 2θ range, the observed changes in the peak intensity ratio can be well modeled by changes in the preferred orientation. Thus, the peak intensity ratio indicates that hot-pressing compared to cold-pressing induces an increased orientation of the (110) plane parallel to the substrate, i.e., the [110] direction is parallel to the direction where the pressure is applied. This is in line with the observations from our previous work[32] and with the results of Moon et al., where increased crystallite size and preferential crystal plane orientation parallel to the substrate are found for increased temperature during pressing of halide perovskite thin films.[14] In passing, we mention that we observe small amounts of PbI$_2$ in both samples, reflected by low-intensity reflexes at 12.7°, which are slightly higher in HP than in CP samples (Figure S3c). The increased PbI$_2$ content after hot-pressing is also reflected in the reduction of the I/Pb ratio from 3.08
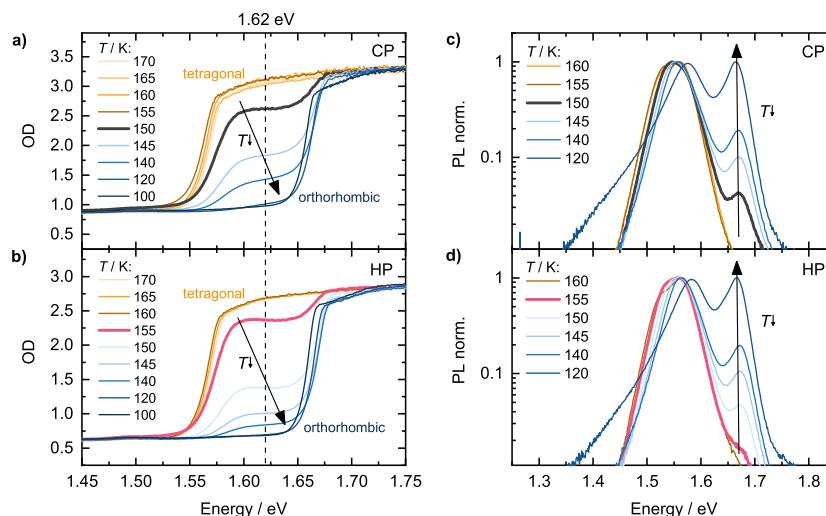
Figure 2. Absorption and PL spectra of MAPbI$_3$ thin films in the phase transition region between 170 and 100 K: optical density of (a) a CP film and (b) an HP film. Normalized PL of (c) a CP film and (d) an HP film. Arrows indicate the phase transition from the tetragonal to orthorhombic phase upon cooling. Gray and red lines represent the first sign of phase transition for CP and HP films, respectively.

(before pressing) to 2.76 after hot-pressing, extracted from XPS spectra (see Figure S4 and Section S1 for details).

Overall, by employing increased temperature during the pressing of the MAPbI$_3$ films, we were able to increase the grain size and induce higher preferred orientation in the film.

3.2. Structural Properties. To investigate how the changes in orientation and grain size of the MAPbI$_3$ films impact their defect properties, degree of energetic disorder, and their behavior when undergoing structural changes, such as crystallographic phase transitions, we measured temperature-dependent steady-state PL and absorption spectra from 300 K down to 5 K of the CP and HP samples.

When cooling and reheating a MAPbI$_3$ thin film across the phase transition between the tetragonal and orthorhombic phases, as it is done in this work, morphological changes are known to occur upon the second passing of the phase transition, i.e., during reheating.[31] To ensure that the small morphology differences induced by hot-pressing are not obscured by additional unintended morphology changes in our case, we first focus on the cooling stage (Sections 3.2.1 and 3.2.2) before also addressing the samples after reheating, shown in Section 3.2.3.

3.2.1. Phase Transition. In the following, we first focus on the phase transition behavior. Between ~330 and ~163 K, MAPbI$_3$ exhibits a tetragonal phase, while at temperatures below ~160 K, it adopts an orthorhombic crystal structure.[33−35]

Figure 2 shows absorption and PL spectra of the CP and HP films between 170 and 100 K, i.e., in the temperature range of the phase transition. When transitioning between tetragonal and orthorhombic phases, it is known that the electronic structure and thus the optical properties of MAPbI$_3$ change substantially.[34,36] In the absorption spectra (Figure 2a,b) at 170 K, an absorption edge is present for both samples at about 1.56 eV, which is associated with the tetragonal phase.[37−39] Upon cooling below 160 K, the absorption reduces in the energy range up to 1.65 eV and vanishes below 120 K. In this temperature range, an absorption edge at about 1.65 eV becomes visible, which is associated to absorption of the

orthorhombic phase.[37−39] In general, the temperature-dependent changes of the spectra of CP and HP appear similar. Nevertheless, the first indicator for the phase transition upon cooling is the initial decrease of absorption intensity of the tetragonal phase, occurring at 150 K for the CP sample (gray line in Figure 2a), but it is already occurring at 155 K for the HP sample (red line in Figure 2b). In passing, we mention that the absorption spectra saturate above an OD value of about 2.7 due to limited setup sensitivity.

Similar to the observations in absorption, the PL spectra measured in the phase transition region also exhibit distinct changes. Figure 2c,d shows the corresponding PL spectra between 160 and 120 K of both MAPbI$_3$ samples CP and HP normalized to the PL peak at ~1.56 eV, which is associated with PL from the tetragonal phase (see Figure S5a,b for unnormalized PL spectra).[36,40,41] Upon cooling, a second PL peak at ~1.67 eV arises, which corresponds to PL from the orthorhombic phase.[36,40,41] Similar to the absorption, the PL of the orthorhombic phase appears at 150 K for CP (see the gray line in Figure 2c), but it emerges already at 155 K for HP (see the red line in Figure 2d).

For a quantitative analysis of these differences in the phase transition dynamics between the two sample types, we determined the critical phase transition temperature from the absorption spectra in Figure 2a,b following an approach from earlier works.[42,43] To this end, for CP and HP samples, we considered the temperature dependence of the OD at 1.62 eV (Figure 3a), i.e., an energy where only the tetragonal phase absorbs. Then, we calculated the derivative of the temperature-dependent OD resulting in a peak in the temperature range of the phase transition (Figure 3b). The latter was fitted using a Gaussian function, where we associate the peak position with the critical phase transition temperature T_c and the full width at half-maximum (fwhm) with the temperature range over which the phase transition proceeds. We find T_c to be higher for HP ($T_{c,HP}$ = 151.9 K ± 0.3 K) compared to CP ($T_{c,CP}$ = 147.5 K ± 0.4 K). Both values are in agreement with reported phase transition temperatures of polycrystalline MAPbI$_3$ thin films, which cover a range from about 145 to 160
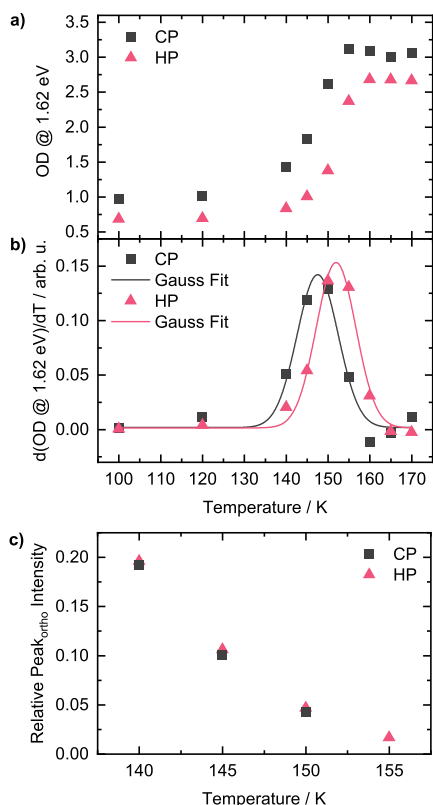
Figure 3. Phase transition analyses for CP (gray) and HP (red) MAPbI$_3$ thin films: (a) optical density@1.62 eV for temperatures between 170 and 100 K extracted from absorption spectra in Figure 2a,b. (b) Derivative of (a) resulting in a peak shape, where the peak position is associated with the critical phase transition temperature. (c) Intensity of the PL peak attributed to the orthorhombic phase relative to the intensity of the PL peak attributed to the tetragonal phase for temperatures between 155 and 140 K.

K.[31,37,39,40,43−45] The extracted fwhms of the transition are similar within the error range for the CP and HP films with fwhm$_{CP}$ = (11.6 ± 1.2) K and fwhm$_{HP}$ = (11.1 ± 0.8) K. These fwhm values are in line with the corresponding value of a solution-processed MAPbI$_3$ thin film found in a previous work.[43]

As a next step, we analyzed in more detail how the differences in phase transition are reflected in the PL properties of the two samples. We considered the intensity of the PL of the orthorhombic phase between 155 and 140 K relative to the one of the tetragonal phase (Figure 3c). With decreasing temperature, the relative intensity of the orthorhombic peak increases similarly for both HP and CP, with slightly higher relative intensity values for HP (see also comparison of PL spectra in Figure S5c).

Overall, a retention in the onset of the phase transition to lower temperatures is identified for the CP sample compared to the HP sample.

In the past, the phase transition temperature in MAPbI$_3$ was found to alter depending on the morphology of the investigated sample. For example, decreased phase transition temperatures were observed for MAPbI$_3$ films with smaller grains.[23,44] For nanoparticles and nanocrystals, even a fully

suppressed phase transition was reported.[44] Such changes in phase transition behavior were associated with the degree of strain in the perovskite, which is supposed to increase for smaller grain sizes due to a higher fraction of grain boundaries.[19,23,31]

This conclusion is in good agreement with our identified lower phase transition temperature for the CP film, which exhibits a smaller grain size and a higher microstrain compared to that of the HP film (see Section 3.1). The increased PbI$_2$ content in HP (Figures S3 and S4) is not expected to induce a significant amount of additional distortion related strain[46] compared to strain located at the grain boundaries and thus should not affect the phase transition temperature significantly (see also Section S1). Overall, we suggest that the observed decrease in critical phase transition temperature of the CP sample compared to the HP sample in Figure 3 is associated with an increased amount of strain in the CP sample.

3.2.2. Energetic Disorder. As the degree of strain is known to be correlated with the degree of energetic disorder in halide perovskites,[18,47,48] we next focus on investigating the latter for our samples.

Energetic disorder in semiconductors impacts their optical properties. For example, often, an exponentially decreasing absorption tail below the band gap is observed, which is referred to as Urbach tail absorption.[49,50] The slope of this Urbach tail is determined by the so-called Urbach energy E_U, which in turn is influenced by static and dynamic disorder.[49,50]

E_U, and thus the degree of energetic disorder, is also reflected in the shape of the corresponding PL. Based on the reciprocity theorem, the (intrinsic) PL is proportional to

$$PL \propto \alpha(E) \cdot E^2 \cdot \exp\left(-\frac{E}{k_B T}\right) \tag{1}$$

where E is the photon energy, α is the absorption coefficient, k_B is the Boltzmann constant, and T is the absolute temperature of the sample.[36,50,51] Equation 1 is valid for any two-state system that can be described by a spatially independent quasi-Fermi level splitting, which is a good approximation for lead halide perovskite thin films in the tetragonal phase.[52,53] Considering Urbach tail absorption and a constant absorption above the band gap, the shape of the absorption spectrum of MAPbI$_3$ can be satisfyingly approximated in the spectral range where PL occurs as

$$\alpha(E) \propto \frac{1}{\exp\left(-\frac{E - E_0}{E_U}\right) + 1} \tag{2}$$

with E_0 being a fitting constant with a value near the band gap energy.[36] Inserting eq 2 into eq 1, it follows that the high energy edge of the PL (i.e., $E \gg E_0$) is essentially determined by $\exp(-E/k_B T)$, while the low energy edge (i.e., $E \ll E_0$) is proportional to $\exp\left(\frac{E - E_0}{E_U} - \frac{E}{k_B T}\right)$. Analysis approaches based on eq 1 have been used successfully in the past, e.g., by Fassl et al., to extract the Urbach energy from the PL spectra of MAPbI$_3$.[54]

For extracting the Urbach energy from our PL data, we focus on the PL of the tetragonal phase between 300 and 160 K as at lower temperatures, additional PL contributions (such as defect-associated PL, see, e.g., Figure S5) complicate or even inhibit the reliable extraction of the Urbach energy from the PL spectra. Figure 4a shows the PL spectra of the CP film
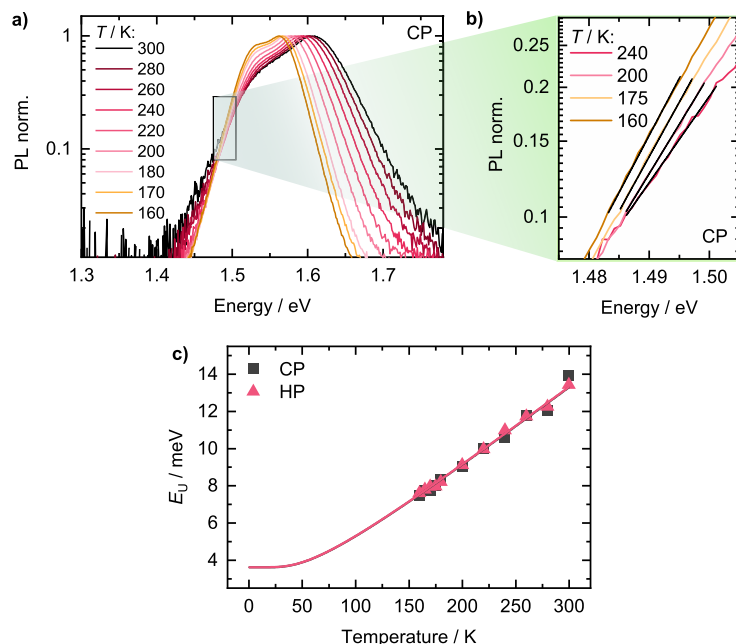
148

Figure 4. Energetic disorder analysis for pressed MAPbI$_3$ thin films by extracting the Urbach energy from PL spectra: (a) normalized PL spectra of a CP film in the tetragonal phase between 300 and 160 K and (b) corresponding exemplary fits of the low energy edge based on eq 1. (c) Extracted Urbach energies from fits as shown in (b) for a CP film (gray squares) and an HP film (red triangles). The lines represent fits according to eq 3 to extract the static disorder.

between 300 and 160 K (corresponding PL spectra of HP in Figure S6a). At 300 K, the spectrum consists of one main peak at 1.61 eV and a shoulder at about 1.53 eV, with the latter being associated with a self-absorption effect. The main PL peak originates from PL that comes directly from (near) the surface of the sample, whereas the feature at lower energies is caused by PL that is internally reflected and filtered by the absorption of the sample (see Figure S6b,c).[43,54,55] Upon cooling, the PL spectrum shifts to lower energies and becomes narrower.[44,45]

To extract the Urbach energies from the PL spectra, we fitted the low energy edge of the PL based on eq 1 according to

$$PL(E \ll E_0) = C \cdot \exp\left(\frac{E - E_0}{E_U} - \frac{E}{k_B T}\right),$$ where C is a fitting parameter accounting for the PL intensity (exemplary fits in Figure 4b). Figure 4c shows the extracted E_U values between 300 and 160 K for both samples CP and HP. Upon cooling, E_U decreases similarly for both samples from about 14 meV at 300 K to 7.5 meV at 160 K. The extracted Urbach energies are in very good agreement with results from our previous work about MAPbI$_3$ single crystals[36] and the work of Ledinsky et al. about MAPbI$_3$ thin films.[50]

As mentioned above, the Urbach energy is determined by static disorder E_U^{stat} and dynamic disorder E_U^{dyn}, and its temperature-dependence can be described by[50,56]

$$E_U(T) = E_U^{stat} + E_U^{dyn} = E_U^{stat} + 2 \cdot E_U^{stat}\left[\exp\left(\frac{\Theta}{T}\right) - 1\right]^{-1} \tag{3}$$

Here, E_U^{stat} is assumed to be temperature-independent. The temperature-dependence of E_U^{dyn} is described in terms of the interaction of charge carriers with phonons in the coupled Einstein oscillator model with the Einstein temperature Θ.[49,50,56] We fitted the extracted Urbach energies in Figure 4c using eq 3 (solid lines in Figure 4c). Assuming that the energies of the phonons interacting with charge carriers are essentially identical for both samples, we fixed $\Theta = 167$ K (corresponding to a phonon energy of 14.4 meV) based on the work of Xia et al.[57] With this, we obtained $E_{U,CP}^{stat} = (3.61 \pm 0.03)$ meV for CP and $E_{U,HP}^{stat} = (3.61 \pm 0.01)$ meV for HP. These static disorder values are in very good agreement with reported values for MAPbI$_3$ single crystals[36] as well as MAPbI$_3$ thin films, and they are remarkably low compared to classical inorganic crystalline semiconductors (e.g., GaAs and c-Si).[50]

The identical values for the static disorder of both CP and HP are somewhat surprising as differences in phase transition behavior associated with different amounts of strain in the samples were identified in Section 3.2.1, and strain in turn is expected to affect the energetic disorder.[18,47] One reason for the identical E_U^{stat} values observed in our analysis for both CP and HP might be that PL tends to track more sites with lower energetic disorder since charge carriers relax to beneficial sites with lower energy before recombining radiatively.[58,59] Additionally, lower nonradiative decay rates are typically present at sites with lower energetic disorder.[16,20,60] Therefore, sites with lower energetic disorder may contribute overproportionally to the PL spectra and obscure the signatures of sites with higher energetic disorder. Another reason might be that PL, which mainly probes the top side of the films,[48] is not bulk-sensitive enough to detect strain-associated energetic disorder from the perovskite–substrate interface.[21,61−63] A systematic investigation differentiating the above-mentioned aspects by elaborating and applying more sophisticated Urbach analysis methods is beyond the scope of this work, but it will be addressed in a future study.
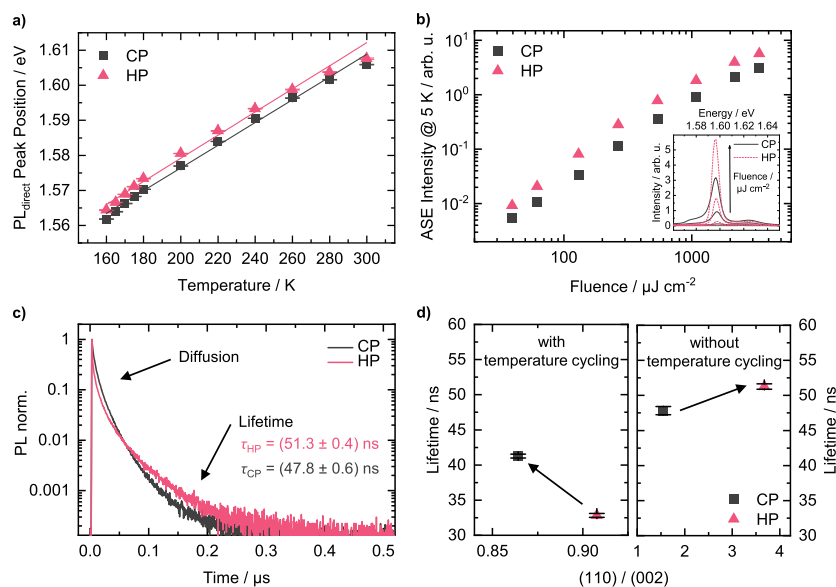
Figure 5. Excited state properties of CP (gray) and HP (red) MAPbI$_3$ thin films: (a) PL peak position between 300 and 160 K with linear fits. (b) Fluence-dependent ASE peak intensity@5 K and inset with corresponding exemplary PL spectra. (c) TRPL curves measured at room temperature with extracted lifetimes from the mono-exponential tail. (d) Left panel: lifetimes dependent on 002-preferred orientation after temperature cycling, i.e., cooling the sample to 5 K for the temperature-dependent measurements and heating it back to room temperature. Right panel: lifetimes dependent on the 110-preferred orientation without temperature cycling measured at room temperature.

3.2.3. Excited State Properties—Defects. Increased strain in halide perovskite films is correlated with increased energetic disorder,[18] and increased energetic disorder in turn is related to more defect states.[16,20,22] Moreover, increased strain in halide perovskites is known to be directly correlated with increased non-radiative losses and defect states.[17,19,21,23] Therefore, in the following, we investigate whether the larger strain in CP identified in Sections 3.1 and 3.2.1 is reflected in the excited state properties and thus in the defect densities. To this end, we performed further PL analyses.

Figure 5a shows the peak positions of the direct PL signature as a function of temperature between 300 and 160 K for both, CP and HP (see Section S2 for details). Solid lines represent linear fits to the data, with the corresponding slopes s serving as a measure of the known PL red shift with decreasing temperature (see also Figures 4a and S6a).[39,44,45] The extracted shifts of $s_{CP} = (0.32 \pm 0.01)$ meV K^{-1} for CP ($R^2 \approx 0.99$) and $s_{HP} = (0.33 \pm 0.01)$ meV K^{-1} for HP ($R^2 \approx 0.99$) are identical within the uncertainty of the fit. This suggests that the additional tensile strain induced by the substrate upon cooling[19,43,62,63] is similar in CP and HP, which is reasonable considering the identical substrate materials and the similar layer thickness for both samples (for details, see Section S2). The overall peak position of HP, however, is shifted by approximately 2 meV to higher energies compared to the values of CP. We associate this PL peak shift between both samples with different impacts of self-absorption on the direct PL caused by a lower defect density near the film surface in HP compared to CP: with lower defect density near the surface, more direct PL is emitted closer to the surface. Thereby, the influence of self-absorption on the direct PL is reduced, enabling more high-energy photons to contribute to the measured PL spectra. This, in turn, results in less peak shift to lower energies compared to the intrinsic PL spectrum.[43,64]

To verify the conclusion about differences in defect densities between CP and HP, we measured fluence-dependent PL spectra between about 40 μJ cm^{-2} and 3400 μJ cm^{-2} at 5 K, which are shown in the inset of Figure 5b and in detail in Figure S7. With increasing fluence, a sharp peak arises at 1.597 eV in the PL spectra, which is attributed to amplified spontaneous emission (ASE).[65,66] In Figure 5b, the fluence-dependent intensity of the ASE peak is shown for both CP and HP. The ASE intensity of HP is higher by about 70−150%, indicating higher crystallinity as well as longer charge carrier lifetimes in HP.[67,68] This is in line with the lower defect density in HP concluded from the analyses of Figure 5a.

To extract the charge carrier lifetimes for CP and HP, we measured TRPL of both samples at room temperature. The results are shown in Figure 5c. Up to 0.05 μs, the PL intensity of HP decreases faster than for CP, but it shows a slower decay at longer times. The faster initial decrease of the PL intensity of HP can be explained by stronger diffusion of charge carriers,[69] which is consistent with a higher crystallinity of HP compared to the CP film.[70] Furthermore, the slower decay of the PL intensity at longer times for HP indicates longer charge carrier lifetimes in HP. We extracted charge carrier lifetimes by applying mono-exponential fits to the tail of the PL curves at times higher than $\sim$0.1 μs (see Figure S8a). As expected from the higher crystallinity and the slower decay at longer times of HP, the charge carrier lifetime $\tau_{HP} = (51.3 \pm 0.4)$ ns of HP is higher than the extracted charge carrier lifetime $\tau_{CP} = (47.8 \pm 0.6)$ ns of CP, again indicating less defects being present in HP than in CP.[59,71]

Since CP and HP show different degrees of preferred orientation (see Figure 1f), we aim to correlate the charge carrier lifetime with the degree of preferred orientation in our samples (Figure 5d). From Figure 5d right panel, it appears that the charge carrier lifetime increases with increasing

150

orientation of the (110) plane parallel to the substrate, i.e., from CP to HP. We note that this increase might be promoted by the larger grain sizes in HP. Remarkably, after a temperature cycle (i.e., cooling the sample to 5 K for the temperature-dependent measurements and heating it back to room temperature), the preferred orientation parallel to the substrate changed for both samples toward a 002-preferred orientation, where the CP sample shows a more pronounced 002 orientation than HP (Figure S8c,d). Here again, the charge carrier lifetime increases with increasing orientation, this time from HP to CP (see Figure 5d left panel) though CP consists of smaller grains than HP.

The crystallographic reorientation upon temperature cycling through a phase transition accompanied by a fusion of grain domains (Figure S9a) observed in our case has also been observed by Kavadiya et al. for the transition between tetragonal and cubic phases[72] as well as by Osherov et al. for the transition between tetragonal and orthorhombic phases.[31] By temperature-dependent XRD measurements, Osherov et al. found these morphological changes in MAPbI$_3$ thin films not to occur in the course of the initial phase transition during cooling but after the subsequent phase transition upon reheating the films.[31] We speculate that the overall decreased charge carrier lifetimes of the films after temperature cycling (Figure 5d) result from a detrimental effect of the morphological changes in the course of temperature cycling.

However, stronger crystallographic orientation—preferred either in the (110) or in (002) plane—in general seems to result in an increased excited state lifetime (Figure 5d). This might be related to the quality of the grain boundaries, which is expected to improve for a more aligned orientation of adjacent grains.[46] This observation is an interesting qualitative insight, possibly highlighting the importance of the degree of crystallographic orientation for the optimization of the perovskite's optoelectronic properties. In this regard, a detailed study about the correlation between crystallographic orientation and excited state properties would be interesting in the future, including consideration of aspects such as in-plane orientation or the role of a certain amount of PbI$_2$ present in the films due to processing and degradation.

4. CONCLUSIONS

In summary, we investigate the influence of small morphology differences in MAPbI$_3$ thin films on phase transition, energetic disorder, and defects by detailed PL and absorption analyses. To this end, MAPbI$_3$ thin films are manufactured via a two-step processing method comprising MAPbI$_3$ film deposition via PADM and pressing as post-treatment. By higher pressing temperature, we induce small increases in grain size and preferred orientation in the thin films.

The larger grains and increased orientation of the (110) plane parallel to the substrate go along with a higher phase transition temperature concluded from temperature-dependent PL and absorption analyses, which we attribute to less strain in HP samples. Although strain is known to correlate with energetic disorder, our Urbach analyses from temperature-dependent PL spectra do not show differences in static disorder between CP and HP films. However, differences in the excited state properties are observed. Here, a lower defect density in films with increased grain size and a higher degree of 110-preferred orientation is found from fluence-dependent and transient PL measurements. The observed interdependency of strain and defect density with grain size and orientation

suggests that small differences in energetic disorder are indeed present. More sophisticated analysis methods of the optical spectra as they are currently developing[73,74] yield high potential to fully resolve these small differences in the future. Increased 110- or 002-preferred orientation is observed to result in longer charge carrier lifetimes. This emphasizes that besides the commonly considered grain size, the degree of orientation also seems to play an important role regarding the optoelectronic properties of halide perovskite thin films.

Thus, with the insights gained in this work, it will be possible to better understand and advance the functionality of halide perovskite-based optoelectronic devices such as solar cells in the future.

■ ASSOCIATED CONTENT

⑤ Supporting Information

The Supporting Information is available free of charge at https://pubs.acs.org/doi/10.1021/acs.jpcc.2c08968.

Details on film preparation via dry powder-based two-step processing method (PADM + pressing) and additional film morphology analyses including SEM images, XRD patterns, and XPS spectra; additional (temperature- or fluence-dependent) PL spectra, discussion of temperature-dependent PL peak shift, and sketch about direct and filtered PL; fits of TRPL curves for extraction of lifetimes; and XRD patterns, sketch of MAPbI$_3$ unit-cells, SEM and microscopy images for MAPbI$_3$ thin films without, with, and during temperature cycling together with a discussion of structural changes like reorientation in the course of temperature cycling (PDF)

■ AUTHOR INFORMATION

Corresponding Author

Fabian Panzer − *Soft Matter Optoelectronics, University of Bayreuth, Bayreuth 95440, Germany;* ⓞ orcid.org/0000-0002-2191-9011; Email: fabian.panzer@uni-bayreuth.de

Authors

Christina Witt − *Soft Matter Optoelectronics, University of Bayreuth, Bayreuth 95440, Germany*

Konstantin Schötz − *Soft Matter Optoelectronics, University of Bayreuth, Bayreuth 95440, Germany*

Meike Kuhn − *Dynamics and Structure Formation—Herzig Group, University of Bayreuth, Bayreuth 95440, Germany*

Nico Leupold − *Department of Functional Materials, University of Bayreuth, Bayreuth 95440, Germany*

Simon Biberger − *Soft Matter Optoelectronics, University of Bayreuth, Bayreuth 95440, Germany*

Philipp Ramming − *Soft Matter Optoelectronics, University of Bayreuth, Bayreuth 95440, Germany*

Frank-Julian Kahle − *Soft Matter Optoelectronics, University of Bayreuth, Bayreuth 95440, Germany;* ⓞ orcid.org/0000-0003-3416-0072

Anna Köhler − *Soft Matter Optoelectronics, University of Bayreuth, Bayreuth 95440, Germany;* ⓞ orcid.org/0000-0001-5029-4420

Ralf Moos − *Department of Functional Materials, University of Bayreuth, Bayreuth 95440, Germany*

Eva M. Herzig − *Dynamics and Structure Formation—Herzig Group, University of Bayreuth, Bayreuth 95440, Germany;* ⓞ orcid.org/0000-0002-0151-5562

Complete contact information is available at:
https://pubs.acs.org/10.1021/acs.jpcc.2c08968

Notes
The authors declare no competing financial interest.

■ ACKNOWLEDGMENTS

■ REFERENCES

(1) Teixeira, C. O.; Castro, D.; Andrade, L.; Mendes, A. Selection of the Ultimate Perovskite Solar Cell Materials and Fabrication Processes towards its Industrialization: A Review. *Energy Sci. Eng.* **2022**, *10*, 1478−1525.

(2) Leupold, N.; Panzer, F. Recent Advances and Perspectives on Powder-Based Halide Perovskite Film Processing. *Adv. Funct. Mater.* **2021**, *31*, 2007350.

(3) Buin, A.; Pietsch, P.; Xu, J.; Voznyy, O.; Ip, A. H.; Comin, R.; Sargent, E. H. Materials Processing Routes to Trap-Free Halide Perovskites. *Nano Lett.* **2014**, *14*, 6281−6286.

(4) Jena, A. K.; Kulkarni, A.; Miyasaka, T. Halide Perovskite Photovoltaics: Background, Status, and Future Prospects. *Chem. Rev.* **2019**, *119*, 3036−3103.

(5) Maiti, A.; Chatterjee, S.; Peedikakkandy, L.; Pal, A. J. Defects and Their Passivation in Hybrid Halide Perovskites toward Solar Cell Applications. *Sol. RRL* **2020**, *4*, 2000505.

(6) Jeong, M.; Choi, I. W.; Go, E. M.; Cho, Y.; Kim, M.; Lee, B.; Jeong, S.; Jo, Y.; Choi, H. W.; Lee, J.; et al. Stable Perovskite Solar Cells with Efficiency Exceeding 24.8% and 0.3-V Voltage Loss. *Science* **2020**, *369*, 1615−1620.

(7) Min, H.; Lee, D. Y.; Kim, J.; Kim, G.; Lee, K. S.; Kim, J.; Paik, M. J.; Kim, Y. K.; Kim, K. S.; Kim, M. G.; et al. Perovskite Solar Cells with Atomically Coherent Interlayers on SnO₂ Electrodes. *Nature* **2021**, *598*, 444−450.

(8) NREL. Best Research-Cell Efficiency Chart. https://www.nrel.gov/pv/cell-efficiency.html (accessed Nov 16, 2022).

(9) Kim, M.; Kim, G.-H.; Lee, T. K.; Choi, I. W.; Choi, H. W.; Jo, Y.; Yoon, Y. J.; Kim, J. W.; Lee, J.; Huh, D.; et al. Methylammonium Chloride Induces Intermediate Phase Stabilization for Efficient Perovskite Solar Cells. *Joule* **2019**, *3*, 2179−2192.

(10) Li, Y.; Ji, L.; Liu, R.; Zhang, C.; Mak, C. H.; Zou, X.; Shen, H.-H.; Leu, S.-Y.; Hsu, H.-Y. A Review on Morphology Engineering for Highly Efficient and Stable Hybrid Perovskite Solar Cells. *J. Mater. Chem. A* **2018**, *6*, 12842−12875.

(11) Salim, T.; Sun, S.; Abe, Y.; Krishna, A.; Grimsdale, A. C.; Lam, Y. M. Perovskite-Based Solar Cells: Impact of Morphology and Device Architecture on Device Performance. *J. Mater. Chem. A* **2015**, *3*, 8943−8969.

(12) Wieghold, S.; Correa-Baena, J.-P.; Nienhaus, L.; Sun, S.; Shulenberger, K. E.; Liu, Z.; Tresback, J. S.; Shin, S. S.; Bawendi, M. G.; Buonassisi, T. Precursor Concentration Affects Grain Size, Crystal

Orientation, and Local Performance in Mixed-Ion Lead Perovskite Solar Cells. *ACS Appl. Energy Mater.* **2018**, *1*, 6801−6808.

(13) Wu, J.; Zhang, W.; Wang, Q.; Liu, S.; Du, J.; Mei, A.; Rong, Y.; Hu, Y.; Han, H. A Favored Crystal Orientation for Efficient Printable Mesoscopic Perovskite Solar Cells. *J. Mater. Chem. A* **2020**, *8*, 11148−11154.

(14) Moon, J.; Kwon, S.; Alahbakhshi, M.; Lee, Y.; Cho, K.; Zakhidov, A.; Kim, M. J.; Gu, Q. Surface Energy-Driven Preferential Grain Growth of Metal Halide Perovskites: Effects of Nanoimprint Lithography Beyond Direct Patterning. *ACS Appl. Mater. Interfaces* **2021**, *13*, 5368−5378.

(15) Liu, H.; Lee, J.; Kang, J. Characteristics of a Hybrid Detector Combined with a Perovskite Active Layer for Indirect X-ray Detection. *Sensors* **2020**, *20*, 6872.

(16) Frohna, K.; Anaya, M.; Macpherson, S.; Sung, J.; Doherty, T. A. S.; Chiang, Y.-H.; Winchester, A. J.; Orr, K. W. P.; Parker, J. E.; Quinn, P. D.; et al. Nanoscale Chemical Heterogeneity Dominates the Optoelectronic Response of Alloyed Perovskite Solar Cells. *Nat. Nanotechnol.* **2022**, *17*, 190−196.

(17) Jones, T. W.; Osherov, A.; Alsari, M.; Sponseller, M.; Duck, B. C.; Jung, Y.-K.; Settens, C.; Niroui, F.; Brenes, R.; Stan, C. V.; et al. Lattice Strain Causes Non-radiative Losses in Halide Perovskites. *Energy Environ. Sci.* **2019**, *12*, 596−606.

(18) Kim, G.; Min, H.; Lee, K. S.; Lee, D. Y.; Yoon, S. M.; Seok, S. I. Impact of strain relaxation on performance of α-formamidinium lead iodide perovskite solar cells. *Science* **2020**, *370*, 108−112.

(19) Liu, D.; Luo, D.; Iqbal, A. N.; Orr, K. W. P.; Doherty, T. A. S.; Lu, Z.-H.; Stranks, S. D.; Zhang, W. Strain Analysis and Engineering in Halide Perovskite Photovoltaics. *Nat. Mater.* **2021**, *20*, 1337−1346.

(20) Mehdizadeh-Rad, H.; Singh, J. Influence of Urbach Energy, Temperature, and Longitudinal Position in the Active Layer on Carrier Diffusion Length in Perovskite Solar Cells. *ChemPhysChem* **2019**, *20*, 2712−2717.

(21) Moloney, E. G.; Yeddu, V.; Saidaminov, M. I. Strain Engineering in Halide Perovskites. *ACS Mater. Lett.* **2020**, *2*, 1495−1508.

(22) Rajagopal, A.; Liang, P.-W.; Chueh, C.-C.; Yang, Z.; Jen, A. K. Y. Defect Passivation via a Graded Fullerene Heterojunction in Low-Bandgap Pb−Sn Binary Perovskite Photovoltaics. *ACS Energy Lett.* **2017**, *2*, 2531−2539.

(23) Stavrakas, C.; Zelewski, S. J.; Frohna, K.; Booker, E. P.; Galkowski, K.; Ji, K.; Ruggeri, E.; Mackowski, S.; Kudrawiec, R.; Plochocka, P.; et al. Influence of Grain Size on Phase Transitions in Halide Perovskite Films. *Adv. Energy Mater.* **2019**, *9*, 1901883.

(24) Leupold, N.; Seibel, A. L.; Moos, R.; Panzer, F. Electrical Conductivity of Halide Perovskites Follows Expectations from Classical Defect Chemistry. *Eur. J. Inorg. Chem.* **2021**, *2021*, 2882−2889.

(25) Panzer, F.; Hanft, D.; Gujar, T. P.; Kahle, F.-J.; Thelakkat, M.; Köhler, A.; Moos, R. Compact Layers of Hybrid Halide Perovskites Fabricated via the Aerosol Deposition Process—Uncoupling Material Synthesis and Layer Formation. *Materials* **2016**, *9*, 277.

(26) Kim, W.; Jung, M. S.; Lee, S.; Choi, Y. J.; Kim, J. K.; Chai, S. U.; Kim, W.; Choi, D.-G.; Ahn, H.; Cho, J. H.; et al. Oriented Grains with Preferred Low-Angle Grain Boundaries in Halide Perovskite Films by Pressure-Induced Crystallization. *Adv. Energy Mater.* **2018**, *8*, 1702369.

(27) Dunlap-Shohl, W. A.; Li, T.; Mitzi, D. B. Interfacial Effects during Rapid Lamination within MAPbI₃ Thin Films and Solar Cells. *ACS Appl. Energy Mater.* **2019**, *2*, 5083−5093.

(28) Mayer, A.; Buchmüller, M.; Wang, S.; Steinberg, C.; Papenheim, M.; Scheer, H.-C.; Pourdavoud, N.; Haeger, T.; Riedl, T. Thermal Nanoimprint to Improve the Morphology of MAPbX₃ (MA = methylammonium, X = I or Br). *J. Vac. Sci. Technol., B* **2017**, *35*, 06G803.

(29) Xiao, J.; Yang, Y.; Xu, X.; Shi, J.; Zhu, L.; Lv, S.; Wu, H.; Luo, Y.; Li, D.; Meng, Q. Pressure-Assisted CH₃NH₃PbI₃ Morphology Reconstruction to Improve the High Performance of Perovskite Solar Cells. *J. Mater. Chem. A* **2015**, *3*, 5289−5293.

(30) Baikie, T.; Fang, Y.; Kadro, J. M.; Schreyer, M.; Wei, F.; Mhaisalkar, S. G.; Graetzel, M.; White, T. J. Synthesis and Crystal Chemistry of the Hybrid Perovskite $(CH_3NH_3)PbI_3$ for Solid-State Sensitised Solar Cell Applications. *J. Mater. Chem. A* **2013**, *1*, 5628−5641.

(31) Osherov, A.; Hutter, E. M.; Galkowski, K.; Brenes, R.; Maude, D. K.; Nicholas, R. J.; Plochocka, P.; Bulović, V.; Savenije, T. J.; Stranks, S. D. The Impact of Phase Retention on the Structural and Optoelectronic Properties of Metal Halide Perovskites. *Adv. Mater.* **2016**, *28*, 10757−10763.

(32) Witt, C.; Schmid, A.; Leupold, N.; Schultz, M.; Höcker, J.; Baumann, A.; Moos, R.; Panzer, F. Impact of Pressure and Temperature on the Compaction Dynamics and Layer Properties of Powder-Pressed Methylammonium Lead Halide Thick Films. *ACS Appl. Electron. Mater.* **2020**, *2*, 2619−2628.

(33) Guo, X.; McCleese, C.; Kolodziej, C.; Samia, A. C. S.; Zhao, Y.; Burda, C. Identification and Characterization of the Intermediate Phase in Hybrid Organic−Inorganic $MAPbI_3$ Perovskite. *Dalton Trans.* **2016**, *45*, 3806−3813.

(34) Kong, W.; Ye, Z.; Qi, Z.; Zhang, B.; Wang, M.; Rahimi-Iman, A.; Wu, H. Characterization of an Abnormal Photoluminescence Behavior Upon Crystal-Phase Transition of Perovskite $CH_3NH_3PbI_3$. *Phys. Chem. Chem. Phys.* **2015**, *17*, 16405−16411.

(35) Onoda-Yamamuro, N.; Matsuo, T.; Suga, H. Calorimetric and IR Spectroscopic Studies of Phase Transitions in Methylammonium Trihalogenoplumbates (II). *J. Phys. Chem. Solids* **1990**, *51*, 1383−1395.

(36) Schötz, K.; Askar, A. M.; Köhler, A.; Shankar, K.; Panzer, F. Investigating the Tetragonal-to-Orthorhombic Phase Transition of Methylammonium Lead Iodide Single Crystals by Detailed Photoluminescence Analysis. *Adv. Opt. Mater.* **2020**, *8*, 2000455.

(37) Findik, G.; Biliroglu, M.; Seyitliyev, D.; Mendes, J.; Barrette, A.; Ardekani, H.; Lei, L.; Dong, Q.; So, F.; Gundogdu, K. High-temperature Superfluorescence in Methylammonium Lead Iodide. *Nat. Photonics* **2021**, *15*, 676−680.

(38) Panzer, F.; Li, C.; Meier, T.; Köhler, A.; Huettner, S. Impact of Structural Dynamics on the Optical Properties of Methylammonium Lead Iodide Perovskites. *Adv. Energy Mater.* **2017**, *7*, 1700286.

(39) Singh, S.; Li, C.; Panzer, F.; Narasimhan, K. L.; Graeser, A.; Gujar, T. P.; Köhler, A.; Thelakkat, M.; Huettner, S.; Kabra, D. Effect of Thermal and Structural Disorder on the Electronic Structure of Hybrid Perovskite Semiconductor $CH_3NH_3PbI_3$. *J. Phys. Chem. Lett.* **2016**, *7*, 3014−3021.

(40) Panzer, F.; Baderschneider, S.; Gujar, T. P.; Unger, T.; Bagnich, S.; Jakoby, M.; Bässler, H.; Hüttner, S.; Köhler, J.; Moos, R.; et al. Reversible Laser-Induced Amplified Spontaneous Emission from Coexisting Tetragonal and Orthorhombic Phases in Hybrid Lead Halide Perovskites. *Adv. Opt. Mater.* **2016**, *4*, 917−928.

(41) Wu, K.; Bera, A.; Ma, C.; Du, Y.; Yang, Y.; Li, L.; Wu, T. Temperature-Dependent Excitonic Photoluminescence of Hybrid Organometal Halide Perovskite Films. *Phys. Chem. Chem. Phys.* **2014**, *16*, 22476−22481.

(42) Meier, T.; Gujar, T. P.; Schönleber, A.; Olthof, S.; Meerholz, K.; van Smaalen, S.; Panzer, F.; Thelakkat, M.; Köhler, A. Impact of Excess PbI_2 on the Structure and the Temperature Dependent Optical Properties of Methylammonium Lead Iodide Perovskites. *J. Mater. Chem. C* **2018**, *6*, 7512−7519.

(43) Schötz, K.; Askar, A. M.; Peng, W.; Seeberger, D.; Gujar, T. P.; Thelakkat, M.; Köhler, A.; Huettner, S.; Bakr, O. M.; Shankar, K.; et al. Double Peak Emission in Lead Halide Perovskites by Self-Absorption. *J. Mater. Chem. C* **2020**, *8*, 2289−2300.

(44) Lee, K. J.; Turedi, B.; Giugni, A.; Lintangpradipto, M. N.; Zhumekenov, A. A.; Alsalloum, A. Y.; Min, J.-H.; Dursun, I.; Naphade, R.; Mitra, S.; et al. Domain-Size-Dependent Residual Stress Governs the Phase-Transition and Photoluminescence Behavior of Methylammonium Lead Iodide. *Adv. Funct. Mater.* **2021**, *31*, 2008088.

(45) Wright, A. D.; Verdi, C.; Milot, R. L.; Eperon, G. E.; Pérez-Osorio, M. A.; Snaith, H. J.; Giustino, F.; Johnston, M. B.; Herz, L. M.

Electron−Phonon Coupling in Hybrid Lead Halide Perovskites. *Nat. Commun.* **2016**, *7*, 11755.

(46) Rothmann, M. U.; Kim, J. S.; Borchert, J.; Lohmann, K. B.; O'Leary, C. M.; Sheader, A. A.; Clark, L.; Snaith, H. J.; Johnston, M. B.; Nellist, P. D.; et al. Atomic-Scale Microstructure of Metal Halide Perovskite. *Science* **2020**, *370*, No. eabb5940.

(47) Qiao, L.; Fang, W.-H.; Long, R.; Prezhdo, O. V. Elimination of Charge Recombination Centers in Metal Halide Perovskites by Strain. *J. Am. Chem. Soc.* **2021**, *143*, 9982−9990.

(48) Regalado-Pérez, E.; Díaz-Cruz, E. B.; Landa-Bautista, J.; Mathews, N. R.; Mathew, X. Impact of Vertical Inhomogeneity on the Charge Extraction in Perovskite Solar Cells: A Study by Depth-Dependent Photoluminescence. *ACS Appl. Mater. Interfaces* **2021**, *13*, 11833−11844.

(49) Cody, G. D.; Tiedje, T.; Abeles, B.; Moustakas, T. D.; Brooks, B.; Goldstein, Y. Disorder and the Optical-Absorption Edge of Hydrogenated Amorphous Silicon. *Phys. Rev. Lett.* **1981**, *47*, 1480−1483.

(50) Ledinsky, M.; Schönfeldová, T.; Holovský, J.; Aydin, E.; Hájková, Z.; Landová, L.; Neyková, N.; Fejfar, A.; De Wolf, S. Temperature Dependence of the Urbach Energy in Lead Iodide Perovskites. *J. Phys. Chem. Lett.* **2019**, *10*, 1368−1373.

(51) Staub, F.; Hempel, H.; Hebig, J.-C.; Mock, J.; Paetzold, U. W.; Rau, U.; Unold, T.; Kirchartz, T. Beyond Bulk Lifetimes: Insights into Lead Halide Perovskite Films from Time-Resolved Photoluminescence. *Phys. Rev. Appl.* **2016**, *6*, 044017.

(52) Kirchartz, T.; Márquez, J. A.; Stolterfoht, M.; Unold, T. Photoluminescence-Based Characterization of Halide Perovskites for Photovoltaics. *Adv. Energy Mater.* **2020**, *10*, 1904134.

(53) Rey, G.; Spindler, C.; Babbe, F.; Rachad, W.; Siebentritt, S.; Nuys, M.; Carius, R.; Li, S.; Platzer-Björkman, C. Absorption Coefficient of a Semiconductor Thin Film from Photoluminescence. *Phys. Rev. Appl.* **2018**, *9*, 064008.

(54) Fassl, P.; Lami, V.; Berger, F. J.; Falk, L. M.; Zaumseil, J.; Richards, B. S.; Howard, I. A.; Vaynzof, Y.; Paetzold, U. W. Revealing the Internal Luminescence Quantum Efficiency of Perovskite Films via Accurate Quantification of Photon Recycling. *Matter* **2021**, *4*, 1391−1412.

(55) Patel, J. B.; Wright, A. D.; Lohmann, K. B.; Peng, K.; Xia, C. Q.; Ball, J. M.; Noel, N. K.; Crothers, T. W.; Wong-Leung, J.; Snaith, H. J.; et al. Light Absorption and Recycling in Hybrid Metal Halide Perovskite Photovoltaic Devices. *Adv. Energy Mater.* **2020**, *10*, 1903653.

(56) Ayik, C.; Studenyak, I.; Kranjec, M.; Kurik, M. Urbach Rule in Solid State Physics. *Int. J. Opt. Appl.* **2014**, *4*, 76−83.

(57) Xia, C. Q.; Peng, J.; Poncé, S.; Patel, J. B.; Wright, A. D.; Crothers, T. W.; Uller Rothmann, M.; Borchert, J.; Milot, R. L.; Kraus, H.; et al. Limits to Electrical Mobility in Lead-Halide Perovskite Semiconductors. *J. Phys. Chem. Lett.* **2021**, *12*, 3607−3617.

(58) Bhuyan, S.; Mondal, R.; Pal, B.; Bansal, B. Distinguishing Quantum Dot-like Localized States from Quantum Well-like Extended States Across the Exciton Emission Line in a Quantum Well. *J. Phys.: Condens. Matter* **2018**, *30*, 105402.

(59) Herz, L. M. Charge-Carrier Dynamics in Organic-Inorganic Metal Halide Perovskites. *Annu. Rev. Phys. Chem.* **2016**, *67*, 65−89.

(60) Mrkyvkova, N.; Held, V.; Nádaždy, P.; Subair, R.; Majkova, E.; Jergel, M.; Vlk, A.; Ledinsky, M.; Kotlár, M.; Tian, J.; et al. Combined in Situ Photoluminescence and X-ray Scattering Reveals Defect Formation in Lead-Halide Perovskite Films. *J. Phys. Chem. Lett.* **2021**, *12*, 10156−10162.

(61) Haeger, T.; Heiderhoff, R.; Riedl, T. Thermal Properties of Metal-Halide Perovskites. *J. Mater. Chem. C* **2020**, *8*, 14289−14311.

(62) Meng, W.; Zhang, K.; Osvet, A.; Zhang, J.; Gruber, W.; Forberich, K.; Meyer, B.; Heiss, W.; Unruh, T.; Li, N.; et al. Revealing the Strain-associated Physical Mechanisms Impacting the Performance and Stability of Perovskite Solar Cells. *Joule* **2022**, *6*, 458−475.

(63) Zhao, J.; Deng, Y.; Wei, H.; Zheng, X.; Yu, Z.; Shao, Y.; Shield, J. E.; Huang, J. Strained Hybrid Perovskite Thin Films and their

153

Impact on the Intrinsic Stability of Perovskite Solar Cells. *Sci. Adv.* **2017**, *3*, No. eaao5616.

(64) van der Pol, T. P. A.; Datta, K.; Wienk, M. M.; Janssen, R. A. J. The Intrinsic Photoluminescence Spectrum of Perovskite Films. *Adv. Opt. Mater.* **2022**, *10*, 2102557.

(65) Qaid, S. M. H.; Khan, M. N.; Alqasem, A.; Hezam, M.; Aldwayyan, A. Restraining Effect of Film Thickness on the Behaviour of Amplified Spontaneous Emission from Methylammonium Lead Iodide Perovskite. *IET Optoelectron.* **2019**, *13*, 2−6.

(66) Qin, L.; Lv, L.; Li, C.; Zhu, L.; Cui, Q.; Hu, Y.; Lou, Z.; Teng, F.; Hou, Y. Temperature Dependent Amplified Spontaneous Emission of Vacuum Annealed Perovskite Films. *RSC Adv.* **2017**, *7*, 15911−15916.

(67) Li, Y.; Allegro, I.; Kaiser, M.; Malla, A. J.; Richards, B. S.; Lemmer, U.; Paetzold, U. W.; Howard, I. A. Exciton Versus Free Carrier Emission: Implications for Photoluminescence Efficiency and Amplified Spontaneous Emission Thresholds in Quasi-2D and 3D Perovskites. *Mater. Today* **2021**, *49*, 35−47.

(68) Pourdavoud, N.; Haeger, T.; Mayer, A.; Cegielski, P. J.; Giesecke, A. L.; Heiderhoff, R.; Olthof, S.; Zaefferer, S.; Shutsko, I.; Henkel, A.; et al. Room-Temperature Stimulated Emission and Lasing in Recrystallized Cesium Lead Bromide Perovskite Thin Films. *Adv. Mater.* **2019**, *31*, 1903717.

(69) Witt, C.; Leupold, N.; Ramming, P.; Schötz, K.; Moos, R.; Panzer, F. How the Microstructure of MAPbI$_3$ Powder Impacts Pressure-Induced Compaction and Optoelectronic Thick-Film Properties. *J. Phys. Chem. C* **2022**, *126*, 15424−15435.

(70) Adhyaksa, G. W. P.; Veldhuizen, L. W.; Kuang, Y.; Brittman, S.; Schropp, R. E. I.; Garnett, E. C. Carrier Diffusion Lengths in Hybrid Perovskites: Processing, Composition, Aging, and Surface Passivation Effects. *Chem. Mater.* **2016**, *28*, 5259−5263.

(71) Crothers, T. W.; Milot, R. L.; Patel, J. B.; Parrott, E. S.; Schlipf, J.; Müller-Buschbaum, P.; Johnston, M. B.; Herz, L. M. Photon Reabsorption Masks Intrinsic Bimolecular Charge-Carrier Recombination in CH$_3$NH$_3$PbI$_3$ Perovskite. *Nano Lett.* **2017**, *17*, 5782−5789.

(72) Kavadiya, S.; Strzalka, J.; Niedzwiedzki, D. M.; Biswas, P. Crystal Reorientation in Methylammonium Lead Iodide Perovskite Thin Film with Thermal Annealing. *J. Mater. Chem. A* **2019**, *7*, 12790−12799.

(73) Ugur, E.; Ledinský, M.; Allen, T. G.; Holovský, J.; Vlk, A.; De Wolf, S. Life on the Urbach Edge. *J. Phys. Chem. Lett.* **2022**, *13*, 7702−7711.

(74) Zeiske, S.; Sandberg, O. J.; Zarrabi, N.; Wolff, C. M.; Raoufi, M.; Peña-Camargo, F.; Gutierrez-Partida, E.; Meredith, P.; Stolterfoht, M.; Armin, A. Static Disorder in Lead Halide Perovskites. *J. Phys. Chem. Lett.* **2022**, *13*, 7280−7285.

154

Supporting Information to

Orientation and Grain Size in MAPbI₃ Thin Films: Influence on Phase Transition, Disorder and Defects

Christina Witt[1], Konstantin Schötz[1], Meike Kuhn[2], Nico Leupold[3], Simon Biberger[1], Philipp Ramming[1], Frank-Julian Kahle[1], Anna Köhler[1], Ralf Moos[3], Eva M. Herzig[2], Fabian Panzer[1*]

[1] Soft Matter Optoelectronics, University of Bayreuth, Bayreuth 95440, Germany

[2] Dynamics and Structure Formation - Herzig Group, University of Bayreuth,

  Bayreuth 95440, Germany

[3] Department of Functional Materials, University of Bayreuth, Bayreuth 95440, Germany

Corresponding Author:

[*]E-Mail: fabian.panzer@uni-bayreuth.de

1. Film Preparation
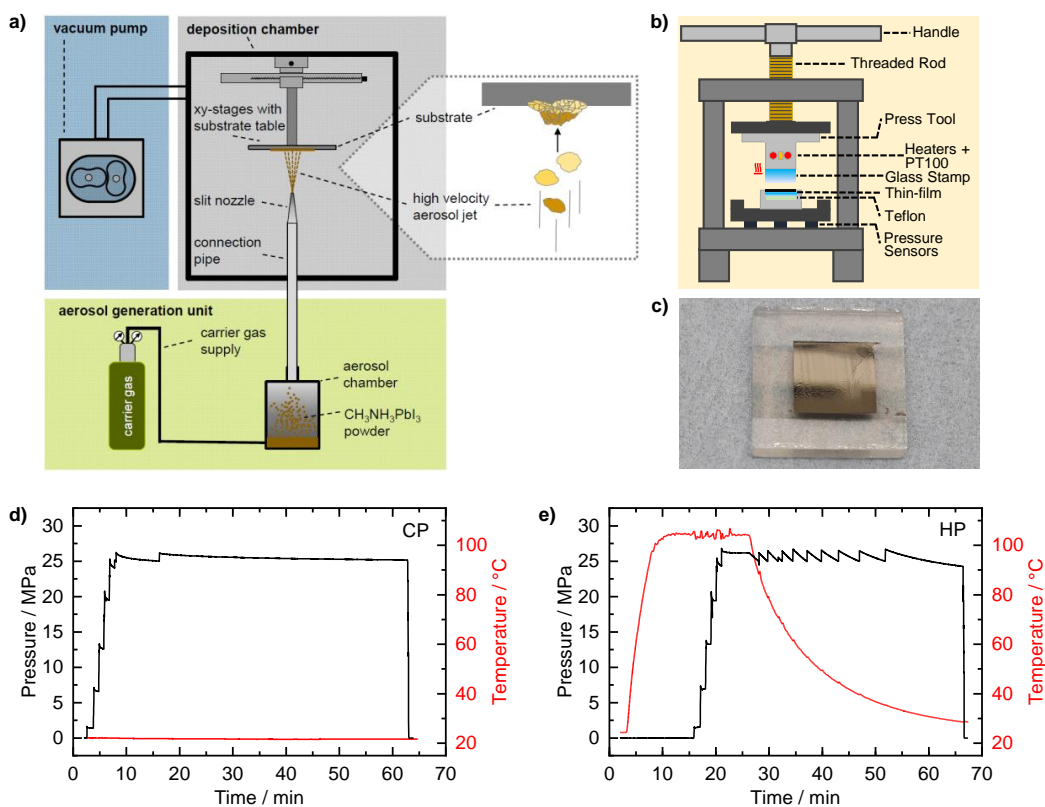
Figure S1: Dry powder-based two-step processing method for MAPbI$_3$ thin films: (a) Film formation via powder aerosol deposition method by using MAPbI$_3$ powder. Adapted under the terms of the CC-BY license.[1] Copyright 2016, the authors. Published by MDPI AG. (b) Post-treatment by (hot-) pressing the thin films with a home-built manual press. (c) Image of an as prepared MAPbI$_3$ thin film (hot-pressed) on a glass substrate. Temporal evolution of pressure and temperature of (d) a cold-pressed (CP) and (e) a hot-pressed (HP) film.

For the film formation we used the so-called powder aerosol deposition method (PADM) illustrated in Figure S1a. In this method, a dry powder aerosol is formed from mechanochemically synthesized MAPbI$_3$ powder in the aerosol generation unit using a carrier gas (for details regarding the powder synthesis see Experimental Section and Leupold N. et al. *ACS Applied Materials & Interfaces* **2019**, 11, 30259-30268[2]). Then the powder aerosol is transferred to the evacuated deposition chamber, where it is further accelerated by a nozzle and directed onto a glass substrate (3 mm thickness). When the powder particles impact the substrate, they break up, bond, and form a dense layer at room temperature. For more details

S2

156

on PADM we refer to reviews by Hanft et al.,[3] Schubert et al.,[4] and Akedo.[5-6] For our work, before deposition, the powder was dried at 120 °C for 1h. For deposition a total flow rate of 22.5 l/min helium, 0.5 to 1 g of powder, a scan rate of 1 mm/s, at least 24 scans and a substrate-to-nozzle distance of 3 mm were used.

Pressing served as post-treatment for the deposited $MAPbI_3$ films. For this purpose, a manual press was used (sketch in Figure S1b), where pressure can be applied by turning down the installed press stamp. The glass stamp, attached to the metal stamp via heat-conducting paste, was silanized to prevent sticking of the $MAPbI_3$ layer. The substrate with the $MAPbI_3$ film was placed in a press mold. A Teflon plate was placed under the substrate to compensate for possible height differences and thus ensure uniform pressure distribution on the film. The pressure was monitored via the pressure sensors below the press mold. For hot-pressing, the press stamp was heated with two heating cartridges and the temperature was controlled with a PT100 sensor. The temperature could be recorded via the used temperature controller. Figure S1d,e show the time profile of pressure and temperature for a $MAPbI_3$ thin film pressed at room temperature (CP) and a $MAPbI_3$ thin film pressed at elevated temperature (about 100 °C, HP).

Grain sizes were determined for two CP/HP sample pairs from top-view SEM images (Figure 1a,b and Figure S2) using the software imageJ. The grain boundaries were traced with imageJ and the area of all grains completely shown in the image was determined (exemplary selection of grains for a HP film in Figure S3b). An equivalent diameter of a circle was calculated from the area of each grain and referred to as grain size. From all considered grains of a sample, the mean diameter and standard deviation were calculated. The resulting average grain sizes for the sample pair A of (150 ± 75) nm for the CP film and (220 ± 110) nm for the HP film are in good agreement with those of the sample pair B with (130 ± 85) nm for the CP film and (250 ± 150) nm for the HP film (Figure S2).

S3
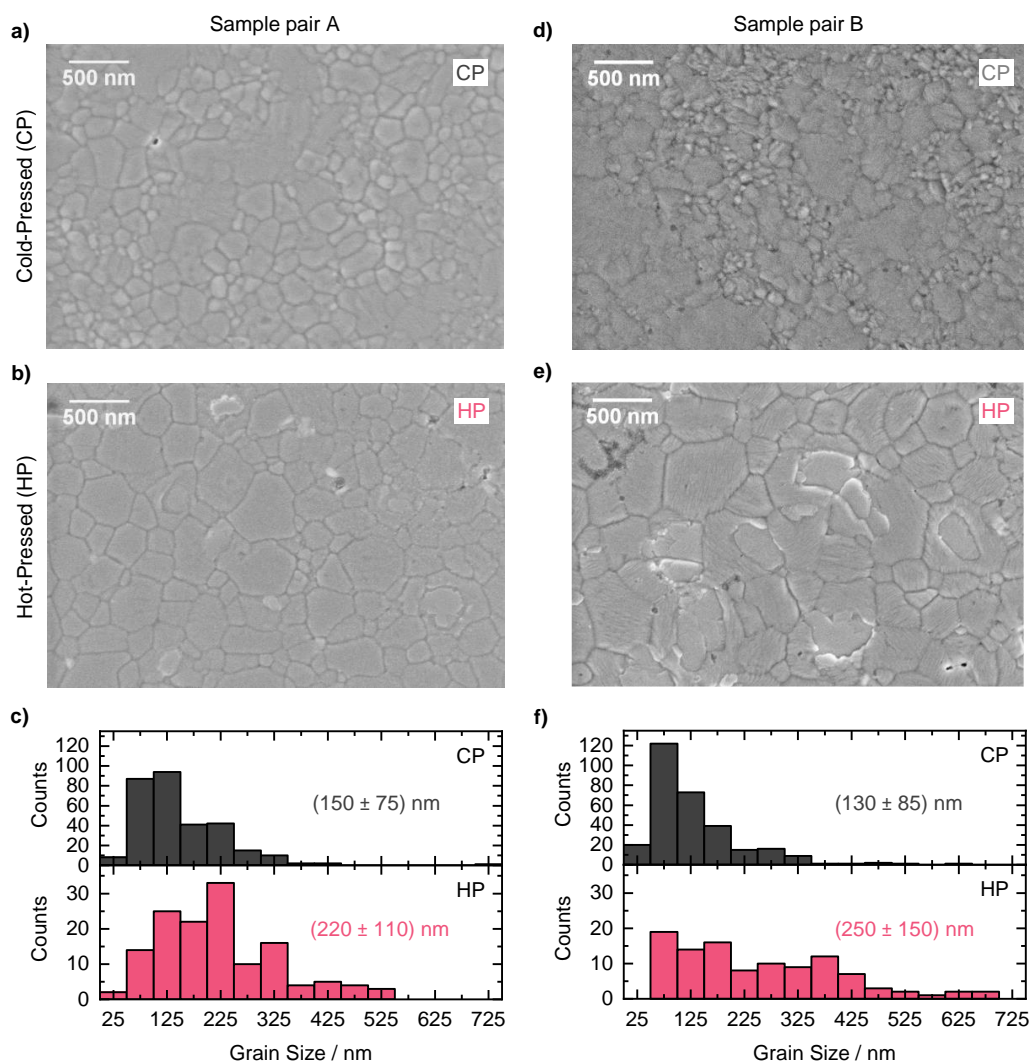
Figure S2: Grain sizes of cold-pressed (CP, grey) and hot-pressed (HP, red) MAPbI$_3$ thin films: (a, b) Top-view SEM images and (c) corresponding grain size distributions for the CP/HP sample pair shown in the main text. (d, e) Top-view SEM images and (f) corresponding grain size distributions for an additional CP/HP sample pair.

The XRD patterns over the entire recorded angular range from 10° to 45° (Figure S3c) are consistent with expectation for MAPbI$_3$ and show that, apart from a small PbI$_2$ reflex at 12.7°, the films are phase pure.[2] The fits from Rietveld Refinement were applied in the angular range from 19° to 45°, as below 15° the measured intensity may be slightly changed due to X-ray radiation blocked by the sample holder.
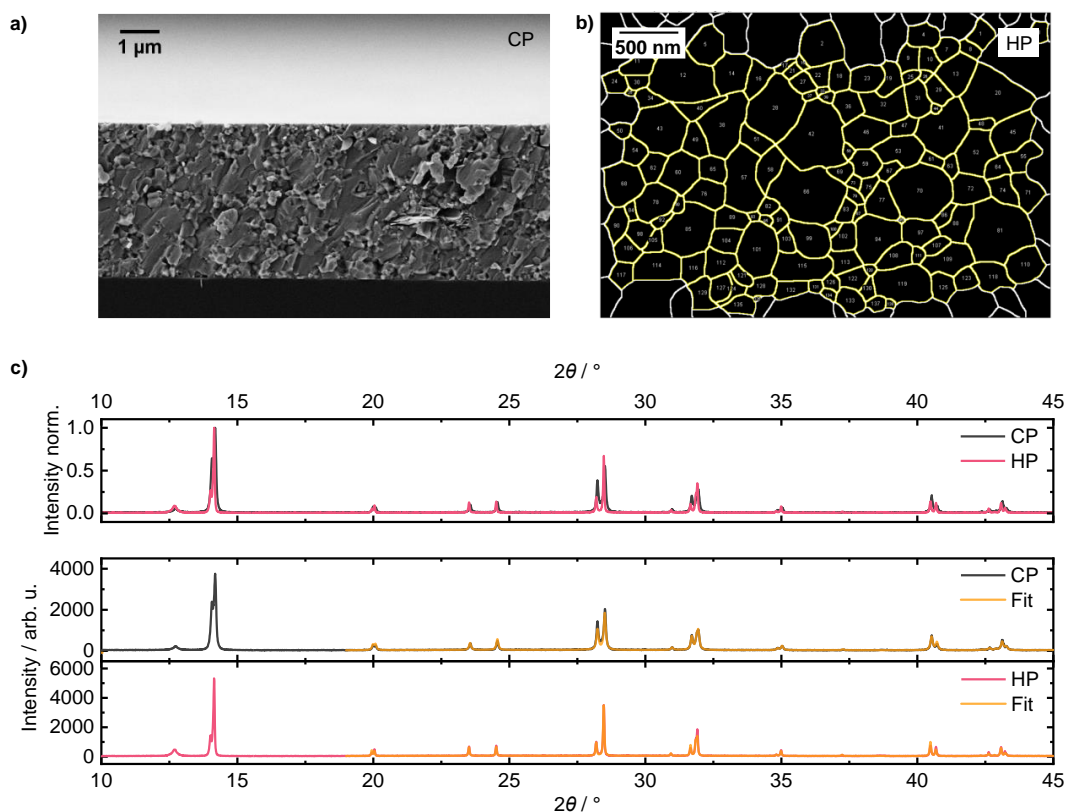
Figure S3: Morphology investigations of pressed MAPbI₃ thin films: (a) Cross-section SEM image of a CP film. (b) Grain size analysis via imageJ software from the top-view SEM image of an HP film shown in Figure 1b in the main text. (c) Normalized measured XRD patterns of a CP film (grey line) and an HP film (red line) in the entire measured angular range from 10° to 45° (top panel) and applied fits to the measured XRD patterns (orange lines) from Rietveld refinement in the angular range from 19° to 45° (bottom panel).

To investigate the influence of hot-pressing on the stoichiometry of our MAPbI₃ films, we measured XPS spectra (Figure S4) of a MAPbI₃ film before pressing (pristine, grey) and after hot-pressing (HP, red).

The XPS spectra give compositional information of the film surface and were measured with a PHI 5000 Versa Probe III Scanning XPS Microscope (ULVAC-PHI). An area of 300 μm x 300 μm in the center of the film was scanned by a microfocused Al Kα X-Ray beam (E = 1486.6 eV, 25 W, 100 μm) and the analyzer. The take-off angle of the photoelectrons was set to 45° and a dual-beam charge neutralizer was utilized for charge compensation.
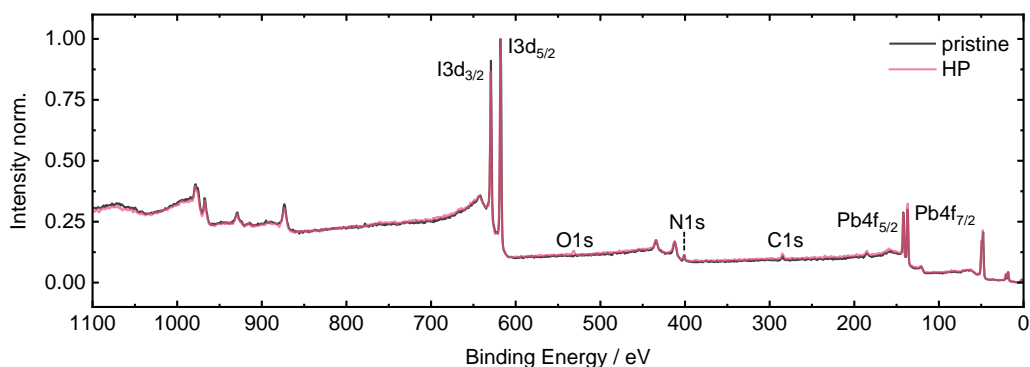
Figure S4: Normalized XPS spectra of a MAPbI₃ film before (pristine, grey) and after hot-pressing (HP, red).

The relevant peaks for the stoichiometry analysis of our MAPbI₃ (CH₃NH₃PbI₃) film corresponding to I3d, N1s, C1s and Pb4f are labeled in Figure S4 (H1s cannot be detected).[7] Overall, the spectra of the pristine and hot-pressed film appear similar at first. However, after hot-pressing an additional small peak corresponding to O1s at about 530 eV appears, as the hot-pressing is performed at ambient conditions. Furthermore, the peak intensities corresponding to I3d and Pb4f indicate a lower I:Pb ratio after hot-pressing. To quantify this, we determined the atomic concentrations from detail scans of the labeled peaks after background correction by evaluating the area under the peaks (for which the peaks were fitted). The atomic concentrations for I and Pb and the resulting I:Pb ratio for the pristine and hot-pressed film are summarized in Table S1. The I:Pb ratio of 3.08 for the pristine film is close to the expected value of 3. After hot-pressing the I:Pb ratio is reduced to a value of 2.76, which indicates more PbI₂ being present at the film surface of HP. This is in line with the increased amount of PbI₂ in the HP sample observed in XRD patterns.

MAPbI₃ film	I / %	Pb / %	I:Pb
pristine	47.38	15.37	3.08
HP	40.63	14.72	2.76

Table S1: Atomic concentrations of I and Pb and resulting I:Pb ratio extracted from the XPS spectra of a MAPbI₃ film measured before pressing (pristine) and after hot-pressing (HP).

As discussed in Section 3.2.1 in the main text, a decreased phase transition temperature is associated with an increased amount of strain located at the grain boundaries. As an increased amount of PbI_2 indicates imperfections / iodide vacancies in the film, it may be conceivable that PbI_2 leads to additional distortion related strain which further lowers the phase transition temperature.

In a previous work about solution processed $MAPbI_3$ thin films, an increased PbI_2 content was found to correlate with decreased grain size and lower phase transition temperature,[8] indicating that strain at the grain boundaries and/or PbI_2 induced distortion related strain are responsible for lower phase transition temperatures. In the current work, however, an increased PbI_2 content in the HP film goes along with a higher grain size and increased phase transition temperature, emphasizing strain at the grain boundaries to be the main aspect to impact the phase transition temperature. In contrast, PbI_2 induced distortion related strain seems not to have a significant effect on the phase transition temperature. The work of Rothmann et al. supports the minor relevance of PbI_2 induced distortion related strain, as atomic-resolution LAADF micrographs of $FAPbI_3$ show distortion-free transitions between $FAPbI_3$ and PbI_2.[9] Therefore, we conclude that strain at grain boundaries and thus the grain size is mainly affecting the phase transition temperature, whereas PbI_2 induced strain is negligible and thus not relevant regarding the phase transition.

2. PL Spectra
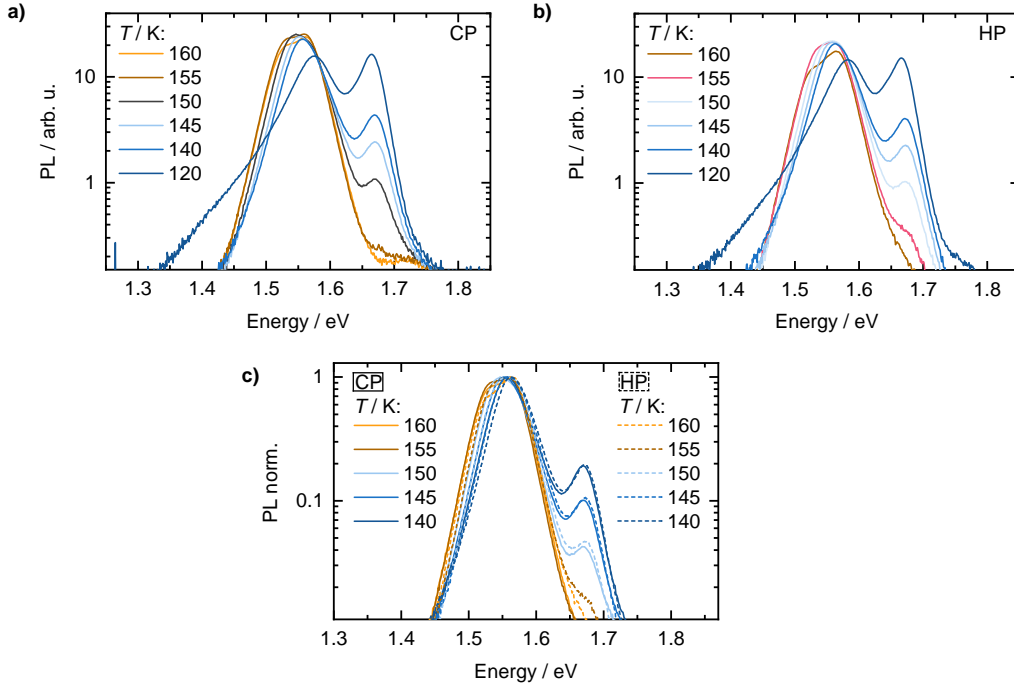
Figure S5: PL spectra of MAPbI$_3$ thin films in the phase transition region between 160 K and 120 K: PL spectra of (a) a CP film and (b) an HP film. (c) Normalized PL spectra of a CP film (solid lines) and an HP film (dashed lines).

The PL spectra between 300 K and 160 K (Figure S6a, Figure 4a in the main text) show a red-shift with decreasing temperature, in line with literature.[10-11] PL$_{direct}$ peak positions were determined from the center of Gauss fits to the PL$_{direct}$ peaks in the PL spectra. The red-shift was evaluated by the slope of linear fits to the temperature-dependent direct PL peak positions (see Figure 5a in the main text). The red-shift is identical within the uncertainty of the linear fits for both CP and HP with a value of about 0.32 meV K^{-1}. This value is in good agreement with reported values for halide perovskites.[12-13] In the past, it was found that in-plane tensile strain is induced by the substrate upon cooling due to its lower thermal expansion coefficient compared to the perovskite layer.[14-15] This substrate induced tensile strain hinders the perovskite lattice constant to decrease during cooling, resulting in a decreased temperature-dependent PL peak shift.[12-14] Since our PL shifts for CP and HP are identical, we conclude that the substrate induced tensile strain is similar in both samples,

which is reasonable with regard to the same substrate materials and the similar film thickness of both samples.
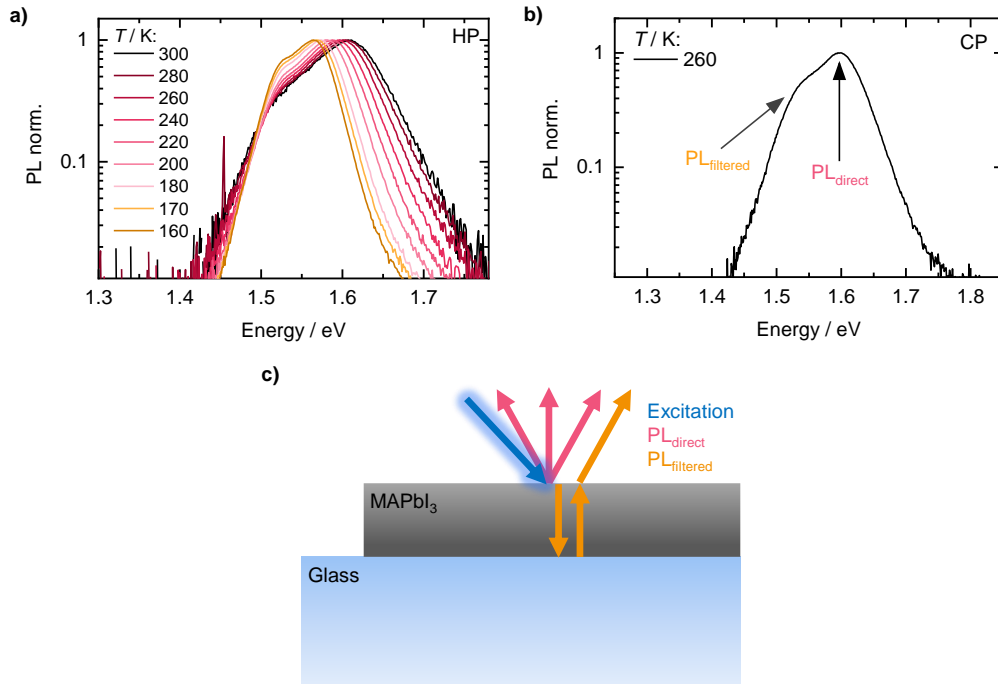
Figure S6: PL in MAPbI₃ thin films: (a) Normalized PL spectra of an HP film in the tetragonal phase between 300 K and 160 K. (b) Normalized PL spectrum of a CP film at 260 K with arrows indicating the direct PL peak and the shoulder due to filtered PL. (c) Illustration of emitted PL after excitation of a MAPbI₃ thin film on a glass substrate: After excitation (blue arrow) direct PL (red arrows) is emitted from (near) the surface. In addition, filtered PL (orange arrows) is emitted, which is PL travelling through the film, getting internally reflected and overall filtered by the absorption of the sample.
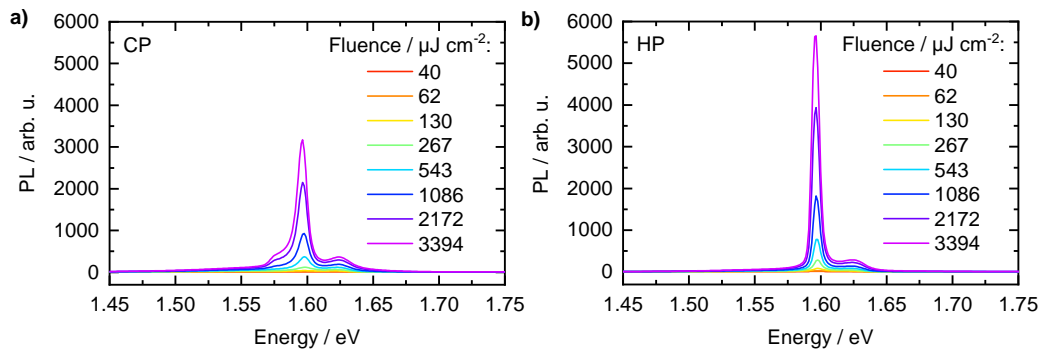
Figure S7: Fluence-dependent PL spectra of (a) a CP and (b) an HP MAPbI₃ thin film measured at 5 K.

3. PL Lifetime and Orientation

After temperature cycling (cooling from 300 K to 5 K and reheating to 300 K), our MAPbI₃ thin films exhibit morphological changes reflected in reorientation from the 110- to the 002-preferred orientation (see Figure S8b,c,d) and in the formation of strongly fused grain domains
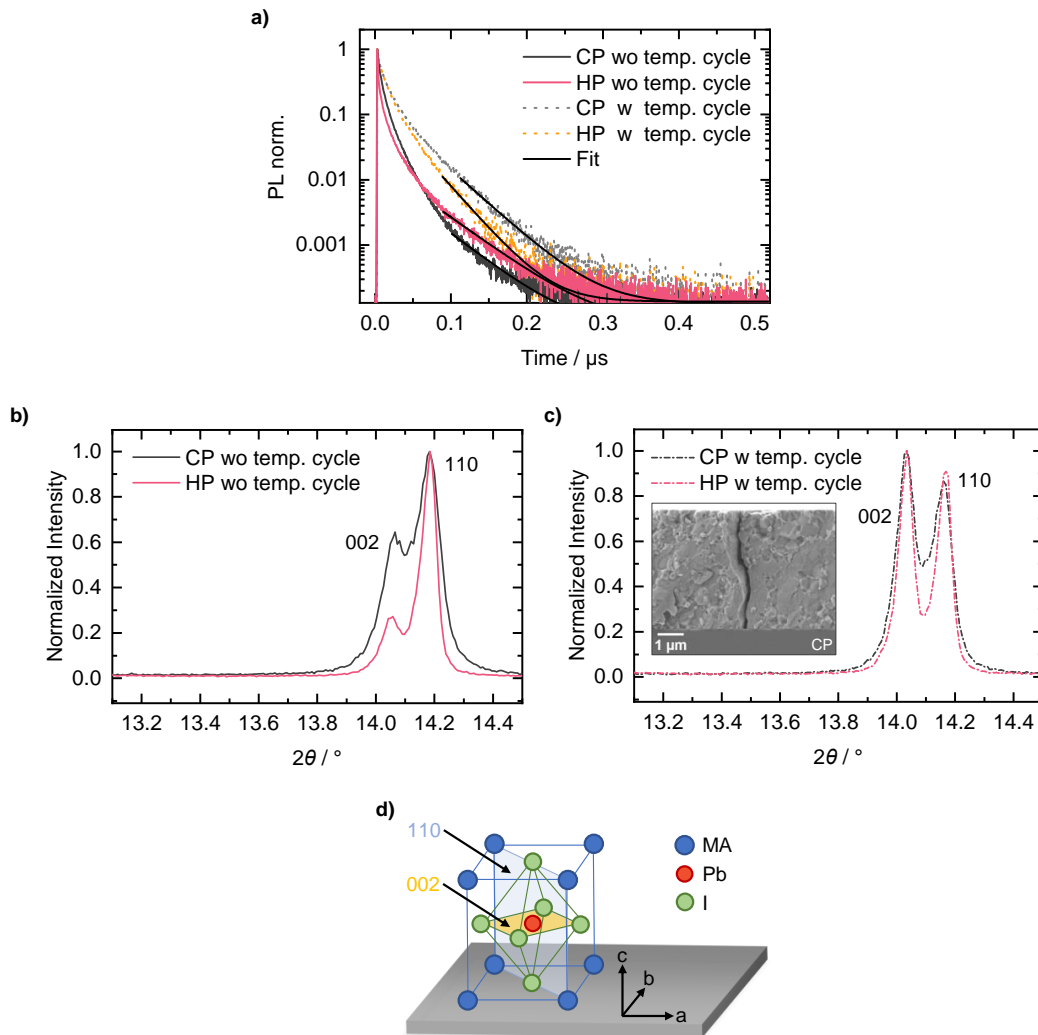
Figure S8: (a) TRPL curves of CP and HP MAPbI₃ thin films without (grey and red solid lines) and with (grey and orange dashed lines) temperature cycling. To extract charge carrier lifetimes, mono-exponential fits were applied to the tail of the PL curves (black solid lines). XRD pattern of the 002, 110 reflex pair for a CP (grey) and an HP (red) MAPbI₃ thin film (b) without and (c) with temperature cycling. The inset in (c) shows a cross-section SEM image of a CP film with a crack throughout the

film thickness after temperature cycling. (d) Sketch of MAPbI$_3$ unit cell with 110 (blue) and 002 (yellow) planes indicated.

(separated by cracks, see inset in Figure S8c and Figure S9a). Crystallographic reorientation in MAPbI$_3$ thin films due to temperature cycling through phase transitions as well as associated fusion of grains and grain domains have already been observed earlier.[16-17] Osherov et al. have investigated the morphological changes due to temperature cycling across the transition between tetragonal and orthorhombic phase using temperature-dependent XRD measurements. They observed that reorientation does not yet occur when MAPbI$_3$ thin films are cooled below the phase transition temperature but when they are reheated and pass the phase transition again. Since reorientation has been observed only in MAPbI$_3$ thin films and not in MAPbI$_3$ powder samples, Osherov et al. suggest that the morphological changes result from the (hindering or promoting) influence of the substrate in the alignment of crystallographic domains.[17] During temperature cycling, such an influence of the substrate can possibly result from the thermal coefficient mismatch between the glass substrate and the perovskite layer.[14] We suppose that similar to the morphological changes observed by Osherov et al., morphological changes were induced in our MAPbI$_3$ thin films by temperature cycling between 300 K and 5 K. In parallel to the observations of Osherov et al. we assume that the morphological changes occur when the phase transition is crossed during reheating.[17] Therefore, all optical measurements in this work, which were already recorded in the first part of the temperature cycle during cooling, are considered as unaffected by the discussed morphological changes, i.e., reorientation and fusion of grain domains with associated formation of cracks. Microscope images of an HP film during a temperature cycle between 300 K and 80 K (see Figure S9b,c and end of this Section), which show no formation of cracks, support our assumption that our optical measurements taken during initial cooling are unaffected by morphological changes. In addition, morphological changes in our MAPbI$_3$ thin films seem to occur only when the temperature is cycled significantly below the phase transition, e.g., down to 5 K (Figure S9a).

The microscope images of an HP film (pressing temperature about 120 °C) during a temperature cycle between 300 K and 80 K (Figure S9b,c) were taken with a digital microscope (Keyence VHX 970F with VH-Z250L objective). The microscope images were taken through the window of a LINKAM stage (THMS600 heating and freezing stage system, Serial No. DV1558-

0009 THMS600E-4), in which the MAPbI$_3$ thin film was placed for temperature cycling. A nitrogen atmosphere was created in the LINKAM stage before the start of the temperature cycle to prevent moisture from condensing on the film during cooling. Cooling of the sample in the LINKAM stage was performed by a nitrogen flow from a liquid nitrogen tank through the sample holder in the LINKAM stage using a LNP95 cooling pump. Warm recycled nitrogen gas was blown across the window of the LINKAM stage to avoid condensation. In addition to cooling with nitrogen flow, a heating unit integrated in the LINKAM stage was also provided for temperature control. The temperature was controlled and recorded via a controller with the LINK software.
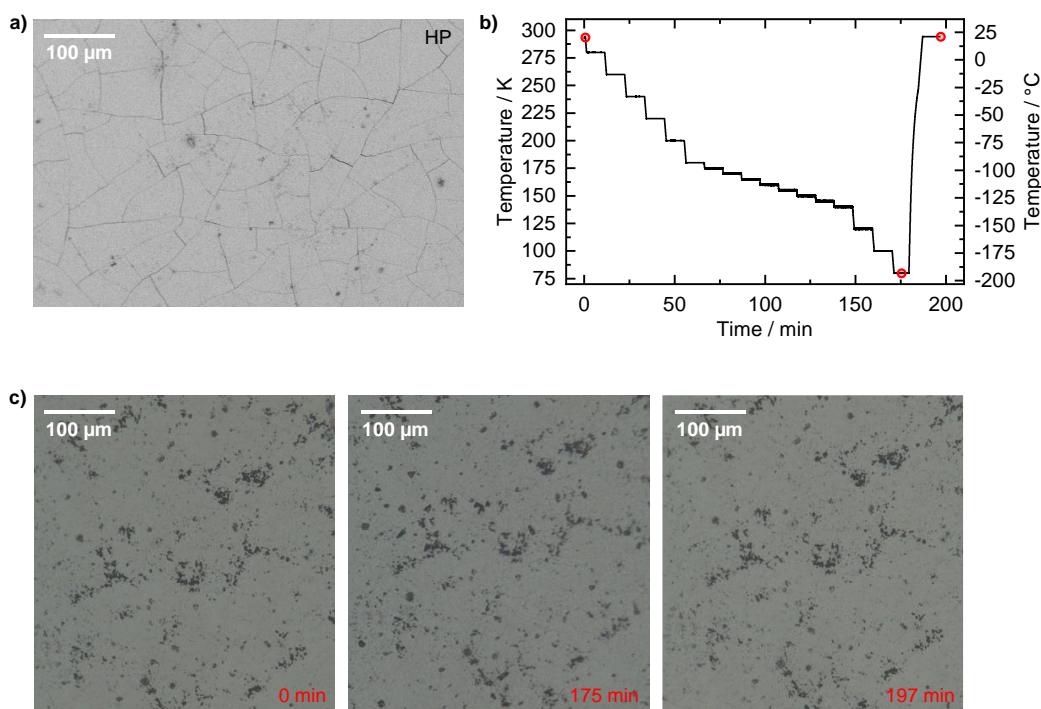
Figure S9: (a) Top-view SEM image of an HP MAPbI$_3$ thin film after temperature cycling between 300 K and 5 K. (b) Temperature as a function of time during a temperature cycle between 300 K and 80 K and (c) top-view microscope images of an HP MAPbI$_3$ thin film during the temperature cycling shown in (b) at different times as indicated (also see red open circles in b). The microscope images show no cracks even when crossing the phase transition.

S12

166

References

1. Panzer, F.; Hanft, D.; Gujar, T. P.; Kahle, F.-J.; Thelakkat, M.; Köhler, A.; Moos, R. Compact Layers of Hybrid Halide Perovskites Fabricated via the Aerosol Deposition Process—Uncoupling Material Synthesis and Layer Formation. *Materials* **2016,** *9*, 277.

2. Leupold, N.; Schötz, K.; Cacovich, S.; Bauer, I.; Schultz, M.; Daubinger, M.; Kaiser, L.; Rebai, A.; Rousset, J.; Köhler, A., et al. High Versatility and Stability of Mechanochemically Synthesized Halide Perovskite Powders for Optoelectronic Devices. *ACS Appl. Mater. Interfaces* **2019,** *11*, 30259-30268.

3. Hanft, D.; Exner, J.; Schubert, M.; Stöcker, T.; Fuierer, P.; Moos, R. An Overview of the Aerosol Deposition Method: Process Fundamentals and New Trends in Materials Applications. *J. Ceram. Sci. Technol.* **2015,** *6*, 147-182.

4. Schubert, M.; Hanft, D.; Nazarenus, T.; Exner, J.; Schubert, M.; Nieke, P.; Glosse, P.; Leupold, N.; Kita, J.; Moos, R. Powder Aerosol Deposition Method — Novel Applications in the Field of Sensing and Energy Technology. *Funct. Mater. Lett.* **2019,** *12*, 1930005.

5. Akedo, J. Room Temperature Impact Consolidation (RTIC) of Fine Ceramic Powder by Aerosol Deposition Method and Applications to Microdevices. *J. Therm. Spray Technol.* **2008,** *17*, 181-198.

6. Akedo, J. Room Temperature Impact Consolidation and Application to Ceramic Coatings: Aerosol Deposition Method. *J. Ceram. Soc. Jpn.* **2020,** *128*, 101-116.

7. Dunlap-Shohl, W. A.; Li, T.; Mitzi, D. B. Interfacial Effects during Rapid Lamination within MAPbI$_3$ Thin Films and Solar Cells. *ACS Appl. Energy Mater.* **2019,** *2*, 5083-5093.

8. Meier, T.; Gujar, T. P.; Schönleber, A.; Olthof, S.; Meerholz, K.; van Smaalen, S.; Panzer, F.; Thelakkat, M.; Köhler, A. Impact of Excess PbI$_2$ on the Structure and the Temperature Dependent Optical Properties of Methylammonium Lead Iodide Perovskites. *J. Mater. Chem. C* **2018,** *6*, 7512-7519.

9. Rothmann, M. U.; Kim, J. S.; Borchert, J.; Lohmann, K. B.; O'Leary, C. M.; Sheader, A. A.; Clark, L.; Snaith, H. J.; Johnston, M. B.; Nellist, P. D., et al. Atomic-Scale Microstructure of Metal Halide Perovskite. *Science* **2020,** *370*, eabb5940.

10. Lee, K. J.; Turedi, B.; Giugni, A.; Lintangpradipto, M. N.; Zhumekenov, A. A.; Alsalloum, A. Y.; Min, J.-H.; Dursun, I.; Naphade, R.; Mitra, S., et al. Domain-Size-Dependent Residual Stress Governs the Phase-Transition and Photoluminescence Behavior of Methylammonium Lead Iodide. *Adv. Funct. Mater.* **2021,** *31*, 2008088.

11. Wright, A. D.; Verdi, C.; Milot, R. L.; Eperon, G. E.; Pérez-Osorio, M. A.; Snaith, H. J.; Giustino, F.; Johnston, M. B.; Herz, L. M. Electron–Phonon Coupling in Hybrid Lead Halide Perovskites. *Nat. Commun.* **2016,** *7*, 11755.

12. Meng, W.; Zhang, K.; Osvet, A.; Zhang, J.; Gruber, W.; Forberich, K.; Meyer, B.; Heiss, W.; Unruh, T.; Li, N., et al. Revealing the Strain-associated Physical Mechanisms Impacting the Performance and Stability of Perovskite Solar Cells. *Joule* **2022,** *6*, 458-475.

13. Schötz, K.; Askar, A. M.; Peng, W.; Seeberger, D.; Gujar, T. P.; Thelakkat, M.; Köhler, A.; Huettner, S.; Bakr, O. M.; Shankar, K., et al. Double Peak Emission in Lead Halide Perovskites by Self-Absorption. *J. Mater. Chem. C* **2020,** *8*, 2289-2300.

14. Liu, D.; Luo, D.; Iqbal, A. N.; Orr, K. W. P.; Doherty, T. A. S.; Lu, Z.-H.; Stranks, S. D.; Zhang, W. Strain Analysis and Engineering in Halide Perovskite Photovoltaics. *Nat. Mater.* **2021,** *20*, 1337-1346.

15. Zhao, J.; Deng, Y.; Wei, H.; Zheng, X.; Yu, Z.; Shao, Y.; Shield, J. E.; Huang, J. Strained Hybrid Perovskite Thin Films and their Impact on the Intrinsic Stability of Perovskite Solar Cells. *Sci. Adv.* **2017,** *3*, eaao5616.

16. Kavadiya, S.; Strzalka, J.; Niedzwiedzki, Dariusz M.; Biswas, P. Crystal Reorientation in Methylammonium Lead Iodide Perovskite Thin Film with Thermal Annealing. *J. Mater. Chem. A* **2019,** *7*, 12790-12799.

17. Osherov, A.; Hutter, E. M.; Galkowski, K.; Brenes, R.; Maude, D. K.; Nicholas, R. J.; Plochocka, P.; Bulović, V.; Savenije, T. J.; Stranks, S. D. The Impact of Phase Retention on the Structural and Optoelectronic Properties of Metal Halide Perovskites. *Adv. Mater.* **2016,** *28*, 10757-10763.

4.5 Understanding Method-Dependent Differences in Urbach Energies in Halide Perovskites

**Christina Witt**, Konstantin Schötz, Anna Köhler, Fabian Panzer.

Understanding Method-Dependent Differences in Urbach Energies in Halide Perovskites

Christina Witt[1], Konstantin Schötz[1], Anna Köhler[1], Fabian Panzer[1*]

[1] Soft Matter Optoelectronics, University of Bayreuth, Bayreuth 95440, Germany

Corresponding Author:

[*]E-Mail: fabian.panzer@uni-bayreuth.de

Keywords: halide perovskites, Urbach energy, static and dynamic disorder, solar cells, temperature-dependent PL and absorption measurements, spectroscopy, semiconductor

TOC Graphic
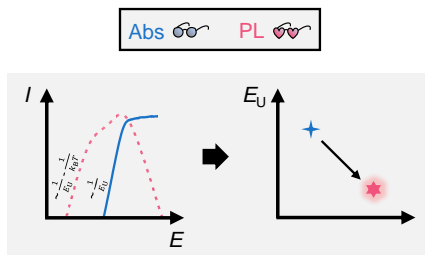
Abstract

The Urbach energy as a measure of energetic disorder is an important characteristic of semiconductors to evaluate their optoelectronic functionality. However, discrepancies occur in Urbach energy values E_U determined via different measurement and analysis methods, for whose origin a profound understanding is still missing. To reliably analyze the origin of such discrepancies we recorded quasi-simultaneously temperature-dependent absorption and photoluminescence (PL) spectra of halide perovskite (MAPbI$_3$) thin film and single crystal samples. Performing profound Urbach analyses in an extended energy range down to 0.2 eV below the bandgap, we find energy-range-dependent exaggeration effects on Urbach energy values to be only present in the near bandgap region (~0.02 eV below the bandgap), where non-Urbach absorption states start to contribute. Besides that, general lower E_U values and a lower temperature-dependence of E_U are obtained from PL than from absorption, which originates from the sensitivity of PL for sites with lower energetic disorder and/or higher phonon energies in the excited state geometry. Thus, our work sensitizes for proper interpretation and comparison of E_U values and with that contributes to develop a more fundamental understanding of semiconductor materials.

1. Introduction

The Urbach energy is a popular structural characteristic representing energetic disorder in crystalline (e.g., GaAs, Si, MAPbI$_3$, CIGS)[1-2] and also semi-crystalline (such as organic) semiconductors for optoelectronic applications.[3-4] The relevance of the Urbach energy manifests itself in its correlation with structural and optoelectronic properties[5-11] and thus also with optoelectronic functionality.[2, 4, 12-14] For example, the Urbach energy is related to the minimal open-circuit-voltage deficit achievable when a semiconductor is used for solar cell applications.[1-2, 4, 12, 14-16] Accordingly, the Urbach energy is a valuable figure of merit, expressing the performance potential of present and future semiconductor materials in a single number.[14]

The Urbach energy of crystalline semiconductors is composed of temperature-dependent dynamic disorder (i.e., electron-phonon interaction) and temperature-independent static disorder (i.e., zero-point phonon energy and (deep)-defect-induced disorder).[12, 17-20] Thus by determining the temperature dependence of the Urbach Energy together with appropriate modelling one can quantify the static as well as dynamic disorder of an investigated semiconductor.[17-18, 20-21]

A viable way to access the Urbach energy is to measure the optical spectra of a semiconductor. For example, the disorder-induced tail state absorption of a semiconductor often appears in a characteristic exponential band edge, whose steepness is related to the inverse of the Urbach energy.[2, 9, 14-15, 17-19, 22-25] Furthermore, the characteristic of disorder-induced tail state absorption is also contained in the low energy edge of measured photoluminescence (PL) spectra, as absorption and PL are related via the so-called reciprocity theorem.[18, 21, 26]

Recently, Ugur et al. highlighted discrepancies in evaluated Urbach energy values extracted via different measurement methods (absorption, photoluminescence - PL, external quantum efficiency - EQE, Fourier-transform photocurrent spectroscopy - FTPS, photothermal deflection spectroscopy - PDS) and different analysis methods from similarly manufactured halide perovskite samples (MAPbI$_3$).[14] Such discrepancies in Urbach energy values have also been observed by Ledinsky et al. when comparing temperature-dependent FTPS and PL based Urbach energy analyses of MAPbI$_3$ films.[18] In both works, the discrepancies are assumed to result from considering different analyzed energy ranges with different contribution of band-to-band absorption increasing near the band edge, which causes deviations from the disorder-

4

induced exponential band edge shape.[14, 18] Such energy range dependent discrepancies have also been discussed in the field of organic semiconductors (optical PDS, optical FTPS, electrical admittance spectroscopy).[3, 27] However, although the Urbach energy is a popular and important figure of merit for the performance potential of semiconductor materials, a profound understanding of the origin of the prevailing discrepancies in Urbach energy values is still missing.

To address this issue, in this work, we use MAPbI$_3$ films and single crystals, i.e., metal halide perovskite samples, to investigate in depth the origin of the present discrepancies in Urbach energy values extracted via different measurement and analysis methods. We use a home-built setup to record temperature-dependent steady-state PL and absorption spectra quasi simultaneously (time delay between absorption and PL measurement of only a few minutes at a set temperature level) on the same sample. Using this approach ensures reliable sample- and aging-independent investigations of the role of measurement and analysis methods on extracted Urbach energies. Systematically comparing the different optical Urbach analysis approaches, discrepancies in Urbach energy values are identified and analyzed, sensitizing for profound interpretation and comparison of E_U values.

5

2. Methods

<u>MAPbI$_3$ Samples:</u>

For information about manufacturing and resulting properties of the MAPbI$_3$ thin films see our previous work.[11] For analogous information for the single crystal samples, see two more of our previous works.[21, 28]

<u>Temperature-dependent Absorption and PL Measurements:</u>

The temperature-dependent steady-state absorption and PL spectra were recorded quasi simultaneously (within ~10 minutes at a set temperature level) from the same sample via a homebuilt setup. For this, the MAPbI$_3$ samples were inserted in an electrically heatable continuous flow cryostat (Oxford Instruments, Optistat CF) with an automated temperature controller (Oxford Instruments ITC503S) and the temperature was regulated from 300 K down to 5 K. Around the phase transition between tetragonal and orthorhombic phase (~ 160 K) the temperature steps were set smaller (data below 160 K in Supporting Information). Once a temperature level was reached, we waited 5 minutes before starting to record spectra. A tungsten lamp served as white-light source for the absorption measurements. The optical density was obtained by recording transmission through the sample and a reference beam that did not pass through the sample. To remove the 2nd diffraction order of the spectrograph, a 630 nm long-pass filter was inserted in the optical detection path. The absorption coefficient α was calculated from the measured optical density OD and sample thickness z following the Beer Lambert law $\alpha = \frac{OD \ln(10)}{z}$. For recording PL spectra, a 337 nm nitrogen laser (LTB MNL 100, 20 Hz, 102 μJ cm^{-2}) was used for excitation. To remove scattered excitation light, a 400 nm long-pass filter was inserted in the optical detection path. The transmission and reference beams measured when recording absorption spectra and the photoluminescence of the investigated sample when recording PL spectra were focused into a spectrograph (Andor Shamrock SR303i), respectively, and detected with a Si-CCD camera (Andor iDus DU420a-OE). All recorded absorption and PL spectra were corrected for transmission and detection efficiency of the utilized setup. For correction of measured PL spectra in terms of wavelength-dependent setup sensitivity a calibration measurement was performed by using a calibration lamp in combination with the chosen set of spectrometer grating, filter (LP400) and appropriate center-wavelength of the PL (750 nm), from which a correction function was determined by considering the certified spectrum of the calibration

6

lamp. The measured PL spectra were all multiplied with this correction function before analyses.

3. Results and Discussion

3.1. E_U Extraction Methods

Aging effects as well as small differences in film morphology and thickness are known to affect the Urbach energy.[2, 12, 20] To exclude any complicating impact of such effects on the comparison of Urbach energies in the following, temperature-dependent steady-state absorption and PL measurements for Urbach energy extraction were recorded quasi-simultaneously on the same MAPbI$_3$ thin film sample (thickness ~4 μm). This measuring procedure guarantees for a reliable, sample-independent comparison of the resulting Urbach energy values in terms of the individual measurement and analysis method (details on setup, film manufacturing and film properties in Section 2 and Supporting Information Section S1). In the following, the set of Urbach analysis methods applied in this work is presented for absorption (Section 3.1.1) and PL (Section 3.1.2) spectra from 300 K down to 160 K (tetragonal phase of MAPbI$_3$).

3.1.1. Absorption Coefficient

A common method for Urbach energy extraction from absorption spectra is fitting the absorption edge with an exponential function according to the so called Urbach Rule

$$\alpha(E) = \alpha_0 \exp\left(\frac{E - E_0}{E_U}\right) + D, \tag{1}$$

where E represents the photon energy, E_U the Urbach energy, D an optional offset accounting for light scattering in the data, E_0 a material constant and α_0 a fitting parameter.[2, 9, 15, 17-19, 21-25]

Typically, Equation 1 is fitted (solid lines) to measured absorption spectra (circles), as shown in Figure 1a between 300 K and 160 K. At 300 K, the absorption coefficient below 1.53 eV is artificially constant, with a value of about $4.5*10^3$ cm^{-1} due to the influence of light scattering on the optical density because of the transmissive setup geometry used in this study. At higher energies, the absorption coefficient increases exponentially to about $1.7*10^4$ cm^{-1} at 1.62 eV, where the absorption spectrum saturates due to limited setup sensitivity (in combination with relatively high film thickness). The exponential absorption edge becomes steeper and shifts to lower energies upon cooling, in line with literature reports for MAPbI$_3$ films.[18, 23, 29]

8

Correspondingly, the Urbach energy extracted using eq. 1 decreases upon cooling from ~20 meV at 300 K to ~11 meV at 160 K (Figure 1b). The decrease in Urbach energy upon cooling stems from reduced dynamic disorder at lower temperatures.[18, 23]
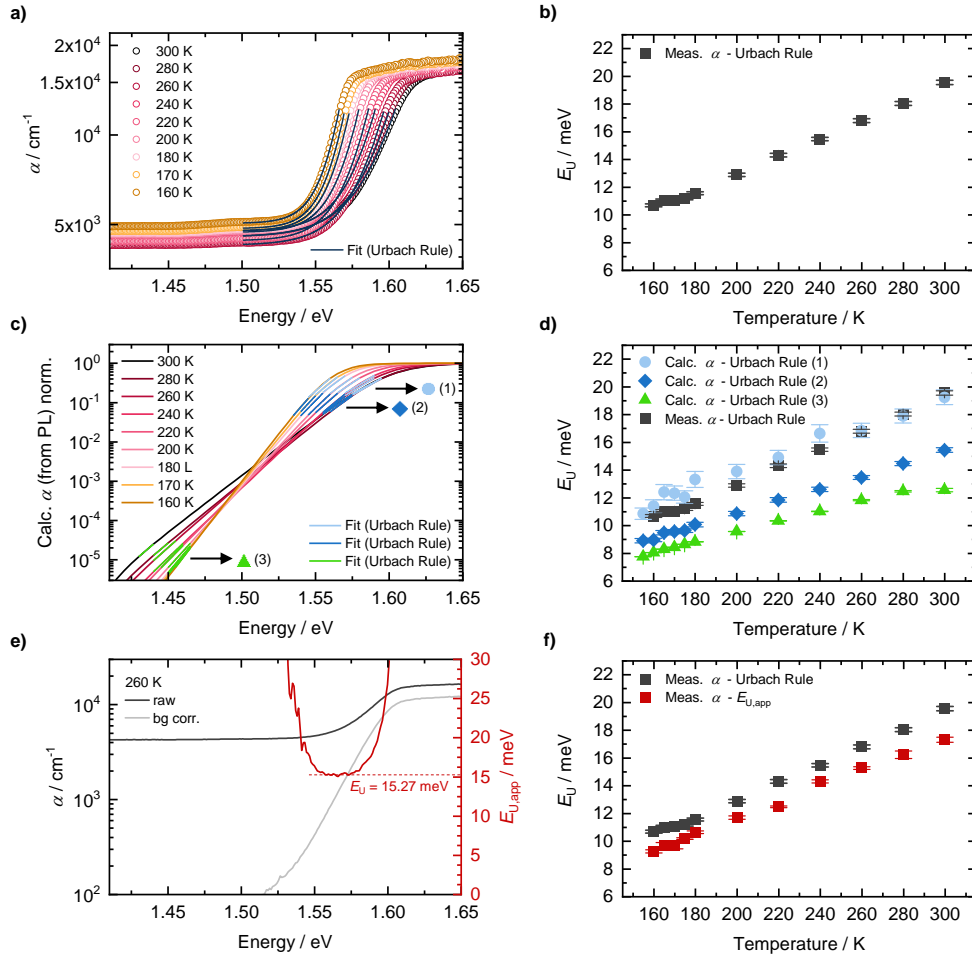
Figure 1: E_U **extraction methods from absorption for a MAPbI₃ thin film: (a) Measured absorption spectra from 300 K down to 160 K (circles) with Urbach Rule fits according to eq. 1 (solid lines) and (b) resulting** E_U **values (grey squares). (c) Absorption coefficient from 300 K down to 160 K calculated from measured PL spectra via the reciprocity theorem (eq. 2), together with Urbach Rule fits in three different energy ranges (green, dark blue, light blue). (d)** E_U **values from the fits in (c) (green, dark blue, light blue symbols) and from (b) (grey squares). (e) Absorption spectra as measured (black) and without scattering offset (grey) at 260 K and therefrom calculated apparent Urbach energy** $E_{U,app}$ **(red) using eq. 3. The Urbach energy** E_U **is given by the horizontal part of the** E_{Uapp} **profile (indicated by red dashed line). (f)** E_U **values from 300 K down to 160 K extracted via the apparent Urbach energy (e, Figures S2-4) and from (b).**

9

Alternatively, E_U can be extracted by fitting the Urbach Rule (eq. 1) to absorption spectra $\alpha(E)$ calculated from measured PL spectra $\mathrm{PL}(E)$ (Figure 2) via the reciprocity theorem

$$\alpha(E) \; \propto \; \frac{\mathrm{PL}(E)}{E^2 \cdot \exp\left(-\frac{E}{k_{\mathrm{B}}T}\right)} \tag{2}$$

(E: photon energy, k_{B}: Boltzmann constant, T: temperature).[18, 21, 26, 30] In contrast to the energy range accessible from direct absorption measurements, which are typically limited by the scattering offset to energies above ~1.53 eV, calculated absorption spectra based on measured PL spectra were shown to give access to lower energies (< 1.5 eV) and thus to an enlarged energy range.[12, 14, 18, 31] Figure 1c shows such calculated absorption spectra between 300 K and 160 K (details in Supporting Information Section S1.1.5), where indeed the band edge down to 1.425 eV is fully resolvable, so that an Urbach focus point at about 1.5 eV becomes visible. The focus point is the consequence from a similar temperature-dependence of the band gap energy and the steepness of the band edge, i.e., the Urbach energy,[17, 19, 32] and has been reported for a wide range of semiconductors.[12, 17-19, 33-36] Above the focus point the calculated absorption spectra exhibit a similar behavior as the measured absorption spectra in Figure 1a, i.e., increasing steepness and shift to lower energies of the band-edge upon cooling. Below the focus point the band edge shift is inverse. We fitted the Urbach Rule (eq. 1) in three different energy ranges to the calculated absorption spectra in Figure 1c: (1) In an upper energy range comparable to the relevant energy range from the analysis in Figure 1a (light blue), (2) in a lower energy range above the focus point (dark blue) and (3) in a low energy range below the focus point (green). The resulting temperature-dependent Urbach energy values in Figure 1d (light blue, dark blue and green symbols) show the expected decrease upon cooling in line with the values extracted in Figure 1b (grey symbols). However, differences are clearly visible in the magnitude of the extracted Urbach energies between the different fitting ranges from Figure 1c. Fitting in an upper energy range up to about 1.6 eV, i.e., comparable to the energy range considered in the analysis in Figure 1a, results in Urbach energy values (light blue symbols) between 20 meV (300 K) and 10 meV (160 K), comparable to the values from the fits in Figure 1a (grey symbols). Lowering the energy range in which the fits of eq. 1 are applied slightly below ~1.575 eV, lowers the resulting Urbach energies (dark blue symbols) to values between 16 meV (300 K) and 8 meV (160 K). Further lowering the energy range substantially, i.e., below the focus point (Figure 1c green lines), results in a rather

10

small additional reduction of Urbach energy values being in between 14 meV (300 K) and 7 meV (160 K). From this we conclude that at higher energies close to the bandgap not only exponential disorder related Urbach tail absorption but also significant contribution of band-to-band absorption affects the shape and slope of the band edge leading to exaggerated Urbach energy values.[14, 18]

To exclude effects of non-Urbach absorption states on the extracted Urbach energy values, recently, an analysis method via an apparent Urbach energy has been demonstrated for halide perovskites, considering only the purely disorder related exponential part of the absorption spectrum.[14, 20] Zeiske et al. adopted this analysis method from investigations on organic semiconductors[37] and applied it to EQE spectra of crystalline halide perovskite semiconductors,[20] followed by Ugur et al., who applied this analysis method to absorption spectra of MAPbI$_3$.[14] Here, the absorption spectrum, which is linked to the Urbach energy according to eq. 1, is converted into the so-called apparent Urbach energy

$$E_{\text{U,app}} = \left(\frac{\text{d}}{\text{d}E} [\ln(\alpha - D)] \right)^{-1}.^{[14, 20]} \tag{3}$$

Figure 1e exemplarily shows the measured absorption spectrum at 260 K from Figure 1a (black), the corresponding offset corrected absorption spectrum (grey) and the apparent Urbach energy (red) calculated from the measured absorption spectrum via eq. 3 (other temperatures in Supporting Information Figures S2-4). The Urbach energy of 15.27 meV (red dashed line) is read out from the constant horizontal part of the apparent Urbach energy, i.e., where the band edge is purely exponential.[37] The temperature-dependent Urbach energies between 300 K and 160 K extracted this way from the measured absorption spectra in Figure 1a are given in Figure 1f (red symbols). It becomes clear that the Urbach energy values between 18 meV (300 K) and 9 meV (160 K) extracted via the apparent Urbach energy (eq. 3) are lower than the ones from Figure 1b extracted via the Urbach Rule (eq. 1) in the near bandgap region (grey). This is expected since the consideration of only the horizonal part of the spectra obtained from eq. 3 implies that only the exponential disorder related part of the band edge is taken into account. Any exaggeration effects due to band-to-band absorption are hence avoided. However, the Urbach energies extracted via the apparent Urbach energy from measured absorption spectra are still larger than the ones extracted via Urbach Rule fits at energies below about 1.575 eV to absorption spectra calculated from measured PL spectra (Figure 1d, dark blue and green symbols). For this reason, using different analysis approaches,

11

in the following we investigate in more detail the quantification of E_U based on measured PL spectra.

3.1.2. Photoluminescence

Absorption spectra $\alpha(E)$ and PL spectra $\mathrm{PL}(E)$ are related via the reciprocity theorem (eq. 2).[18, 21, 26, 30] Accordingly, intrinsic PL spectra are given by

$$\mathrm{PL}(E) \propto \alpha(E) \cdot E^2 \cdot \exp\left(-\frac{E}{k_B T}\right).^{[18, 21]} \tag{4}$$

Inserting here in eq. 4 the absorption spectrum

$$\alpha(E) \propto \frac{1}{\exp\left(-\frac{E-E_0}{E_U}\right)+1},^{[21]} \tag{5}$$

essentially approximated by a combination of exponential Urbach tail absorption (eq. 1) and a constant absorption above the bandgap, the low energy PL edge ($E \ll E_0$) results to be proportional to $\exp\left(\frac{E-E_0}{E_U} - \frac{E}{k_B T}\right)$, whereas the high energy edge of the PL ($E \gg E_0$) is defined by $\exp(-E/k_B T)$. Hence, information on Urbach energy and thus the energetic disorder is contained in the low energy PL edge exclusively.

Consequently, a simple Urbach energy extraction approach is to fit the low energy PL edge according to

$$\mathrm{PL}(E \ll E_0) = C \cdot \exp\left(\frac{E-E_0}{E_U} - \frac{E}{k_B T}\right) \tag{6}$$

with C being a fitting parameter for the PL intensity. This method was applied by e.g., Fassl et al. for MAPbI$_3$ thin films[38] as well as by our group in a previous work.[11] Figure 2a shows the PL spectra and exemplary fits of the low energy edge (below ~1.5 eV) according to eq. 6 between 300 K and 160 K for a MAPbI$_3$ thin film sample. The sample measured is the same as in Figure 1 and the data from Figure 2a were reported previously in Ref. 11. The PL spectra, and thus their low energy edge shifts to lower energies and becomes steeper upon cooling (Figure 2a), similar to the cooling behavior of the absorption edge (Figure 1a). The Urbach energies extracted from the PL fits according to eq. 6 (orange crosses in Figure 2d) show the typical

decrease upon cooling due to the decrease of dynamic disorder as already observed from absorption in Figure 1.
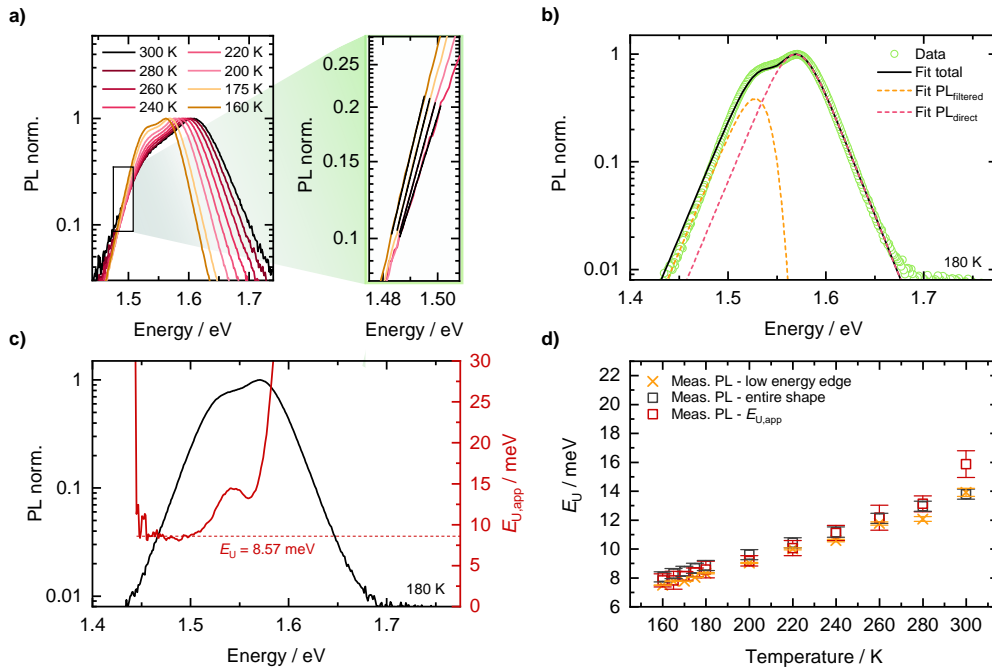
Figure 2: E_U **extraction methods from PL for the MAPbI$_3$ thin film from Figure 1: (a) Measured PL spectra from 300 K down to 160 K (left) and exemplary low energy edge fits according to eq. 6 (right). Adapted with permission from Witt et al. [11] Copyright 2023 American Chemical Society. (b) Measured PL spectrum at 180 K (green circles) with fit describing its entire shape (black line, eq. 7) as sum of direct PL (red dashed line) and filtered PL (orange dashed line). (c) Measured PL spectrum at 180 K (black) and therefrom calculated apparent Urbach energy $E_{U,app}$ (red) via eq. 9. The Urbach energy E_U is given by the horizontal part of the $E_{U,app}$ profile (indicated by red dashed line). (d) E_U values from 300 K down to 160 K determined via the methods presented in (a) (orange crosses), (b) (grey squares) and (c) (red squares). Values shown as orange crosses adapted with permission from Witt et al. [11] Copyright 2023 American Chemical Society.**

A more comprehensive Urbach analysis method is fitting the entire PL spectrum (between 1.4 and 1.7 eV), as performed in a previous work of our group for MAPbI$_3$ single crystals.[21] This fitting includes the main direct PL peak (PL$_{direct}$ around 1.61 eV at 300 K) originating from (near) surface PL and the red-shifted filtered PL peak (PL$_{filtered}$ around 1.53 eV at 300 K), which appears as a shoulder and results from a self-absorption effect, i.e., PL which is internally

13

reflected and filtered by the sample's intrinsic absorption (Figure 2a). PL$_{direct}$ and PL$_{filtered}$ are calculated via the Beer-Lambert law using the intrinsic PL lineshape[21]

$$\mathrm{PL}(E) \approx I_0 * \frac{1}{\exp\left(-\frac{E-E_0}{E_{\mathrm{U,inc}}}\right)+1} * E^2 * \exp\left(-\frac{E}{k_{\mathrm{B}}T_{\mathrm{inc}}}\right) \tag{7}$$

resulting from eq. 4 and 5, where an increased temperature T_{inc} is necessary to account for a flattening of the high energy PL edge. This flattening is assumed to result from a self-absorption effect.[21] As the temperature is also contained in the description of the low energy edge (eq. 6), fitting with increased temperature T_{inc} results in an artificially increased extracted Urbach energy $E_{\mathrm{U,inc}}$. Considering that (according to eq. 6 and 7) the measured low energy PL edge is described by the fitting parameters T_{inc} and $E_{\mathrm{U,inc}}$ but also by the actual values T and E_{U}, where the four parameters can be related and the actual Urbach energy can be calculated via

$$E_{\mathrm{U}} = \left[\frac{1}{E_{\mathrm{U,inc}}} + \frac{1}{k_{\mathrm{B}}}\left(\frac{1}{T} - \frac{1}{T_{\mathrm{inc}}}\right)\right]^{-1} \tag{8}$$

(more details on fitting the entire PL spectrum in previous works).[21, 28] Figure 2b shows exemplarily the PL spectrum of the investigated MAPbI$_3$ thin film at 180 K (green circles) together with a fit (black line) describing the entire spectrum (other temperatures in Supporting Information Figures S7-9). The fit of the entire spectrum is composed of filtered PL (orange dashed line) and direct PL (red dashed line). The resulting temperature-dependent Urbach energy values extracted from fitting the entire PL lineshape in Figure 2d (grey squares) are similar to the values extracted from simply fitting the low energy edge (orange crosses).

To make sure that non-Urbach absorption states do not affect our Urbach analyses from PL spectra, we transfer the Urbach analysis method via the apparent Urbach energy (eq. 3) known for absorption spectra to PL spectra. For this purpose, we replace the absorption coefficient α in eq. 3 by the PL spectrum PL(E) (using eq. 2 reciprocity theorem) to calculate the apparent Urbach energy

$$E_{\mathrm{U,app}} = \left(\frac{\mathrm{d}}{\mathrm{d}E}\left[\ln\left(\frac{\mathrm{PL}(E)}{E^2 \cdot \exp\left(-\frac{E}{k_{\mathrm{B}}T}\right)}\right)\right]\right)^{-1}. \tag{9}$$

14

Figure 2c exemplarily shows the as calculated apparent Urbach energy (red) from the PL spectrum (black) of the investigated MAPbI$_3$ thin film at 180 K (other temperatures in Supporting Information Figures S10-12). Again, the constant horizontal part of the apparent Urbach energy represents the purely exponential part of the spectrum from which the Urbach energy of 8.57 meV is retrieved. The resulting temperature-dependent Urbach energies extracted via the apparent Urbach energy from PL spectra following eq. 9 are given in Figure 2d (red squares). The Urbach energy value at 300 K seems to be exaggerated, which we attribute to the limited altitude and quality of the low energy edge at this temperature, where the overall signal to noise ratio of the measured PL spectrum is low compared to the spectra measured at lower temperatures. Apart from this, the temperature-dependent Urbach energies extracted from the measured PL spectra via the three Urbach analysis methods presented in Figures 2a,b,c are quite similar with values between ~14 meV (300 K) and ~7 meV (160 K) decreasing upon cooling (Figure 2d). In addition, these Urbach energy values are also similar to the ones in Figure 1d extracted below 1.5 eV (i.e., without significant contribution of non-Urbach absorption states, see Figure S14a). This similarity is reasonable as the absorption spectra in Figure 1d were calculated via eq. 2 from the same measured PL spectra. However, discrepancies between Urbach energies extracted from measured PL spectra (Figure 2) and Urbach energies extracted from measured absorption spectra (Figure 1) exist.

15

184

3.2. Investigating Discrepancies in Urbach Energy Values

3.2.1. Measurement Method Sensitivity and Energy Range Dependent Effects

To find the origin of the discrepancies in Urbach energy values extracted from different measurement and analysis methods, first we compare the Urbach energy values derived in Section 3.1 from 300 K down to 160 K (Figure 3a).
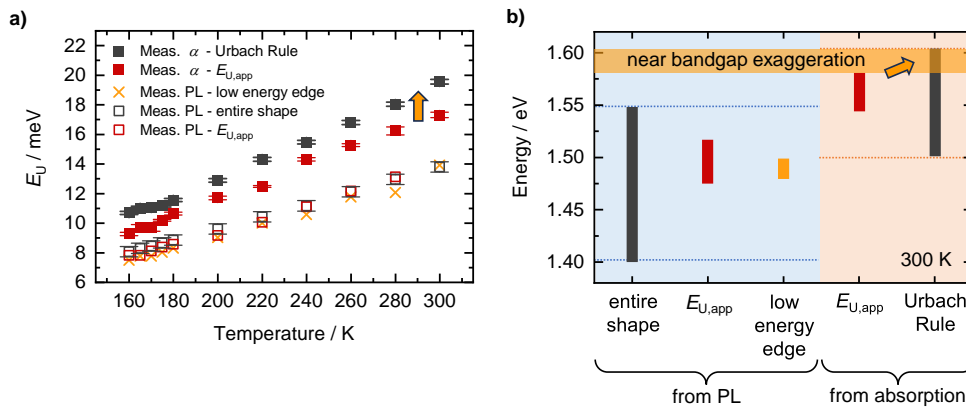
Figure 3: (a) Comparison of Urbach energies between 300 K and 160 K (of the MAPbI$_3$ thin film from Figure 1 and 2) extracted from absorption (full symbols) and PL measurements (open symbols) using different analyses methods: Urbach Rule Fits (eq. 1) to measured absorption spectra (full grey squares), apparent Urbach energy $E_{U,app}$ (eq. 3) calculated from measured absorption spectra (full red squares), low energy edge fits (eq. 6) to measured PL spectra (orange crosses), entire shape fits (eq. 7) of measured PL spectra (open grey squares) and apparent Urbach energy $E_{U,app}$ (eq. 9) calculated from measured PL spectra (open red squares). For clarity, some error bars from Figure 2d are left out. Values shown as orange crosses adapted with permission from Witt et al. [11] Copyright 2023 American Chemical Society. (b) Energy range used for the extraction of the Urbach energies in (a) at 300 K (for details and all temperatures down to 160 K see Figure S14).

Basically, two major differences are observed: (1) The Urbach energy values between 20 meV (300 K) and 9 meV (160 K) extracted from measured absorption spectra are higher than the respective values between 14 meV (300 K) and 7 meV (160 K) extracted from measured PL spectra (2) For the analyses of measured absorption spectra, the apparent Urbach energy method (eq. 3) leads to lower Urbach energy values compared to corresponding values from Urbach Rule fits. This is in contrast to the analyses of measured PL spectra, where essentially all methods lead to similar Urbach energies.

16

To address the latter observation, we recall that the apparent Urbach energy method takes only the purely exponential disorder-related energy range of the spectra into account without contribution of non-Urbach absorption states like band-to-band absorption close to the bandgap.[14, 18] To evaluate the relevance of such non-Urbach absorption states for all Urbach energy values from Figure 3a we consider the energy range used for their extraction in Figure 3b (300 K) and Figure S14c-d (300 K down to 160 K). Figure 3b illustrates that the Urbach energies from absorption were extracted in an energy range above 1.50 eV, whereas the Urbach energies from PL were extracted in a lower energy range below ~1.55 eV. Notable influence of the energy range on resulting Urbach energies is only seen from absorption (Figure 3a closed symbols). Here, a reduced upper energy range until ~0.02 eV below the bandgap (Figure 3b orange bar) leads to lower Urbach energy values (Figure 3a red closed symbols), considering only purely exponential disorder-related parts of the absorption edge. Thus, exaggeration effects on Urbach energy values due to non-Urbach absorption states, e.g., band-to-band absorption,[14, 18] appear to be relevant up to ~0.02 eV below the bandgap ($E_{bandgap} \approx 1.6$ eV at 300 K)[39]. From PL no significant differences of the analysis method on the Urbach energy values are observed (Figure 3a open symbols). We consider this to result from the fact that in the PL spectra, all three analysis methods use an upper energy range that is more than ~0.02 eV below the maximum of the respective PL peak (Figure S14d) and thus non-disorder-related near bandgap absorption effects do not contribute.

Independent of near bandgap effects, however, there still remain differences of ~(1.5-3.5) meV between the Urbach energy values from measured absorption and the values from measured PL (Figure 3a). These differences can be caused either by an additional energy range dependent effect, which leads to a lowering of the Urbach energies extracted below ~1.55 eV, or by differences in the sensitivity of the absorption and PL measurement methods in terms of disorder.

Hence, in Figure 4a we compare Urbach energy values extracted from measured absorption and PL in the same energy range (red area above 1.5 eV in Figure 3b and S14c). Here we consider the Urbach energies extracted via the apparent Urbach energy (eq. 3) from measured absorption (full red squares). In addition, Urbach energies are derived from measured PL spectra by first calculating the absorption spectra (eq. 2) and then performing Urbach rule fits in the designated area (open rose squares, fits according to eq. 1 in Figure S13).

17
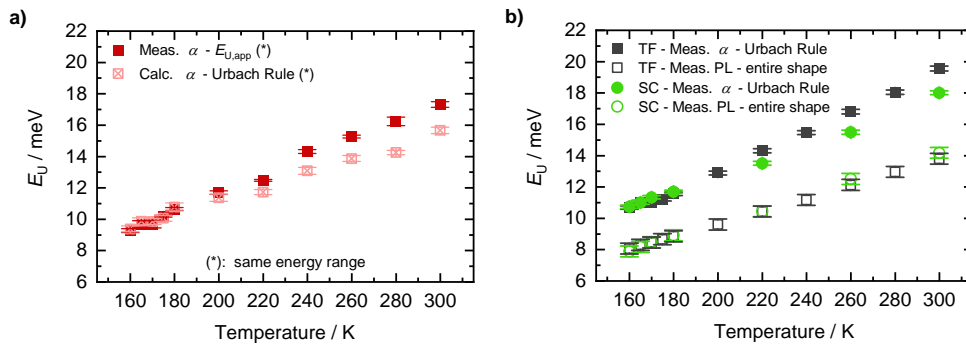
Figure 4: (a) Urbach energies between 300 K and 160 K (of the MAPbI₃ thin film from Figures 1,2 and 3) extracted in the same energy range from absorption (via eq. 3: apparent Urbach energy $E_{U,app}$, full red squares) and PL measurements (via eq. 1 and 2: Urbach Rule fits to calculated absorption, open rose squares). (b) Comparison of MAPbI₃ thin film (grey squares) with MAPbI₃ single crystal (green circles, E_U from PL adapted under the terms of the CC-BY 4.0 license. [21] Copyright 2020, the authors. Published by WILEY-VCH Verlag GmbH & Co. KGaA, Weinheim.): Urbach energies E_U extracted via Urbach Rule Fits (eq. 1) to measured absorption spectra (full symbols) and via entire shape fits (eq. 7) of measured PL spectra (open symbols).

We find that at 300 K the Urbach energy from measured PL is ~1.7 meV lower than from measured absorption (Figure 4a). Down to 200 K this difference in Urbach energy values decreases resulting in similar values from both measured absorption and measured PL between 180 K and 160 K. According to Figure 1c,d (dark blue, energy range for E_U extraction similar to red area above 1.5 eV in Figure 3b and S14c) we consider the Urbach energies from measured PL in Figure 4a to be slightly exaggerated, which we refer to the filter effect. This filter effect leads to slightly red-shifted PL compared to intrinsic PL and absorption and thus shifts parts of the PL spectra near the bandgap with signatures of non-Urbach absorption states in the energy range used for Urbach energy extraction. Nevertheless, considering a similar energy range above ~1.5 eV, from measured PL we definitely find lower absolute Urbach energy values and also lower temperature-dependence of the Urbach energy compared to measured absorption, which hints to different sensitivity of both applied measurement methods.

To check if differences in Urbach energy values due to different sensitivity of the applied measurement methods (absorption and PL) are of general nature, we compare Urbach analyses from absorption and PL measurements applied in the energy range below ~1.5 eV. For this purpose, we consider a second type of MAPbI₃ sample, namely single crystal sample,

18

for which not only the filtered PL but also the absorption edge is observed below 1.5 eV (i.e., below the Urbach focus point, Figure S16).[21, 28] Here the measured single crystal absorption is red-shifted compared to thin film absorption, which results from the larger sample thickness (~1 mm instead of only ~4 µm) and lower polycrystallinity of the single crystal.[40-43] Urbach energies between 300 K and 160 K extracted below ~1.5 eV from the measured single crystal absorption via Urbach Rule fits (eq. 1, full green circles; similar values as those extracted via $E_{U,app}$ see Figure S16) and from the measured single crystal PL via entire shape fits (eq. 7, open green circles) are shown in Figure 4b, together with values for the thin film sample (grey symbols). The single crystal sample shows Urbach energy values from measured PL to be more than 2.5 meV lower compared to the values extracted from measured absorption. In addition to the lower absolute Urbach energy values the single crystal PL also shows less temperature-dependence of the Urbach energy compared to single crystal absorption. Consequently, in both the energy range above and below 1.5 eV, lower absolute Urbach energy values as well as a lower temperature dependence of the Urbach energy are obtained from measured PL compared to measured absorption, independent of near bandgap exaggeration effects on the Urbach energy.

Thus, we conclude a fundamentally different sensitivity of both applied measurement methods (absorption and PL) in terms of energetic disorder independent of the considered energy range. Energy range dependent effects on Urbach energy values are only present near the bandgap region, i.e., ~ 0.02 eV below the bandgap.

3.2.2. Origin of Different Measurement Method Sensitivity

As identified in Section 3.2.1 and summarized in Figure 5, we derive lower absolute Urbach energy values from PL than from absorption measurements (Fig. 5b). Furthermore, we find a lower temperature dependence of the Urbach energy from PL than from absorption. This can be quantified by applying linear fits to the temperature dependent Urbach energy values between 300 K and 160 K (also see Supporting Information Figure S17) and considering the values of the slopes, as shown in Figure 5c. In both cases, the differences between the values obtained from measured absorption and PL are independent from the energy range considered for Urbach energy extraction (Figure 5). Therefore, we consider these differences to result from different sensitivity of the measurement methods. Only above ~1.58 eV (i.e., closer than ~0.02 eV to the bandgap) an additional exaggeration effect on Urbach energy

values due to non-Urbach absorption states occurs (indicated by orange bar and arrows in Figure 5a,b).
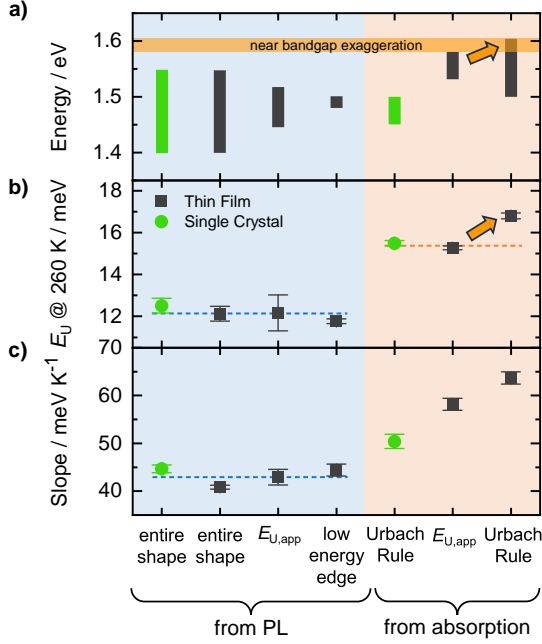
Figure 5: Comparison of Urbach analysis methods of measured PL (left) and absorption spectra (right) presented in previous Figures applied for a MAPbI₃ thin film (grey squares) and MAPbI₃ single crystal samples (green circles): (a) Maximum E_U extraction energy range between 300 K and 160 K used for the respective Urbach analysis method. (b) Urbach energy E_U at 260 K. (c) Slope of linear fitting to the temperature-dependence of the Urbach energy E_U.

The temperature-dependence of the Urbach energy, which is the sum of temperature-independent static disorder E_U^{stat} and temperature-dependent dynamic disorder E_U^{dyn}, can be described by

$$E_U(T) = E_U^{stat} + E_U^{dyn} = E_U^{stat} + 2 \cdot E_U^{stat} \left[\exp\left(\frac{\Theta}{T}\right) - 1 \right]^{-1} \text{,[18-19]} \qquad (10)$$

where E_U^{dyn} is characterized by the interaction of charge carriers with phonons in the coupled Einstein oscillator model via the Einstein temperature Θ.[17-19] This implies that the overall Urbach energy values are defined by the static disorder E_U^{stat} and the temperature-dependence of the Urbach energy is defined by the slope $\sim \left(\frac{E_U^{stat}}{\Theta}\right)$.

20

Accordingly, the lower overall Urbach energy values and lower temperature dependence of the Urbach energy observed from PL (Figure 5b,c) could be explained by a lower static disorder E_U^{stat} that is manifested in the PL spectra compared to the absorption spectra.

Lower detected static disorder E_U^{stat} from measured PL might be conceivable, as the optical penetration depth of the PL excitation is limited to the upper ~50 nm of the sample (whereby besides direct PL from near the surface also PL from the bulk occurs due to charge carrier diffusion).[10] Consequently, for our thin film samples with a thickness of ~4 μm, PL measurements might be less sensitive to possible strain associated disorder from the buried substrate perovskite interface, which might be induced due to the thermal expansion coefficient mismatch between perovskite layer and substrate.[44-47] In contrast, our absorption measurements recorded via transmission through the whole sample thickness would be more sensitive to such substrate related disorder. However, in Section 3.2.1, the differences in resulting Urbach energy values due to different sensitivity of the applied measurement methods are observed not only for thin film but also for free standing single crystal samples. From this, we conclude that these differences are of general intrinsic nature independent of the presence of a substrate. Thus, we exclude a limited depth sensitivity of PL to be responsible for lower detected static disorder E_U^{stat} from measured PL compared to absorption.

Since our investigation focus on the tetragonal phase of MAPbI$_3$ (i.e. 300 K down to 160 K) we also do not expect effects of excitonic contributions to be relevant for the lower detected static disorder E_U^{stat} from measured PL compared to absorption as such contribution is known to get significant only in the orthorhombic phase namely below 80 K.[48] However, it is known that on sites with lower energetic disorder also lower nonradiative decay rates are present.[5, 7, 49] Furthermore, after PL excitation, charge carriers relax spatially in the sample volume to sites with lower energy and lower energetic disorder before they recombine radiatively.[39, 50] Both aspects indicate that PL tends to track more sites with lower energetic disorder leading to an overproportional contribution of such low energetic disorder sites in the measured PL spectra, obscuring signatures from higher disorder sites.

Besides the lower absolute Urbach energy values, the higher sensitivity of PL for sites with lower static disorder E_U^{stat} can also explain the observed lower temperature-dependence of the Urbach energy ~ $\left(\frac{E_U^{stat}}{\Theta}\right)$ from PL. Moreover, this lower temperature-dependence could

21

190

also result from a higher Einstein temperature Θ in the PL measurements compared to the absorption measurements. Such differences in Θ are conceivable as absorption probes the ground state geometry whereas PL probes the excited state geometry of the investigated sample. In excited state geometry a stronger interaction of charge carriers with phonons would be characterized by an increased value of Θ in comparison to the ground state geometry. In single crystal samples with large domain sizes and less barriers for charge carriers one might expect this increase in Θ to be more pronounced compared to polycrystalline thin film samples with lower domain size and many grain boundaries. Indeed, from fits analogous to eq. 10 to temperature-dependent Urbach energies extracted from PL, Ledinsky et al. observed slightly higher phonon energies for single crystals than for thin films of the same lead halide perovskite stoichiometry.[12]

22

4. Conclusions

In summary, we investigate in detail the origin of present discrepancies in Urbach energy values extracted via different measurement and analysis methods. To this end, from 300 K down to 160 K, steady-state PL and absorption spectra of $MAPbI_3$ samples are recorded quasi simultaneously to enable reliable comparison between both measurement methods. Urbach energies are extracted via six different analysis methods applied to the measured absorption and PL spectra in an extended energy range down to 0.2 eV below the bandgap. We show that Urbach energy values are exaggerated due to band-to-band contributions only close to the bandgap, i.e., ~0.02 eV and less below the bandgap. Besides that, we reveal that independent of the investigated energy range, general discrepancies in Urbach energy values occur due to different sensitivity of the applied measurement methods (absorption vs PL). Here, lower absolute Urbach energy values are obtained from measured PL, as well as a lower temperature-dependence of the Urbach energy compared to absorption. We conclude that the lower absolute Urbach energy values from PL originate from the higher sensitivity of PL for sites with lower energetic disorder, as PL is preferably emitted from sites with low energetic disorder. Furthermore, the lower temperature dependence of the Urbach energy from PL appears to originate also from the high sensitivity of PL for sites with low energetic disorder and/or a higher phonon energy in PL measurements, as PL probes the excited state geometry of the semiconductor. Differences in Urbach energies between thin film and single crystal samples are only observed when extracted from absorption, as PL mainly occurs from the low energetic disorder sites.

Thus, in contrast to PL, absorption measurements might appear to be better suited to identify differences in energetic disorder (i.e., in defect induced static disorder and zero-point phonon energy) between different samples. However, even between single crystal and thin film samples, the differences in Urbach energy are small (< 2 meV), which is likely associated to the inherent high electronic quality of halide perovskites.[12] This is in line with the findings from Gehrmann et al, who, from molecular dynamics and density functional theory calculations, identified such high electronic quality to originate from the dynamic shortening of the disorder potential by thermally activated nuclear motions, resulting in a reduced number of tail states and thus general small Urbach energies.[14, 51]

23

Overall, our work demonstrates that no single true value of the Urbach energy exists, but that the value of the Urbach energy depends on the sensitivity of the applied optical measurement method for spatially distributed sites of lower energetic disorder in the sample volume. Thus, our work contributes to further develop a fundamental understanding of energetic disorder and sensitizes for meaningful interpretation and comparison of Urbach energy values.

Supporting Information

Details on thin film samples and performed temperature-dependent Urbach energy analyses from measured absorption and PL spectra; PL and absorption spectra of single crystal samples and corresponding temperature-dependent Urbach energy analyses; Linear fits to temperature-dependent Urbach energies for extraction of the slope parameter.

Acknowledgement

References

1. De Wolf, S.; Holovsky, J.; Moon, S.-J.; Löper, P.; Niesen, B.; Ledinsky, M.; Haug, F.-J.; Yum, J.-H.; Ballif, C. Organometallic Halide Perovskites: Sharp Optical Absorption Edge and Its Relation to Photovoltaic Performance. *J. Phys. Chem. Lett.* **2014,** *5*, 1035-1039.
2. Jean, J.; Mahony, T. S.; Bozyigit, D.; Sponseller, M.; Holovský, J.; Bawendi, M. G.; Bulović, V. Radiative Efficiency Limit with Band Tailing Exceeds 30% for Quantum Dot Solar Cells. *ACS Energy Lett.* **2017,** *2*, 2616-2624.
3. Hartnagel, P.; Ravishankar, S.; Klingebiel, B.; Thimm, O.; Kirchartz, T. Comparing Methods of Characterizing Energetic Disorder in Organic Solar Cells. *Adv. Energy Mater.* **2023,** *13*, 2300329.
4. Zhang, C.; Mahadevan, S.; Yuan, J.; Ho, J. K. W.; Gao, Y.; Liu, W.; Zhong, H.; Yan, H.; Zou, Y.; Tsang, S.-W., et al. Unraveling Urbach Tail Effects in High-Performance Organic Photovoltaics: Dynamic vs Static Disorder. *ACS Energy Lett.* **2022,** *7*, 1971-1979.
5. Frohna, K.; Anaya, M.; Macpherson, S.; Sung, J.; Doherty, T. A. S.; Chiang, Y.-H.; Winchester, A. J.; Orr, K. W. P.; Parker, J. E.; Quinn, P. D., et al. Nanoscale Chemical Heterogeneity Dominates the Optoelectronic Response of Alloyed Perovskite Solar Cells. *Nat. Nanotechnol.* **2022,** *17*, 190-196.
6. Kim, G.; Min, H.; Lee, K. S.; Lee, D. Y.; Yoon, S. M.; Seok, S. I. Impact of Strain Relaxation on Performance of α-Formamidinium Lead Iodide Perovskite Solar Cells. *Science* **2020,** *370*, 108-112.
7. Mehdizadeh-Rad, H.; Singh, J. Influence of Urbach Energy, Temperature, and Longitudinal Position in the Active Layer on Carrier Diffusion Length in Perovskite Solar Cells. *ChemPhysChem* **2019,** *20*, 2712-2717.
8. Qiao, L.; Fang, W.-H.; Long, R.; Prezhdo, O. V. Elimination of Charge Recombination Centers in Metal Halide Perovskites by Strain. *J. Am. Chem. Soc.* **2021,** *143*, 9982-9990.
9. Rajagopal, A.; Liang, P.-W.; Chueh, C.-C.; Yang, Z.; Jen, A. K. Y. Defect Passivation via a Graded Fullerene Heterojunction in Low-Bandgap Pb–Sn Binary Perovskite Photovoltaics. *ACS Energy Lett.* **2017,** *2*, 2531-2539.
10. Regalado-Pérez, E.; Díaz-Cruz, E. B.; Landa-Bautista, J.; Mathews, N. R.; Mathew, X. Impact of Vertical Inhomogeneity on the Charge Extraction in Perovskite Solar Cells: A Study by Depth-Dependent Photoluminescence. *ACS Appl. Mater. Interfaces* **2021,** *13*, 11833-11844.
11. Witt, C.; Schötz, K.; Kuhn, M.; Leupold, N.; Biberger, S.; Ramming, P.; Kahle, F.-J.; Köhler, A.; Moos, R.; Herzig, E. M., et al. Orientation and Grain Size in MAPbI$_3$ Thin Films: Influence on Phase Transition, Disorder, and Defects. *J. Phys. Chem. C* **2023,** *127*, 10563-10573.
12. Ledinský, M.; Vlk, A.; Schönfeldová, T.; Holovský, J.; Aydin, E.; Dang, H. X.; Hájková, Z.; Landová, L.; Valenta, J.; Fejfar, A., et al. Impact of Cation Multiplicity on Halide Perovskite Defect Densities and Solar Cell Voltages. *J. Phys. Chem. C* **2020,** *124*, 27333-27339.
13. Lin, Q.; Kubicki, D. J.; Omrani, M.; Alam, F.; Abdi-Jalebi, M. The Race Between Complicated Multiple Cation/Anion Compositions and Stabilization of FAPbI$_3$ for Halide Perovskite Solar Cells. *J. Mater. Chem. C* **2023,** *11*, 2449-2468.
14. Ugur, E.; Ledinský, M.; Allen, T. G.; Holovský, J.; Vlk, A.; De Wolf, S. Life on the Urbach Edge. *J. Phys. Chem. Lett.* **2022,** *13*, 7702-7711.
15. Haris, M. P. U.; Kazim, S.; Ahmad, S. Microstrain and Urbach Energy Relaxation in FAPbI$_3$-Based Solar Cells through Powder Engineering and Perfluoroalkyl Phosphate Ionic Liquid Additives. *ACS Appl. Mater. Interfaces* **2022,** *14*, 24546-24556.
16. Subedi, B.; Li, C.; Chen, C.; Liu, D.; Junda, M. M.; Song, Z.; Yan, Y.; Podraza, N. J. Urbach Energy and Open-Circuit Voltage Deficit for Mixed Anion–Cation Perovskite Solar Cells. *ACS Appl. Mater. Interfaces* **2022,** *14*, 7796-7804.
17. Cody, G. D.; Tiedje, T.; Abeles, B.; Brooks, B.; Goldstein, Y. Disorder and the Optical-Absorption Edge of Hydrogenated Amorphous Silicon. *Phys. Rev. Lett.* **1981,** *47*, 1480-1483.
18. Ledinský, M.; Schönfeldová, T.; Holovský, J.; Aydin, E.; Hájková, Z.; Landová, L.; Neyková, N.; Fejfar, A.; De Wolf, S. Temperature Dependence of the Urbach Energy in Lead Iodide Perovskites. *J. Phys. Chem. Lett.* **2019,** *10*, 1368-1373.
19. Studenyak, I.; Kranjčec, M.; Kurik, M. Urbach Rule in Solid State Physics. *Int. J. Opt. Appl.* **2014,** *4*, 76-83.
20. Zeiske, S.; Sandberg, O. J.; Zarrabi, N.; Wolff, C. M.; Raoufi, M.; Peña-Camargo, F.; Gutierrez-Partida, E.; Meredith, P.; Stolterfoht, M.; Armin, A. Static Disorder in Lead Halide Perovskites. *J. Phys. Chem. Lett.* **2022,** *13*, 7280-7285.
21. Schötz, K.; Askar, A. M.; Köhler, A.; Shankar, K.; Panzer, F. Investigating the Tetragonal-to-Orthorhombic Phase Transition of Methylammonium Lead Iodide Single Crystals by Detailed Photoluminescence Analysis. *Adv. Opt. Mater.* **2020,** *8*, 2000455.

22. Armer, M.; Höcker, J.; Büchner, C.; Häfele, S.; Dörflinger, P.; Sirtl, M. T.; Tvingstedt, K.; Bein, T.; Dyakonov, V. Influence of Crystallisation on the Structural and Optical Properties of Lead-Free $Cs_2AgBiBr_6$ Perovskite Crystals. *CrystEngComm* **2021**, *23*, 6848-6854.

23. Singh, S.; Li, C.; Panzer, F.; Narasimhan, K. L.; Graeser, A.; Gujar, T. P.; Köhler, A.; Thelakkat, M.; Huettner, S.; Kabra, D. Effect of Thermal and Structural Disorder on the Electronic Structure of Hybrid Perovskite Semiconductor $CH_3NH_3PbI_3$. *J. Phys. Chem. Lett.* **2016,** *7*, 3014-3021.

24. Zhang, W.; Pathak, S.; Sakai, N.; Stergiopoulos, T.; Nayak, P. K.; Noel, N. K.; Haghighirad, A. A.; Burlakov, V. M.; deQuilettes, D. W.; Sadhanala, A., et al. Enhanced Optoelectronic Quality of Perovskite Thin Films with Hypophosphorous Acid for Planar Heterojunction Solar Cells. *Nat. Commun.* **2015,** *6*, 10030.

25. Liu, Y.; Banon, J.-P.; Frohna, K.; Chiang, Y.-H.; Tumen-Ulzii, G.; Stranks, S. D.; Filoche, M.; Friend, R. H. The Electronic Disorder Landscape of Mixed Halide Perovskites. *ACS Energy Lett.* **2023**, *8*, 250-258.

26. Staub, F.; Hempel, H.; Hebig, J.-C.; Mock, J.; Paetzold, U. W.; Rau, U.; Unold, T.; Kirchartz, T. Beyond Bulk Lifetimes: Insights into Lead Halide Perovskite Films from Time-Resolved Photoluminescence. *Phys. Rev. Appl.* **2016,** *6*, 044017.

27. Kronemeijer, A. J.; Pecunia, V.; Venkateshvaran, D.; Nikolka, M.; Sadhanala, A.; Moriarty, J.; Szumilo, M.; Sirringhaus, H. Two-Dimensional Carrier Distribution in Top-Gate Polymer Field-Effect Transistors: Correlation between Width of Density of Localized States and Urbach Energy. *Adv. Mater.* **2014,** *26*, 728-733.

28. Schötz, K.; Askar, A. M.; Peng, W.; Seeberger, D.; Gujar, T. P.; Thelakkat, M.; Köhler, A.; Huettner, S.; Bakr, O. M.; Shankar, K., et al. Double Peak Emission in Lead Halide Perovskites by Self-Absorption. *J. Mater. Chem. C* **2020**, *8*, 2289-2300.

29. Panzer, F.; Li, C.; Meier, T.; Köhler, A.; Huettner, S. Impact of Structural Dynamics on the Optical Properties of Methylammonium Lead Iodide Perovskites. *Adv. Energy Mater.* **2017,** *7*, 1700286.

30. Würfel, P. The Chemical Potential of Radiation. *J. Phys. C: Solid State Phys.* **1982**, *15*, 3967.

31. Ugur, E.; Alarousu, E.; Khan, J. I.; Vlk, A.; Aydin, E.; De Bastiani, M.; Balawi, A. H.; Gonzalez Lopez, S. P.; Ledinský, M.; De Wolf, S., et al. How Humidity and Light Exposure Change the Photophysics of Metal Halide Perovskite Solar Cells. *Sol. RRL* **2020,** *4*, 2000382.

32. Beaudoin, M.; DeVries, A. J. G.; Johnson, S. R.; Laman, H.; Tiedje, T. Optical Absorption Edge of Semi-Insulating GaAs and InP at High Temperatures. *Appl. Phys. Lett.* **1997,** *70*, 3540-3542.

33. Bansal, B.; Dixit, V. K.; Venkataraman, V.; Bhat, H. L. Alloying Induced Degradation of the Absorption Edge of $InAs_xSb_{1-x}$. *Appl. Phys. Lett.* **2007,** *90*, 101905.

34. Bhattacharya, R.; Mondal, R.; Khatua, P.; Rudra, A.; Kapon, E.; Malzer, S.; Döhler, G.; Pal, B.; Bansal, B. Measurements of the Electric Field of Zero-Point Optical Phonons in GaAs Quantum Wells Support the Urbach Rule for Zero-Temperature Lifetime Broadening. *Phys. Rev. Lett.* **2015,** *114*, 047402.

35. Falsini, N.; Roini, G.; Ristori, A.; Calisi, N.; Biccari, F.; Vinattieri, A. Analysis of the Urbach Tail in Cesium Lead Halide Perovskites. *J. Appl. Phys.* **2022,** *131*, 010902.

36. Montañez, L.; Guerra, J.; Zegarra, K.; Kreppel, S.; De Zela, F.; Winnacker, A.; Weingärtner, R. Optical Bandgap Enhancement of a-SiC through Hydrogen Incorporation and Thermal Annealing Treatments. *Proc. SPIE* **2013,** *8785*, S1-S6.

37. Kaiser, C.; Sandberg, O. J.; Zarrabi, N.; Li, W.; Meredith, P.; Armin, A. A Universal Urbach Rule for Disordered Organic Semiconductors. *Nat. Commun.* **2021,** *12*, 3988.

38. Fassl, P.; Lami, V.; Berger, F. J.; Falk, L. M.; Zaumseil, J.; Richards, B. S.; Howard, I. A.; Vaynzof, Y.; Paetzold, U. W. Revealing the Internal Luminescence Quantum Efficiency of Perovskite Films via Accurate Quantification of Photon Recycling. *Matter* **2021,** *4*, 1391-1412.

39. Herz, L. M. Charge-Carrier Dynamics in Organic-Inorganic Metal Halide Perovskites. *Annu. Rev. Phys. Chem.* **2016,** *67*, 65-89.

40. Chen, Z.; Dong, Q.; Liu, Y.; Bao, C.; Fang, Y.; Lin, Y.; Tang, S.; Wang, Q.; Xiao, X.; Bai, Y., et al. Thin Single Crystal Perovskite Solar Cells to Harvest Below-Bandgap Light Absorption. *Nat. Commun.* **2017,** *8*, 1890.

41. D'Innocenzo, V.; Srimath Kandada, A. R.; De Bastiani, M.; Gandini, M.; Petrozza, A. Tuning the Light Emission Properties by Band Gap Engineering in Hybrid Lead Halide Perovskite. *J. Am. Chem. Soc.* **2014,** *136*, 17730-17733.

42. Maculan, G.; Sheikh, A. D.; Abdelhady, A. L.; Saidaminov, M. I.; Haque, M. A.; Murali, B.; Alarousu, E.; Mohammed, O. F.; Wu, T.; Bakr, O. M. $CH_3NH_3PbCl_3$ Single Crystals: Inverse Temperature Crystallization and Visible-Blind UV-Photodetector. *J. Phys. Chem. Lett.* **2015,** *6*, 3781-3786.

43. Trivedi, S.; Prochowicz, D.; Parikh, N.; Mahapatra, A.; Pandey, M. K.; Kalam, A.; Tavakoli, M. M.; Yadav, P. Recent Progress in Growth of Single-Crystal Perovskites for Photovoltaic Applications. *ACS Omega* **2021,** *6*, 1030-1042.

27

44. Haeger, T.; Heiderhoff, R.; Riedl, T. Thermal Properties of Metal-Halide Perovskites. *J. Mater. Chem. C* **2020,** *8*, 14289-14311.

45. Meng, W.; Zhang, K.; Osvet, A.; Zhang, J.; Gruber, W.; Forberich, K.; Meyer, B.; Heiss, W.; Unruh, T.; Li, N., et al. Revealing the Strain-associated Physical Mechanisms Impacting the Performance and Stability of Perovskite Solar Cells. *Joule* **2022,** *6*, 458-475.

46. Moloney, E. G.; Yeddu, V.; Saidaminov, M. I. Strain Engineering in Halide Perovskites. *ACS Mater. Lett.* **2020,** *2*, 1495-1508.

47. Zhao, J.; Deng, Y.; Wei, H.; Zheng, X.; Yu, Z.; Shao, Y.; Shield, J. E.; Huang, J. Strained Hybrid Perovskite Thin Films and their Impact on the Intrinsic Stability of Perovskite Solar Cells. *Sci. Adv.* **2017,** *3*, eaao5616.

48. Milot, R. L.; Eperon, G. E.; Snaith, H. J.; Johnston, M. B.; Herz, L. M. Temperature-Dependent Charge-Carrier Dynamics in $CH_3NH_3PbI_3$ Perovskite Thin Films. *Adv. Funct. Mater.* **2015,** *25*, 6218-6227.

49. Mrkyvkova, N.; Held, V.; Nádaždy, P.; Subair, R.; Majkova, E.; Jergel, M.; Vlk, A.; Ledinsky, M.; Kotlár, M.; Tian, J., et al. Combined in Situ Photoluminescence and X-ray Scattering Reveals Defect Formation in Lead-Halide Perovskite Films. *J. Phys. Chem. Lett.* **2021,** *12*, 10156-10162.

50. Bhuyan, S.; Mondal, R.; Pal, B.; Bansal, B. Distinguishing Quantum Dot-like Localized States from Quantum Well-like Extended States Across the Exciton Emission Line in a Quantum Well. *J. Phys.: Condens. Matter* **2018,** *30*, 105402.

51. Gehrmann, C.; Egger, D. A. Dynamic Shortening of Disorder Potentials in Anharmonic Halide Perovskites. *Nat. Commun.* **2019,** *10*, 3141.

28

Supporting Information to

Understanding Method-Dependent Differences in Urbach Energies in Halide Perovskites

Christina Witt[1], Konstantin Schötz[1], Anna Köhler[1], Fabian Panzer[1*]

[1] Soft Matter Optoelectronics, University of Bayreuth, Bayreuth 95440, Germany

Corresponding Author:

[*]E-Mail: fabian.panzer@uni-bayreuth.de

1. Urbach Energy Analyses of CP an HP Thin Films

All Urbach analyses of thin film samples using measured absorption spectra (from 300 K down to 5 K) and measured PL spectra (from 300 K down to 160 K, as the PL shape gets too complex for reliable Urbach energy extraction below 160 K)[1] are presented here. The Urbach analyses are shown for the cold-pressed MAPbI$_3$ thin film (CP) discussed in the main paper (left) and a second hot-pressed MAPbI$_3$ thin film (HP) shown on the right. The HP film exhibits a slightly different morphology compared to the CP film, i.e., larger grain size and preferred crystallographic orientation resulting in improved structural and optoelectronic properties, namely decreased defect density, reduced strain and lower energetic disorder (Figure S15a).[1]

1.1. Urbach Analyses

1.1.1 Urbach Rule Fits to Measured Absorption Spectra
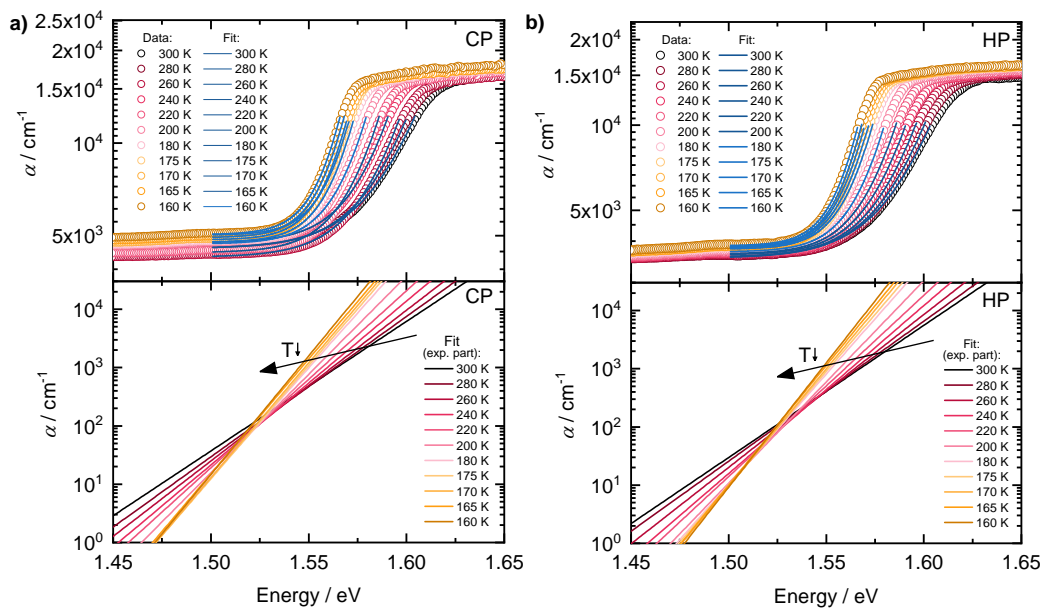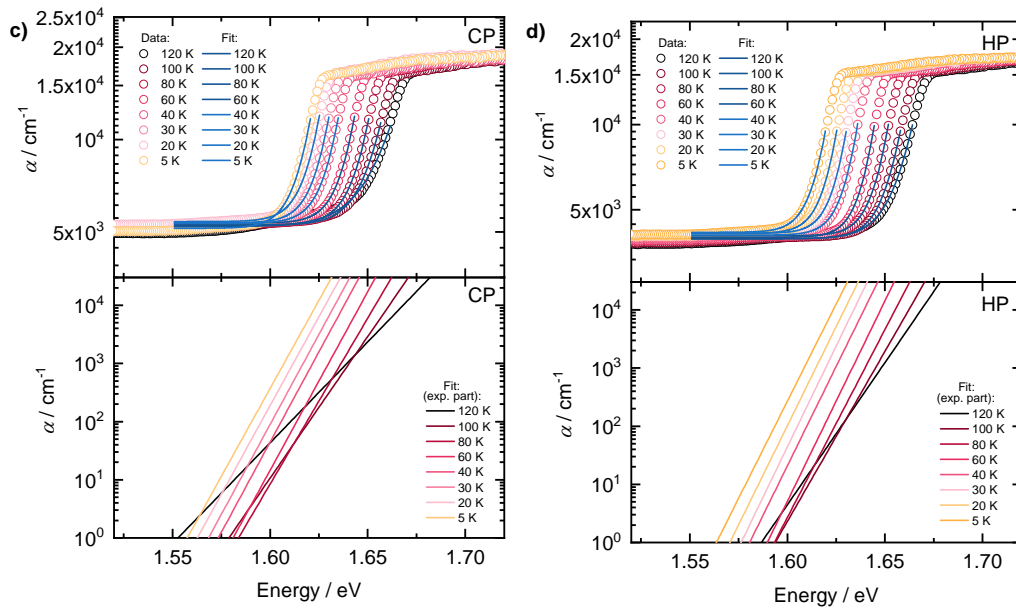
Figure S1: Urbach Rule fits according to eq. 1 in the main text (blue lines) to measured absorption spectra (circles) of CP (left) and HP (right) thin films in tetragonal (a,b) and orthorhombic (c,d) phase of MAPbI₃ in top panels and exponential parts of the fits in bottom panels.

From classical crystalline inorganic semiconductors, a focus point at about 1.5 eV is known to result from a similar temperature-dependence of the band gap energy and the steepness of the band edge, i.e., the Urbach energy.[2-4] Such focus point has already been reported for halide perovskite films as well.[5-7] Here in Figure S1, below 80 K no intersection of the fits is observed since at these low temperatures the dynamic disorder becomes vanishingly small and thus the Urbach energy (slope of the absorption edge) saturates while the band gap energy continues to shift to lower energies.

1.1.2 Urbach Energy Extraction via $E_{U,app}$ Calculated from Absorption Spectra
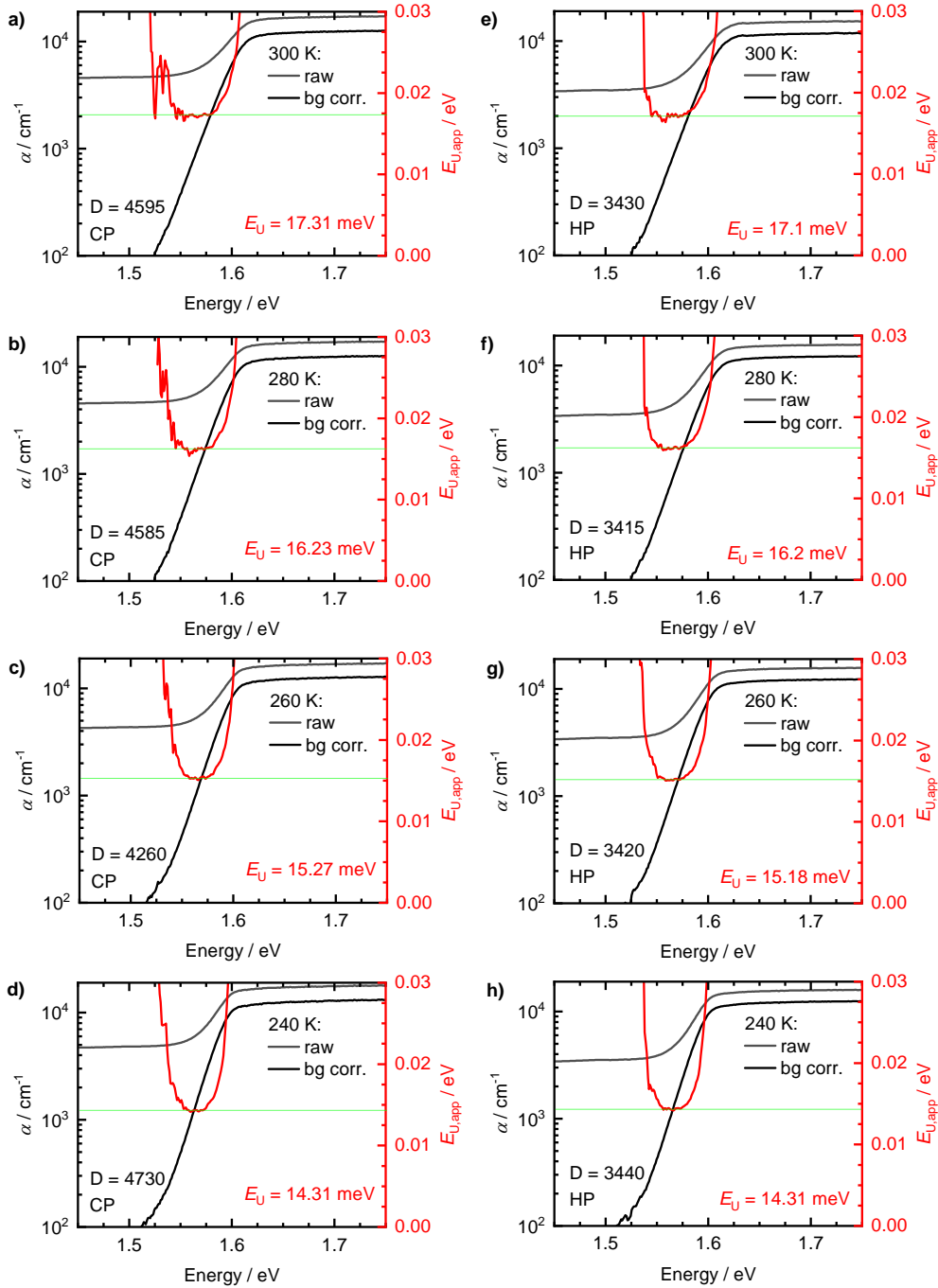
Figure S2: Extraction of Urbach energy values from measured absorption spectra (grey, offset corrected spectra in black) via the calculation of the apparent Urbach energy (red) via eq. 3 in the main text for CP thin film (a-d) and HP thin film (e-h) between 300 K and 240 K. The Urbach energy is determined from the horizontal part of the apparent Urbach energy (green line).
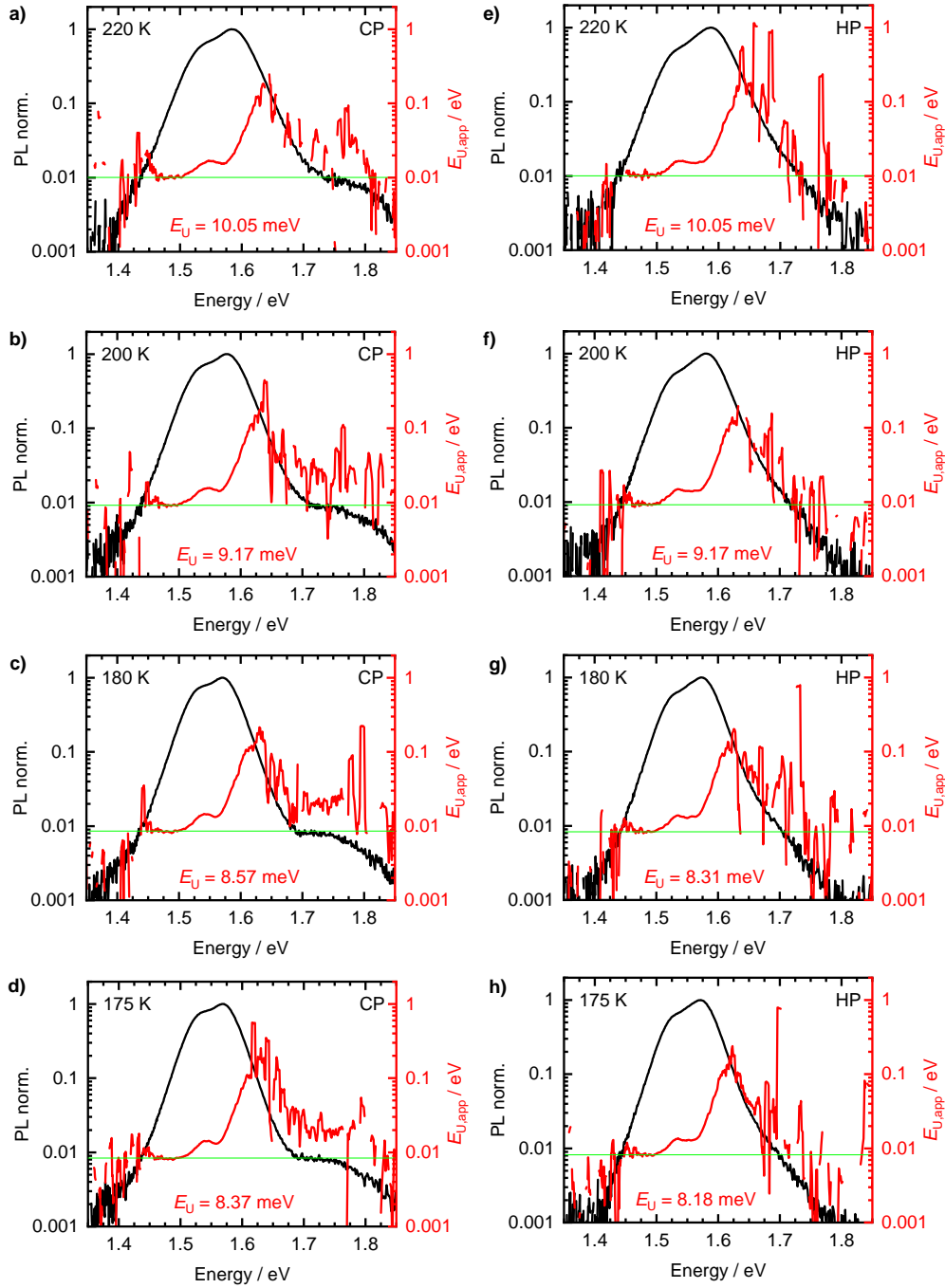
S4
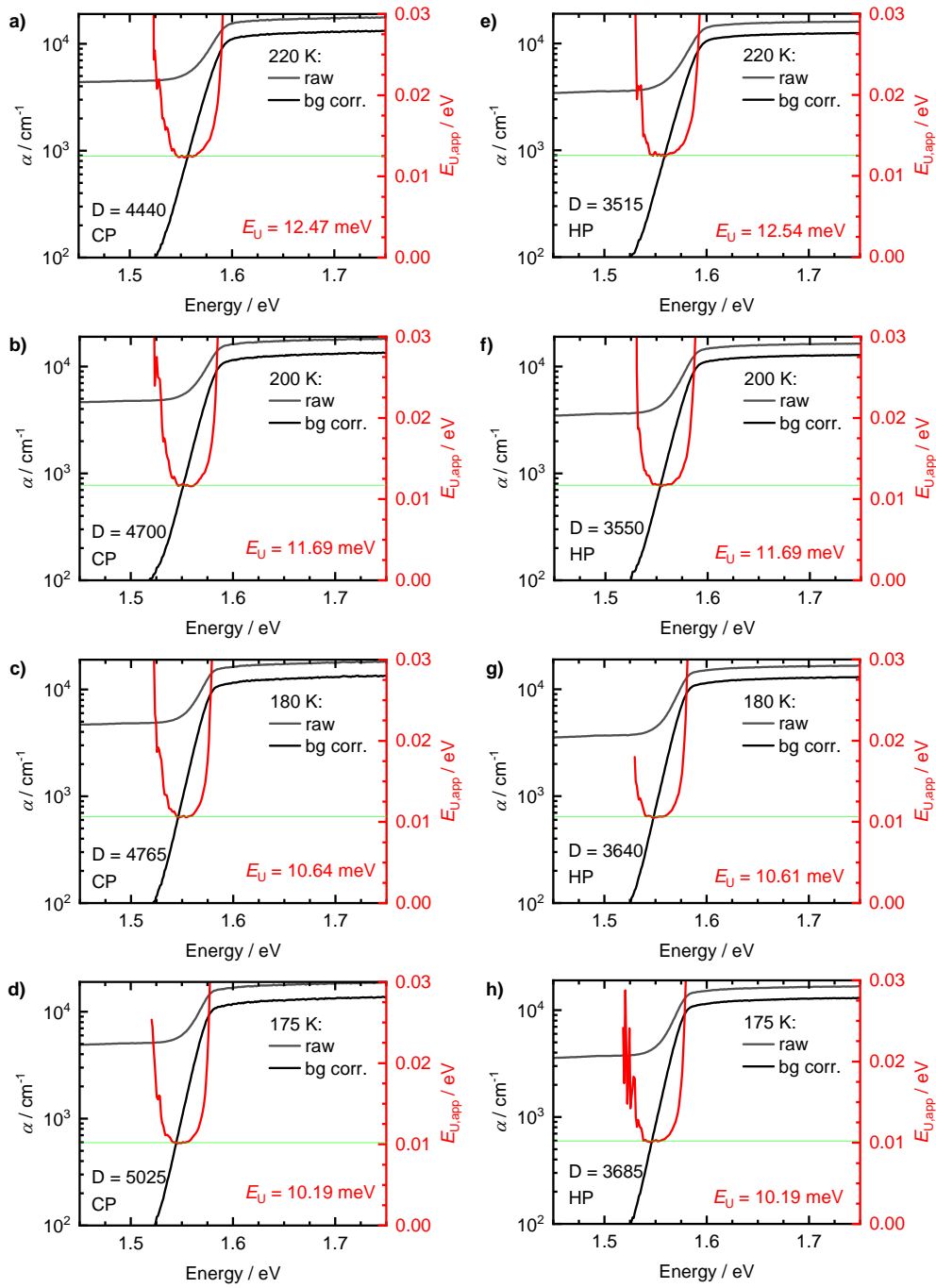
Figure S3: Extraction of Urbach energy values from measured absorption spectra (grey, offset corrected spectra in black) via the calculation of the apparent Urbach energy (red) via eq. 3 in the main text for CP thin film (a-d) and HP thin film (e-h) between 220 K and 175 K. The Urbach energy is determined from the horizontal part of the apparent Urbach energy (green line).
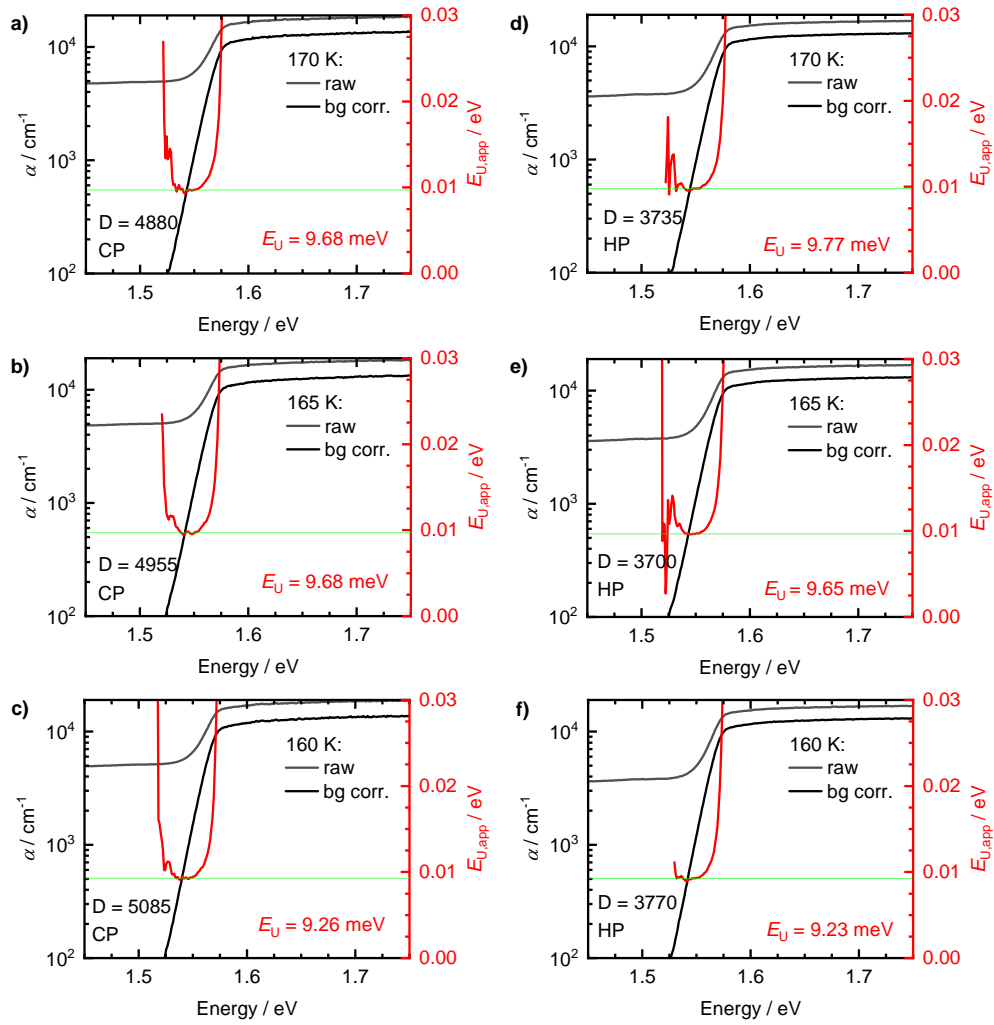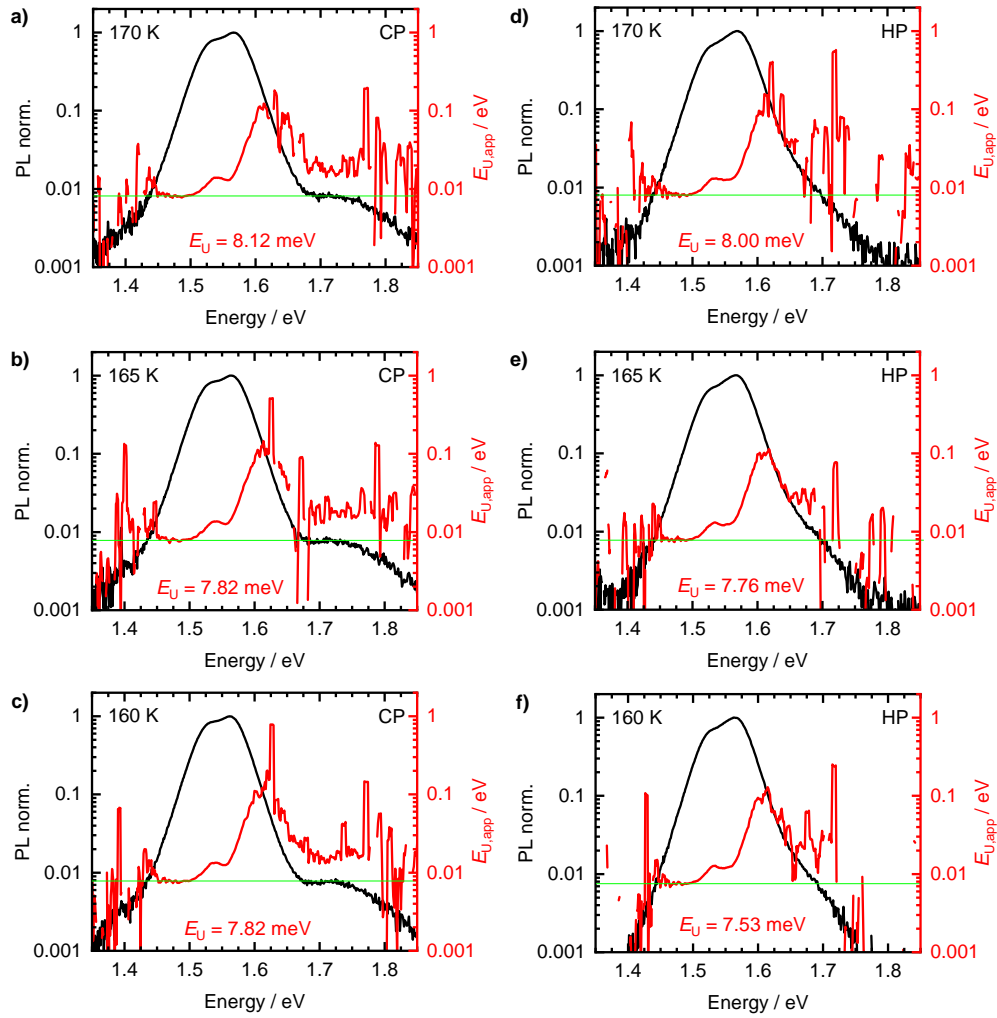
Figure S4: Extraction of Urbach energy values from measured absorption spectra (grey, offset corrected spectra in black) via the calculation of the apparent Urbach energy (red) via eq. 3 in the main text for CP thin film (a-c) and HP thin film (d-f) between 170 K and 160 K. The Urbach energy is determined from the horizontal part of the apparent Urbach energy (green line).
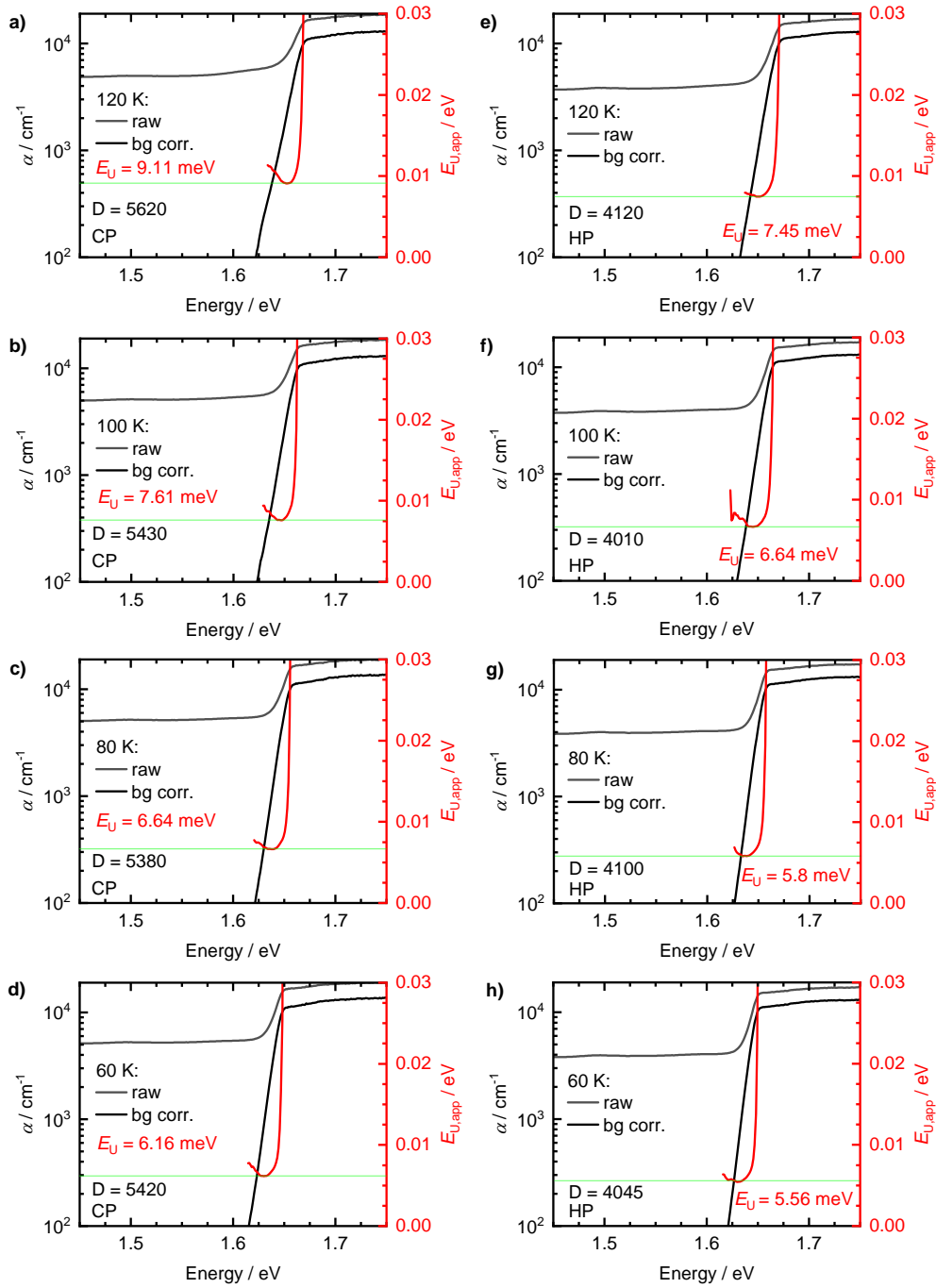
Figure S5: Extraction of Urbach energy values from measured absorption spectra (grey, offset corrected spectra in black) via the calculation of the apparent Urbach energy (red) via eq. 3 in the main text for CP thin film (a-d) and HP thin film (e-h) between 120 K and 60 K. The Urbach energy is determined from the horizontal part of the apparent Urbach energy (green line).

S7
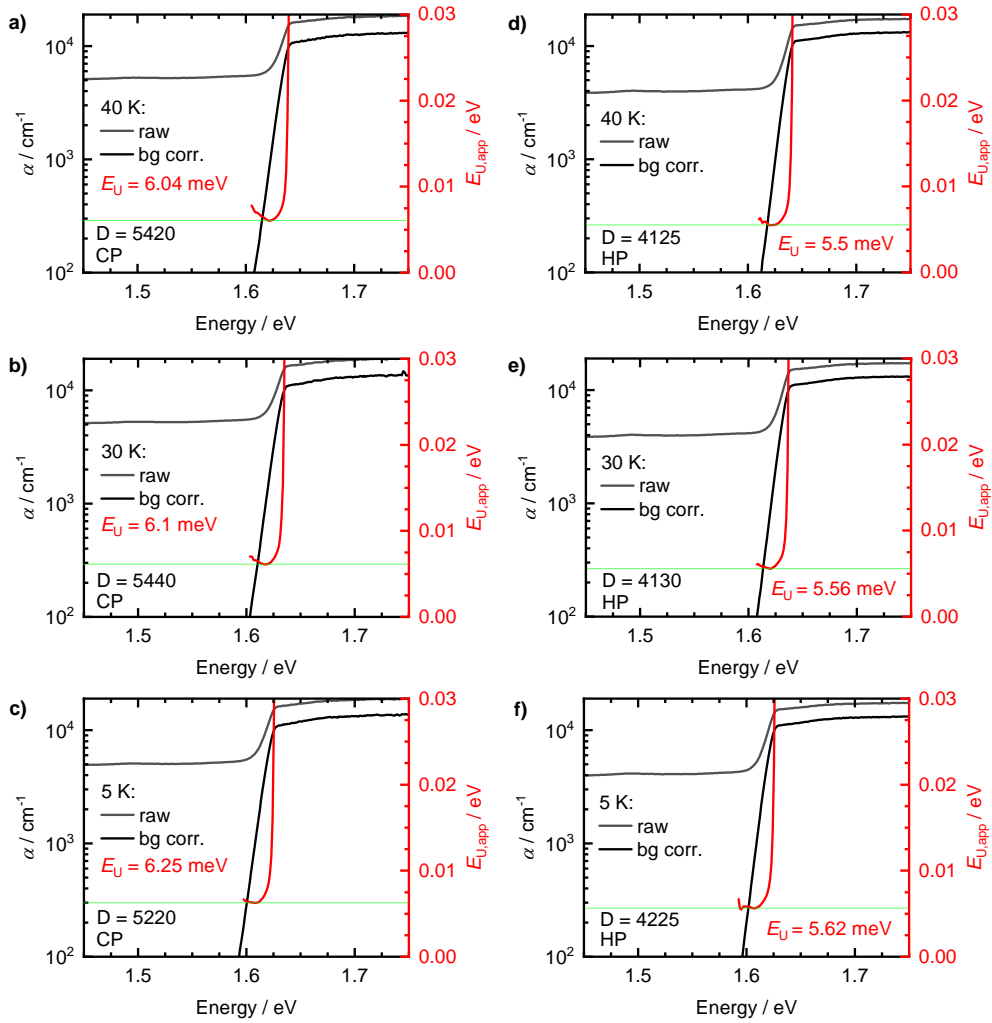
Figure S6: Extraction of Urbach energy values from measured absorption spectra (grey, offset corrected spectra in black) via the calculation of the apparent Urbach energy (red) via eq. 3 in the main text for CP thin film (a-c) and HP thin film (d-f) between 40 K and 5 K. The Urbach energy is determined from the horizontal part of the apparent Urbach energy (green line).

The background correction of the measured absorption spectra in Figures S2-6 was performed carefully: An offset value (4260 cm^{-1} in case of Figure 1e) has been subtracted from the measured absorption spectrum. This offset value has been determined by a first read out of the scattering offset of the absorption spectrum below 1.5 eV, followed by a finetuning revealing the purely exponential part of the absorption edge reflected in the horizontal part of $E_{U,app}$. Without such finetuning, it might be, that no perfectly horizontal part of $E_{U,app}$ is given.

1.1.3 Entire PL Shape Fits
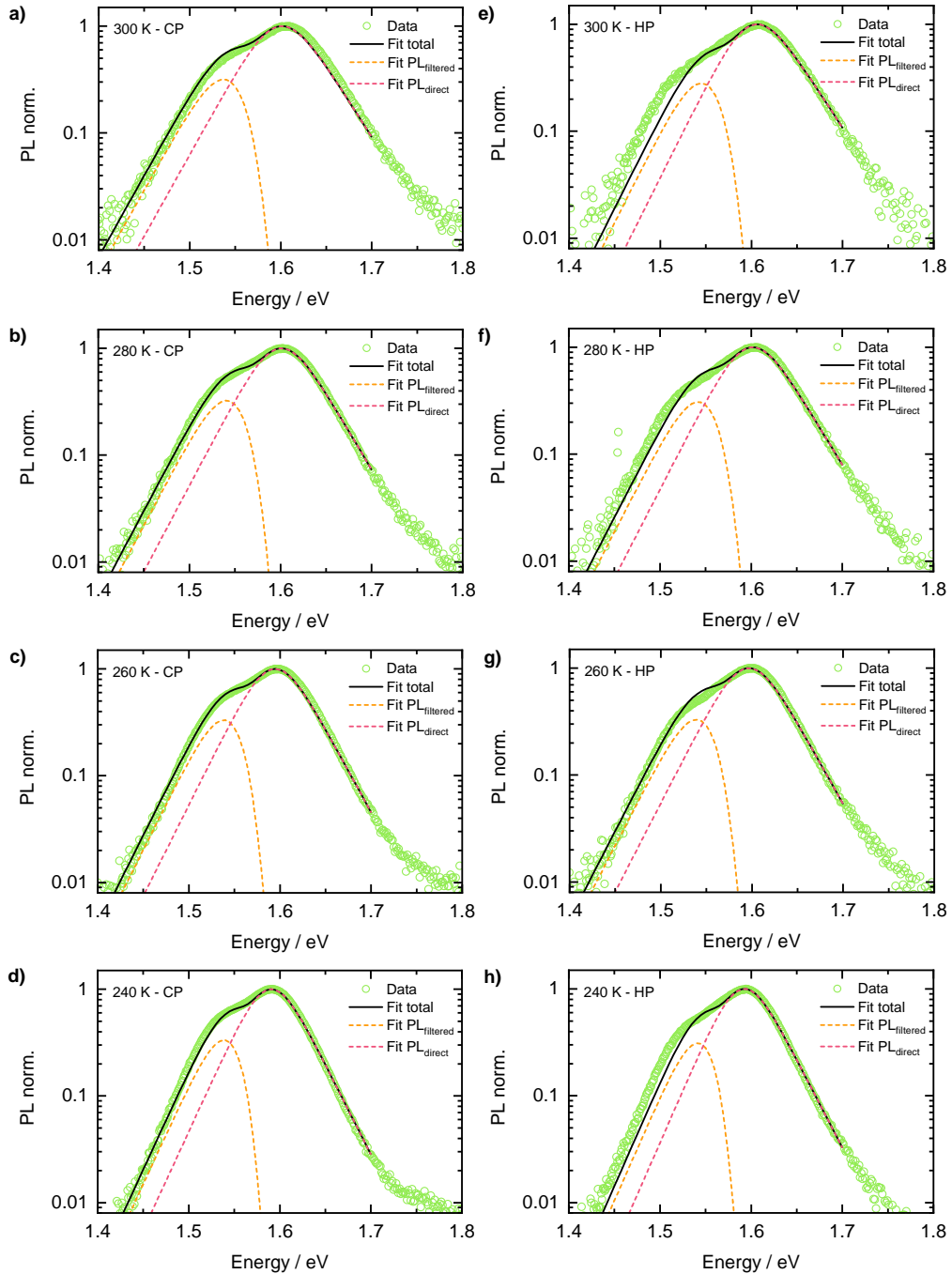
Figure S7: Extraction of Urbach energy values from measured PL spectra (green circles) via entire shape fits (black lines) according to eq. 7 in the main text for CP thin film (a-d) and HP thin film (e-h) between 300 K and 240 K. The fit is composed of filtered PL (orange dashed line) and direct PL (red dashed line).

S9
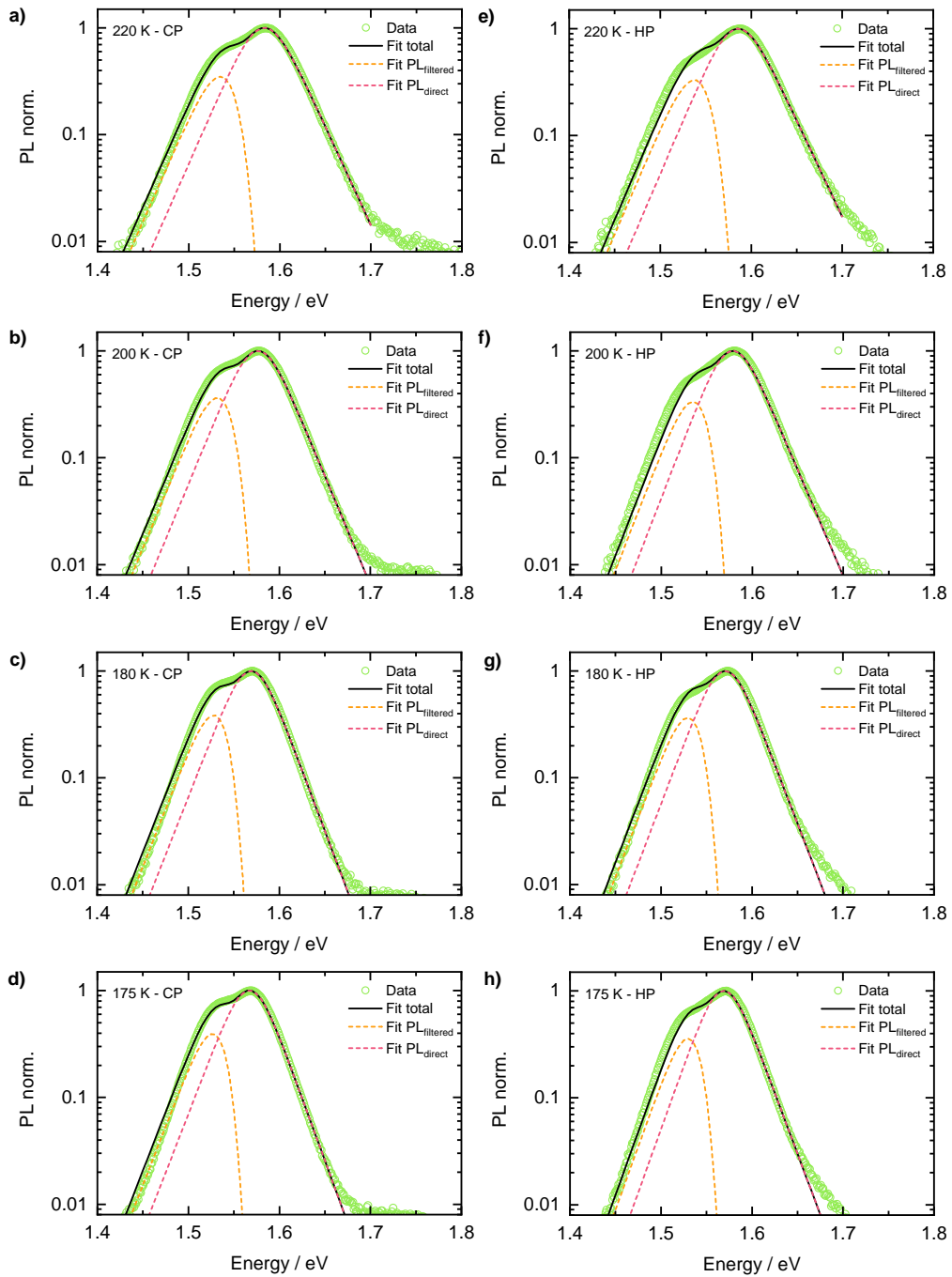
Figure S8: Extraction of Urbach energy values from measured PL spectra (green circles) via entire shape fits (black lines) according to eq. 7 in the main text for CP thin film (a-d) and HP thin film (e-h) between 220 K and 175 K. The fit is composed of filtered PL (orange dashed line) and direct PL (red dashed line).
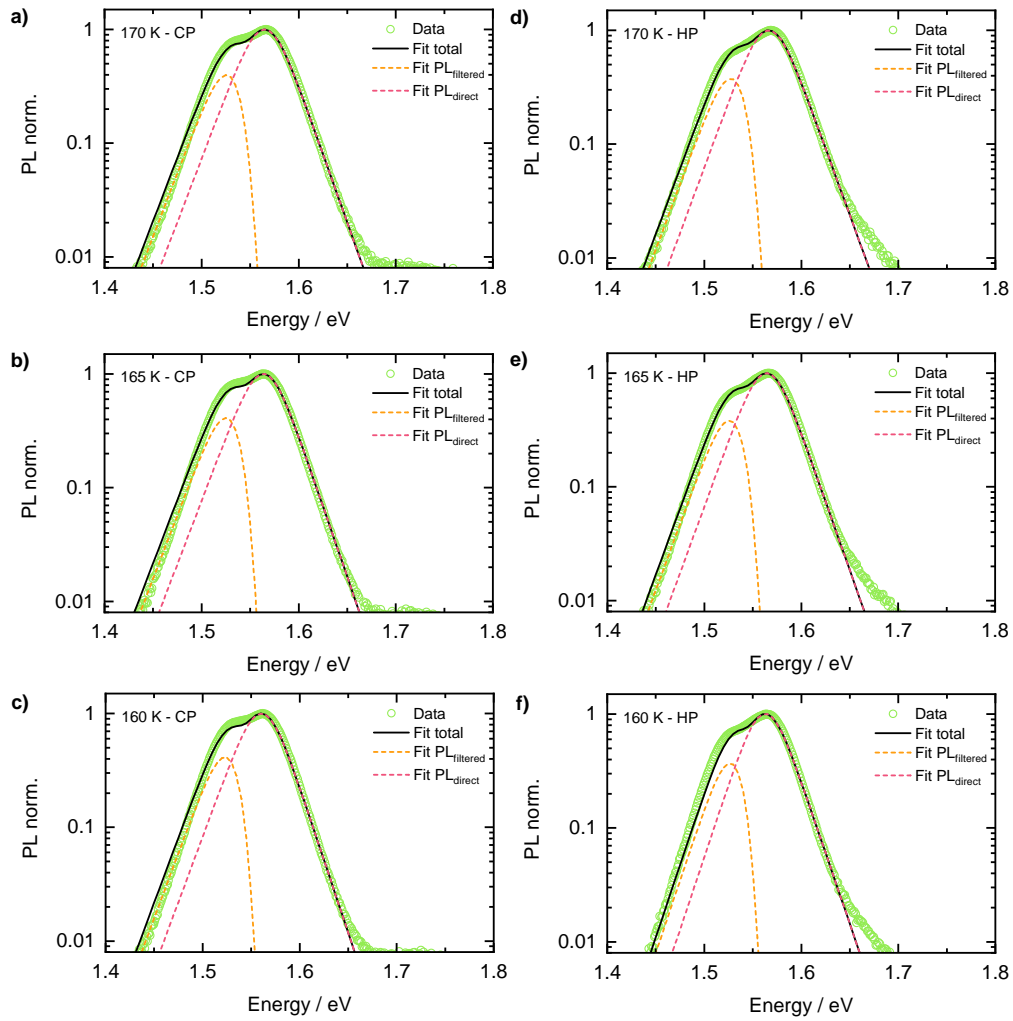
Figure S9: Extraction of Urbach energy values from measured PL spectra (green circles) via entire shape fits (black lines) according to eq. 7 in the main text for CP thin film (a-c) and HP thin film (d-f) between 170 K and 160 K. The fit is composed of filtered PL (orange dashed line) and direct PL (red dashed line).

S11

1.1.4 Urbach Energy Extraction via $E_{U,app}$ Calculated from PL Spectra
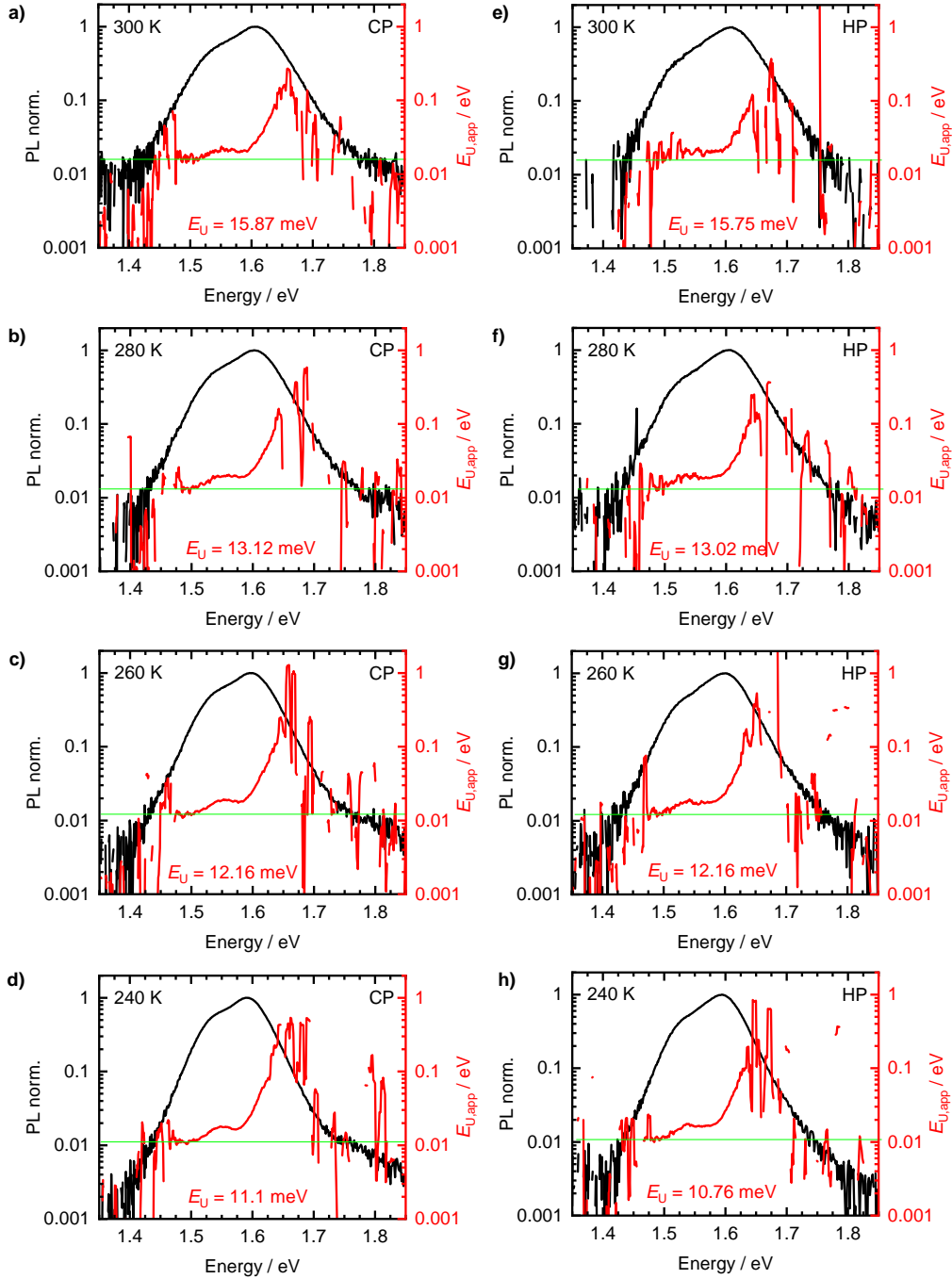
Figure S10: Extraction of Urbach energy values from measured PL spectra (black) via the calculation of the apparent Urbach energy (red) via eq. 9 in the main text for CP thin film (a-d) and HP thin film (e-h) between 300 K and 240 K. The Urbach energy is determined from the horizontal part of the apparent Urbach energy (green line).

S12

Figure S11: Extraction of Urbach energy values from measured PL spectra (black) via the calculation of the apparent Urbach energy (red) via eq. 9 in the main text for CP thin film (a-d) and HP thin film (e-h) between 220 K and 175 K. The Urbach energy is determined from the horizontal part of the apparent Urbach energy (green line).

S13

210

Figure S12: Extraction of Urbach energy values from measured PL spectra (black) via the calculation of the apparent Urbach energy (red) via eq. 9 in the main text for CP thin film (a-c) and HP thin film (d-f) between 170 K and 160 K. The Urbach energy is determined from the horizontal part of the apparent Urbach energy (green line).

S14

1.1.5 Calculating Absorption Spectra from Measured PL Spectra
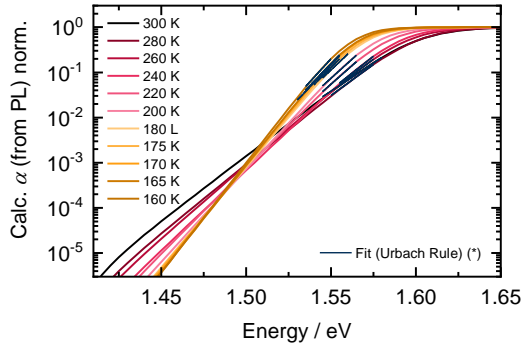
Figure S13: Absorption calculated from PL spectra via eq. 2 in the main text and applied Urbach Rule fits according to eq. 1 in the main text (blue lines). The energy range of the fits is similar to the energy range used for Urbach energy extraction via the apparent Urbach energy calculated from measured absorption spectra. The resulting Urbach energies are shown in Figure 4a in the main text (rose squares).

Figure S13 shows absorption spectra calculated from PL spectra via eq. 2 in the main text. As PL spectrum PL(E), the direct PL from entire shape fits to the measured PL (Figures S7-9) was used. As temperature, the increased temperature T_{inc} from the high energy PL edge was used, making a correction of the extracted increased Urbach energy $E_{U,inc}$ according to eq. 8 in the main text necessary to get the Urbach energy E_U (details on parameters T_{inc} and $E_{U,inc}$ are given in the main text in Section 3.1.2). The absorption spectra in Figure 1c in the main text were calculated similarly.

1.2. Energy Range for Urbach Energy Extraction
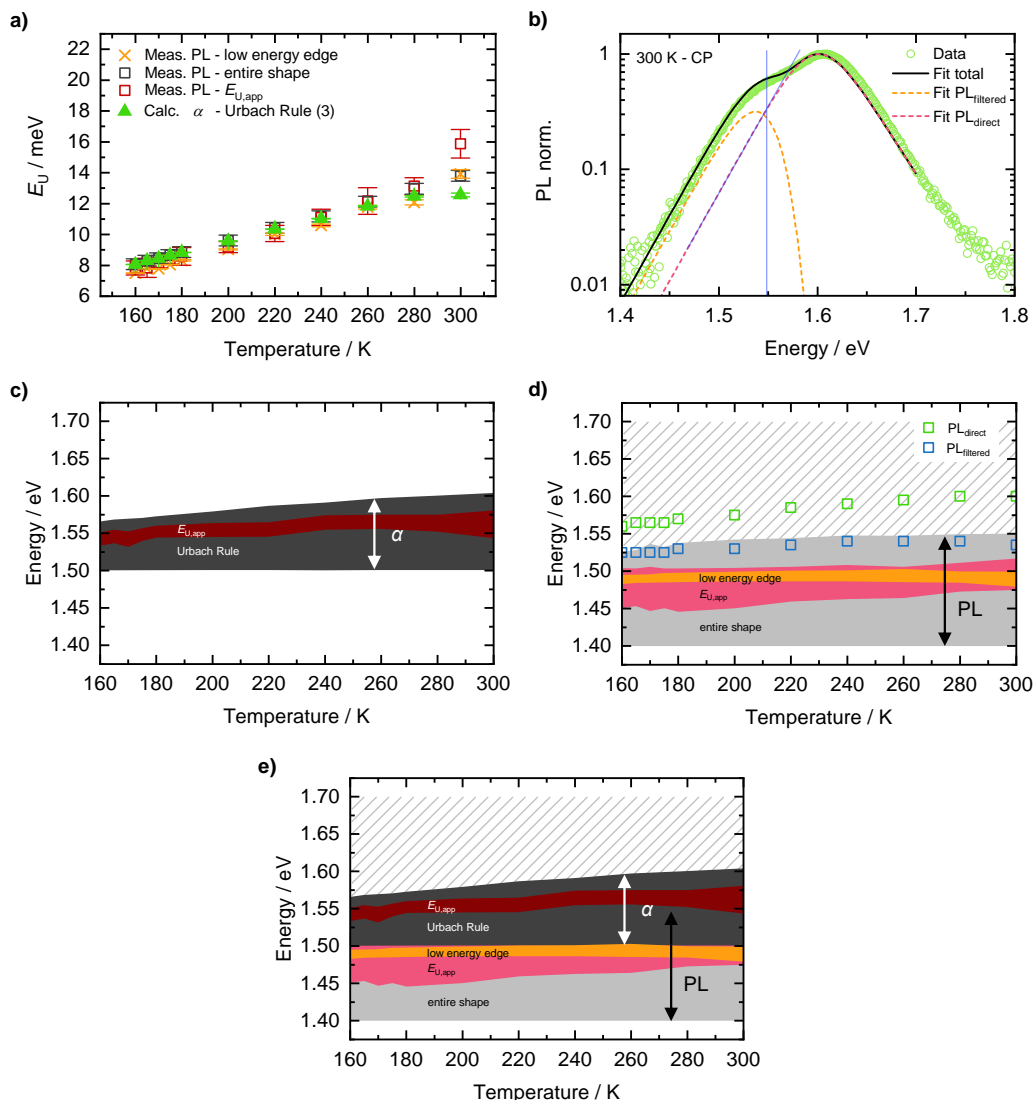
Figure S14: (a) E_U **values from 300 K down to 160 K determined via the methods presented in Figure 1c,d (green triangles) and Figure 2 in the main text (orange crosses, grey squares, red squares). Values shown as orange crosses adapted with permission from Witt et al.** [1] **Copyright 2023 American Chemical Society. (b) Extraction of Urbach energy via entire shape fit (black line) according to eq. 7 in the main text to CP thin film PL spectrum measured at 300 K (green circles). The fit is composed of filtered PL (orange dashed line) and direct PL (red dashed line). Using the blue lines, the maximum energy at which the low energy edge of PL_direct exhibits a purely exponential shape (i.e., where information about** E_U **is contained) is read out. (c-e) Temperature-dependent energy range used for**

the extraction of the Urbach energies in Figure 3a in the main text from measured PL and absorption together with filtered (blue) and direct (green) PL peak positions in (d).

For E_U extraction via entire shape fits of PL spectra, the maximum of the E_U extraction energy range (grey area in Figure S14d) for all temperatures was determined analogously to Figure S14b (blue lines) by evaluating up to which energy the low-energy edge of PL_{direct} exhibits a purely exponential shape (i.e., up to which energy the low-energy edge is determined by E_U according to eq. 7 in the main text). The resulting maximum energies of the E_U extraction energy range in Figure S14d are located more than ~0.02 eV below the respective PL_{direct} peak position (green squares), indicating that non-disorder-related near bandgap absorption effects do not contribute.

For E_U extraction via fitting the low energy edge of PL spectra and via applying the apparent Urbach energy approach to PL spectra, the low energy edge of the filtered PL is considered. Here, the maximum of the E_U extraction energy range (orange and red area in Figure S14d) is located more than ~0.02 eV below the respective $PL_{filtered}$ peak position (blue squares) for both approaches, indicating that non-disorder-related near bandgap absorption effects do not contribute.

1.3. Comparison of E_U between CP and HP
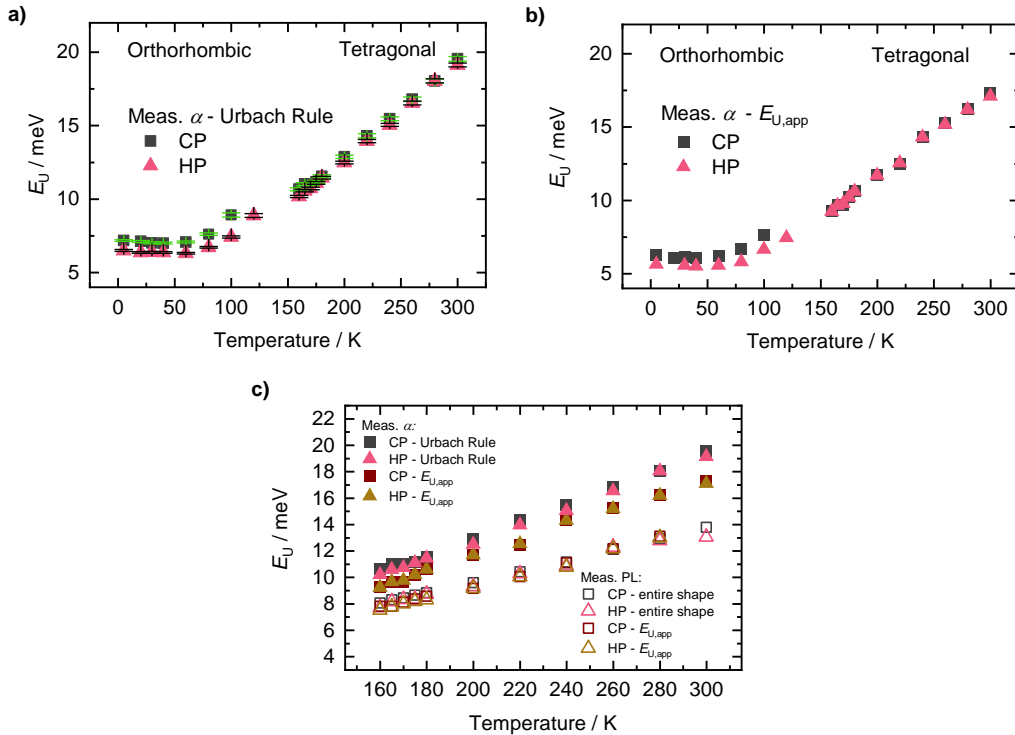
Figure S15: Urbach energies between 300 K and 5 K for CP (grey) and HP (red) thin films extracted from measured absorption spectra (a) via Urbach Rule Fits according to eq. 1 in the main text and (b) via the apparent Urbach energy using eq. 3 in the main text. (c) Urbach energies from (a,b, closed symbols) and extracted from measured PL (open symbols) via entire shape fits according to eq. 7 in the main text and via the apparent Urbach energy using eq. 9 in the main text for CP (squares) and HP (triangles) thin film.

The Urbach energy E_U decreases with decreasing temperature due to decreasing dynamic disorder and saturates to the static disorder value at 0 K. From Urbach Rule fits to measured absorption spectra slightly lower Urbach energy values are derived for the HP film compared to the CP film. Especially in the low temperature orthorhombic phase such differences in E_U between both films are visible (Figure S15a). Similar differences in orthorhombic phase are also found in Urbach energies extracted from measured absorption spectra via the apparent Urbach energy (Figure S15b). The slightly lower Urbach energy values for the HP film compared to the CP film are reasonable due to larger grain sizes and increased preferred orientation in the HP film, which was shown to result in decreased strain and defect density in our previous work.[1] However, using PL analyses, differences in E_U between both films are

S18

not resolvable (Figure S15c).[1] We attribute this to the preferential sensitivity of PL for sites with low energetic disorder, i.e., sites with high film quality and the overall small differences between both films. Thus, absorption measurements allow for a higher resolution of differences in energetic disorder between different samples than PL measurements. In Figure S15c Urbach energies of the CP (squares) and HP (triangles) film extracted from measured absorption (closed symbols) and PL (open symbols) via different analysis methods are summarized. Here, a similar temperature-dependence of the respective Urbach energies is found for both films.

The comparison of thin film and single crystal samples also yields only small or even no differences in Urbach energy values (Figure 5, Figure S16), although the morphology of both samples is obviously differing, which might be due to an inherent high electronic quality and short-range correlation of energetic disorder in halide perovskites.

S19

216

2. Urbach Energy Analyses of Single Crystal Samples
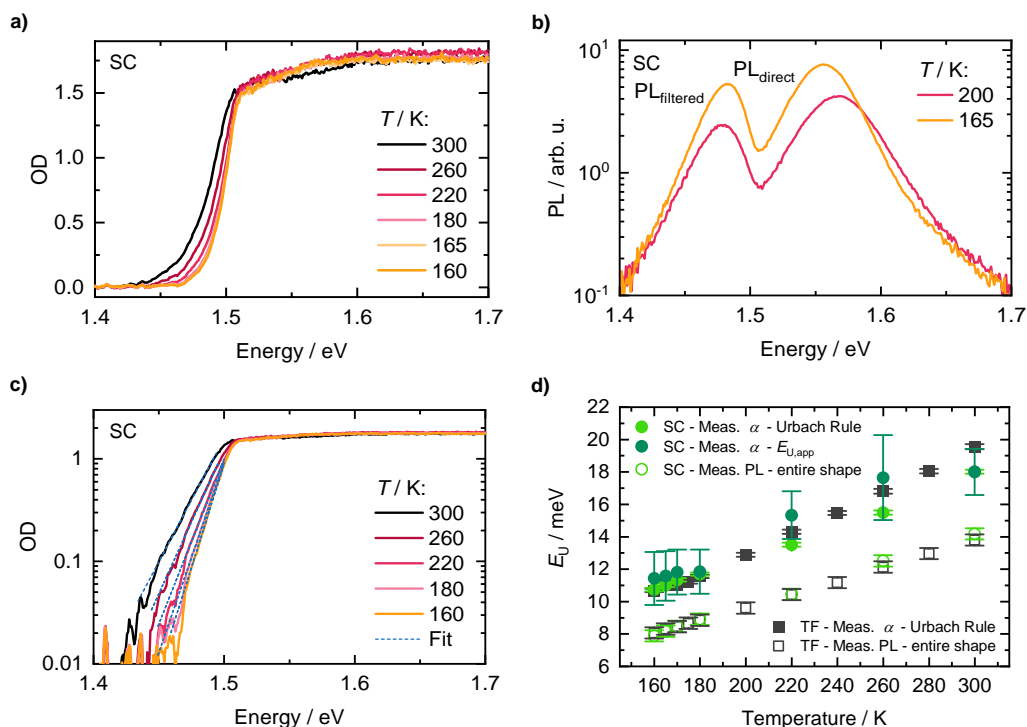
Figure S16: (a) Absorption and (b) PL spectra of MAPbI₃ single crystals between 300 K and 160 K. (c) Urbach Rule fits (blue dashed lines) according to eq. 1 in the main text to the absorption spectra from (a). Spectra in (a), (b), (c) adapted from Schötz et al. [8] Copyright 2020 The Royal Society of Chemistry. (d) Urbach energy values between 300 K and 160 K for the CP thin film (grey squares) and similar single crystal samples (green circles) extracted from absorption (full symbols) and PL (open symbols). E_U from single crystal PL adapted under the terms of the CC-BY 4.0 license from Schötz et al. [9] Copyright 2020, the authors. Published by WILEY-VCH Verlag GmbH & Co. KGaA, Weinheim.

Due to the higher sample thickness of the single crystal compared to the thin film, the quality of the measured absorption edge is somewhat lower for the single crystal, resulting in larger error bars for the Urbach energies determined via the apparent Urbach energy (dark green circles in Figure S16d). Nevertheless, these Urbach energy values are in agreement with the values determined from Urbach rule fits to the absorption spectra (light green circles).

3. Slope – Temperature-Dependence of E_U
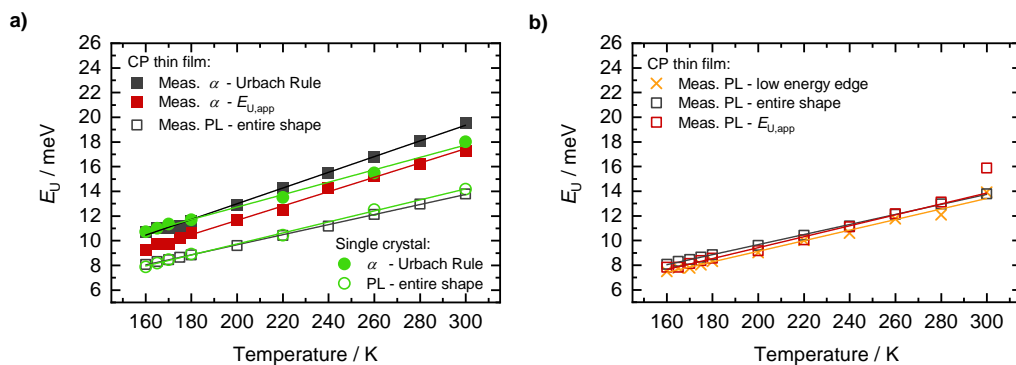
Figure S17: Linear fits to temperature-dependent Urbach energies from Figures 3a and 4b in the main text for determination of the slope values summarized in Figure 5c in the main text. Values shown as orange crosses adapted with permission from Witt et al. [1] **Copyright 2023 American Chemical Society.**

References

1. Witt, C.; Schötz, K.; Kuhn, M.; Leupold, N.; Biberger, S.; Ramming, P.; Kahle, F.-J.; Köhler, A.; Moos, R.; Herzig, E. M., et al. Orientation and Grain Size in MAPbI$_3$ Thin Films: Influence on Phase Transition, Disorder, and Defects. *J. Phys. Chem. C* **2023,** *127*, 10563-10573.
2. Beaudoin, M.; DeVries, A. J. G.; Johnson, S. R.; Laman, H.; Tiedje, T. Optical Absorption Edge of Semi-Insulating GaAs and InP at High Temperatures. *Appl. Phys. Lett.* **1997,** *70*, 3540-3542.
3. Cody, G. D.; Tiedje, T.; Abeles, B.; Brooks, B.; Goldstein, Y. Disorder and the Optical-Absorption Edge of Hydrogenated Amorphous Silicon. *Phys. Rev. Lett.* **1981,** *47*, 1480-1483.
4. Studenyak, I.; Kranjčec, M.; Kurik, M. Urbach Rule in Solid State Physics. *Int. J. Opt. Appl.* **2014,** *4*, 76-83.
5. Falsini, N.; Roini, G.; Ristori, A.; Calisi, N.; Biccari, F.; Vinattieri, A. Analysis of the Urbach Tail in Cesium Lead Halide Perovskites. *J. Appl. Phys.* **2022,** *131*.
6. Ledinsky, M.; Schönfeldová, T.; Holovský, J.; Aydin, E.; Hájková, Z.; Landová, L.; Neyková, N.; Fejfar, A.; De Wolf, S. Temperature Dependence of the Urbach Energy in Lead Iodide Perovskites. *J. Phys. Chem. Lett.* **2019,** *10*, 1368-1373.
7. Ledinský, M.; Vlk, A.; Schönfeldová, T.; Holovský, J.; Aydin, E.; Dang, H. X.; Hájková, Z.; Landová, L.; Valenta, J.; Fejfar, A., et al. Impact of Cation Multiplicity on Halide Perovskite Defect Densities and Solar Cell Voltages. *J. Phys. Chem. C* **2020,** *124*, 27333-27339.
8. Schötz, K.; Askar, A. M.; Peng, W.; Seeberger, D.; Gujar, T. P.; Thelakkat, M.; Köhler, A.; Huettner, S.; Bakr, O. M.; Shankar, K., et al. Double Peak Emission in Lead Halide Perovskites by Self-Absorption. *J. Mater. Chem. C* **2020,** *8*, 2289-2300.
9. Schötz, K.; Askar, A. M.; Köhler, A.; Shankar, K.; Panzer, F. Investigating the Tetragonal-to-Orthorhombic Phase Transition of Methylammonium Lead Iodide Single Crystals by Detailed Photoluminescence Analysis. *Adv. Opt. Mater.* **2020,** *8*, 2000455.

4.6 First of Their Kind: Solar Cells with a Dry-Processed Perovskite Absorber Layer via Powder Aerosol Deposition and Hot-Pressing

Simon Biberger*, Nico Leupold*, **Christina Witt***, Christopher Greve, Paul Markus, Philipp Ramming, Daniel Lukas, Konstantin Schötz, Frank-Julian Kahle, Chenhui Zhu, Georg Papastavrou, Anna Köhler, Eva M. Herzig, Ralf Moos, and Fabian Panzer.
* Contributed equally

First of Their Kind: Solar Cells with a Dry-Processed Perovskite Absorber Layer via Powder Aerosol Deposition and Hot-Pressing

Simon Biberger, Nico Leupold, Christina Witt, Christopher Greve, Paul Markus, Philipp Ramming, Daniel Lukas, Konstantin Schötz, Frank-Julian Kahle, Chenhui Zhu, Georg Papastavrou, Anna Köhler, Eva M. Herzig, Ralf Moos, and Fabian Panzer*

Preparing halide perovskite films by solvent-free, powder-based processing approaches currently attracts more and more attention. However, working solar cells employing dry, powder-based halide perovskite thin films, have not been demonstrated so far. Herein, perovskite solar cells are presented where the absorber layer is prepared by transferring readily synthesized perovskite powders into a compact thin film using a fully dry-powder-processing concept. Compact thin films are deposited via an optimized powder aerosol deposition (PAD) process. Pressing at 120 °C further improves the morphology and the optoelectronic film properties. Integrating the perovskite films in a solar cell configuration results in fully working devices, with champion power conversion efficiencies of >6%. While the (optoelectronic) properties of the PAD-processed films are found to be comparable with their solution-processed counterparts, investigations of the solar cell stack suggest deterioration of the electron-transport layer properties due to the PAD process, and the presence of hydrates at the perovskite surface to be important factors that contribute to the limited solar cell efficiency. Herein, perspectives to overcome the identified limitations are outlined, emphasizing the high potential and realizability of efficient perovskite solar cells based on dry-powder-processing approaches in the future.

1. Introduction

Within the last decade, the rise of metal-halide perovskites (MHP) as light absorber in solar cells has been remarkable. Power conversion efficiencies (PCEs) of up to 25.7%[1,2] and increasing device stabilities of up to several thousand hours[3,4] currently push perovskite solar cells on the verge to commercialization.

For high PCEs however, high-quality MHP films are required. Most of such high-quality perovskite films are currently prepared either by solution-based processing or evaporation methods.[2,4–6] Despite their widespread application in perovskite film fabrication, these approaches are still facing limitations.

One inherent limitation of solution-based and evaporation methods is the intrinsic coupling between perovskite synthesis and film formation, rendering the morphology and final optoelectronic functionality of perovskite films to be extremely sensitive to the precise processing conditions.[7–10] Moreover, a second drawback of solution-based processing is the need for toxic solvents such as dimethylfluorene (DMF)[11,12] to prepare the precursor

S. Biberger, C. Witt, P. Ramming, K. Schötz, F.-J. Kahle, A. Köhler, F. Panzer
Soft Matter Optoelectronics (EP II)
University of Bayreuth
95440 Bayreuth, Germany
E-mail: fabian.panzer@uni-bayreuth.de

The ORCID identification number(s) for the author(s) of this article can be found under https://doi.org/10.1002/solr.202300261.

N. Leupold, D. Lukas, R. Moos
Department of Functional Materials
University of Bayreuth
95440 Bayreuth, Germany

C. Greve, E. M. Herzig
Dynamics and Structure Formation - Herzig Group
University of Bayreuth
95440 Bayreuth, Germany

P. Markus, G. Papastavrou
Physical Chemistry II
University of Bayreuth
95440 Bayreuth, Germany

C. Zhu
Advanced Light Source
Lawrence Berkeley National Lab
Berkeley, CA 94720, USA

stock solutions. Replacing these toxic solvents was already subject of several studies with the aim to find greener alternatives for perovskite stock solutions.[13–16]

An attractive film-processing approach, which does not rely on solvents and that decouples the perovskite synthesis and film formation, is the dry processing of already synthesized MHP powders via powder aerosol deposition (PAD).[17–19] Here, an aerosol is generated from powder and accelerated onto a substrate, where the powder particles break up and form a dense film. PAD is well established for a variety of different ceramic materials, like technical ceramics,[20–23] and ceramics for sensing and energy applications.[24] First commercial applications of PAD are already tested.[25]

Using a basic PAD setup, we showed in a previous work that thin films of MHPs such as the model perovskite methylammonium lead iodide (MAPbI₃) can be produced via PAD.[26] Yet, clear improvements in film morphology (compactness, surface roughness) were still required to realize film properties suitable for applications in optoelectronic thin film devices, such as perovskite solar cells.

In the past, it was demonstrated that the compactness and surface roughness of MHP can be improved by pressure treatment.[27–30] In addition, it became clear that performing the pressure treatment under elevated temperature not only further improved the surface roughness and the compactness, but even led to enlarged grain sizes, which is known to be beneficial regarding the MHP's optoelectronic functionality.[31–34]

Here, we present sophisticated technical developments in the PAD process that enable the deposition of thin ($\approx 1\,\mu m$), yet dense MAPbI₃ films. In addition, we successfully employ pressure treatment of the optimized PAD films to further improve morphology and optoelectronic properties.

With these improvements, we demonstrate the first realization of pressed and unpressed PAD-processed MAPbI₃ thin films in a solar cell configuration, resulting in fully working devices with PCEs of >6%. We highlight in detail the challenges that remain and discuss approaches to tackle the current limitations to manufacture highly efficient solar cells in the future based on the here presented novel perovskite-processing method.

2. Process Development toward Dry-Processed Perovskite Absorber Layers Suitable for the Use in PSCs

2.1. PSC Fabrication Concept

The fabrication process of our perovskite solar cells with a completely dry, powder-based perovskite-processing approach is presented in **Figure 1**. First, we synthesize MAPbI₃ powder mechanochemically via ball milling (details in previous work[35,36]), and use this powder in a dry PAD process.

A PAD system consists of three main components: 1) a vacuum pump for generating a rough vacuum with an absolute pressure in the range of 1 mbar, 2) a deposition chamber in which the substrate is mounted on a movable substrate holder, and 3) an aerosol generating unit (Figure S1, Supporting Information). In the latter, a powder aerosol is generated from the dry mechanochemically synthesized powder by passing a carrier gas such as N₂, O₂, or He, for example, through a powder bed located on a porous tray in a glass flask.

The powder aerosol is transported from the aerosol generating unit to the evacuated deposition chamber due to the pressure difference between both components. In the deposition chamber, the powder aerosol is further accelerated through a nozzle to velocities between 100 and 600 m s^{-1} and directed onto a glass substrate coated with indium tin oxide (ITO) as transparent electrode and SnO₂ as electron-transport layer (ETL).

Upon impact on the substrate, the powder particles in the aerosol deform, break up, and adhere to the substrate. Subsequently impacting particles increase the film thickness, further fragment previously deposited particles and densify the film. This mechanism is called room-temperature impact consolidation (RTIC).[37] The MAPbI₃ films, deposited via the PAD approach (further referred to as pristine films), are dense, fully covering the substrate (Figure S11, Supporting Information). To reduce the surface roughness and further improve the film quality of the pristine MAPbI₃ PAD films, we applied hot-pressing as an optional posttreatment step before spin-coating 2,2′,7,7′-Tetrakis[N,N-di(4-methoxyphenyl)amino]-9,9′-spirobifluorene (spiro-MeOTAD) as hole-transport layer (HTL) onto the MAPbI₃ film and thermally evaporating gold as top electrode to complete the solar cells.
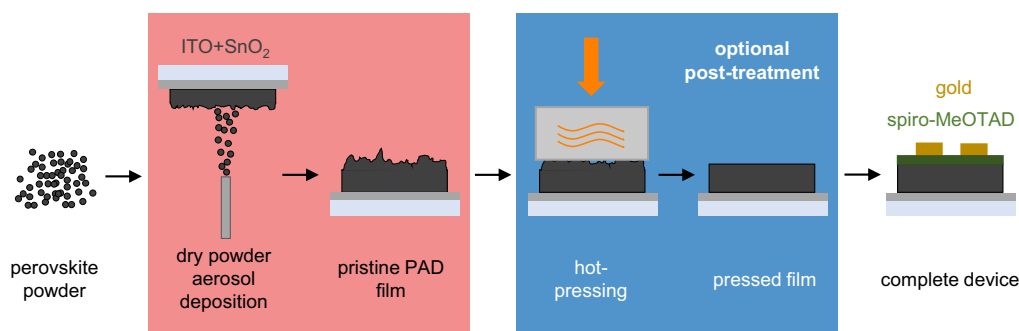

Figure 1. Fabrication concept for a solar cell with a perovskite absorber layer processed via the powder aerosol deposition (PAD) method and optional subsequent hot-pressing.

In the following, we first describe the key improvements in the PAD process that allow for successful fabrication of compact perovskite films with thicknesses in the range of $\approx 1\,\mu m$ (Section 2.2.). Then, we outline relevant aspects in the hot-pressing step of the PAD perovskite films (Section 2.3) and discuss the properties of the fully dry-processed powder-based perovskite solar cells in Section 3.

2.2. Key Improvements in the PAD Process

In general, the powder particle size and the presence of agglomerates consisting of those powder particles are decisive for the film formation during PAD. Desired particle sizes are typically in the range between 200 nm to 5 μm.[38] Due to their low mass, smaller particles exhibit low kinetic energy and inertia so that they either do not reach the substrate or bounce off the substrate upon impact. In contrast, too high kinetic energy of larger particles can result in abrasion of the substrate, similar to sandblasting.[38]

The presence of large agglomerates in the PAD process is also detrimental to the film properties, as a large fraction of their kinetic energy is used to break up the initially large agglomerates into smaller agglomerates and individual powder particles when impacting the substrate. Thus, less energy is available for deforming and fracturing the individual particles as necessary for densification of the film via RTIC.[38] As a result, porous films with voids (pinholes through the whole film thickness) and bad contact to the substrate (Figure S2, Supporting Information) are deposited. Thus, the aerosol generation, that is, especially the reduction of the number of agglomerates within the powder aerosol, is a key to allow for PAD-deposited MAPbI₃ thin films suitable for solar cells.

Our mechanochemically synthesized powder used for PAD is phase pure und consists of 30–50 μm large agglomerates of powder particles in the 1 μm range (Figure S3 and S4, Supporting Information). While the powder particle size is well suitable for PAD, size and number of agglomerates impacting on the substrate have to be reduced to obtain high-quality PAD films. To fragment the agglomerates before they reach the substrate, we implemented an ejector unit after the aerosol flask. The ejector consists of 1) a horizontal tube, whose cross section narrows at a throat and expands afterward and 2) a second tube, that enters the first tube perpendicular in the expansion zone (**Figure 2**a).

The ejector unit serves two beneficial purposes. First, strong shear forces are present when $\dot{V}_{acc}$ (gas flow for acceleration of aerosol) and $\dot{V}_{flask}$ (gas flow of carrier gas for aerosol generation in the flask) are merging perpendicular to each other after the throat in the ejector unit. In addition, agglomerates accelerate upon entering the gas flow $\dot{V}_{total}$ (Figure 2a). Both effects contribute to break up agglomerates within the aerosol.[39] The second advantage of the ejector is the possibility to independently control $\dot{V}_{flask}$ and $\dot{V}_{acc}$. This allows to apply a low $\dot{V}_{flask}$, and thus to reduce the overall MAPbI₃ aerosol concentration significantly. Consequently, while more passes, that is, a higher number of movements of the substrate over the nozzle, are necessary to realize a certain film thickness, fluctuations in the aerosol concentration are much better compensated, compared to a PAD setup without ejector unit. This eventually allows for producing PAD films with more homogeneous film coverage. In passing, we note that replacing the ejector with a simple tee to reduce the complexity of the setup does not result in satisfying film quality (Figure S5, Supporting Information).

Figure 2b, top panel, shows a scanning electron microscope (SEM) image of a MAPbI₃ PAD film deposited using the ejector. The film is compact with only small pores and has an overall good contact to the bottom layer. Yet, even with the ejector, the MAPbI₃ PAD films still exhibit voids (Figure 2b top). In addition, the film area deposited from the middle of the 10 mm slit nozzle is thicker compared to the area from the edges of the nozzle. This inhomogeneity in film thickness indicates that agglomerates are still present in the aerosol, most likely in the center of the aerosol jet hitting the substrate. An explanation of this observation is that agglomerates do not follow the gas flow due to their large inertia when the circular cross section of the tube leading the gas flow to the nozzle changes from a diameter of 4 mm to a slit orifice of 10 mm × 0.5 mm of the nozzle.

To finally remove these persisting agglomerates from the aerosol, we employed an inertial separator unit, consisting of a tee and a tube between the ejector and slit nozzle (Figure 2a). In the inertial separator, the aerosol jet coming from the ejector is deflected by 90° and directed to the slit nozzle. Consequently,
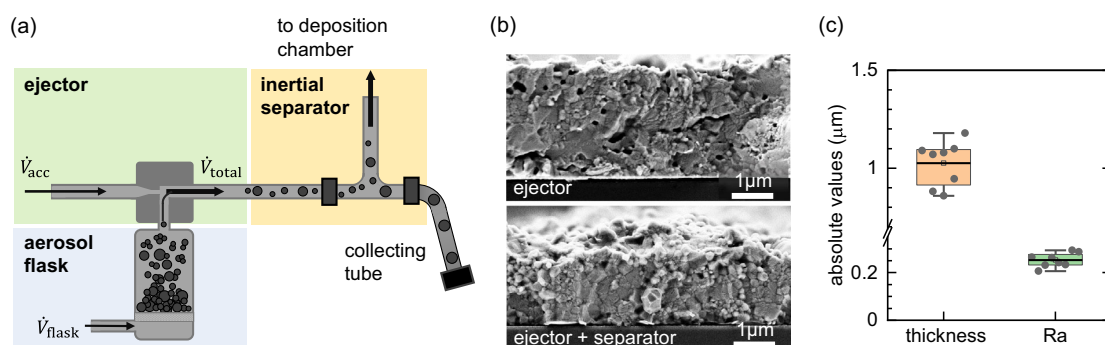

Figure 2. a) Concept of the improved aerosol generation employing an ejector unit and inertial separator. b) Scanning electron microscope (SEM) cross-section images of PAD films deposited with ejector (top) and with ejector and inertial separator (bottom). c) Resulting thickness and surface roughness Ra of the optimized pristine PAD films deposited with ejector and inertial separator.

only smaller agglomerates and particles in the aerosol jet can follow the gas flow to the nozzle, while larger agglomerates end up in the collecting tube due to their larger inertia.

In passing, we mention that in addition to these technical improvements addressing the agglomerates issue, we also integrated a smaller flask with a diameter of 3 cm in the aerosol generation unit allowing to use low powder quantities (<1 g) to further reduce the aerosol concentration and increase the general process control.

By these setup improvements, we obtain dense and void-free MAPbI$_3$ films (Figure 2b bottom) with mean thickness of (1.0 ± 0.1) μm and reasonable arithmetic mean roughness Ra of (0.25 ± 0.03) μm (Figure 2c, for details about chosen PAD process parameters, see Section S1, Supporting Information). Thus, the modified aerosol generation with ejector and inertial separator allows to deposit 1 μm thick MAPbI$_3$ films from highly agglomerated powders with, considering the field of PAD, high reproducibility.

2.3. Posttreatment via Hot-Pressing

Pressing at elevated temperature has emerged as powerful technique to improve MAPbI$_3$ film properties, that is, film morphology, optoelectronic properties, as well as related solar cell efficiencies.[31–34,40–42] In particular, a higher pressure–temperature combination is known to result in stronger improvements of MAPbI$_3$ film morphology and optoelectronic properties.[27,28,31–33,40,41,43] To further improve the perovskite film quality of the pristine PAD films, we therefore applied an additional hot-pressing posttreatment step.

First, we explored the possibility to employ press die materials commonly used for pressing MHP films. While silicon wafers and PTFE sheets were often used in the past,[31,33,34,40–45] their form stability is limited to pressures below 15 MPa in single action pressing.[31,34,40,41,44] To achieve clear improvements upon pressure treatment of our PAD films, we aimed for a pressure of 25 MPa, rendering silicon wafers and PTFE sheets unsuited for our approach. Polyimide foil exhibits high form stability under mechanical and thermal stress,[46] and was already used as press die material for the fabrication of MHP films with promising optoelectronic properties in the past.[47,48] We examined polyimide foil as press die material in our press setup but observed that after pressing the polyimide foil exhibited significant wear and the PAD film tended to stick to the polyimide foil (for detailed discussion, see Figure S6, Supporting Information).

Due to these issues, we explored the possibility to use glass blocks (thickness: 8 mm, roughness: 2 nm) as press die material, covered with a silanization coating (trichloro(octadecyl)silane in toluene from liquid phase) to prevent the glass blocks from sticking to the perovskite film. Using the silanized glass blocks, our PAD films can be pressed reliably and without breakage of glass substrates and glass blocks employing up to 25 MPa at 120 °C for 5 min. For our experiments, we thus choose this set of process parameters, as it is known that increased temperature and pressure are beneficial for improving the morphology and optoelectronic properties when pressing halide perovskite films[27,28,31–33,40,41,43] (also see Figure S7, Supporting Information, and previous work[28] for details on press setup and protocol).

Applying this pressing procedure to the pristine PAD films, which appear matt black before pressing, we obtain shiny gray films after the pressing step (**Figure 3**b left). This change in optical appearance already indicates a reduction in surface roughness, which is further evidenced from the comparison of top-view SEM images of a pressed film and a pristine film (Figure 3b right). We quantified the mean Ra value of the pressed films to be 18 nm, compared to 250 nm of the pristine films, confirming a reduction in surface roughness by >92% upon pressing (Figure 3c). Additionally, pressing the PAD films with 25 MPa at 120 °C reduced the film thickness by about 37% (Figure 3c), indicating an increased compaction of the pressed MAPbI$_3$ films. More details on the changes of morphology and optoelectronic properties of pristine and pressed MAPbI$_3$ films are discussed in Section 4.2.

In summary, by employing the previously described key developments in the PAD process, in combination with an optional hot-pressing step of the pristine PAD perovskite films, we demonstrated the successful production of phase pure and dense polycrystalline MAPbI$_3$ thin films that meet the film requirements for the use in functional perovskite solar cells.
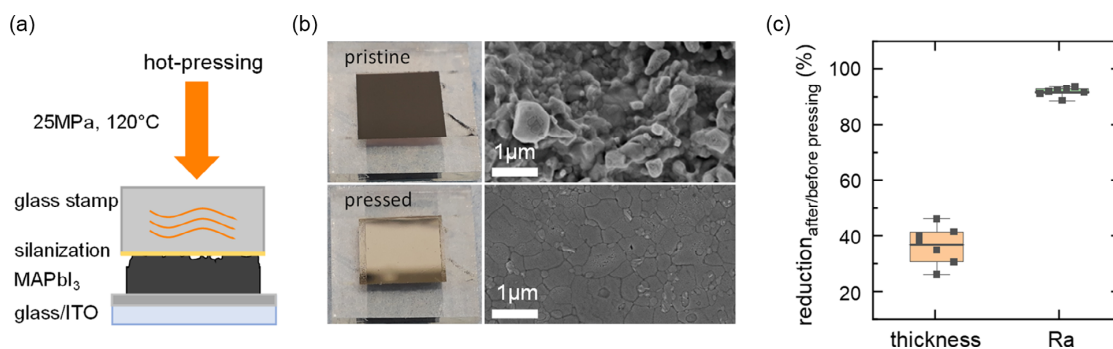

Figure 3. a) Sketch of hot-pressing a PAD film. b) Photographs (left) and top-view SEM images (right) of pristine (top) and pressed (bottom) MAPbI$_3$ PAD films. c) Reduction of thickness and surface roughness (Ra) of PAD films due to pressing (see Figure S8, Supporting Information, for absolute values).

3. Solar Cells

Based on the described process improvements and following the concept in Figure 1, we manufactured two types of complete solar cell stacks. One type uses a pristine PAD film as the absorber layer (hereafter referred to as "pristine" devices), while for the other type, we posttreated the PAD absorber layer via hot-pressing (referred to as "pressed" devices).

Figure 4a shows cross-section SEM images of the resulting n–i–p solar cell stacks with pristine (left) and pressed (right) MAPbI$_3$ film. To allow for a systematic comparison of the morphology before and after pressing, we choose devices with similar thickness. From Figure 4a, the glass substrate covered with ITO electrode (grey), the SnO$_2$ ETL (purple), the perovskite film (brown), the spiro-MeOTAD HTL (green), and the gold top electrode can be distinguished.

Exemplary current density–voltage (J–V) curves for each solar cell type are plotted in Figure 4b. Both, the pristine and the pressed devices exhibit a diode-like dark current characteristic (rectangles). Under AM1.5G illumination, the J–V curves measured in reverse direction (colored circles) exhibit photovoltaic behavior for both the pristine and the pressed devices. Considering the J–V curves measured in forward direction

(grey circles), both types of devices show a pronounced hysteresis.

The solar cell metrics determined from the reverse measurement direction for 12 devices each are shown in Figure 3c for the pristine (red) and pressed (blue) absorber layer. These metrics were measured after storing the devices in dry ambient conditions in the lab for 9 weeks, where the metrics were stable and even slightly improved compared to the metrics measured 24 h after the fabrication (see Figure S9, Table S1 and S2, Supporting Information, for comparison between metrics determined 24 h and 9 weeks after fabrication including forward direction, for the operational stability, see Figure S10, Supporting Information). The mean open-circuit voltage (V_{OC}) for the pristine absorber layer is (0.90 ± 0.11) V, while the pressed devices exhibit an increased mean V_{OC} of (0.95 ± 0.04) V. The mean short-circuit current density (J_{sc}) also increases upon pressing from (7.2 ± 3.1) mA cm^{-2} for the pristine devices to (7.6 ± 2.7) mA cm^{-2} for the pressed devices. Similarly, the fill factor (FF) yields mean values of $(52 \pm 9)\%$ and $(56 \pm 6)\%$ for the pristine and pressed absorber layers, respectively. Overall, the resulting average PCE for the pristine absorber layer of $(3.5 \pm 1.8)\%$ improves to a PCE of $(4.1 \pm 1.8)\%$ for the pressed absorber layer, where the champion devices of
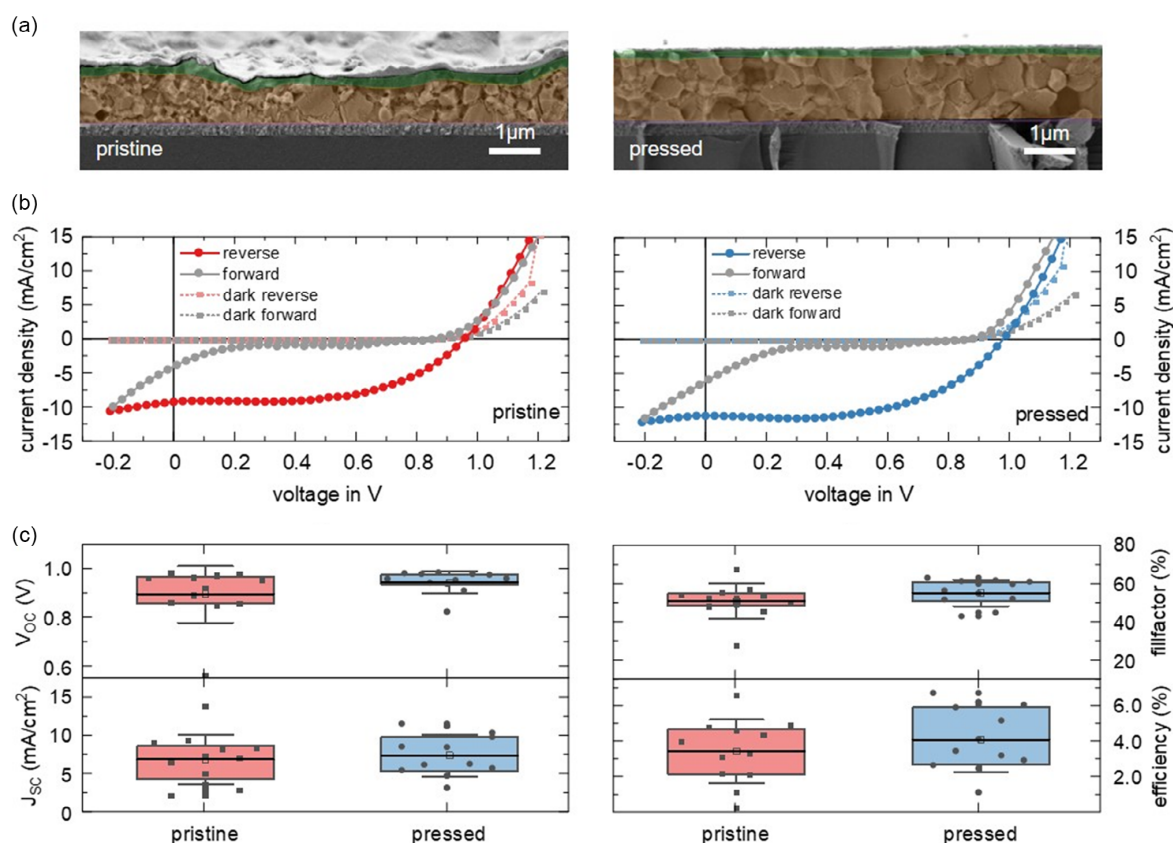
Figure 4. a) SEM cross-section images and b) current density–voltage (J–V) curves of a MAPbI$_3$ solar cell with a pristine (left) and with a pressed (right) PAD-processed absorber layer. c) Batch statistics (reverse direction) of solar cells fabricated with a pristine (red) and with a pressed (blue) absorber layer.

Table 1. Summary of solar cell metrics (mean values; individual champion values in brackets) for MAPbI₃ solar cells with pristine and with pressed PAD-processed absorber layer as extracted from reverse direction.

Type	V_{oc} [V]	J_{sc} [mA cm^{-2}]	FF [%]	PCE [%]
Pristine	0.90 ± 0.11 (0.96)	7.2 ± 3.1 (13.9)	52 ± 9 (49.5)	3.5 ± 1.8 (6.6)
Pressed	0.95 ± 0.04 (0.98)	7.6 ± 2.7 (11.2)	56 ± 6 (56.5)	4.1 ± 1.8 (6.2)

both types show an efficiency of >6% (see **Table 1** for a summary of the device metrics extracted from the reverse direction). Evidently, the additional pressing as posttreatment step results in a clearly increased number of devices with an efficiency of more than 6%.

Comparing these results with MAPbI₃ n–i–p solar cells that are solution-processed under ambient conditions with typical PCE values in the range of ≈15%,[49–53] it becomes clear that the V_{OC} values are in good agreement with literature values (0.85–1.10 V). While the FF values are at the lower end of the reported range (55%–75%), the obtained J_{sc} values are clearly below the literature values of around 21 mA cm^{-2}. Thus, the low J_{sc} values of our PAD-processed perovskite solar cells are the main limiting factor for the clearly lower PCE compared to corresponding solution-processed PSCs.

To better understand the origins of the losses and limitations in our PSCs with dry-processed MAPbI₃ film, in the following, we systematically investigate the device stack layer by layer, also deriving perspectives for strategies to optimize the PCE.

4. Detailed Evaluation of the Solar Cell Stack

4.1. SnO₂ Layer

First, we investigate the SnO₂ layer, acting as the ETL. To ensure proper electrical contact between the ETL and the MAPbI₃ film, sufficient physical contact and adhesion between both are mandatory. The physical contact is confirmed in the cross-section SEM image in **Figure 5**a. By scotch tape tests, we observe that the pristine MAPbI₃ film remains on the ETL after repeated applying and peeling off of a stripe of tape (Figure S11, Supporting Information), confirming good mechanical adhesion between ETL and perovskite film. On the peeled-off tape, only a marginal amount of MAPbI₃ powder is visible (Figure S11, Supporting Information), which stems from loose and uncompressed powder particles remaining on top of the film after PAD.

The ETL layer is subject to high mechanical and thermal stress during MAPbI₃ film deposition via PAD and pressing at elevated temperatures. During the deposition of the MAPbI₃ film via PAD, the accelerated perovskite powder particles impact on the ETL and potentially affect its electrical and optical properties. Similarly, the combination of pressure and temperature during hot-pressing may also alter the ETL properties.

To identify such potential changes in ETL properties, we carried out morphology characterizations and conductive atomic force microscopy (cAFM) for four different samples: 1) a native SnO₂ layer serving as reference, 2) a SnO₂ layer after removing a solution-processed MAPbI₃ film, 3) a SnO₂ layer after removing a pristine MAPbI₃ PAD film, and 4) a SnO₂ layer after removing a
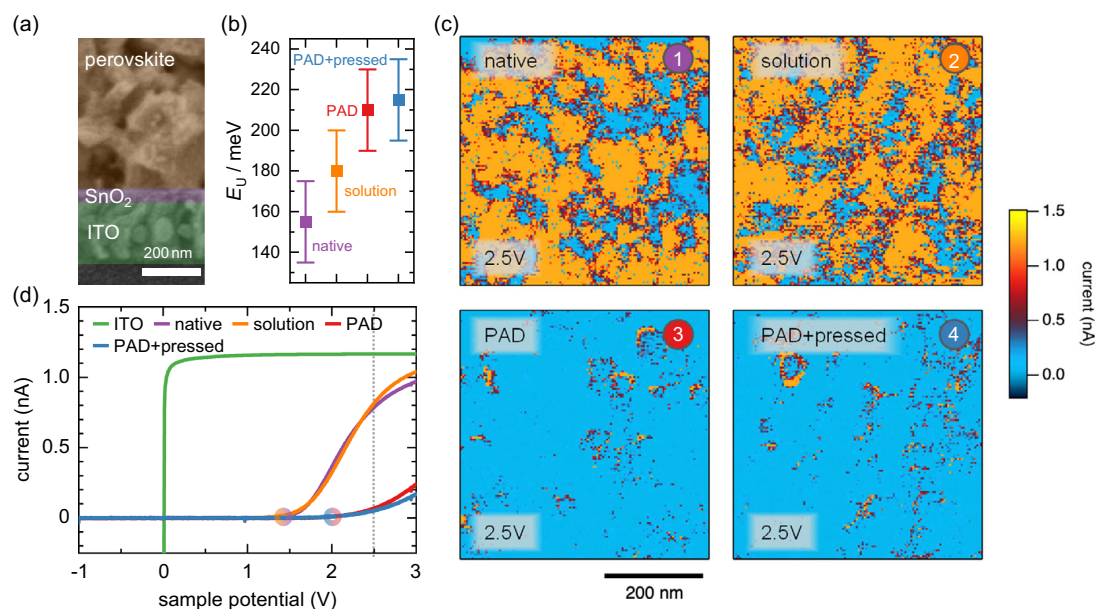
Figure 5. a) Cross-section SEM image of MAPbI₃ PAD film on indium tin oxide (ITO)/SnO₂. b) Urbach energy E_U of 1) a native SnO₂ layer serving as reference, 2) SnO₂ layer after removing a solution-processed MAPbI₃ film, 3) SnO₂ layer after removing a pristine MAPbI₃ PAD film, and 4) SnO₂ layer after removing a pressed MAPbI₃ PAD film. c) Conductive atomic force microscopy (cAFM) measurements at 2.5 V for the samples in (b). d) Current–voltage (I–V) characteristics for the samples in (c), averaged over the whole investigated area. For comparison, the I–V curve of an ITO layer is also shown.

pressed MAPbI$_3$ PAD film. The MAPbI$_3$ films were removed by dissolving them in dimethyl sulfoxide (DMSO).

First, we address possible changes in morphology and layer properties, where a reduction of the SnO$_2$ layer thickness or a fractioning of the grains within the layer might occur due to the PAD process. Here, height profiles of the four SnO$_2$ samples suggest that the SnO$_2$ layer thickness does not reduce due to the PAD process (see Figure S12, Supporting Information). Furthermore, no morphological changes between samples (1) and (4) are observed in atomic force microscopy (AFM) images (Figure S13, Supporting Information), suggesting that no lateral fractioning of the SnO$_2$ grains in the layer occurs.

In contrast to the morphology, the electrical properties of the ETL clearly change after the PAD deposition and pressing, as evident from cAFM measurements. At an applied potential of 2.5 V, the cAFM images (Figure 5c) show a decreased current for samples (3) and (4), compared to samples (1) and (2). This decreased current at 2.5 V is also reflected in corresponding I–V curves between −1 and 3 V (Figure 5d), where the current is averaged over the whole sampled areas in Figure 5c. Here, for samples (1) and (2), the onset potential is 1.4 V, compared to ≈2.0 V for samples (3) and (4), where also the steepness of the current rise appears lower compared to the corresponding steepness of samples (1) + (2). The latter observation suggests a lower electric conductivity in the ETLs that exhibited a prior PAD MAPbI$_3$ processing.

To better understand the origin of the decreased electrical conductivity of the PAD-treated SnO$_2$ layers, we conducted optical absorption measurements of all four SnO$_2$ samples in an integrating sphere, with a focus on investigating their Urbach absorption edge (Figure S14, Supporting Information). From the latter, we extract the so-called Urbach energy, a measure for the degree of energetic disorder within the investigated material.[54,55] Our analysis suggests that samples (3) + (4) exhibit E_U values in the range of ≈210 meV, compared to E_U values in the range of 160–180 meV for samples (1) + (2) (Figure 5b), indicating that indeed the PAD processing increases the energetic disorder and thus also the defect density of the SnO$_2$ ETL layer.

Here, increased disorder and defect density could result from the harsh impact of the MAPbI$_3$ powder particles and agglomerates on the SnO$_2$, where high mechanical stress might foster the formation of defects. Another aspect that could explain the increased disorder values for samples (3) + (4) is the incorporation of MAPbI$_3$ constituents into the SnO$_2$ layer. To investigate the latter aspect in more detail, we performed X-ray photoelectron spectroscopy (XPS) survey scans of all four samples, showing that lead species (signals at 138/143 and 414/436 eV) are present in samples (2)–(4) even after thorough removal of MAPbI$_3$ with DMSO (Figure S15, Supporting Information).[56,57] Here the Pb-concentration in samples (3) + (4) is ≈3–4 at%, twice as high as in sample (2). Interestingly, in all four samples we do not detect any iodine signals (619/631 eV).[56] This emphasizes that no iodo-plumbate residuals are present on the SnO$_2$ layer, but rather metallic lead remains in the SnO$_2$ layer.

The incorporation of various materials such as Sb, Cr, or Nb$_2$O$_5$ into SnO$_2$ is known to lead to increased E_U (i.e., energetic disorder), and to a shift of the onset potential toward higher values,[58–60] fully in line with the findings from Figure 5. Thus, we conclude that the incorporation of Pb into the SnO$_2$

layers that exhibited a PAD-process contributes to the observed reduced conductivity and increased onset potential.

It is also clear that the increase in disorder is at first closely linked to the PAD process method. However, this issue could be addressed in the future, e.g., with the help of defect-chemical approaches, where, for example, Ru- or Sb-doped SnO$_2$ could be used to compensate for the presence of the Pb-induced defects.[61,62]

To counteract a possible mechanically induced increase in disorder, the use of SnO$_2$ layers with a more robust morphology and potentially higher mechanical hardness appears promising. For example, it was shown that SnO$_2$ layers prepared by an e-beam process show remarkably compact morphologies and that sputtered SnO$_2$ layers, in contrast to other preparation methods, show higher hardness values of up to 14 GPa.[63] Furthermore, it could be demonstrated that SnON coatings resulting from the incorporation of nitrogen into SnO$_2$ can exhibit hardness values of up to 23 GPa while maintaining excellent electrical properties.[64]

These examples underline that, by choosing a suitable preparation method and introducing additional constituents, it appears possible to produce mechanically more robust and defect-chemically optimized SnO$_2$ layers that still feature desired electrical properties even after the harsh mechanical treatment during perovskite powder deposition by PAD.

4.2. Dry-Processed MAPbI$_3$ Absorber Layer

Next, we investigate the film properties of our pristine and pressed MAPbI$_3$ thin films.

We first addressed whether our anti-sticking silanization coating (molecular formula: C$_{18}$H$_{37}$Cl$_3$Si) is transferred to our MAPbI$_3$ films upon pressing. **Figure 6**a shows an XPS spectrum of a pressed perovskite film, where only peaks corresponding to MAPbI$_3$ constituents and in particular no signatures of Si are visible.[56,65,66] Thus, we conclude that no significant amount of silane is transferred to the perovskite film during our pressing process.

Concerning the morphology of both types of MAPbI$_3$ films, deposited with our modified PAD setup, corresponding cross-section SEM images show that the pristine film is dense and void free, with a surface roughness in the range of Ra ≈ 200 nm (Figure 4a left). The films exhibit a thickness of about 1 μm. While the perovskite film thickness of highly efficient solar cells often is below 1 μm, it was shown that a PCE of 20% can be achieved using MAPbI$_3$ films with thickness of about 1 μm, if the grain size is large thus the number of grain boundaries in vertical direction is low.[67] Cross-sectional SEM images of the pressed film demonstrate that hot-pressing increases the grain size, narrows grain boundaries, reduces surface roughness, and diminishes the number of pores (Figure 4a, right), indicating morphology improvements toward better PCE. These morphology improvements are fully consistent with the insights gained in Section 2.2 and 2.3., and can be associated to stem from a sintering effect occurring during hot-pressing.[27,68] From XPS measurements in a previous work, it is known that hot-pressing induces small amount of PbI$_2$ at the MAPbI$_3$ film surface.[28] However, in Figure S18, Supporting Information, the XRD
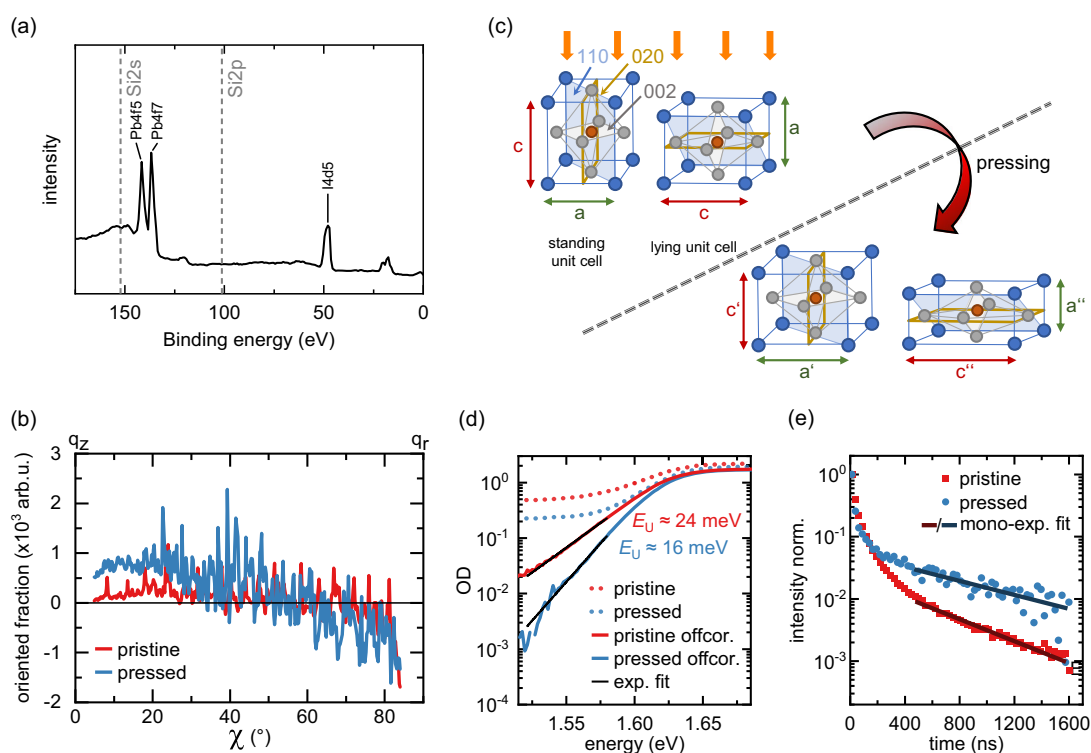
Figure 6. a) XPS spectrum of a MAPbI$_3$ PAD film after pressing. b) Oriented fraction of the (110) and (002) double peak as a function of χ for a pristine (red) and pressed (blue) MAPbI$_3$ film determined by grazing incidence wide-angle X-ray scattering (GIWAXS). c) Sketch of unit cell deformation due to hot-pressing as indicated by GIWAXS. d) Absorption spectra of a pristine and pressed MAPbI$_3$ film on glass as measured (dotted) and offset corrected (line). The Urbach energy E_U is extracted from an exponential fit for each sample. e) Time-resolved photoluminescence of a pristine and pressed MAPbI$_3$ film on glass, together with a mono-exponential fit.

spectra show only a negligible amount of PbI$_2$ for the pressed film, that is, all MAPbI$_3$ films are considered to be essentially phase pure.

To characterize the crystallographic orientation of the pristine and pressed MAPbI$_3$ films, we performed grazing incidence wide-angle X-ray scattering (GIWAXS). The corresponding 2D GIWAXS patterns of a pristine and a pressed MAPbI$_3$ film (Figure S16, Supporting Information) were examined using a χ analysis, that is, a reciprocal space analysis as a function of direction, on the (110) & (002) double peak (Figure 6b). Therefore, a semicircular cut over the full peak width of the (110) & (002) double peak was extracted (details in Figure S16, Supporting Information). Hereby, 90° corresponds to the direction along q_r (in-plane of the sample) and 0° corresponds to the direction along q_z (out-of-plane of the sample). The intensity distribution along the χ arc of the pristine film (red line in Figure 6b) shows a random (isotropic) orientation of the crystallites. In contrast, the intensity along χ deviates from the isotropic distribution for the pressed film (blue line in Figure 6b), indicating a preferred orientation particularly in q_z-direction (planes parallel to sample surface) due to hot-pressing.

A single pixel analysis within the χ arc (details in Figure S16 and S17, Supporting Information) indicates an overall increased

number of large crystallites in the pressed film, consistent with XRD patterns measured in Bragg–Brentano geometry of pristine and pressed PAD-processed MAPbI$_3$ films (Figure S18, Supporting Information). Here, a smaller reflex width is found for a pressed film compared to a pristine film, again suggesting larger crystallite sizes in the pressed film. Moreover, the XRD patterns provide information about the crystallographic orientation in out-of-plane direction, where a random orientation is found in pristine films, changing to a (110) & (020)-preferred orientation upon pressing.

To further understand the impact of hot-pressing on the lattice parameters, we examine deformations of the unit cell by analyzing the GIWAXS data along different directions. The (110) and the (002) plane show the strongest changes as a function of direction. Depending on whether the interplanar distance d is examined parallel to the substrate (Figure S19 left, Supporting Information) or perpendicular to the substrate (Figure S19 right, Supporting Information), the separation increases or decreases upon hot-pressing. The shift of the (002) lattice spacing to smaller values along q_z in combination with the shift of the (110) spacing to larger values along q_r indicates the compression of the standing unit cell along the c-axis and its elongation along the a-axis (Figure 6c). Analogously, the change of the (002)

229

ADVANCED
SCIENCE NEWS
www.advancedsciencenews.com

Solar
RRL
www.solar-rrl.com

spacing to larger values along q_r, in combination with the shift of the (110) spacing to smaller values along q_z, indicates the compression of lying unit cells along the a-axis and their elongation along the c-axis (sketch in Figure 6c). Thus, the unit cells are flattened by pressing.

Overall, the analysis of the GIWAXS and XRD measurements suggest a compression of standing and lying MAPbI$_3$ unit cells, as well as an increase in (110)- and (020)-preferred orientation parallel to the substrate by hot-pressing. Such an increase in preferred orientation is known to correlate with improved excited-state properties.[28]

Thus, in the following, we analyze how the identified morphology differences between the pristine and pressed MAPbI$_3$ films are reflected in their optoelectronic properties. Figure 6d shows the optical absorption spectra of a pristine (red dotted line) and pressed (blue dotted line) MAPbI$_3$ film on glass with the typical absorption edge around 1.59 eV.[69,70] The absorption intensity for photon energies below the absorption edge is due to optical scattering, which we find to be strongly reduced for the pressed film compared to the pristine film. This indicates a more uniform morphology of the pressed film, in line with the previously identified higher compaction after hot-pressing. The Urbach energy, E_U, extracted from exponential fits to the offset corrected spectra, clearly reduces from (24.3 ± 0.2) meV for the pristine film to (15.5 ± 0.2) meV for the pressed film (see also Figure S20, Supporting Information), where the latter E_U value is in line with typical Urbach energies of solution-processed MAPbI$_3$ films.[55,71,72] The reduction of the Urbach energy upon pressing suggests less energetic disorder and a reduction in associated defect density in the pressed film.[73–75]

To examine differences in defect density between the PAD-processed films in more detail, we measured time-resolved photoluminescence (TRPL) decay curves after laser excitation (Figure 6e). Here, we considered pristine (red squares) and pressed (blue dots) MAPbI$_3$ films deposited on glass to exclude any impact of charge recombination processes at the perovskite/ETL interface. Compared to the pristine film, the pressed film shows a slower decrease of the TRPL intensity at times longer than 200 ns. By fitting the tail of the TRPL curves after 400 ns with a mono-exponential function (lines in Figure 6e), we extracted the defect-associated nonradiative decay rates k_1 according to

$$PL(t) \propto A_1 \times \exp(-2 \times k_1 \times t) \qquad (1)$$

By doing so, we find k_1 values of $(10.1 \pm 0.3) \times 10^5$ and $(6.5 \pm 0.6) \times 10^5 \, \mathrm{s}^{-1}$ for the pristine and the pressed film, respectively. Thus, our films exhibit k_1 values similar to typical values of solution-processed MAPbI$_3$ films.[76,77] The decrease in defect-associated decay rate upon pressing transfers to an increase in charge-carrier lifetime from (493 ± 15) ns for the pristine film to (768 ± 66) ns for the pressed film, indicating less defects being present in pressed films.

Overall, our characterizations of the pristine and pressed PAD-processed MAPbI$_3$ films prove that they exhibit suitable morphology and optoelectronic properties for solar cell application, in particular when the films are posttreated by pressing.

4.3. Perovskite-Transport Layer Interfaces

Having verified the satisfactory optoelectronic and morphological properties of the PAD-processed MAPbI$_3$ films, we finally evaluate the interface between the perovskite film and both charge-transport layers (ETL and HTL).

By light-intensity-dependent J–V measurements and corresponding analysis of the solar cell metrics, Glowienka et al. in detail investigated the electrical functionality of the perovskite/ETL and perovskite/HTL interfaces. Together with drift-diffusion modeling, they succeeded in pinpointing the dominating performance limiting effects in their perovskite solar cells.[78]

Following this approach, we measured the J–V curves for the pristine (red triangles) and pressed (blue dots) PAD-processed MAPbI$_3$ solar cells. We then compared the light dependency of the measured solar cell metrics with the expectations from Glowienka et al. for an ideal (i.e., without any recombination processes) and a more realistic (i.e., including perovskite bulk and interface recombination) perovskite solar cell. **Figure 7**a shows the experimentally determined light-intensity-dependent FF and V_{oc} of our devices, while in Figure 7b, the corresponding expectations from Glowienka et al. are shown.

For our devices with pristine and pressed absorber layer, the FF increases in the light intensity range from 10^{-3} to 10^{-1} sun. In contrast to the devices with pressed MAPbI$_3$ film where the FF monotonously increases, the FF of the devices with pristine MAPbI$_3$ film decreases again for light intensities above 10^{-1} sun. Overall, the pristine devices exhibit lower FF values over the whole measurement range. For an ideal device, the FF is expected to be independent of the light intensity, while including interface recombination, the FF is expected to exhibit a maximum. Furthermore, the presence of perovskite bulk recombination lowers the FF.[78] Comparing our experimental results with the theoretical expectations, it thus becomes clear that the light dependence of the FF in our case fits best to the theoretical expectations including interface recombination. Therefore, we conclude that in our PAD-processed solar cells interface recombination processes are present, limiting the overall device efficiency. Furthermore, the decrease of the FF for pristine devices above 10^{-1} sun indicates an increased interface recombination compared to pressed devices.[78] Furthermore, the overall lower FF values of the pristine devices compared to the pressed devices suggest more nonradiative recombination in the perovskite bulk of the pristine absorber layers, consistent with the higher nonradiative recombination rate k_1 found in the transient PL measurements (Figure 6e).

The V_{oc} for ideal device is expected to show a linear dependence on the light intensity in a semilogarithmic plot and a deviation at high intensities when interface recombination is present. For our pristine devices, we observe this deviation from the linear dependence for light intensities above 10^{-1} sun, further supporting that more pronounced interface recombination is present in the pristine devices than in the pressed devices.

To identify if monomolecular (trap-assisted, nonradiative) or bimolecular (band to band, radiative) recombination predominantly takes place at the interfaces, we determined the ideality factor n and the inverse Langevin recombination factor α from
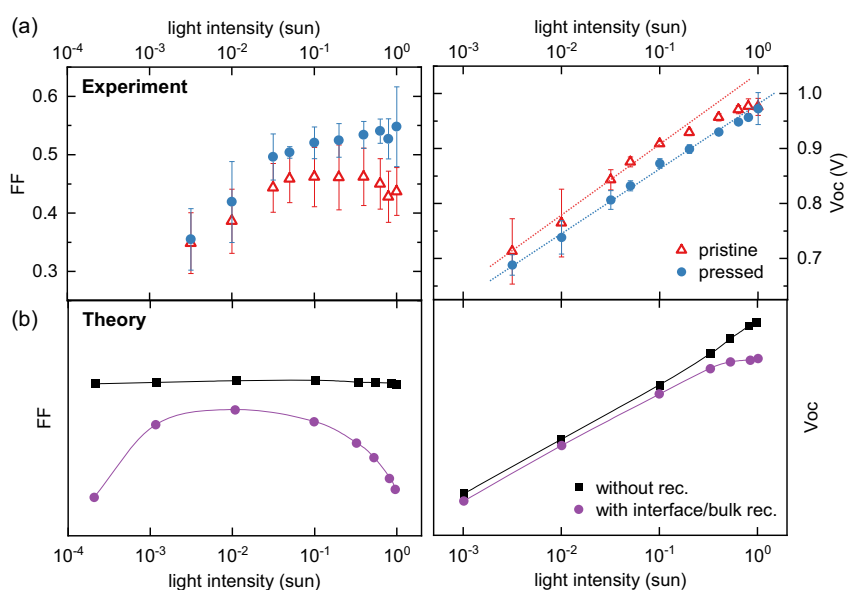
Figure 7. a) Measured light-intensity dependence of the fill factor (FF) (left) and the open-circuit voltage (V_{oc}) (right) for pristine (red triangles) and pressed (blue dots) MAPbI$_3$ absorber layers. b) Theoretical expectations for FF (left) and the V_{oc} (right) of ideal devices without any recombination (black squares) and of devices with recombination (purple circles), after Glowienka et al.[78] The lines in (a,b) serve as guide for the eye.

the V_{oc} versus J_{sc} plot and the J_{sc} versus light intensity plot, respectively (Figure S21, Supporting Information). In general, the ideality factor n ranges between values of 1 and 2, where a value of 1 is expected for ideal solar cells in which only bulk recombination occurs.[79] Deviations from 1 indicate energy misalignment and trap-assisted recombination at the interfaces.[80,81] We find values of $n \approx 2$ for all measured cells, which suggests trap-assisted monomolecular recombination as the dominant recombination mechanism at the interfaces in our case.

Theoretically expected values for α range from 0.5 to 1, with a value of 0.5 indicating pure bimolecular recombination and values close to 1 suggesting monomolecular recombination as the dominant recombination process. Thus, the extracted α values of ≈ 0.9 for our solar cells further support trap-assisted recombination being the dominant recombination mechanism at the interface.[82,83] This is consistent with the observed hysteresis in the J–V curves (Figure 4b) indicating an accumulation of ions at the interface, screening the internal electric field and promoting recombination there.[84]

Summing up the light-intensity-dependent investigations of the PAD-processed solar cells, we conclude that recombination losses at the interfaces between perovskite and charge-carrier extraction layers are present in our devices, likely contributing to their limited PCE. On the basis of our analyses, it is not possible to distinguish which interface (i.e., whether the perovskite/ETL or the perovskite/HTL interface) is predominantly responsible for the recombination losses. However, due to the alteration of the SnO$_2$ layer upon perovskite deposition via PAD discussed in Section 4.1, it is conceivable that the identified interface recombination losses mainly originate from the ETL/perovskite interface.

However, another aspect that might contribute to significant interface recombination and thus limit current values in our devices is the presence of hydrates at the transport layer/perovskite interface. The processing of the ETL and the perovskite, including pressing, was carried out under ambient conditions (relative humidity: 40%–50%), that is, within a humidity range, where the formation of monohydrates at the perovskite surface is known to happen.[85] And indeed the formation of hydrates on the perovskite film in our case can already be conjectured from the grey tarnishing perovskite surface after PAD processing (Figure 3b). It was shown that hydrates are mainly formed at the surface and the grain boundaries of the perovskite, where they act as defects within the perovskite film and the interface.[85,86] Thus, the presence of hydrates lead to additional pathways for charge recombination, reducing charge extraction from the perovskite to the transport layer. This is in line with the generally low current density of our PAD-processed devices.[87,88] Furthermore, the presence of hydrates also reduces the barrier for ion migration,[89] facilitating hysteresis in J–V curves of corresponding PSCs,[90] which is also fully consistent with our results in Section 3. Thus, we presume that the presence of hydrates also contributes considerably to the limited performance and pronounced hysteresis of the PAD-processed solar cells.

5. Conclusion and Perspective

We have successfully manufactured the first solar cells containing a completely dry-processed powder-based MAPbI$_3$ absorber layer. These absorber layers were deposited via PAD, where necessary key modifications such as the use of an ejector and an

inertial separator unit were introduced into our setup, resulting in dense and void-free MAPbI$_3$ films with thicknesses of $\approx$1 µm.

The solar cells are fully working with champion device efficiencies >6% in backward direction. Here, the V_{oc} (0.95 V) values, and to some extent also the FF values (56%) match literature values of cells processed from solution under ambient conditions. However, in addition to a pronounced hysteresis between the J–V sweep directions, especially the low J_{sc} values (7.6 mA cm^{-2}) limit the overall efficiency of our powder-processed devices.

We systematically analyzed our solar cell stacks and found that the pristine MAPbI$_3$ films show well-suited morphology and optoelectronic properties for solar cell application. The film properties further improve by posttreatment via (hot-)pressing, leading to increased grain size, crystallinity, crystallographic orientation, compaction, reduced surface roughness, and energetic disorder, as well as a longer charge-carrier lifetime, making the optoelectronic functionality of the optimized PAD-processed MAPbI$_3$ films to be on par with their typical solution-processed counterparts.

While the harsh mechanical impact of the MAPbI$_3$ powder particles in the course of the PAD process appears to not alter the SnO$_2$ layer thickness and its morphology, cAFM characterizations show a clearly reduced electrical functionality, that is, an increase of the onset potential for electrical conduction and a decreased overall conductivity. Here, absorption measurements indicate that the PAD processing increases the disorder of the SnO$_2$ layer. This increase could be associated to an increase in defect density within the SnO$_2$ due to the high mechanical impact, and/or the incorporation of metallic Pb into the SnO$_2$ (as suggested by XPS investigations).

Furthermore, analyzing light-intensity-dependent J–V measurements, we find that recombination at the interfaces between the perovskite and charge-transport layers also contributes to the limited performance of the PAD-processed solar cells.

Here, it appears plausible that the formation of hydrates at the perovskite surfaces, which lowers the barrier for ion migration associated to a more pronounced hysteresis, is a major contributing aspect, since the perovskite processing and posttreatment of our films happen under ambient conditions.

In summary, our work successfully demonstrates that it is possible to produce PSCs with completely dry-processed absorber layer based on perovskite powders. As we could pinpoint the main performance-limiting aspects to be associated with the presence of hydrates at the perovskite surface and the deterioration of the electrical properties of the SnO$_2$ layer due to the PAD process, optimized preparation methods and defect engineering of the SnO$_2$ layer, as well as moving all processing steps into a dry atmosphere and using passivated powders, represent important optimization strategies to reduce hysteresis and to improve overall device performance. Based on the various approaches already presented in the literature, we are thus confident that the current hurdles to optimize the efficiency of PAD-processed perovskite solar cells will be successfully overcome in the future.

6. Experimental Section

Powder Synthesis: For the mechanochemical synthesis of MAPbI$_3$, 1.9 g of the methylammonium iodide (MAI) reactant powder and 5.509 g of PbI$_2$

(99%, Acros Organics) were added to 80 mL ZrO$_2$ milling jars under ambient conditions. Then, 8 mL cyclohexane as a milling agent and 25 ZrO$_2$ milling balls with a diameter of 10 mm were added to the milling jar. A Fritsch "Pulverisette 5" planetary ball mill with 400 rpm was used for synthesis. After 5 min of milling, a pause of 20 min was implemented to prevent excessive heating of the milling jar. The process was repeated until a total milling time of 50 min was achieved. Afterward, the cyclohexane was evaporated in air and the obtained black MAPbI$_3$ powder was sieved using a mesh size of 63 µm.

Solar Cell Fabrication: Substrate Preparation and ETL: Substrates were cleaned in an ultrasonic bath with soap water (Hellmanex), deionized water, acetone, and isopropanol and treated with UV–ozone. SnO$_2$ nanoparticles (Alfa Aesar 15% in H$_2$O) were spin-coated onto the clean substrate at 3000 rpm for 30 s and the substrates were annealed at 180 °C for 30 min and again UV–ozone treated prior to perovskite deposition.

Solar Cell Fabrication: Perovskite Film Deposition: MAPbI$_3$ films were produced via PAD method using a custom-made apparatus. Prior to deposition, the mechanochemically synthesized MAPbI$_3$ powder was dried for at least 1 h at 120 °C. For each film, 1 g of the dried powder was filled into the aerosol generation unit. Using helium as a processing gas, 0.25 L min^{-1} were passed through the unit to generate the aerosol while the ejector was fed with 20 L min^{-1} to enhance acceleration of the aerosol through the converging slit nozzle with orifice size of 10 × 0.5 mm. The substrate to nozzle distance was set to 3 mm. The substrate was moved past the nozzle 30 times at a velocity of 1 mm s^{-1}. During deposition, a pressure of 122 mbar resulted in the aerosol generation unit and 6 mbar in the deposition chamber (for details about chosen PAD process parameters, as well as a discussion about lead safety considerations for the PAD, see Section S1, Supporting Information). The MAPbI$_3$ films for untreated devices were blown off with nitrogen before the HTL layer was applied to remove the loose MAPbI$_3$ particles on the surface.

Solar Cell Fabrication: HTL and Back Contact: Spiro-MeOTAD (Sigma Aldrich) solutions (72.5 mg mL^{-1} in chlorobenzene (CB), 17.5 mL Li-TFSI [520 mg mL^{-1} in acetonitrile], 42.5 mL tBP) were spin-coated at 3000 rpm for 30 s onto the perovskite film. Finally, 100 nm gold was thermally evaporated onto the substrates as back contact which results in active area of 12.5 mm^2 for each solar cell.

Solar Cell Fabrication: Pressing: Pristine MAPbI$_3$ PAD films were hot-pressed with a homebuilt manual press (details on press setup in previous work).[28] The films were pressed with 25 MPa at 120 °C for 5 min (at target levels). For optimum pressing results, loose powder particles and agglomerates on the pristine PAD films were removed by means of a nitrogen gun before the pressing process. The glass blocks used as press die were treated with an anti-sticking coating (trichloro(octadecyl)silane in toluene from liquid phase) to prevent the pressed film from sticking.

Solar Cell Characterization: The J–V curves were obtained using an ORIEL Sol2A (Newport) solar simulator with a calibrated AM 1.5 G spectrum in combination with a Keithley 2400 sourcemeter and an aperture mask of 10 mm^2. The scan rate for all measurements was set to 150 mV s^{-1}. For the light-intensity-dependent measurements different neutral density filters were placed above the devices to reduce the light intensity.

Absorption: Absorption spectra were recorded using a Cary 5000 (Varian) equipped with an integrating sphere in reflection mode.

TRPL: For TRPL curves, time-correlated single-photon counting (TCSPC) measurements were performed with a PicoQuant MT200 confocal fluorescence microscope in combination with a PMA Hybrid PMT 40 photomultiplier tube (PicoQuant) and a TimeHarp 260 Pico TCSPC board (PicoQuant). The samples were excited with a 560 nm diode Laser (PicoQuant LDH-D-TA-560) with a frequency of 2.0 MHz and a pulse width of 68 ps. The laser beam was focused on the sample with an Olympus Objective with 4× magnification and the emission was filtered with a 561 nm long-pass filter before detection. The excitation fluence was set to 300 nJ cm^{-2}.

AFM: AFM was performed using a dimension ICON-GB system, equipped with a Nanoscope V controller (Bruker Corp., USA). The AFM unit was located in a glove box under argon atmosphere (water < 5 ppm; oxygen < 0.1 ppm). Multidimensional IV-Spectroscopy images were

**ADVANCED
SCIENCE NEWS**

www.advancedsciencenews.com

Solar
RRL

www.solar-rrl.com

obtained using the DataCube-TUNA mode of the measurement system in combination with the PF-TUNA application module. We used a conductive NSC14/Cr-Au Probe from MikroMasch for nanoscale electrical characterization (calibrated spring constant via Sader: $6.9 \, N \, m^{-1}$). The applied loading force for I–V measurements was 100 nN and the sample bias voltage was swept from -1 to 3 V. The maximum current was limited to ± 1.3 nA. Data processing and visualization of multidimensional AFM data was performed using Igor Pro (Wavemetrics Inc., USA). Additional AFM topography images (Supporting Information) were recorded under ambient conditions in TappingMode, using an AC160TS-R3 probe (Olympus Corp., Japan) with a nominal resonance frequency of 300 kHz.

GIWAXS: GIWAXS experiments were conducted at the beamline 7.3.3 at the Advanced Light Source at Lawrence Berkeley National Lab (Berkeley, USA).[91] The samples were illuminated with 10 keV radiation ($\lambda = 1.24$ Å) at an incident angle (α_i) of 0.25° at room temperature. The beam size was 300 µm (height) $\times$ 700 µm (width). The scattering signal was captured on a Pilatus 2M (172 µm pixel size, file format EDF, 1475×1679 pixels) located 274 mm from the sample. Acquisition times were 10 s for each frame. After correction for Ewald-sphere curvature with Xi-CAM,[92] the 2D data was reduced to 1D horizontal and vertical cuts using customized Python scripts. The software DPDAK (v1.4.1)[93] was used for Chi-integration. To track scattering peak parameters, the 1D intensity profiles were fitted with Gaussians and a local background using a Trust-Region-Reflective Least Squares algorithm.

X-Ray Diffraction: A Bruker "D8 Discover A25" with Cu-K$_{\alpha1}$ radiation ($\lambda = 0.15406$ nm) and Ge-K$_{\alpha1}$ monochromator in reflection mode was used to acquire XRD patterns with a 2θ step size of 0.008° in the 2θ range from 10° to 45° under ambient conditions. The X-ray source was operated with 40 kV and 40 mA.

Film Thickness and Surface Roughness: The film thickness and surface roughness Ra of the (pressed) PAD films were measured using either an LSM 900 M (Carl Zeiss AG) laser scanning microscope with a 405 nm laser or using a profilometer (Dektak 150, Veeco).

SEM: The film morphology was characterized by SEM using a Zeiss Leo 1530 instrument FE-SEM with Schottky-field-emission cathode, In-lens detector, and SE2 detector. The accelerating voltage was 3 kV. Prior to measurement, the samples were sputtered with 2 nm platinum.

XPS: XPS measurements were carried out with a Versa Probe III photoelectron spectrometer (PHI). The excitation was provided by an Al Kα source ($h\nu = 1486.6$ eV) at a pass energy of 224 eV to achieve high sensitivity. The X-ray beam had a diameter of 100 µm and a power of 25 W. Ion (Ar$^+$) and electron neutralization was applied to the sample to avoid charging-induced energy shifts.

Supporting Information

Supporting Information is available from the Wiley Online Library or from the author.

Conflict of Interest

The authors declare no conflict of interest.

Data Availability Statement

The data that support the findings of this study are available from the corresponding author upon reasonable request.

[1] NREL, Best Research-Cell Efficiency Chart **2023**, https://www.nrel.gov/pv/cell-efficiency.html (accessed: April 2023).

[2] J. Jeong, M. Kim, J. Seo, H. Lu, P. Ahlawat, A. Mishra, Y. Yang, M. A. Hope, F. T. Eickemeyer, M. Kim, Y. J. Yoon, I. W. Choi, B. P. Darwich, S. J. Choi, Y. Jo, J. H. Lee, B. Walker, S. M. Zakeeruddin, L. Emsley, U. Rothlisberger, A. Hagfeldt, D. S. Kim, M. Grätzel, J. Y. Kim, *Nature* **2021**, *592*, 381.

[3] Q. Cao, Y. Li, H. Zhang, J. Yang, J. Han, T. Xu, S. Wang, Z. Wang, B. Gao, J. Zhao, X. Li, X. Ma, S. M. Zakeeruddin, W. E. I. Sha, X. Li, M. Grätzel, *Sci. Adv.* **2021**, *7*, eabg0633.

[4] Y. Zhao, T. Heumueller, J. Zhang, J. Luo, O. Kasian, S. Langner, C. Kupfer, B. Liu, Y. Zhong, J. Elia, A. Osvet, J. Wu, C. Liu, Z. Wan, C. Jia, N. Li, J. Hauch, C. J. Brabec, *Nat. Energy* **2022**, *7*, 144.

[5] H. Li, J. Zhou, L. Tan, M. Li, C. Jiang, S. Wang, X. Zhao, Y. Liu, Y. Zhang, Y. Ye, W. Tress, C. Yi, *Sci. Adv.* **2022**, *8*, eabo7422.

[6] J. Li, H. Wang, X. Y. Chin, H. A. Dewi, K. Vergeer, T. W. Goh, J. W. M. Lim, J. H. Lew, K. P. Loh, C. Soci, T. C. Sum, H. J. Bolink, N. Mathews, S. Mhaisalkar, A. Bruno, *Joule* **2020**, *4*, 1035.

[7] S. Biberger, K. Schötz, P. Ramming, N. Leupold, R. Moos, A. Köhler, H. Grüninger, F. Panzer, *J. Mater. Chem. A* **2022**, *10*, 18038.

[8] K. Schötz, C. Greve, A. Langen, H. Gorter, I. Dogan, Y. Galagan, A. J. J. M. van Breemen, G. H. Gelinck, E. M. Herzig, F. Panzer, *Adv. Opt. Mater.* **2021**, *9*, 2101161.

[9] O. Telschow, M. Albaladejo-Siguan, L. Merten, A. D. Taylor, K. P. Goetz, T. Schramm, O. V. Konovalov, M. Jankowski, A. Hinderhofer, F. Paulus, F. Schreiber, Y. Vaynzof, *J. Mater. Chem. A* **2022**, *10*, 19743.

[10] K. P. Goetz, Y. Vaynzof, *ACS Energy Lett.* **2022**, *7*, 1750.

[11] W. Massmann, *Occup. Environ. Med.* **1956**, *13*, 51.

[12] G. L. Kennedy, *Drug Chem. Toxicol.* **1986**, *9*, 147.

[13] D. Liu, C. J. Traverse, P. Chen, M. Elinski, C. Yang, L. Wang, M. Young, R. R. Lunt, *Adv. Sci.* **2018**, *5*, 1700484.

[14] X. Cao, G. Zhang, Y. Cai, L. Jiang, X. He, Q. Zeng, J. Wei, Y. Jia, G. Xing, W. Huang, *Sol. RRL* **2020**, *4*, 2000008.

[15] S. Öz, J. Burschka, E. Jung, R. Bhattacharjee, T. Fischer, A. Mettenbörger, H. Wang, S. Mathur, *Nano Energy* **2018**, *51*, 632.

[16] H.-S. Kim, Y.-J. An, J. I. Kwak, H. J. Kim, H. S. Jung, N.-G. Park, *ACS Energy Lett.* **2022**, *7*, 1154.

[17] A. These, N. H. Khansur, O. Almora, L. Luer, G. J. Matt, U. Eckstein, A. Barabash, A. Osvet, K. G. Webber, C. J. Brabec, *Adv. Electron. Mater.* **2021**, *7*, 2001165.

[18] M.-Y. Cho, S. Kim, I.-S. Kim, E.-S. Kim, Z.-J. Wang, N.-Y. Kim, S.-W. Kim, J.-M. Oh, *Adv. Funct. Mater.* **2020**, *30*, 1907449.

[19] N. Leupold, A. L. Seibel, R. Moos, F. Panzer, *Eur. J. Inorg. Chem.* **2021**, *2021*, 2882.

[20] K. Naoe, M. Nishiki, A. Yumoto, *J. Therm. Spray Technol.* **2013**, *22*, 1267.

[21] H. S. Ryu, T. S. Lim, J. Ryu, S.-H. Hong, *J. Electrochem. Soc.* **2012**, *160*, C42.

[22] J.-Y. Park, K.-A. Lee, S.-H. Kim, G.-S. Ham, *Arch. Metall. Mater.* **2017**, *62*, 2017.

[23] J.-H. Park, D.-S. Park, B.-D. Hahn, J.-J. Choi, J. Ryu, S.-Y. Choi, J. Kim, W.-H. Yoon, C. Park, *Ceram. Int.* **2016**, *42*, 3584.

[24] M. Schubert, D. Hanft, T. Nazarenus, J. Exner, M. Schubert, P. Nieke, P. Glosse, N. Leupold, J. Kita, R. Moos, *Funct. Mater. Lett.* **2019**, *12*, 1930005.

[25] J. Akedo, *J. Ceram. Soc. Jpn.* **2020**, *128*, 101.

[26] F. Panzer, D. Hanft, T. P. Gujar, F.-J. Kahle, M. Thelakkat, A. Köhler, R. Moos, *Materials* **2016**, *9*, 277.

[27] C. Witt, A. Schmid, N. Leupold, M. Schultz, J. Höcker, A. Baumann, R. Moos, F. Panzer, *ACS Appl. Electron. Mater.* **2020**, *2*, 2619.

[28] C. Witt, K. Schötz, M. Kuhn, N. Leupold, S. Biberger, P. Ramming, F.-J. Kahle, A. Köhler, R. Moos, E. M. Herzig, F. Panzer, *J. Phys. Chem. C* **2023**, *127*, 10563.

[29] P. Ramming, N. Leupold, K. Schötz, A. Köhler, R. Moos, H. Grüninger, F. Panzer, *J. Mater. Chem. C* **2021**, *9*, 11827.

[30] S. Shrestha, R. Fischer, G. J. Matt, P. Feldner, T. Michel, A. Osvet, I. Levchuk, B. Merle, S. Golkar, H. Chen, S. F. Tedde, O. Schmidt, R. Hock, M. Rührig, M. Göken, W. Heiss, G. Anton, C. J. Brabec, *Nat. Photonics* **2017**, *11*, 436.

[31] W. A. Dunlap-Shohl, T. Li, D. B. Mitzi, *ACS Appl. Energy Mater.* **2019**, *2*, 5083.

[32] W. Kim, M. S. Jung, S. Lee, Y. J. Choi, J. K. Kim, S. U. Chai, W. Kim, D.-G. Choi, H. Ahn, J. H. Cho, D. Choi, H. Shin, D. Kim, J. H. Park, *Adv. Energy Mater.* **2018**, *8*, 1702369.

[33] A. Mayer, M. Buchmüller, S. Wang, C. Steinberg, M. Papenheim, H.-C. Scheer, N. Pourdavoud, T. Haeger, T. Riedl, *J. Vac. Sci. Technol. B* **2017**, *35*, 06G803.

[34] J. Xiao, Y. Yang, X. Xu, J. Shi, L. Zhu, S. Lv, H. Wu, Y. Luo, D. Li, Q. Meng, *J. Mater. Chem. A* **2015**, *3*, 5289.

[35] N. Leupold, K. Schötz, S. Cacovich, I. Bauer, M. Schultz, M. Daubinger, L. Kaiser, A. Rebai, J. Rousset, A. Köhler, P. Schulz, R. Moos, F. Panzer, *ACS Appl. Mater. Interfaces* **2019**, *11*, 30259.

[36] N. Leupold, P. Ramming, I. Bauer, C. Witt, J. Jungklaus, R. Moos, H. Grüninger, F. Panzer, *Eur. J. Inorg. Chem.* **2023**, *26*.

[37] J. Akedo, *J. Therm. Spray Technol.* **2008**, *17*, 181.

[38] D. Hanft, J. Exner, M. Schubert, T. Stöcker, P. Fuierer, R. Moos, *J. Ceram. Sci. Tech.* **2015**, *6*, 147.

[39] F. S. Kong, Y. Z. Jin, H. D. Kim, *Shock Waves* **2016**, *26*, 771.

[40] B. A. Nejand, V. Gharibzadeh, V. Ahmadi, H. R. Shahverdi, *Sci. Rep.* **2016**, *6*, 33649.

[41] L. Huang, Z. Xing, X. Tang, D. Li, X. Meng, X. Hu, T. Hu, Y. Chen, *J. Mater. Chem. A* **2021**, *9*, 16178.

[42] Y. Yu, M. Shang, T. Wang, Q. Zhou, Y. Hao, Z. Pang, D. Cui, G. Lian, X. Zhang, S. Han, *J. Mater. Chem. C* **2021**, *9*, 15056.

[43] A. Mayer, N. Pourdavoud, Z. Doukkali, K. Brinkmann, J. Rond, J. Staabs, A.-C. Swertz, F. van gen Hassend, P. Görrn, T. Riedl, H.-C. Scheer, *Appl. Phys. A* **2021**, *127*, 237.

[44] J. Moon, S. Kwon, M. Alahbakhshi, Y. Lee, K. Cho, A. Zakhidov, M. J. Kim, Q. Gu, *ACS Appl. Mater. Interfaces* **2021**, *13*, 5368.

[45] T. Zhang, L. Zhang, G. Zhu, D. Cui, Q. Wang, G. Lian, Z. Zheng, H. Yu, *Adv. Mater. Interfaces* **2022**, *9*, 2200447.

[46] C. Qu, J. Hu, X. Liu, Z. Li, Y. Ding, *Materials* **2017**, *10*, 1329.

[47] T. Li, A. M. Zeidell, G. Findik, W. A. Dunlap-Shohl, J. Euvrard, K. Gundogdu, O. D. Jurchescu, D. B. Mitzi, *Chem. Mater.* **2019**, *31*, 4267.

[48] H. Chen, F. Ye, W. Tang, J. He, M. Yin, Y. Wang, F. Xie, E. Bi, X. Yang, M. Grätzel, L. Han, *Nature* **2017**, *550*, 92.

[49] G. Jang, H.-C. Kwon, S. Ma, S.-C. Yun, H. Yang, J. Moon, *Adv. Energy Mater.* **2019**, *9*, 1901719.

[50] R. Herckens, W. T. M. V. Gompel, W. Song, M. C. Gélvez-Rueda, A. Maufort, B. Ruttens, J. D'Haen, F. C. Grozema, T. Aernouts, L. Lutsen, D. Vanderzande, *J. Mater. Chem. A* **2018**, *6*, 22899.

[51] J. Su, H. Cai, X. Ye, X. Zhou, J. Yang, D. Wang, J. Ni, J. Li, J. Zhang, *ACS Appl. Mater. Interfaces* **2019**, *11*, 10689.

[52] C. Du, S. Wang, X. Miao, W. Sun, Y. Zhu, C. Wang, R. Ma, *Beilstein J. Nanotechnol.* **2019**, *10*, 2374.

[53] Z. Guo, L. Gao, Z. Xu, S. Teo, C. Zhang, Y. Kamata, S. Hayase, T. Ma, *Small* **2018**, *14*, 1802738.

[54] G. D. Cody, T. Tiedje, B. Abeles, B. Brooks, Y. Goldstein, *Phys. Rev. Lett.* **1981**, *47*, 1480.

[55] M. Ledinsky, T. Schönfeldová, J. Holovský, E. Aydin, Z. Hájková, L. Landová, N. Neyková, A. Fejfar, S. De Wolf, *J. Phys. Chem. Lett.* **2019**, *10*, 1368.

[56] J. Rodriguez-Pereira, J. Tirado, A. F. Gualdrón-Reyes, F. Jaramillo, R. Ospina, *Surf. Sci. Spectra* **2020**, *27*, 024003.

[57] M. J. Bozack, K. W. Bryant, *Surf. Sci. Spectra* **1992**, *1*, 324.

[58] S. B. O. dos Santos, M. H. Boratto, R. A. Ramos, L. V. A. Scalvi, *Mater. Chem. Phys.* **2022**, *278*, 125571.

[59] S. Tominc, A. Rečnik, Z. Samardžija, G. Dražić, M. Podlogar, S. Bernik, N. Daneu, *Ceram. Int.* **2018**, *44*, 1603.

[60] H. Zhao, W. Liang, F. Wang, Y. Zhou, Q. Xie, *Results Phys.* **2020**, *18*, 103314.

[61] Y. Bai, Y. Fang, Y. Deng, Q. Wang, J. Zhao, X. Zheng, Y. Zhang, J. Huang, *ChemSusChem* **2016**, *9*, 2686.

[62] S. Akin, *ACS Appl. Mater. Interfaces* **2019**, *11*, 39998.

[63] J. Chen, S. J. Bull, *J. Phys. Appl. Phys.* **2008**, *41*, 074009.

[64] H. J. Gwon, N.-R. Kang, Y. Lee, S. O. Won, H. J. Chang, J.-W. Choi, C.-Y. Kang, S. K. Kim, B. Kwon, J.-Y. Kim, J.-S. Kim, S.-H. Baek, *Chem. Mater.* **2016**, *28*, 7051.

[65] G. M. Ingo, N. Zacchetti, D. della Sala, C. Coluzza, *J. Vac. Sci. Technol. Vac. Surf. Films* **1989**, *7*, 3048.

[66] A. Mesarwi, A. Ignatiev, *Surf. Sci.* **1991**, *244*, 15.

[67] Z. Liu, L. Qiu, E. J. Juarez-Perez, Z. Hawash, T. Kim, Y. Jiang, Z. Wu, S. R. Raga, L. K. Ono, S. (Frank) Liu, Y. Qi, *Nat. Commun.* **2018**, *9*, 3880.

[68] S. Deumel, A. van Breemen, G. Gelinck, B. Peeters, J. Maas, R. Verbeek, S. Shanmugam, H. Akkerman, E. Meulenkamp, J. E. Huerdler, M. Acharya, M. García-Batlle, O. Almora, A. Guerrero, G. Garcia-Belmonte, W. Heiss, O. Schmidt, S. F. Tedde, *Nat. Electron.* **2021**, *4*, 681.

[69] F. Panzer, C. Li, T. Meier, A. Köhler, S. Huettner, *Adv. Energy Mater.* **2017**, *7*, 1700286.

[70] K. P. Goetz, A. D. Taylor, F. Paulus, Y. Vaynzof, *Adv. Funct. Mater.* **2020**, *30*, 1910004.

[71] E. Ugur, M. Ledinský, T. G. Allen, J. Holovský, A. Vlk, S. De Wolf, *J. Phys. Chem. Lett.* **2022**, *13*, 7702.

[72] S. Zeiske, O. J. Sandberg, N. Zarrabi, C. M. Wolff, M. Raoufi, F. Peña-Camargo, E. Gutierrez-Partida, P. Meredith, M. Stolterfoht, A. Armin, *J. Phys. Chem. Lett.* **2022**, *13*, 7280.

[73] A. Rajagopal, P.-W. Liang, C.-C. Chueh, Z. Yang, A. K.-Y. Jen, *ACS Energy Lett.* **2017**, *2*, 2531.

[74] H. Mehdizadeh-Rad, J. Singh, *ChemPhysChem* **2019**, *20*, 2712.

[75] K. Frohna, M. Anaya, S. Macpherson, J. Sung, T. A. S. Doherty, Y.-H. Chiang, A. J. Winchester, K. W. P. Orr, J. E. Parker, P. D. Quinn, K. M. Dani, A. Rao, S. D. Stranks, *Nat. Nanotechnol.* **2022**, *17*, 190.

[76] D. W. de Quilettes, S. M. Vorpahl, S. D. Stranks, H. Nagaoka, G. E. Eperon, M. E. Ziffer, H. J. Snaith, D. S. Ginger, *Science* **2015**, *348*, 683.

[77] H. Zhou, Q. Chen, G. Li, S. Luo, T. Song, H.-S. Duan, Z. Hong, J. You, Y. Liu, Y. Yang, *Science* **2014**, *345*, 542.

[78] D. Glowienka, Y. Galagan, *Adv. Mater.* **2022**, *34*, 2105920.

[79] P. Caprioglio, C. M. Wolff, O. J. Sandberg, A. Armin, B. Rech, S. Albrecht, D. Neher, M. Stolterfoht, *Adv. Energy Mater.* **2020**, *10*, 2000502.

[80] Z. Sun, G. Sitbon, T. Pons, A. A. Bakulin, Z. Chen, *Sci. Rep.* **2015**, *5*, 10626.

[81] K. W. Kemp, A. J. Labelle, S. M. Thon, A. H. Ip, I. J. Kramer, S. Hoogland, E. H. Sargent, *Adv. Energy Mater.* **2013**, *3*, 917.

[82] F. Gao, Z. Li, J. Wang, A. Rao, I. A. Howard, A. Abrusci, S. Massip, C. R. McNeill, N. C. Greenham, *ACS Nano* **2014**, *8*, 3213.

[83] I. Riedel, J. Parisi, V. Dyakonov, L. Lutsen, D. Vanderzande, J. C. Hummelen, *Adv. Funct. Mater.* **2004**, *14*, 38.

[84] C. Li, S. Tscheuschner, F. Paulus, P. E. Hopkinson, J. Kießling, A. Köhler, Y. Vaynzof, S. Huettner, *Adv. Mater.* **2016**, *28*, 2446.

[85] A. M. A. Leguy, Y. Hu, M. Campoy-Quiles, M. I. Alonso, O. J. Weber, P. Azarhoosh, M. van Schilfgaarde, M. T. Weller, T. Bein, J. Nelson, P. Docampo, P. R. F. Barnes, *Chem. Mater.* **2015**, *27*, 3397.

[86] J. Huang, S. Tan, P. D. Lund, H. Zhou, *Energy Environ. Sci.* **2017**, *10*, 2284.

[87] S. Y. Kwon, B. Kang, J. H. Won, C. Y. Lee, K. Hwang, H. H. Kim, D. Park, W. K. Choi, I. S. Kim, G. Y. Kim, Y. H. Jang, P. Lee, S. H. Im, T. Kim, *Adv. Mater. Interfaces* **2023**, *10*, 2202249.

[88] I. Mesquita, L. Andrade, A. Mendes, *Sol. Energy* **2020**, *199*, 474.

[89] U.-G. Jong, C.-J. Yu, G.-C. Ri, A. P. McMahon, N. M. Harrison, P. R. F. Barnes, A. Walsh, *J. Mater. Chem. A* **2018**, *6*, 1067.

[90] J. A. Christians, P. A. Miranda Herrera, P. V. Kamat, *J. Am. Chem. Soc.* **2015**, *137*, 1530.

[91] A. Hexemer, W. Bras, J. Glossinger, E. Schaible, E. Gann, R. Kirian, A. MacDowell, M. Church, B. Rude, H. Padmore, *J. Phys. Conf. Ser.* **2010**, *247*, 012007.

[92] R. J. Pandolfi, D. B. Allan, E. Arenholz, L. Barroso-Luque, S. I. Campbell, T. A. Caswell, A. Blair, F. De Carlo, S. Fackler, A. P. Fournier, G. Freychet, M. Fukuto, D. Gürsoy, Z. Jiang, H. Krishnan, D. Kumar, R. J. Kline, R. Li, C. Liman, S. Marchesini, A. Mehta, A. T. N'Diaye, D. Y. Parkinson, H. Parks, L. A. Pellouchoud, T. Perciano, F. Ren, S. Sahoo, J. Strzalka, D. Sunday, et al., *J. Synchrotron Radiat.* **2018**, *25*, 1261.

[93] G. Benecke, W. Wagermaier, C. Li, M. Schwartzkopf, G. Flucke, R. Hoerth, I. Zizak, M. Burghammer, E. Metwalli, P. Müller-Buschbaum, M. Trebbin, S. Förster, O. Paris, S. V. Roth, P. Fratzl, *J. Appl. Crystallogr.* **2014**, *47*, 1797.

First of their kind: Solar cells with a dry-processed perovskite absorber layer via powder aerosol deposition and hot-pressing

Simon Biberger[*,1], **Nico Leupold**[*,2], **Christina Witt**[*,1], *Christopher Greve*[3]*, Paul Markus*[4]*, Philipp Ramming*[1]*, Daniel Lukas*[2]*, Konstantin Schötz*[1]*, Frank-Julian Kahle*[1]*, Chenhui Zhu*[5]*, Georg Papastavrou*[4]*, Anna Köhler*[1]*, Eva M. Herzig*[3]*, Ralf Moos*[2]*, Fabian Panzer*[1#]

[*] Contributed equally

[1]Soft Matter Optoelectronics (EP II), University of Bayreuth, Bayreuth 95440, Germany

[2]Department of Functional Materials, University of Bayreuth, Bayreuth 95440, Germany

[3]Dynamics and Structure Formation - Herzig Group, University of Bayreuth, Bayreuth 95440, Germany

[4]Physical Chemistry II, University of Bayreuth, Bayreuth 95440, Germany

[5]Advanced Light Source, Lawrence Berkeley National Lab, 1 Cyclotron Rd, Berkeley, CA, 94720, USA

Corresponding Author:

[#]E-Mail: fabian.panzer@uni-bayreuth.de

236

1 PAD setup
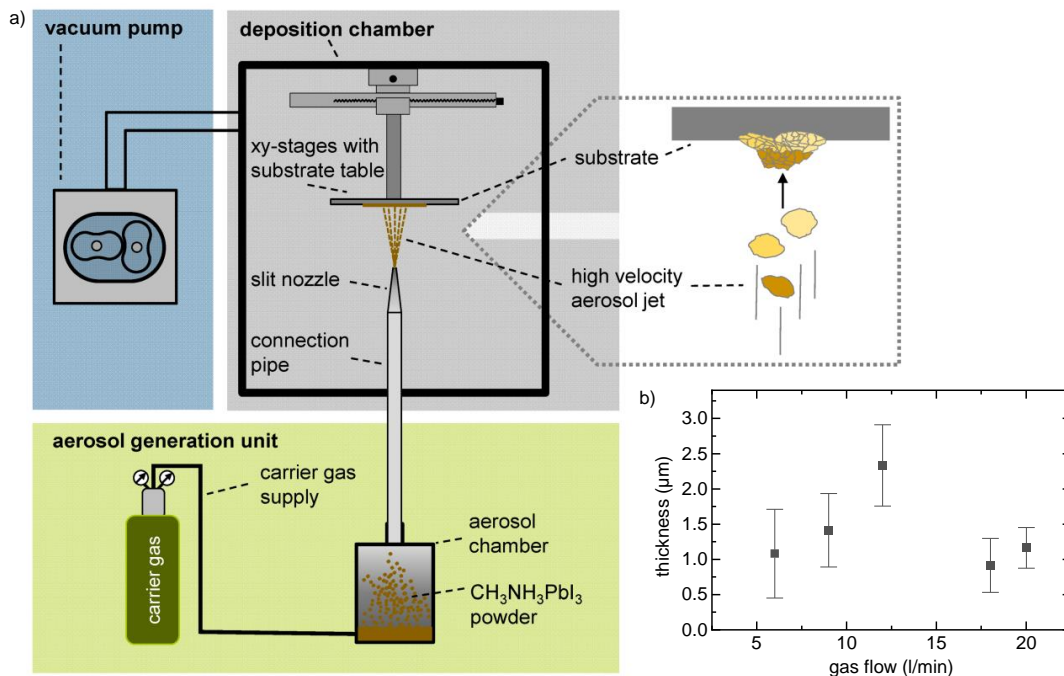
Figure S1: a) Schematic of a setup for powder aerosol deposition (PAD) showing its main components. The zoomed in area illustrates the film formation. Adapted under the terms of the CC-BY 4.0 license.[1] Copyright 2016, the authors. Published by MDPI AG. b) Thickness of MAPbI$_3$ films deposited via PAD using different gas flow.

Derivation of suitable PAD processing parameters

Suitable PAD processing parameters were derived for the deposition of MAPbI$_3$ thin films with appropriate thickness, morphology and homogeneity.

For the aerosol generation, a low gas flow of 0.25 l/min was used to get a low aerosol concentration, which is beneficial for a more homogeneous film coverage.

The gas flow that feeds the ejector to accelerate the aerosol in combination with the reduction of the cross-section at the ejector and the slit nozzle define the resulting carrier gas velocity. We tested different gas flow rates between 6 l/min and 20 l/min and evaluated the resulting film thickness at three different spots across a film. The resulting mean film thicknesses with standard deviation (represented by the error bars) are shown in Figure S1b. Here, a higher gas flow tends to lead to a more homogenous

237

thickness within a film. Consequently, we chose the maximum gas flow of 20 l/min limited by our setup and the geometry of the ejector.

The vacuum level in the deposition chamber of 6 mbar results from the gas flow, the ejector geometry, the nozzle geometry and the performance of the vacuum pump and is in a typical range for PAD.[2]

Regarding the substrate to nozzle distance, we chose a value of 3 mm, that has been proven well suited for deposition in the past in our lab and allows a homogeneous layer thickness across the nozzle width.[2] Moreover, the substrate to nozzle distance seems to have a rather small influence in the chosen range.[3]

Safety aspects of the lead containing PAD process:

Lead-based powder aerosol is a potential safety issue. Nevertheless, no powder aerosol can escape during the coating process, because everything is tightly sealed due to the required vacuum. In addition, a filter is installed before the vacuum pump to remove residual powder in the gas flow. After the deposition is finished and thus after aerosol generation is stopped, the vacuum is maintained for a short time to allow residual powder particles to settle. The machine operator gets in contact with lead-containing powder sticking on the wall of the deposition chamber only when the sample is removed from the coating chamber. For this step, personal protective equipment consisting of safety goggles, gloves, lab coat and particulate respirators is worn. In addition, the PAD machine is located in a fume hood to capture any perovskite particles that may be released into the air. No lead can be found by regular lead tests in the area surrounding the fume hood with the PAD machine. For use in industrial processes, it would be reasonable to use appropriate large-scale extraction systems and a robot to feed the deposition chamber or to employ a continuous process.

2   MAPbI₃ films without optimization of the aerosol generation
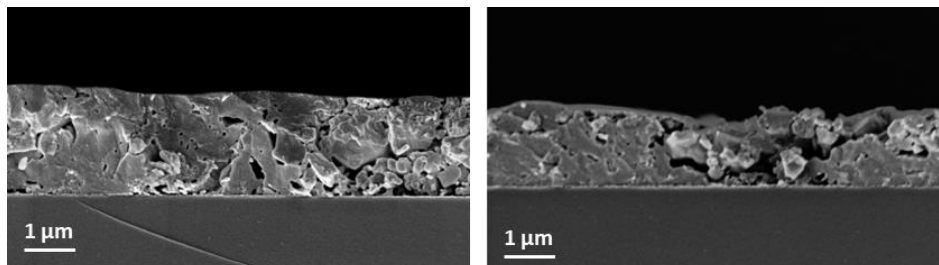
Figure S2: SEM images of rapidly grown MAPbI₃ films deposited using highly agglomerated mechanochemically synthesized MAPbI₃ powders for the PAD process without improvements in the aerosol generation. In the left image, large particles that have not been sufficiently crushed and deformed during deposition are clearly visible, while in the middle of the right image a loosely bound agglomerate can be seen. The films were wiped with a cloth, thus the rather smooth surface.

3 Morphology of mechanochemically synthesized MAPbI$_3$ powder
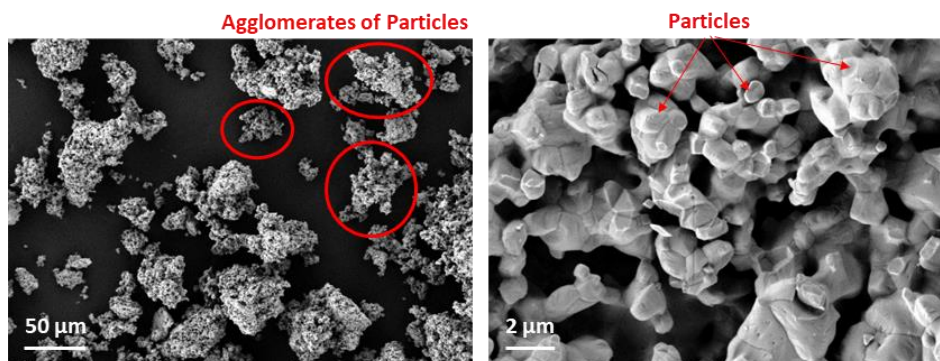
Figure S3: SEM images of mechanochemically synthesized MAPbI$_3$ powder used for PAD.

4 Phase purity of mechanochemically synthesized MAPbI$_3$ powder
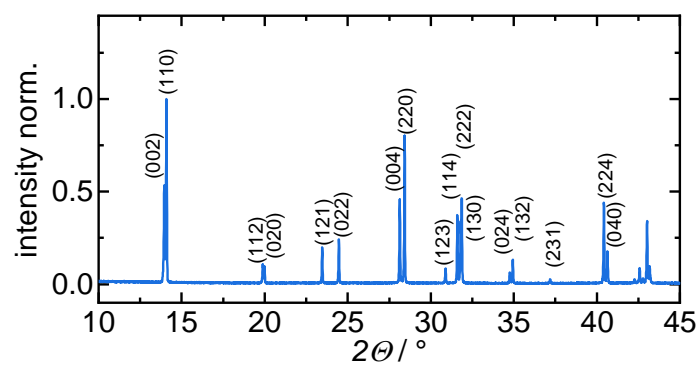
Figure S4: X-ray diffractogram of mechanochemically synthesized MAPbI$_3$ powder. All reflexes can be indexed to MAPbI$_3$ showing the phase purity of the powder[4].

5   Deposition of MAPbI$_3$ films with simple tee instead of the ejector

We also checked if the ejector can be replaced by a simple tee to simplify the setup. However, the resulting deposited films using the tee show large pores, voids (pinholes through the whole film) and particles that have not been crushed, as expected when too much kinetic energy is used to break up larger agglomerates instead of particles (Figure S5). Also, the film deposited with tee is quite thin as the larger agglomerates probably do not bond to the substrate during the first passes.
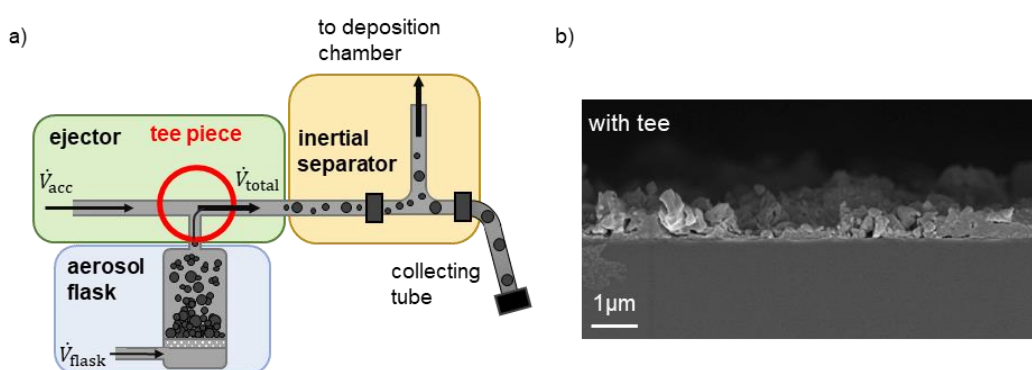
Figure S5: a) Concept of the aerosol generation employing a tee piece as the ejector unit. b) SEM image of a MAPbI$_3$ film deposited with a simple tee instead of the ejector.

6   Detailed discussion of the pressing process

When hot-pressing MHP thin films, silicon wafers are often used as press die because of their low surface roughness and the applicability of a hydrophobic coating.[5–12] This coating is necessary to prevent the perovskite film from sticking to the press die. [5,7–9,12] However, in single-action pressing, as performed in this work by means of a manual press, the use of silicon wafers as press die is limited to pressures below 10 MPa,[8,12] as otherwise the wafers may break. Alternatively, PTFE sheets are used as press die material owing to their anti-sticking behavior. However, due to the low form stability of PTFE, pressure is often kept far below 15 MPa.[13–15] In contrast, polyimide foil is characterized by high form stability under mechanical and thermal stress and also exhibits anti-sticking behavior due to its low surface roughness.[16] Using polyimide foil as press die material, MHP films with promising optoelectronic properties have been fabricated.[17,18] Thus, we tried pressing our pristine PAD films with polyimide foil

S6

as press die material at a pressure of 25 MPa and a temperature of 120 °C. Unfortunately, the used polyimide foil (thickness: 125 μm, roughness: 43 nm) wears off during hot pressing (see Figure S6 top), which might be caused by the rough surface of the pristine PAD films. In addition, the polyimide foil is not reliably anti-sticking (see Figure S6 top), indicating that a lower surface roughness of the foil would be required. Due to these issues, we went over to glass blocks (thickness: 8 mm, roughness: 2 nm) as press die material, whose thickness is decisive for the fracture resistance under pressing. Despite the low surface roughness of the glass blocks, an anti-sticking coating (Trichloro(octadecyl)silane in toluene from liquid phase) is necessary (see Figure S6 bottom). Using the silanized glass blocks as press die in our manual press, our MAPbI$_3$ thin films can be reliably pressed with 25 MPa at 120 °C for 5 min (Figure 3a and previous work[19] for details on press setup, entire time profiles of pressure and temperature in Figure S7).

before pressing   after pressing

before pressing   after pressing
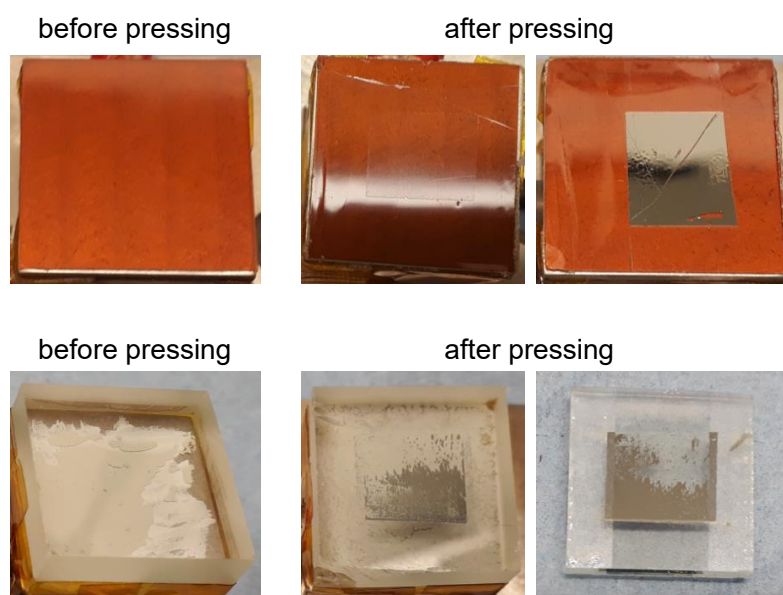
Figure S6: Top: Polyimide foil before (left) and after pressing (right): As a result of the increased pressure and temperature during the pressing process, the foil wears off and the pressed MAPbI$_3$ film may stick to the foil. Bottom: Glass die without silanization coating before (left) and after (middle) hot-pressing a MAPbI$_3$ PAD film (right). Parts of the MAPbI$_3$ PAD film have detached from the substrate and stick on the glass die.
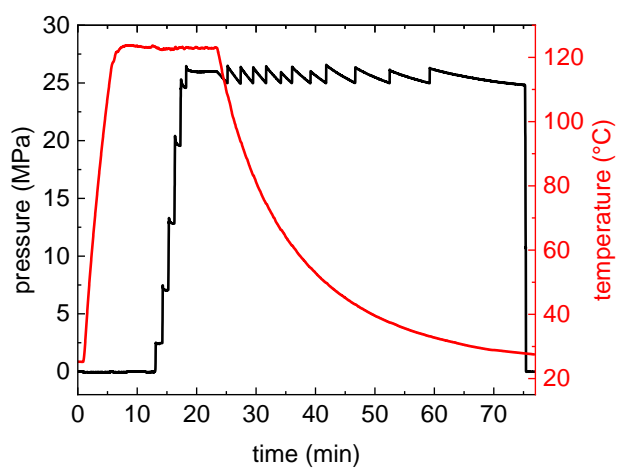
Figure S7: Time evolution of the applied pressure and temperature when pressing a MAPbI$_3$ PAD film 5 minutes at a target level of 25 MPa and 120 °C (pressure was manually readjusted to maintain the target pressure level).
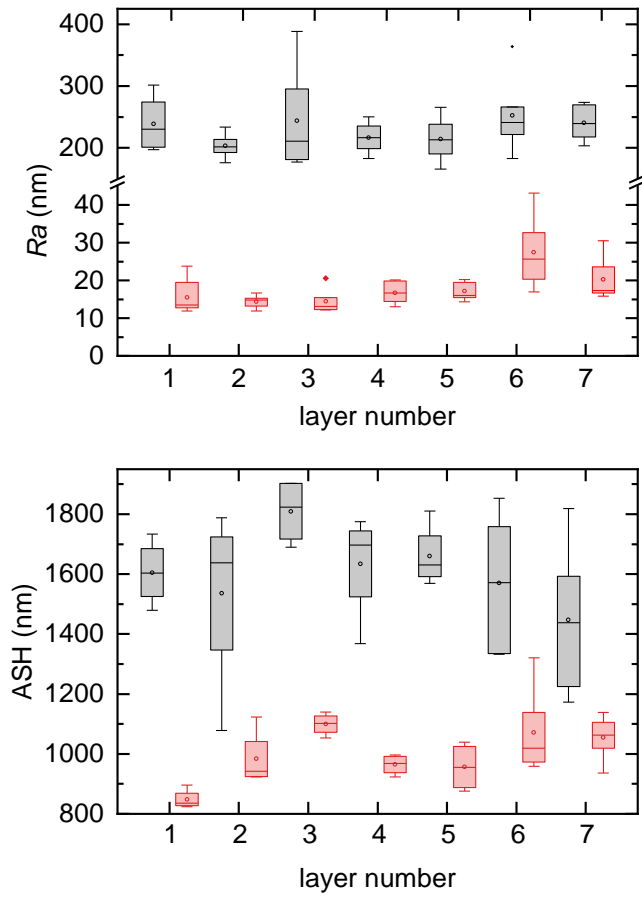
Figure S8: Surface roughness (top) and average surface height specifying film thickness (bottom) of 7 MAPbI$_3$ absorber layers before (grey, "pristine film") and after hot-pressing (red, "pressed film") determined using a profilometer.

7 Solar cell characteristics
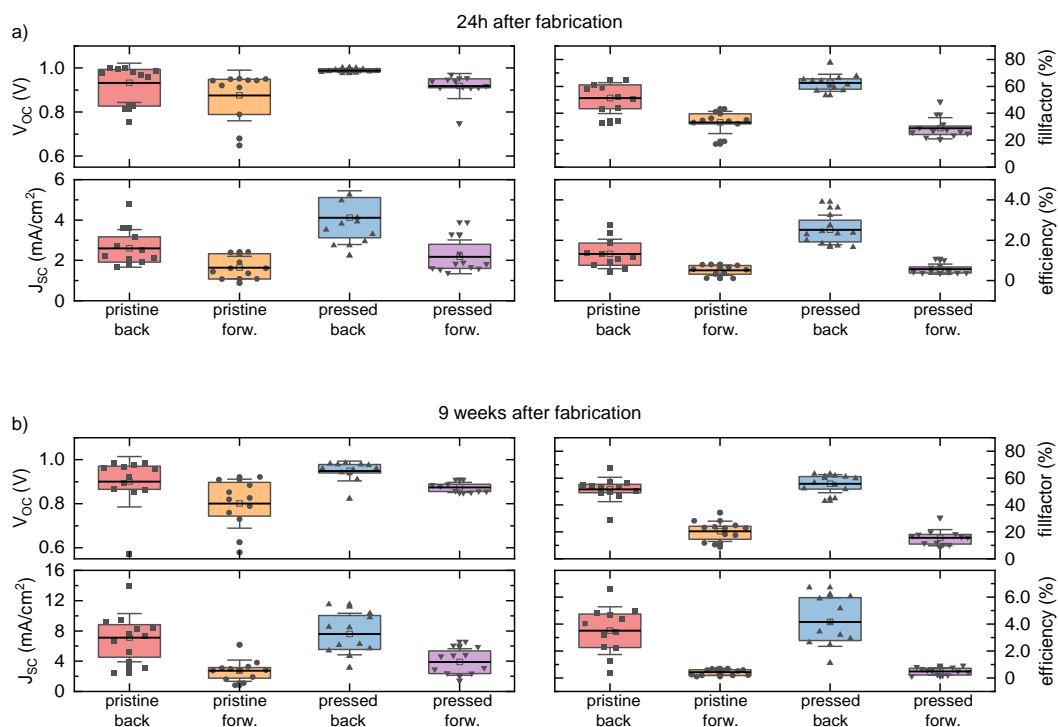
Figure S9: Batch statistics (back and forward direction) of solar cells with pristine absorber layer (red, orange) and with pressed absorber layer (blue, purple) obtained a) 24h after fabrication and b) 9 weeks after fabrication.

Table S1: Summary of solar cell metrics (mean values) for MAPbI$_3$ solar cells with pristine and with pressed PAD processed absorber layer measured 24h after fabrication, values for forward direction in brackets.

type	V_{oc} in V	J_{sc} in mA/cm^2	FF in %	PCE in %
pristine	0.93 ± 0.09	2.6 ± 0.9	52 ± 12	1.3 ± 0.8
	(0.87 ± 0.12)	(1.6 ± 0.6)	(33 ± 8)	(0.5 ± 0.3)
pressed	0.99 ± 0.01	4.1 ± 1.4	63 ± 6	2.5 ± 0.7
	(0.92 ± 0.06)	(2.2 ± 0.8)	(29 ± 8)	(0.6 ± 0.2)

S10

Table S2: Summary of solar cell metrics (mean values) for MAPbI$_3$ solar cells with pristine and with pressed PAD processed absorber layer measured 9 weeks after fabrication, values for forward direction in brackets.

type	V_{oc} in V	J_{sc} in mA/cm^2	FF in %	PCE in %
pristine	0.90 ± 0.11	7.2 ± 3.1	52 ± 9	3.5 ± 1.8
	(0.80± 0.11)	(2.8 ± 1.4)	(21 ± 7)	(0.4 ± 0.3)
pressed	0.95 ± 0.04	7.6 ± 2.7	56 ± 6	4.1 ± 1.8
	(0.87 ± 0.03)	(3.9 ± 1.8)	(16 ± 6)	(0.5 ± 0.3)

Operational Stability

In order to assess the operational stability, we recorded consecutive J-V measurements and plotted the extracted solar cell parameters as a function of number of measurements (Duration per scan: 30 seconds). From this tracking of solar cell parameters, it becomes clear that Voc and FF of the pressed device appears nearly constant, while the Jsc of devices 1 and 2 slightly decrease with the number of consecutive J-V scans. In contrast, for the three devices with pristine absorber layer shown here, the J-V characteristic exhibit different behavior as a function of number of consecutive J-V scans, which we speculate to be attributed to the differences in perovskite layer morphology, compactness and surface roughness.
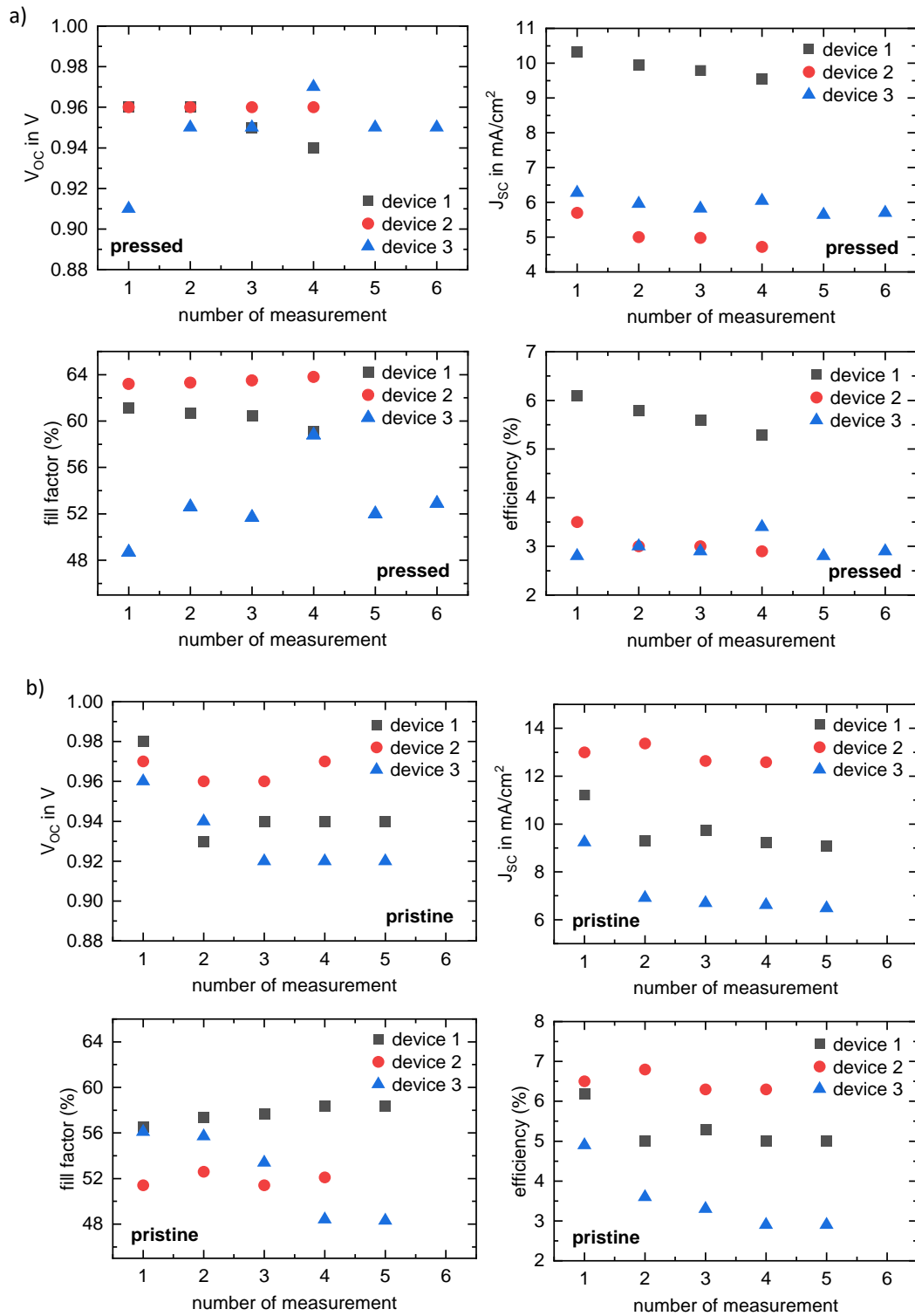
Figure S10: Solar metrics of three devices each for pressed (a) and pristine (b) MAPbI$_3$ absorber layers as function of number of measurements of consecutive J-V sweeps.

8 Prove of perovskite adhesion via scotch tape test
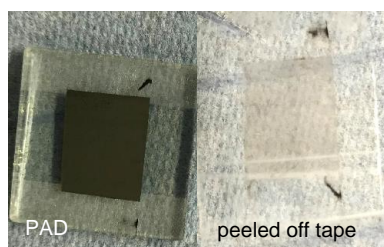
Figure S11: Photograph of the PAD film (left) after applying and removing a stripe of scotch tape on the pristine PAD film. On the peeled off tape (right), only a negligible amount of MAPbI$_3$ powder is visible which originates from loose and uncompressed powder particles remaining on top of the film after PAD.

9 Details on the SnO$_2$ layer
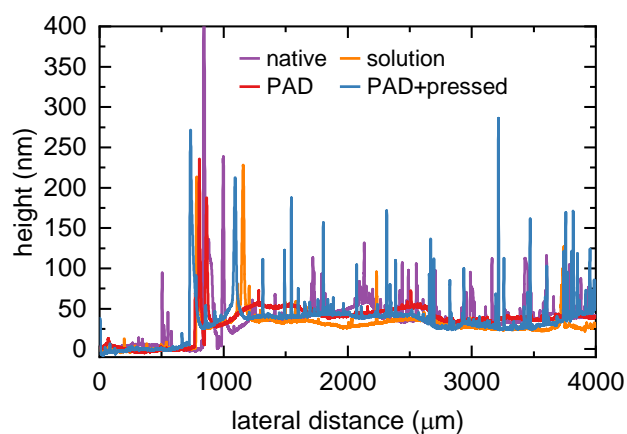
Figure S12: Height profiles of 1) a native SnO$_2$ layer serving as reference, 2) SnO$_2$ layer after removing a solution-processed MAPbI$_3$ film, 3) SnO$_2$ layer after removing a pristine MAPbI$_3$ PAD film, and 4) SnO$_2$ layer after removing a pressed MAPbI$_3$ PAD film.
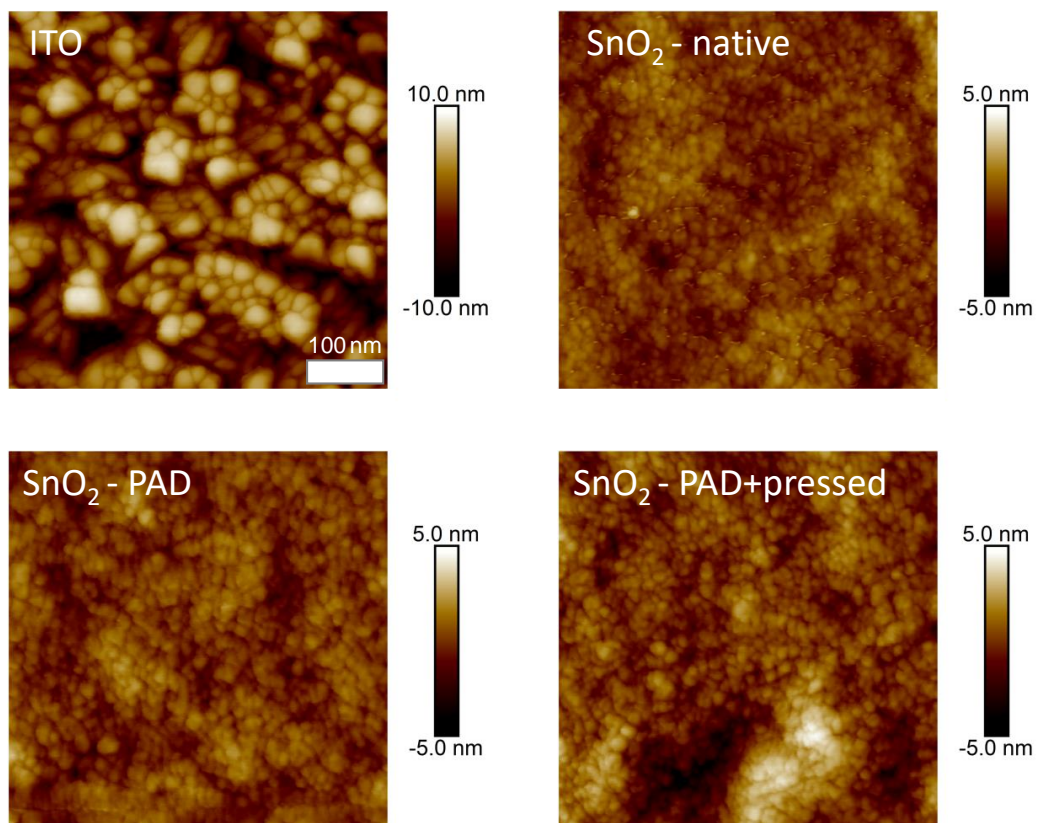
Figure S13: AFM topography images of a native SnO$_2$ layer and SnO$_2$ layers after applying a MAPbI$_3$ film via PAD (and pressing) and removing the MAPbI$_3$ film. The ITO topography is also shown for reference.

S14

SnO$_2$	native	solution	PAD	PAD+pressed
E_U / meV	155 ± 20	180 ± 20	210 ± 20	215 ± 20
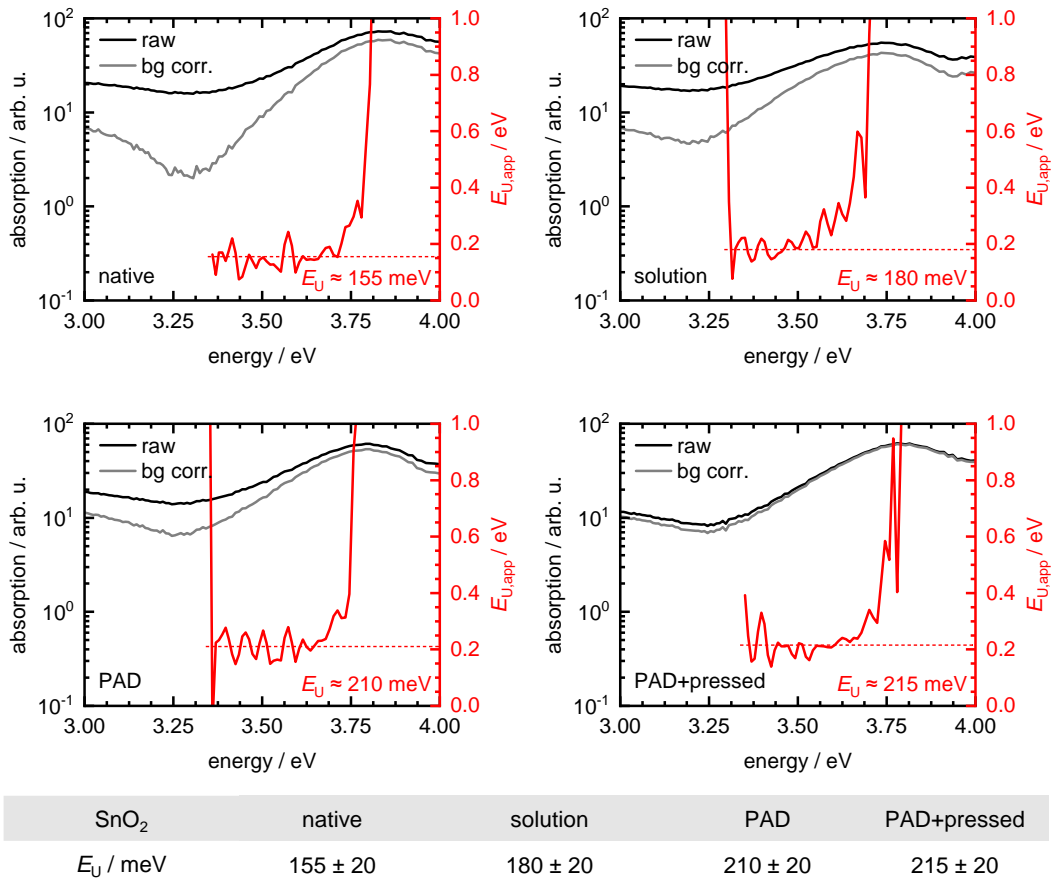
Figure S14: Extraction of Urbach energy E_U via calculated apparent Urbach energy $E_{U,app}$ (red) from measured (black) / background corrected (grey) absorption spectra of 1) a native SnO$_2$ layer serving as reference, 2) SnO$_2$ layer after removing a solution processed MAPbI$_3$ film, 3) SnO$_2$ layer after removing a pristine MAPbI$_3$ PAD film, and 4) SnO$_2$ layer after removing a pressed MAPbI$_3$ PAD film. The E_U values extracted from the horizontal part of $E_{U,app}$ (red dashed line) are summarized in the table below the graphs.

The Urbach energies E_U of the four different presented types of SnO$_2$ layers were extracted via calculating the apparent Urbach energy $E_{U,app}$ according to $E_{U,app} = \left(\frac{d}{dE}[\ln(\alpha - D)]\right)^{-1}$ from the absorption spectra (α) with subtracted scattering offset D. This analysis method has been introduced recently in the field of halide perovskite by Ugur et al. and Zeiske et al.[20,21] The horizontal part of the apparent Urbach energy $E_{U,app}$ represents the exponential part in the absorption spectra and thus yields the Urbach energy value E_U. Large error bars were estimated for the extracted Urbach

energy values E_U, because of the limited quality of the absorption spectra due to the small SnO_2 layer thickness (40-50 nm). This is also the reason why we used the novel more sophisticated analysis method of the Urbach energy via $E_{U,app}$ for the SnO_2 layer instead of fitting the absorption spectra directly with an exponential function as done for the $MAPbI_3$ absorber layer in Figure 6. The extracted higher Urbach energies for PAD treated SnO_2 layers suggest that the PAD-processing increases the energetic disorder in the SnO_2 layer.
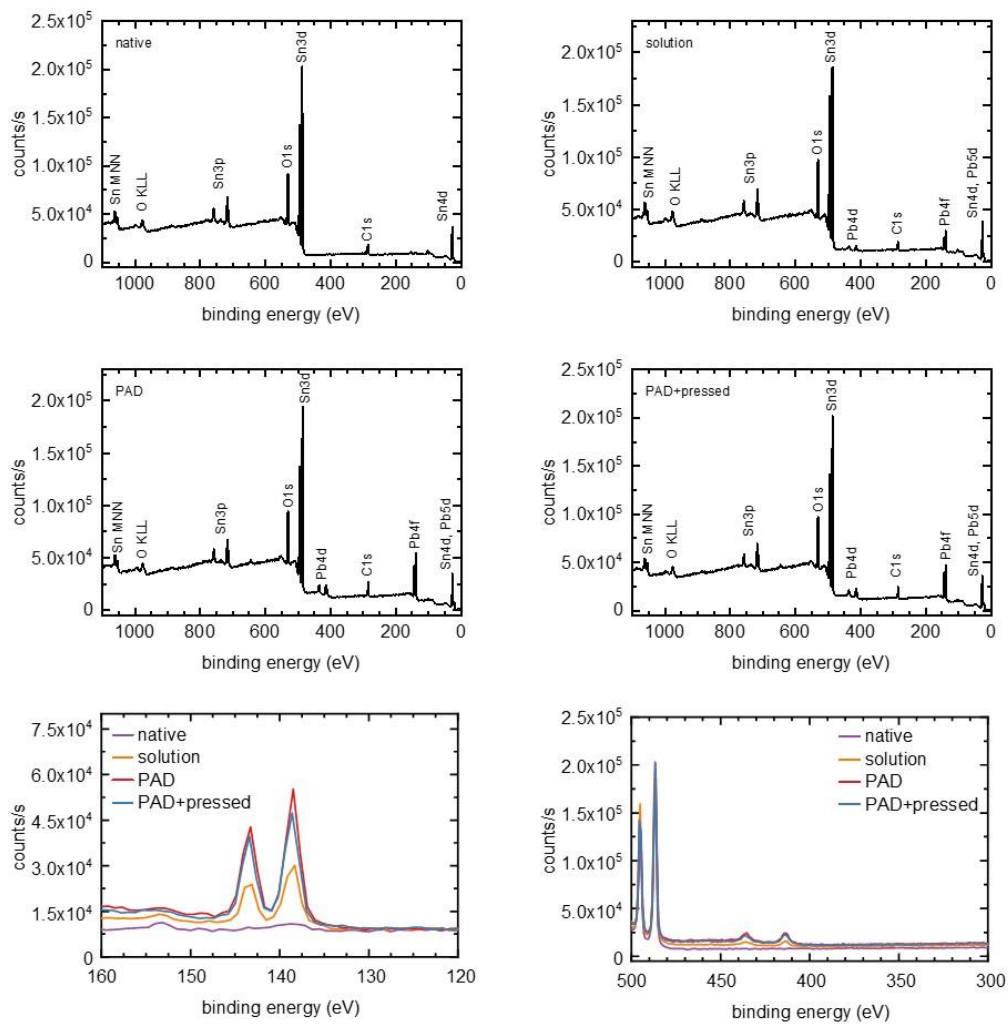
Figure S15: XPS spectra of 1) a native SnO_2 layer serving as reference, 2) SnO_2 layer after removing a solution-processed $MAPbI_3$ film, 3) SnO_2 layer after removing a pristine $MAPbI_3$ PAD film, and 4) SnO_2 layer after removing a pressed $MAPbI_3$ PAD film.

10 Further details on the perovskite layer
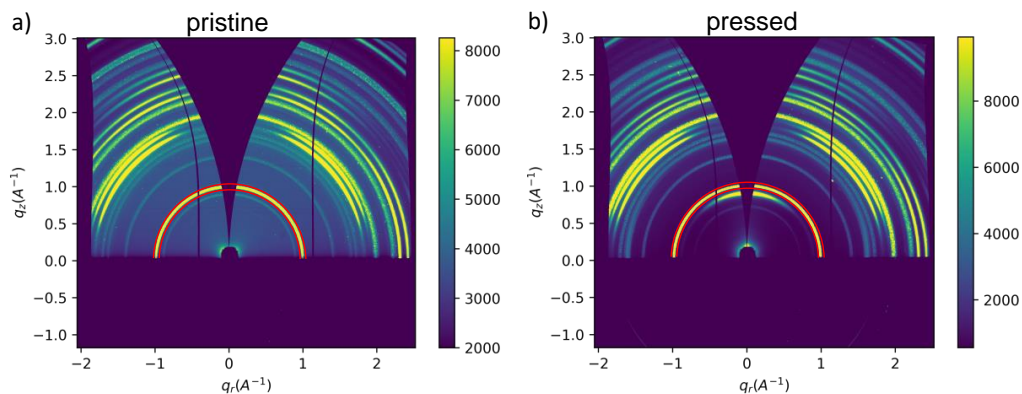
Figure S16: Ewald-curvature corrected 2D GIWAXS data of a) pristine and b) pressed MAPbI$_3$ thin films. The red lines mark the (110) & (002) double peak, which was examined for the χ analysis in the main text.

χ analysis and single pixel intensity variations

To distinguish changes in orientation for the pristine and pressed MAPbI$_3$ films the samples were examined with a χ analysis. Therefore, a line cut over the full peak width of the (110) & (002) double peak marked (red) in Figure S16 was extracted. Hereby 90° corresponds to the direction along q$_r$ (in-plane of the sample) and 0° to the direction along q$_z$ (out-of-plane of the sample). The upper limit of χ is given by the missing gap due to the curvature of the Ewald-sphere, while the lower limit is given by the position of the Yoneda streak at q$_z$ = 0.083 Å^{-1}.[22] The Yoneda region needs to be discarded to ignore its intensity enhancement. Also, the data below the Yoneda region will be discarded because it emerges from below the horizon and is therefore attenuated. The resulting intensity plot versus angle χ was then corrected for the sample isotropy by subtracting the isotropic contribution. The resulting plot showing the oriented fraction is displayed in Figure 6b (main text).

The intensity within the (110) & (002) double peak marked in Figure S16 was further analyzed by extracting single pixel counting statistics to determine how the pressing changes the number of large crystallites within the film. The results are shown in Figure S17. One can see in subfigure b) that the median of the pixel intensity distribution of the hot-pressed MAPbI$_3$ film is at 2.5k counts/pixel, while the median of the distribution

in subfigure a) is at 4.7k counts/pixel. This is related to the overall higher background level of counts for the pristine sample, which is also visible in Figure S16. Further, the overall mean of the ratio of counts/pixel is higher (8.4k counts/pixel) for the hot-pressed sample, resulting in a local maximum visible at 20k counts/pixel. Similar behaviour is observed for the pristine sample, but the overall mean is lower (7.2k counts/pixel) with the local maximum shifting to lower values (15k counts/pixel). The higher mean and the higher single pixel counts of the local maximum around 20k of the pressed sample indicates an increased number of large crystallites within the hot-pressed sample.
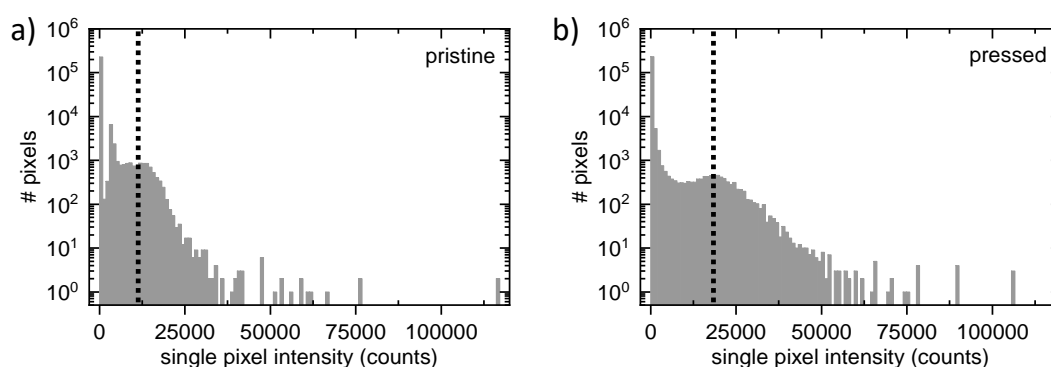
Figure S17: Histograms of single pixel counting statistics of the pixels within the marked area of the (110) & (002) double peak in Figure S15 for a a) pristine and b) pressed MAPbI$_3$ film.
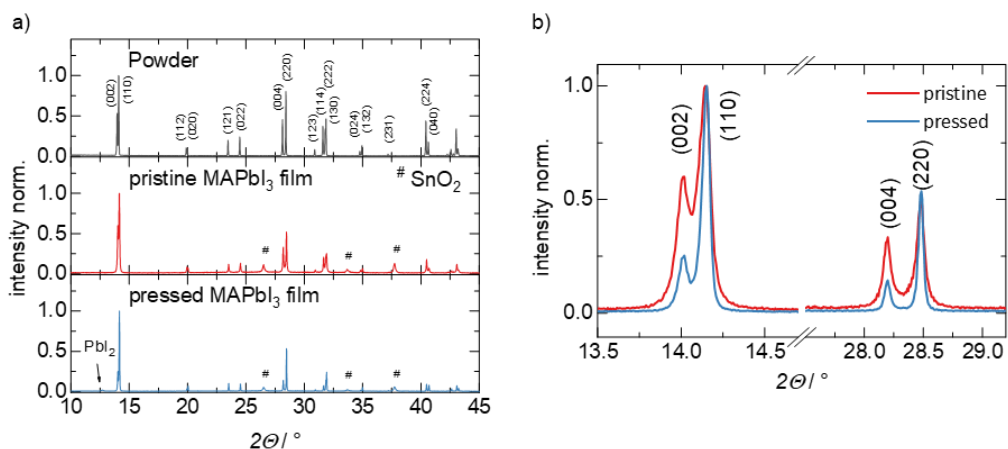
Figure S18: (a) X-ray diffractograms of mechanochemically synthesized MAPbI₃ powder, pristine MAPbI₃ PAD film, and pressed MAPbI₃ PAD film. All reflexes can be indexed to MAPbI₃ showing the phase purity of the powder and the pristine film.[4] In the pressed film only a negligible amount of PbI₂ is found. (b) Zoomed in version of the X-ray diffractograms from (a) for the pristine and pressed film showing the decrease in FWHM and the introduction of preferred orientation upon pressing.

Detailed q_r and q_z analysis

To examine the compression of unit cells upon pressure treatment, the (110) and (002) signal was examined in two perpendicular directions. Peak positions were separated by fitting two gaussian peaks and a local background in q_r and q_z direction. The obtained lattice spacings d are plotted in Fig S19 on the left for q_r and on the right for q_z.
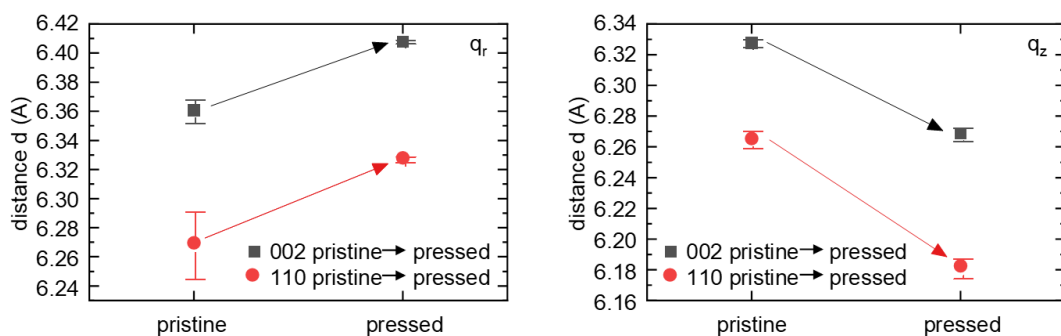
Figure S19: Lattice distances extracted from the (110) & (002) double peak along q_r (left) and q_z (right) for pristine and pressed MAPbI₃ thin films. The arrows indicate the change in lattice spacings with pressing.

S20

11 Urbach Analysis
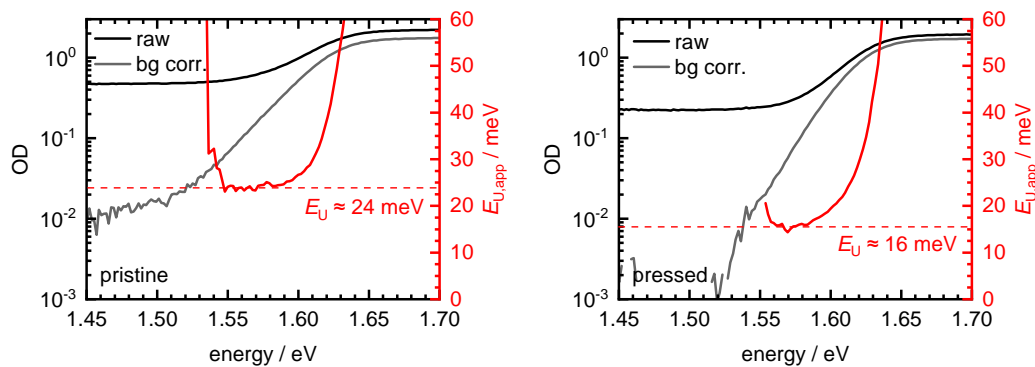
Figure S20: Extraction of Urbach energy E_U via calculated apparent Urbach energy $E_{U,app}$ (red) from measured (black) / background corrected (grey) absorption spectra of pristine (left) and pressed (right) MAPbI$_3$ PAD films. The E_U values are extracted from the horizontal part of $E_{U,app}$ (red dashed line).

The extraction of the Urbach energy in Figure 6 in the main text by exponential fits to the absorption spectra is commonly used. Recently, a novel sophisticated analysis method of the Urbach energy via $E_{U,app}$ has been introduced in the field of perovskites (see also Figure S14).[20,21] We additionally applied this novel method which yields Urbach energy values of approx. 24 meV and 16 meV for pristine and pressed MAPbI$_3$ PAD films, respectively (Figure S20). These values are similar to the values obtained by the method shown in Figure 6.

12 Ideality factors and α values
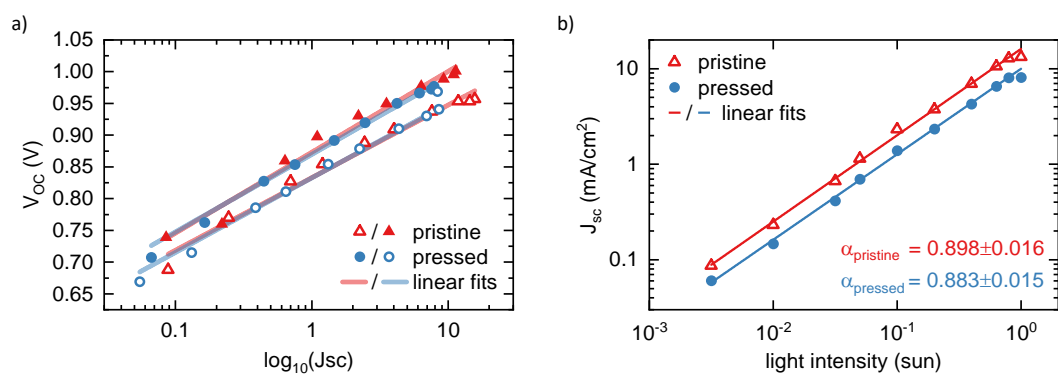
Figure S21: a) V_{OC} as a function of the J_{SC}, obtained from the light intensity-dependent J-V-curves. From the slope of the linear fitting the values of the ideality factors n (see main) are extracted. b) Light intensity-dependence of the J_{SC} for pristine and pressed MAPbI$_3$ PAD films. α values are extracted from the slope of the linear fitting.

Supporting References

[1] F. Panzer, D. Hanft, T. P. Gujar, F.-J. Kahle, M. Thelakkat, A. Köhler, R. Moos, *Materials* **2016**, *9*, 277.

[2] D. Hanft, J. Exner, M. Schubert, T. Stöcker, P. Fuierer, R. Moos, *J Ceram Sci Tech* **2015**, *6*, 147.

[3] A. Zabihi Yeganeh, M. Jadidi, C. Moreau, A. Dolatabadi, *Surf. Coat. Technol.* **2019**, *370*, 269.

[4] T. Baikie, Y. Fang, J. M. Kadro, M. Schreyer, F. Wei, S. G. Mhaisalkar, M. Graetzel, T. J. White, *J. Mater. Chem. A* **2013**, *1*, 5628.

[5] A. Mayer, M. Buchmüller, S. Wang, C. Steinberg, M. Papenheim, H.-C. Scheer, N. Pourdavoud, T. Haeger, T. Riedl, *J. Vac. Sci. Technol. B* **2017**, *35*, 06G803.

[6] T. Zhang, L. Zhang, G. Zhu, D. Cui, Q. Wang, G. Lian, Z. Zheng, H. Yu, *Adv. Mater. Interfaces* **2022**, *9*, 2200447.

[7] Y. Yu, M. Shang, T. Wang, Q. Zhou, Y. Hao, Z. Pang, D. Cui, G. Lian, X. Zhang, S. Han, *J. Mater. Chem. C* **2021**, *9*, 15056.

[8] L. Huang, Z. Xing, X. Tang, D. Li, X. Meng, X. Hu, T. Hu, Y. Chen, *J. Mater. Chem. A* **2021**, *9*, 16178.

[9] A. Mayer, N. Pourdavoud, Z. Doukkali, K. Brinkmann, J. Rond, J. Staabs, A.-C. Swertz, F. van gen Hassend, P. Görrn, T. Riedl, H.-C. Scheer, *Appl. Phys. A* **2021**, *127*, 237.

[10] N. Pourdavoud, A. Mayer, M. Buchmüller, K. Brinkmann, T. Häger, T. Hu, R. Heiderhoff, I. Shutsko, P. Görrn, Y. Chen, H.-C. Scheer, T. Riedl, *Adv. Mater. Technol.* **2018**, *3*, 1700253.

[11] N. Dong, X. Fu, G. Lian, S. Lv, Q. Wang, D. Cui, C.-P. Wong, *ACS Appl. Mater. Interfaces* **2018**, *10*, 8393.

[12] J. Moon, S. Kwon, M. Alahbakhshi, Y. Lee, K. Cho, A. Zakhidov, M. J. Kim, Q. Gu, *ACS Appl. Mater. Interfaces* **2021**, *13*, 5368.

[13] B. A. Nejand, S. Gharibzadeh, V. Ahmadi, H. R. Shahverdi, *Sci. Rep.* **2016**, *6*, 33649.

[14] W. A. Dunlap-Shohl, T. Li, D. B. Mitzi, *ACS Appl. Energy Mater.* **2019**, *2*, 5083.

[15] J. Xiao, Y. Yang, X. Xu, J. Shi, L. Zhu, S. Lv, H. Wu, Y. Luo, D. Li, Q. Meng, *J. Mater. Chem. A* **2015**, *3*, 5289.

[16] C. Qu, J. Hu, X. Liu, Z. Li, Y. Ding, *Materials* **2017**, *10*, 1329.

[17] T. Li, A. M. Zeidell, G. Findik, W. A. Dunlap-Shohl, J. Euvrard, K. Gundogdu, O. D. Jurchescu, D. B. Mitzi, *Chem. Mater.* **2019**, *31*, 4267.

[18] H. Chen, F. Ye, W. Tang, J. He, M. Yin, Y. Wang, F. Xie, E. Bi, X. Yang, M. Grätzel, L. Han, *Nature* **2017**, *550*, 92.

[19] C. Witt, K. Schötz, M. Kuhn, N. Leupold, S. Biberger, P. Ramming, F.-J. Kahle, A. Köhler, R. Moos, E. M. Herzig, F. Panzer, *J. Phys. Chem. C* **2023**, *under revision*.

[20] S. Zeiske, O. J. Sandberg, N. Zarrabi, C. M. Wolff, M. Raoufi, F. Peña-Camargo, E. Gutierrez-Partida, P. Meredith, M. Stolterfoht, A. Armin, *J. Phys. Chem. Lett.* **2022**, *13*, 7280.

[21] E. Ugur, M. Ledinský, T. G. Allen, J. Holovský, A. Vlk, S. De Wolf, *J. Phys. Chem. Lett.* **2022**, *13*, 7702.

[22] Y. Yoneda, *Phys. Rev.* **1963**, *131*, 2010.

5 Appendix

List of Abbreviations

Abs	Absorption
ASE	Amplified Spontaneous Emission
a-Se	Amorphous Selenium
$CaTiO_3$	Calcium Titanate
CB	Conduction Band
CdTe	Cadmium Telluride
$CsPbBr_3$	Cesium Lead Bromide
ΔP	Pressure Difference of Pressure Readjustments at Fixed Target Level
DMF	Dimethylformamid
ETL	Electron Transport Layer
FAI	Formamidinium
GaAs	Gallium Arsenide
GIWAXS	Grazing Incidence Wide-Angle X-ray Scattering
HTL	Hole Transport Layer
IoT	Internet of Things
LED	Light Emitting Diode
LSM	Laser Scanning Microscope
MAI	Methylammonium
$MA_3Bi_2I_9$	Methylammonium Bismuth Iodide
$MAPbBr_3$	Methylammonium Lead Bromide
$MAPbI_3$	Methylammonium Lead Iodide
MHP	Metal Halide Perovskite
NQR	Nuclear Quadrupole Resonance
PAD	Powder Aerosol Deposition
Pb	Lead
PCE	Power Conversion Efficiency
PL	Photoluminescence
RT	Room-Temperature
SEM	Scanning Electron Microscope
Si	Silicon
TRPL	Time-Resolved Photoluminescence
VB	Valence Band
V_{OC}	Open-Circuit-Voltage
XRD	X-Ray Diffraction

Danksagung

Erklärung und Eidesstattliche Versicherung

Hiermit versichere ich an Eides statt, dass ich die vorliegende Arbeit selbstständig verfasst und keine anderen als die von mir angegebenen Quellen und Hilfsmittel verwendet habe.

Weiterhin erkläre ich, dass ich die Hilfe von gewerblichen Promotionsberatern bzw. –vermittlern oder ähnlichen Dienstleistern weder bisher in Anspruch genommen habe, noch künftig in Anspruch nehmen werde.

Zusätzlich erkläre ich hiermit, dass ich keinerlei frühere Promotionsversuche unternommen habe.

Bayreuth, den

Christina Witt